Caractérisation de l'organisation et du trafic de paires récepteur/anticorps thérapeutiques par microscopie de localisation de molécules uniques couplée au criblage à haut débit.

Marine Cabillic

▶ **To cite this version:**

Marine Cabillic. Caractérisation de l'organisation et du trafic de paires récepteur/anticorps thérapeutiques par microscopie de localisation de molécules uniques couplée au criblage à haut débit.. Bioinformatique [q-bio.QM]. Université de Bordeaux, 2021. Français. NNT : 2021BORD0026 . tel-03195697v2

HAL Id: tel-03195697

https://theses.hal.science/tel-03195697v2

Submitted on 12 Apr 2021 (v2), last revised 12 Apr 2021 (v3)

HAL is a multi-disciplinary open access archive for the deposit and dissemination of scientific research documents, whether they are published or not. The documents may come from teaching and research institutions in France or abroad, or from public or private research centers.

L'archive ouverte pluridisciplinaire **HAL**, est destinée au dépôt et à la diffusion de documents scientifiques de niveau recherche, publiés ou non, émanant des établissements d'enseignement et de recherche français ou étrangers, des laboratoires publics ou privés.

THÈSE CIFRE PRÉSENTÉE

POUR OBTENIR LE GRADE DE

DOCTEUR DE

L'UNIVERSITÉ DE BORDEAUX

ÉCOLE DOCTORALE DES SCIENCES DE LA VIE ET DE LA SANTÉ

SPÉCIALITÉ: BIOINFORMATIQUE

Par **Marine CABILLIC**

Characterization of therapeutic antibody/receptor pairs nanoscale organization & trafficking by quantitative single molecule localization microscopy combined with high content screening

Sous la direction de : Jean-Baptiste SIBARITA
co-supervision : Christelle PERRAULT

Soutenue le 28 Janvier 2021

Membres du jury :

SIBARITA, Jean-Baptiste	Ingénieur de Recherche, CNRS	Directeur de Thèse
HEILEMANN, Mike	Professor, Johann Wolfgang Goethe-University	Rapporteur
MURIAUX, Delphine	Directeur de Recherche, Université de Montpellier	Rapporteur
LEVEQUE-FORT, Sandrine	Directeur de Recherche, Université Paris-Saclay	Examinateur
BOURGEOIS, Dominique	Directeur de Recherche, Université Grenoble Alpes	Examinateur
PERRAULT, Christelle	Lab Head, Sanofi- Vitry/Alfortville	Examinateur
NAGERL, U Valentin	Professeur, Université de Bordeaux	Président

Interdisciplinary Institute for NeuroScience (IINS)
CNRS UMR 5297

Université de Bordeaux Centre Broca Nouvelle-Aquitaine
146 Rue Léo Saignat
33076 Bordeaux (France)

Caractérisation de l'organisation et du trafic de paires récepteur/anticorps thérapeutiques par microscopie de localisation de molécules uniques couplée au criblage à haut débit.

Résumé

L'immuno-oncologie est un domaine en pleine expansion, à la frontière de la thérapie du cancer. Les immunothérapies du cancer visent à stimuler le système immunitaire de l'organisme pour qu'il cible et attaque la tumeur, grâce à des anticorps thérapeutiques. Ces anticorps se lient spécifiquement aux récepteurs membranaires des cellules T, lymphocytes jouant un rôle central dans la réponse immunitaire, modifiant leur signalisation intracellulaire. Comprendre comment l'organisation spatiale des récepteurs et des protéines de signalisation est régulée, et comment elle détermine l'activation des lymphocytes, est devenu le "Saint Graal" de l'immunologie cellulaire. Dans cette optique, une meilleure compréhension des fonctions des anticorps et du trafic intracellulaire associé, permettrait d'expliciter les différences d'efficacité des candidats thérapeutiques ciblant les récepteurs d'intérêt. La microscopie de super-résolution permet l'accès à l'organisation et la dynamique des récepteurs membranaires avec des résolutions nanométriques. Elle offre la capacité de révéler des informations sur les évènements précoces déclenchés par la liaison d'un anticorps à son récepteur, permettant à terme l'optimisation de leur efficacité fonctionnelle. Associée aux techniques de criblage à haut débit, elle a le potentiel de jouer un rôle prépondérant dans les phases précoces des projets où il est nécessaire de sélectionner les meilleurs anticorps issus de banques pouvant en compter plusieurs centaines.

L'objectif de cette thèse CIFRE a été de caractériser fonctionnellement l'organisation et le trafic de paires récepteur/anticorps par l'association de méthodes de microscopie super-résolution par localisation de molécules individuelles (SMLM) et de criblage à haut débit (HCS). Dans ce contexte, nous avons mis au point et utilisé une plateforme permettant de caractériser différents anticorps thérapeutiques ciblant des récepteurs de cellules T, dans le but de recueillir des informations quantitatives sur les candidats thérapeutiques potentiels. Nous avons également optimisé la technique d'imagerie à feuille de lumière simple objectif (soSPIM) dans le but de pouvoir réaliser une cartographie 3D des récepteurs membranaires sur d'une cellule T entière avec une résolution nanométrique. Cette nouvelle approche permet l'imagerie de cellules T dans des conditions plus physiologiques, fournissant des informations complémentaires par rapport aux expériences de criblage à grande échelle. Ces deux techniques nous ont permis d'améliorer notre compréhension du mode d'action des anticorps sur les récepteurs au niveau de la cellule unique. Les expériences à grande échelle réalisées dans le cadre de ce travail ont nécessité plusieurs développements logiciels pour l'automatisation de l'acquisition et l'analyse statistique des Téraoctets de données de molécules individuelles générées.

Ce projet de thèse s'est concentré sur la cible PD-1, un point de contrôle crucial du système immunitaire impliqué dans la modulation de l'activation des lymphocytes. La première partie de la thèse a été principalement consacrée à la mise en place de nouveaux protocoles pour l'imagerie de super-résolution des récepteurs PD-1 sur cellules Jurkat activées. La seconde partie concerne l'étude de l'impact d'anticorps thérapeutiques anti-PD-1 utilisés en routine en clinique, sur l'organisation spatiale et la dynamique des récepteurs PD-1 sur cellules vivantes, à l'échelle nanométrique. Ce travail est la preuve concept de l'utilité de ces outils d'imagerie de pointe pour la caractérisation quantitative d'anticorps monoclonaux thérapeutiques ciblant PD-1 à la membrane des cellules T.

Mots clés : Immunothérapie, Criblage à Haut-Débit, Microscopie de Super-Résolution, Localisation de Molécules Individuelles, Développement Logiciel, Datamining

Characterization of therapeutic antibody/receptor pairs nanoscale organization & trafficking by quantitative single molecule localization microscopy combined with high content screening

Abstract

Immuno-oncology is a young and growing field at the frontier of cancer therapy. Immuno-oncology therapies aim to stimulate the body's immune system to target and attack the tumor through therapeutic antibodies, by binding and modifying the intracellular signaling of T-cells (lymphocytes playing a central role in the immune response) surface receptors. Understanding how the spatial organization of receptors and signaling proteins is regulated and how it determines lymphocyte activation and cell fate decisions has become a 'holy grail' for cellular immunology. To achieve this goal, a better comprehension of antibodies functions and subcellular trafficking is requested to explain the differential efficacies of therapeutic candidates targeting receptors of interest. Quantitative super-resolution microscopy provides access to the nanoscale organization of membrane receptors playing a physiological role. It offers a new investigation tool for antibody optimization as well as maximizing their functional efficacy. In combination with high throughput screening techniques, it has the potential to play a crucial role in the early phases of projects in which it is necessary to select the best antibodies from banks that may contain several hundreds of them.

The goal of this PhD thesis was to functionally characterize receptor/antibodies pairs organization and trafficking by quantitative single-molecule localization microscopy (SMLM) combined with high content screening (HCS). In this context, we have developed and used an HCS-SMLM platform to characterize multiple antibodies targeting T-cell membrane receptors, allowing gathering unprecedented quantitative insight of potential therapeutic candidates. We also optimized the single objective light-sheet microscope (soSPIM) to permit 3D mapping of membrane receptors across an entire T-cell, with single molecule resolution. It allows 3D nanoscale imaging of T-cells in more physiological conditions, and provide complementary information compared to large scale single molecule screening experiments. Altogether, these developments improved our comprehension of antibody mode of action on receptors at the single cell level. Large-scale experiments performed during this work required the development of several software for the automation of the acquisition and the statistical analysis of the Terabytes of single molecule data generated.

This project is focused on targeting PD-1, a control point of the immune system involved in the modulation of immune cells activation. The first part of the thesis was mainly devoted to the implementation of new protocols for PD-1 receptors super-resolution imaging on activated Jurkat cells. In the second part, we further investigated the impact of known anti-PD-1 therapeutic antibodies used in clinics, on the nanoscale spatial organization and dynamics of PD-1 receptors in living cells using our HCS-SMLM platform. This work provides the proof of concept of the capacity of these cutting-edge imaging techniques to characterize quantitatively different therapeutic monoclonal antibodies targeting PD-1 on T-cell membrane.

Keywords: Immunotherapy, High Content Screening, Super-Resolution Microscopy, Single Molecule Localization Microscopy, Software Development, Datamining

Remerciements

Je tiens tout d'abord à remercier l'ensemble des membres de mon jury de thèse pour le temps consacré à évaluer mon travail de thèse.

Au terme de cette thèse, je souhaite avant tout de chose exprimer ma gratitude envers Jean-Baptiste Sibarita, mon directeur de thèse, pour son soutien tout au long de ces cinq dernières années. Je lui exprime toute ma reconnaissance pour m'avoir encouragée à poursuive ce doctorat, me témoignant sa confiance pour les trois années qui allaient suivre. Depuis 5 ans, JB a su me faire évoluer au fil des années et m'a permis de m'épanouir professionnellement sur des projets très intéressants. Je le remercie pour sa jovialité, sa franchise et d'avoir toujours su se rendre disponible.

Mes trois années de thèse se sont déroulées dans un environnement chaleureux et stimulant. Je le dois à tous les membres de l'IINS et particulièrement à l'équipe Sibarita et Studer. A peine débarquée fraichement diplômée dans l'équipe, j'ai directement été immergée dans une ambiance conviviale. Equipe avec qui j'ai partagé beaucoup de franches rigolades et que je remercie chaleureusement pour son soutien quotidien. Bien entendu, je remercie mes anciens compères de bureau : PO, Corey et Emanuele avec qui j'ai partagé énormément de rire et bons moments, ainsi que Nath, Julie, Catherine, Sarah, Agata, Mathieu pour leur bonne humeur quotidienne.

Je tiens à remercier particulièrement Anne Beghin avec qui j'ai collaboré sur ce projet et qui m'a soutenue et formée en biologie et en microscopie sur mon projet de thèse. Aussi, je voudrais remercier Zeynep, Andrea, et Ingrid d'avoir répondu à mes éternelles questions existentielles sur la biologie ou l'imagerie. Elever une ingénieure informatique au rang de semi-biologiste ne fut pas chose aisée, mais si j'ai relevé le défi, c'est grâce à vous.

Dans la même optique, sans mauvais jeu de mots, je fais un grand merci à Rémi Galland qui a été l'un des plus présent au quotidien pour m'aider et me conseiller pendant ma thèse. Je remercie aussi Florian pour son aide, et puis Hisham avec qui ce fut un plaisir de collaborer ces dernières années sur le soSPIM. Je remercie également Magalie pour ses conseils et sa bonne humeur partagée lors de nos projets HCS.

Je voudrais adresser un très grand merci à mes supérieurs de chez Sanofi, ma superviseure Christelle Perrault et Michel Partiseti. Je les remercie pour leurs soutiens et surtout le temps qu'ils ont pris pour m'aider et me conseiller. Au même titre que JB, ils m'ont formé et fait évoluer dans d'autre disciplines tels que l'immunologie et les enjeux de l'entreprise.

Je tenais également remercier mes anciens instructeurs, Vincent Jeanne et Franck Michelet, de qui je garde quotidiennement en tête les enseignements.

Enfin et pas des moindres, je souhaiterai remercier ma famille et mes amis qui ont toujours cru en moi, ainsi que tous ceux que j'aurai oublié de citer pour leur soutien et leur sourire !

Merci de tout cœur à Gustave pour son amour et soutien quotidien.

A Georges,

Lexique

CD - Cluster of differentiation
MHC – Major Histocompatibility complex
TCR - T-Cell membrane receptors
PTK - Protein tyrosine kinases
Lck - Lymphocyte protein tyrosine kinase family
ITAM - Immune-receptor tyrosine-based activation motifs
APC - Antigen presenting cell
AA - Amino acids
IL-2 - Interleukin-2
INFg - Interferon gamma
TNFa – Tumor necrosis factor alpha
mAbs - Monoclonal antibodies
CAR-T Cell - Chimeric antigen receptor T-cell
TIL - Tumor-infiltrating T lymphocyte
PD-1 - Programed cell death proteins 1
PD-L1 - Programmed death-ligand 1
ITIM - Immune-receptor tyrosine-based inhibitory motif
ITSM - Immune-receptor tyrosine-based switch motif
FDA – Food and drug administration
EMA - European medicines agency
2D, 3D – Two, three-dimensional
SMLM - Single molecule localization microscopy
PSF - Point spread function
NA - Numerical aperture
TIRF - Total internal reflection fluorescence microscopy
HILO - Highly inclined laminated optical sheet
LSM - Light sheet microscopy
SPIM - Selective plane illumination microscopy (SPIM)
soSPIM – Single objective selective-plane illumination microscopy
SAF - Supercritical angle fluorescence
(d)STORM - (direct) Stochastic optical reconstruction microscopy
PALM - Photo-activated localization microscopy
SPT - Single particle tracking
(DNA/u) PAINT - Point accumulation for imaging in nanoscale topography
FRET - Fluorescence resonance energy transfer
HCS - High content screening
HTS – High-throughput screening
PFS – Perfect focus system
MLR - Mixed leucocyte reaction experiment
GUI - Graphical user Interface
GPU - Graphics processing unit
CPU – Central processing unit
LED - Light-emitting diode
FOV - Field of View
Ca2+- Calcium

Table of Contents

INTRODUCTION

CHAPTER 1: Immuno-oncology, Immuno-therapies
CHAPTER 2: Optical Super-Resolution Microscopy
CHAPTER 3: High-Content-Screening

1.1. CHAPTER 1: Immuno-oncology, Immuno-therapies

1.1.1. Principles of immunology

1.1.1.1. Main mechanisms of immune system response

The immune system response is a defensive reaction from the body against foreign invaders. It represents how the body engages the immune system to recognize and defend itself to viruses, bacteria, fungi or any **non-self-pathogens**. There are two distinct immune mechanisms, the **innate** and **adaptive immune response**. The innate response is non-specific and as the name suggests is the first reaction of the body against a pathogen preventing the foreign pathogen to spread into the body. While innate immunity is immediate, the adaptive immunity is the second line of defense of the body and is specific to the presented pathogen. Many different groups of cells are involved in both types of the immune response: granulocytes, monocytes, macrophages and Natural Killer cells are the main contributors of the innate phase whereas lymphocytes play a key role in the adaptive immune response. Lymphocytes are small and specialized cells which include two subtypes of cells: B-cells and T-cells. Their engagement is antigen-dependent, once activated they have complementary actions to ensure the destruction of the pathogen. T-cells represent 70% of the lymphocytes population, and it exists many different T-cell sub-groups (e.g. helper, cytotoxic, memory and regulatory T-cell), each having specific properties but all of them expressing the specific cell surface markers CD3 for **cluster of differentiation (CDs) 3** and **T-cell receptor (TCR)**. To better apprehend this project, it is important to well understand the main mechanisms of activation pathways of immune T-cells.

1.1.1.2. T-cell activation: a critical step in immunology

In immunology, the presentation of an antigen to the T-cell receptor triggers T-cell activation and proliferation. It is the main mechanism at the origin of immune T-cell response. T-cell activation requires successive steps, involving different partners and underlying signal pathways (Smith-Garvin et al[1], 2009). It is described by a three-signals model: (1) formation of the TCR-CD3 complex, (2) recruitment of co-stimulatory receptor and (3) cytokine production (Figure 1).

T-cell activation occurs in several phases to result in an efficient immune response, including: T-cell receptor dependent signaling, increase of T-cell life-cycle through proliferation, differentiation, cytokine secretion/regulation. Firstly, T-cell intracellular signaling cascade is mostly initiated through the interaction of the **peptide-CMH** domain shown by an antigen presenting cell (APC) as macrophages, dendritic cells, and the **T-cell receptor** (TCR) expressed on T-cells (Figure 1). The peptide (antigen fragment)-CMH / TCR-CD3 complex interaction triggers the activation by phosphorylation of Src-family protein tyrosine kinases (PTKs), such as the **lymphocyte protein tyrosine kinase** (Lck), on specific **immune-receptor tyrosine-based activation** motifs (ITAM). These early intracellular mechanisms lead to other activation signaling events (Gorentla et al[2], 2012).

Secondly, several members of the co-stimulatory receptor family induce additional signals through T-cells, strengthening the stimulation of the immune system response (Figure 2&3): **CD28 receptors** are well known co-stimulatory receptors recruited for the additional signal pathway during T-cell activation. Its engagement with B7 receptors present at the surface of APC cells results in an increase of **the T-cell proliferation** and cytokines production as **Interleukin-2 (IL-2) or Interferon-γ (INFg).**

Finally, the secreted IL-2 cytokine recognizes the T-cell surface IL-2 receptors, which leads to cell cycle engagement and consequently to T-cell proliferation forming a self-activation loop (Figure 1; Kambayashi and Laufer[3], 2014).

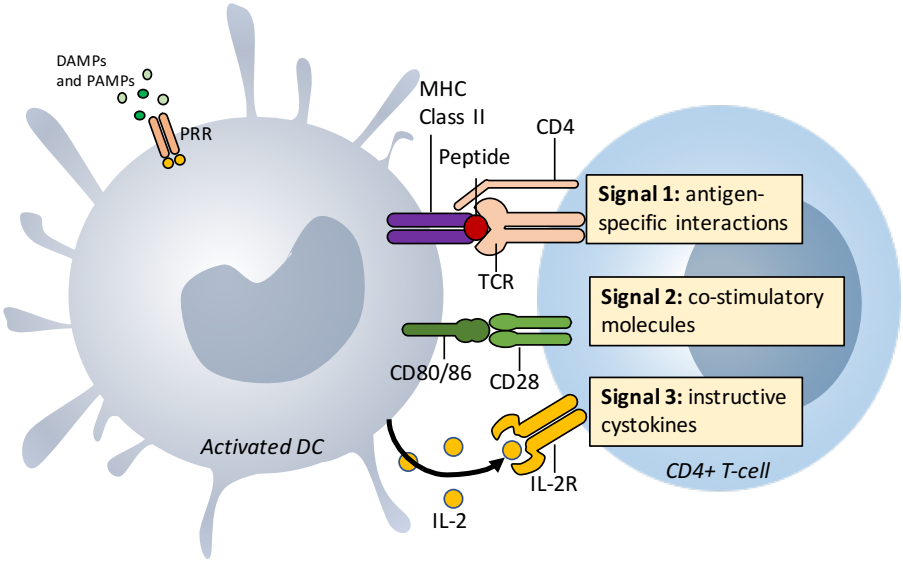

Figure 1. The three-signals model of T-cell activation mechanism. *A full T-cell activation is regulated by 3 distinct signals: (1) An antigen signal trough the TCR-CD3 complex presented by the CMH, (2) co-stimulatory receptors, and (3) via cytokines production (adapted from Kambayashi and Laufer, 2014)*

1.1.1.3. T-cell regulatory pathways via co-inhibitors and co-stimulators

Several T-cell membrane receptors are key actors in the regulation of the immune T-cell response, playing either a **co-stimulatory** or **co-inhibitory** role. The interaction between receptor pairs present on APC and T-cells induces either an activation or an inhibition of T-cell signal pathway (Figure 2). As described in the literature, these co-stimulatory and co-inhibitory receptor functions are context dependent since these receptors present a great diversity in expression, structure and function according to the environment (Chen et al[4], 2013). For example, both receptor families are known to have distinct kinetics of expression. In general, a majority of co-stimulatory receptors are expressed on resting and naïve T-cells, whereas inhibitory receptors are regulated after T-cell activation (Pardoll et al[5], 2012).

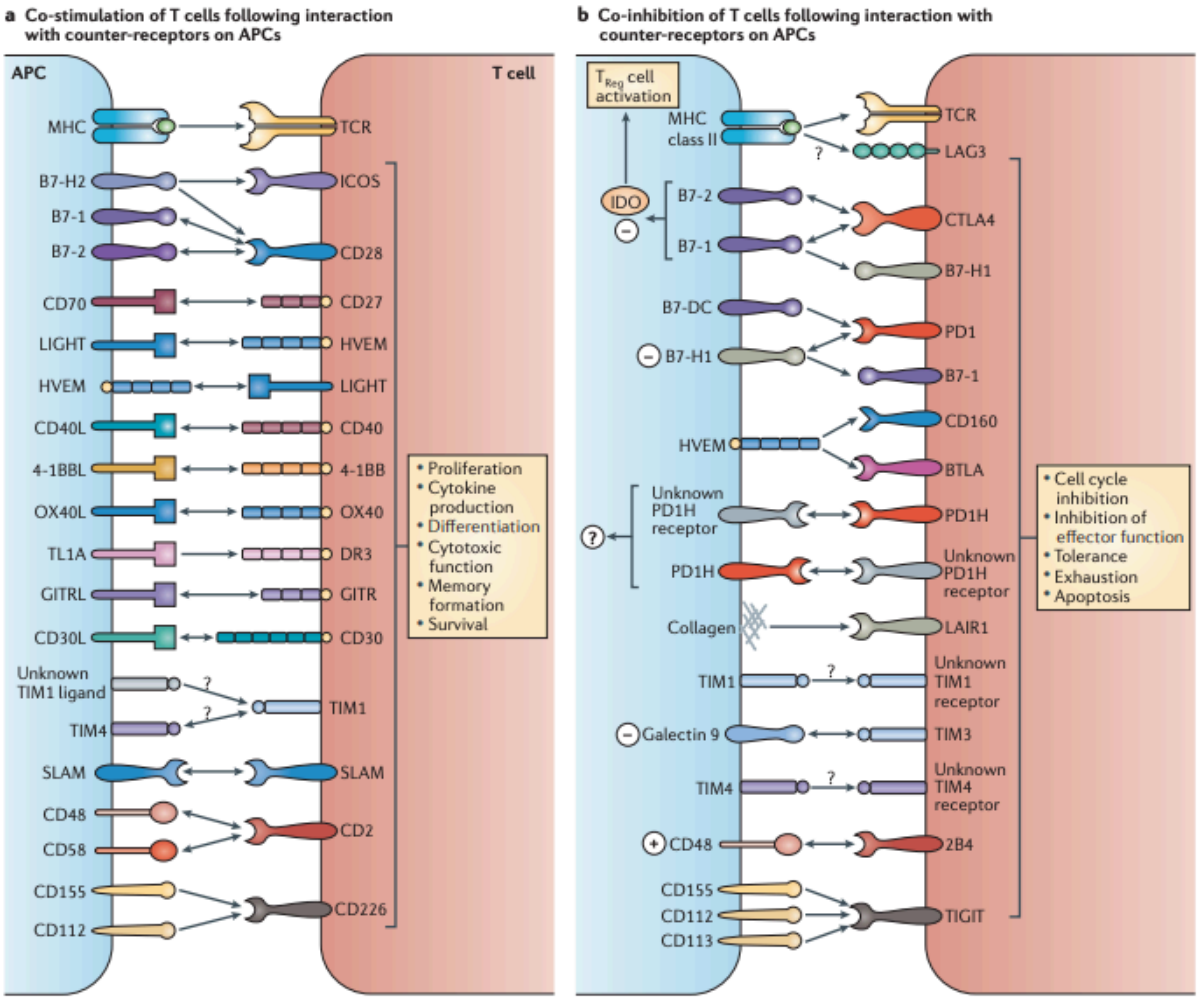

Figure 2. Co-stimulatory and co-inhibitory T-cell receptors families. *Several membrane receptors are key actors in the regulation of the Immune T-cell response, playing a (a) co-stimulatory or (b) co-inhibitory role. The ligation of receptor pairs induces either an activation or an inhibition signals pathway of T-cell. While, co-stimulating signals lead to an increase of T-cell proliferation and cytokine production, a T-cell differentiation to cytotoxic T-cell and better T-cell survival rate. In contrary co-inhibiting signals induce a cell cycle inhibition, a loss of their effector functions, the exhaustion and apoptosis of T-cell. (adapted from Chen et al[4], 2013)*

Co-stimulatory receptor family contributes through additional signals in T-cells to the stimulation of the immune system response. The binding to their ligands or to agonist antibodies conducts to a full T-cell activation. For example, the well-known receptors OX40 and 41BB are part of the **tumor necrosis factor (TNF)receptor superfamily.** An interesting feature of most TNF receptors is their capacity to oligomerize, triggering stronger responses, stronger activation than a single receptor. Certain antibody-based therapy research focuses on this TNF feature (Figure 3). This superfamily and its important regulatory role have inspired huge interest in the development of Ab-targeted for cancer immunotherapy (Bremer et al[6], 2013).

In contrary, co-inhibitory receptor family conducts negative signals leading to a complete T-cell deactivation, compromising the entire immune response process. The PD-1/PD-L1 couple and CTL-4 membrane receptors have been recently discovered. They are now the main targets of new therapies in immune-oncology treatments against cancer called **immuno-therapies**.

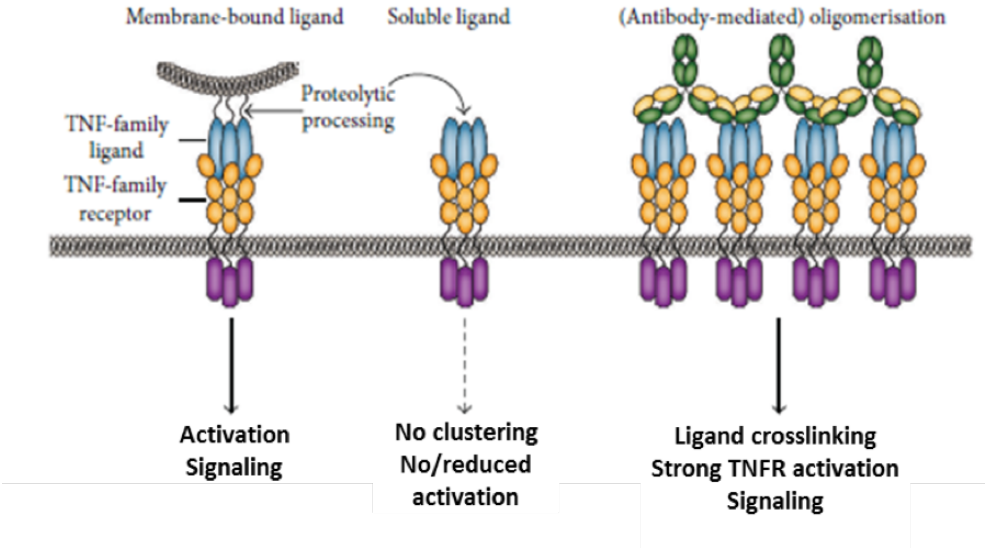

Figure 3. TNFR receptor superfamily. *Main characteristics of the tumor necrosis factor receptor superfamily receptors (TNFR). (adapted from Bremer and al, 2013 and Chen and al, 2013)*

1.1.2. Immunotherapies in the field of oncology

In 2018, more than 18 million people worldwide have been diagnosed with cancer and 9.6 million died from it. These cancer-related numbers have been estimated to increase during the next decade to probably reach 26.4 million of new cases and 17 million of deaths in 2030. This is partly due to the increase of world's population, its global ageing and lifestyles deterioration (Freddie Bray et al[7], 2018). Following local treatments of the tumors by surgery or radiation, chemotherapy remains the main cancer treatment and it has already proven to be very successful in the fight against cancer. Chemotherapy is considered as a systemic treatment, with drugs travelling throughout the body to kill cancer cells that have spread (metastasized) far away from the original (primary) tumor. However, the side effect of this treatment is to also affect healthy cells, especially cells of the immune system, weakening patients. Considering the health harms cause by chemotherapy and that cancer cells are recognized by the host's immune system, the concept of **immuno-therapies** in the field of immuno-oncology have emerged (Figure 4).

1.1.2.1. Concepts of immunotherapies

The aim of cancer immunotherapy is to stimulate the body's immune system to target and attack tumor cells. To reach this goal, several approaches using different mechanisms of action are emerging, such as therapeutic antibodies, modified T-cells, cytokines, vaccines, etc.

Immunotherapies are divided in two distinct approaches: "**passive**" immunotherapies and "**active**" immunotherapies, according to their capacity to enlist immune system against cancer (Lorenzo Galluzzi et al[8], 2014). Passive therapies indirectly engage immune system to fight cancer either via tumor-targeting antibodies, oncolytic viruses, or injection of modified autologous T-cells into patient. Active immunotherapies aim to activate an immune response against cancer through an immune cell-specific activation, without any direct manipulation (Figure 4).

Passive immunotherapies involve an immediate action thanks to the injection of specific immune-cell factors, such as tumor-targeting monoclonal antibodies. Other non-

specific techniques, called **adoptive cell transfer**, allow to induce an immune response against cancer via in-vitro selected or modified T-cells injection able to specifically target malignant cells. Several approaches exist. Amongst them, one is based on the selection and transfer of the most effective T-cells of a patient in the tumor micro-environment (**TIL** for tumor-infiltrating T lymphocyte transfer). Another one seeks to genetically modify patient's T-cells in vitro to recognize the tumor-associated antigens (**CAR-T Cell** for chimeric antigen receptor T-cell). Unfortunately, CAR-T Cells cannot be transferable to other patient making this approach individual and patient-dependent. The improvement of engineered T-cell specificity as well as the development of a new automated cell culture system is a challenge which can render this method more accessible to the public (Kalos et June[9], 2013).

In contrast, **active immunotherapies** adopt another approach: stimulate the patient's immune system against cancer by injections of immuno-stimulatory or immuno-modulatory agents. The non-specific cytokines-based methods induce a general stimulation of immune response, activating a wide range of immune cells. In opposition, specific active immunotherapies, such as vaccines or checkpoint inhibitors therapies, promote specific reactions on targeted cells to incite an immune response.

Recent treatments use **monoclonal antibodies (mAbs)** to target specific membrane receptors on T-cells, which are critical actors on the regulation of immune system response. By binding and modifying the intracellular signaling of T-cells, these types of active therapies have proven to enable and trigger a complete and powerful immune response against malignant cells. **These therapeutic antibodies are at the center of interest of my PhD thesis project. The most widely known mAbs target the PD-1/PD-L1 axis or CTLA-4 receptors. During the last decades, they gave unprecedented results in the treatment of various cancers.**

The latest advances in therapeutic immunomodulatory Ab are the development of modified antibodies called **bi-specific or tri-specific T-cell engagers.** Bi-specific are artificial antibodies that can simultaneously bind two separated and unique antigens (or different epitopes of the same antigen), whereas tri-specific antibodies have three antigen-binding sites, rather than two. They target specific membrane receptors to force the convergence of two types of cells, such as T-cells and tumor cells, favoring an antigen immune recognition. A single antibody capable to target two or three receptors simultaneously is promising for cancer immunotherapy research, since it considerably improves the ability of T-cells to target cancer (Garfall et June[10], 2019, Frans V.Suurs et al[11], 2019).

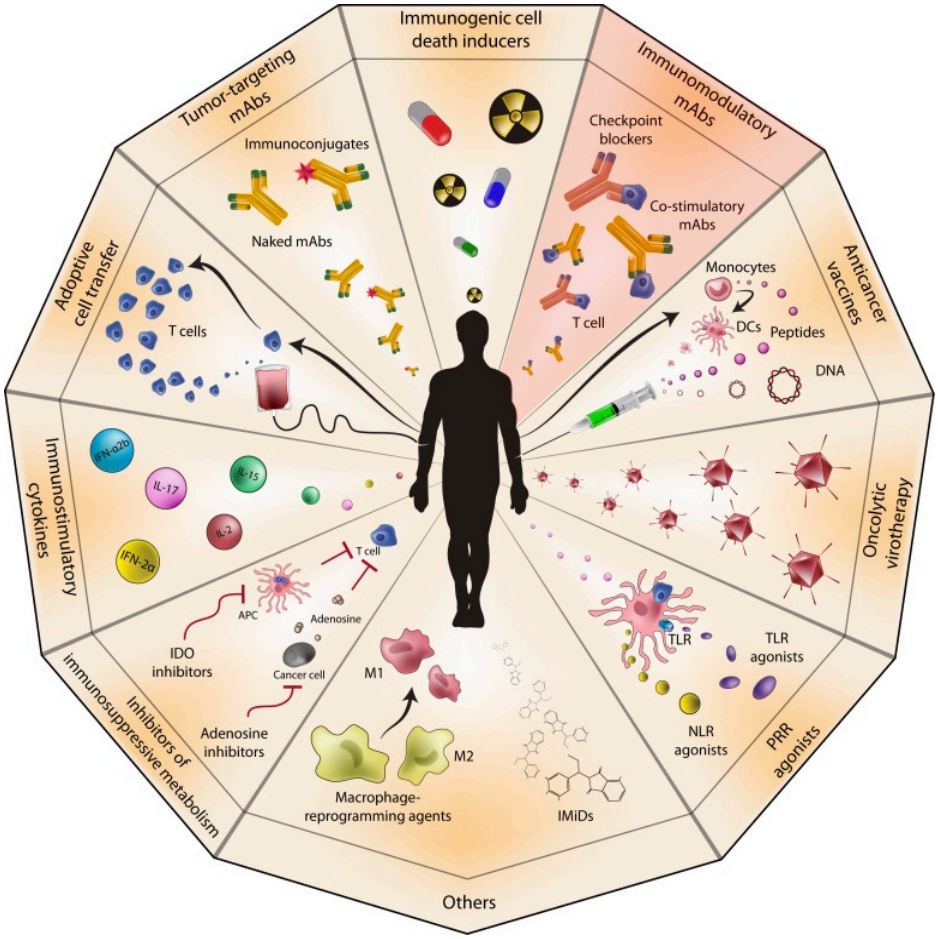

Figure 4. Spectrum of anti-cancer immunotherapies. *Different kind of immunotherapies have been developed during the last decades including adoptive cell transfer; tumor-targeting and immunomodulatory monoclonal antibodies (mAbs); dendritic cell (DC), peptide and DNA-based anticancer vaccines; immunogenic cell death inducers; oncolytic viruses; pattern recognition receptor (PRR) agonists, oncolytic virotherapy; and others. Immunotherapies can be distinguished into "passive" or "active" based on their ability to engage the immune system against cancer cells. (adapted from Galluzzi et al, 2014)*

1.1.2.2. Active immunotherapies: checkpoint inhibitors

The first solution to activate the immune response was to inhibit the co-inhibitory receptors expressed on activated T-cell using specific antibodies. Indeed, these key receptors have a role in down-regulating the immune system and promoting self-tolerance by suppressing T-cell inflammatory activity. In 1992, Pr. Honjo[12] discovered two crucial inhibitor proteins called **checkpoint inhibitors**: the T-cell membrane receptor **PD-1 (Programed cell death proteins 1)** and its ligand **PD-L1 (Programmed cell death-ligand 1)**, (Figure 2&6), a pair of receptors able to block T-cells in a critical phase of immune response against cancer cells. In 1994, Pr. Allison[13] did an unexpected discovery and brought to light another inhibitor protein, the membrane T-cell receptor **CTLA-4**. He demonstrated a self-regulating mechanism of the immune system on mice, and showed that antibody blockade of CTLA4 induced anti-tumor immunity. It is finally 25 years after, in 2018, that Tasuku Honjo and James Allison co-received the medicine Nobel Prize for their research at the origin of the immuno-oncology therapies as new axes to fight cancer.

The activation of those checkpoint inhibitor proteins by their ligands expressed on tumor cells will slow down the entire immune system response. Thereby, cancer cells foil and bypass the immune system controls by inhibiting activated T-cell to ensure their own survival.

Indeed, a T-cell blocked into a non-activated status is not able to provide a proper immune response, meaning a cessation of cytokines production and T-cell proliferation. This major immune resistance mechanism results in the expansion of cancer cells.

By introducing therapeutic antibodies against checkpoint inhibitors in the tumor micro-environment, any interactions with their ligands is blocked, triggering T-cell activation. Then, driving by the signaling cascade, the immune system is turned on and has a chance to kill cancer cells (Figure 6).

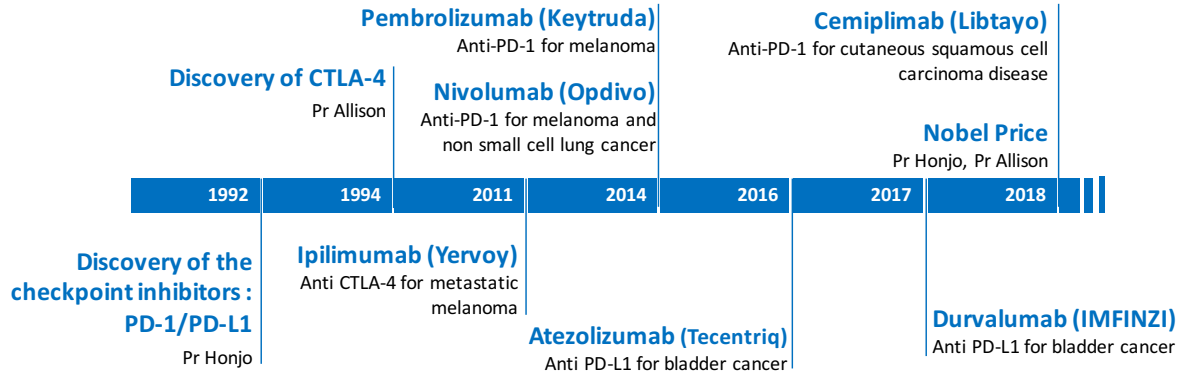

Figure 5. Timeline of therapeutic mAbs discovery and evolutions. *For three decades immunotherapies emerged in the field and present since unprecedented results in the treatment of diverse kind of cancer such as melanoma, non-small cell lung cancer, kidney cancer, bladder cancer, head and neck cancers. (Sivanandam et al[14], 2019)*

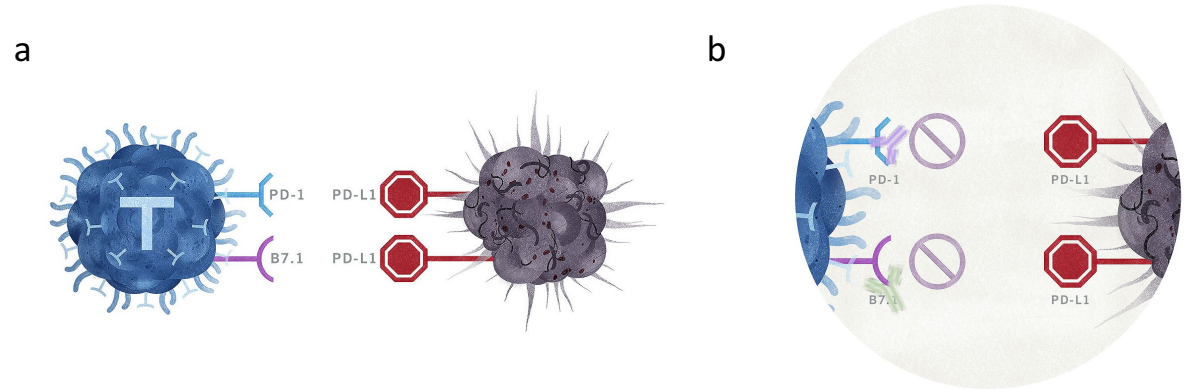

Figure 6. Principle of therapeutics mAbs against the programed cell death receptors PD-1/PD-L1. *(a) the binding of PD-L1 highly expressed on the surface of tumor cells with PD-1 T-cell receptors occurs to a complete inhibition of the activated T-cell. (b) Therapeutic antibodies against PD-1 introduced in the tumor micro-environment, prevent the binding of PD-L1 receptors to PD-1 T-cell receptors, enabling a T-cell activation and the destruction of cancer cells. Images taken from Roche©*

As explained previously, checkpoint inhibitors are not the only receptors playing a key role in the intracellular signalization pathway of T-cells. A list of interesting potential targets for such therapies has been discovered, each of them exhibiting different degrees of stimulation or inhibition actions. Recent discoveries of co-stimulatory receptors emerged, and the use of therapeutic agonist antibodies is particularly interesting (Chin et al[15], 2018). The huge potential of these T-cell surface receptors put them in the focus of **cancer therapies** research axes of pharmaceutical industries and laboratories.

The past 10 years revealed a huge scientific advance on immunotherapy development. In 2011, the FDA and EMA (American and European sanitary authority, respectively) approved the first treatments and clinical assays on patients with therapeutic antibodies targeting CTLA-4 and PD-1 or PD-L1 on various cancer types. Therapies relative to these receptors leaded to very promising results in some aggressive cancers (Callahan et al[16], 2016). They have been particularly efficient on advanced metastatic states of melanoma, non-small cell lung cancers,

kidney cancers, bladder cancers, head and neck cancers, changing patient futures (Figure 5&7).

1.1.3. Existing Therapeutic monoclonal antibodies targeting checkpoint inhibitors

The first **monoclonal antibody** (**mAb**) approved by the FDA in 2011 was the **Ipillumab** (Yervoy-Bristol-Myers Squibb). This is an igG1 human mAb targeting the CTL-4 receptor, which has been used on clinical trials to treat metastatic melanoma diseases.

Three years later, the mAb **Pembrolizumab**, (Keytruda-Merck&Co) and **Nivolumab** (Opdivo-Bristol-Myers Squibb) have been approved by the FDA. They are respectively the third and second best-selling monoclonal antibodies in 2018. They are both humanized/human IgG4kappa against PD-1 antibodies. As Ipillumab, they both are used in advanced melanoma cancer treatment (2015). Over the years, they outperformed in clinical assays compared to other cancer treatments and have now been approved in the treatment of patients suffering from non-small cell lung cancers (2015) and head and neck cancers (2016). Nivolumab is also used to treat renal cell carcinoma (2015) and Pembrolizumab for Hodgkin's lymphoma (2018), cervical cancers (2018), Microsatellite instability-high cancers (2018) and stomach cancers.

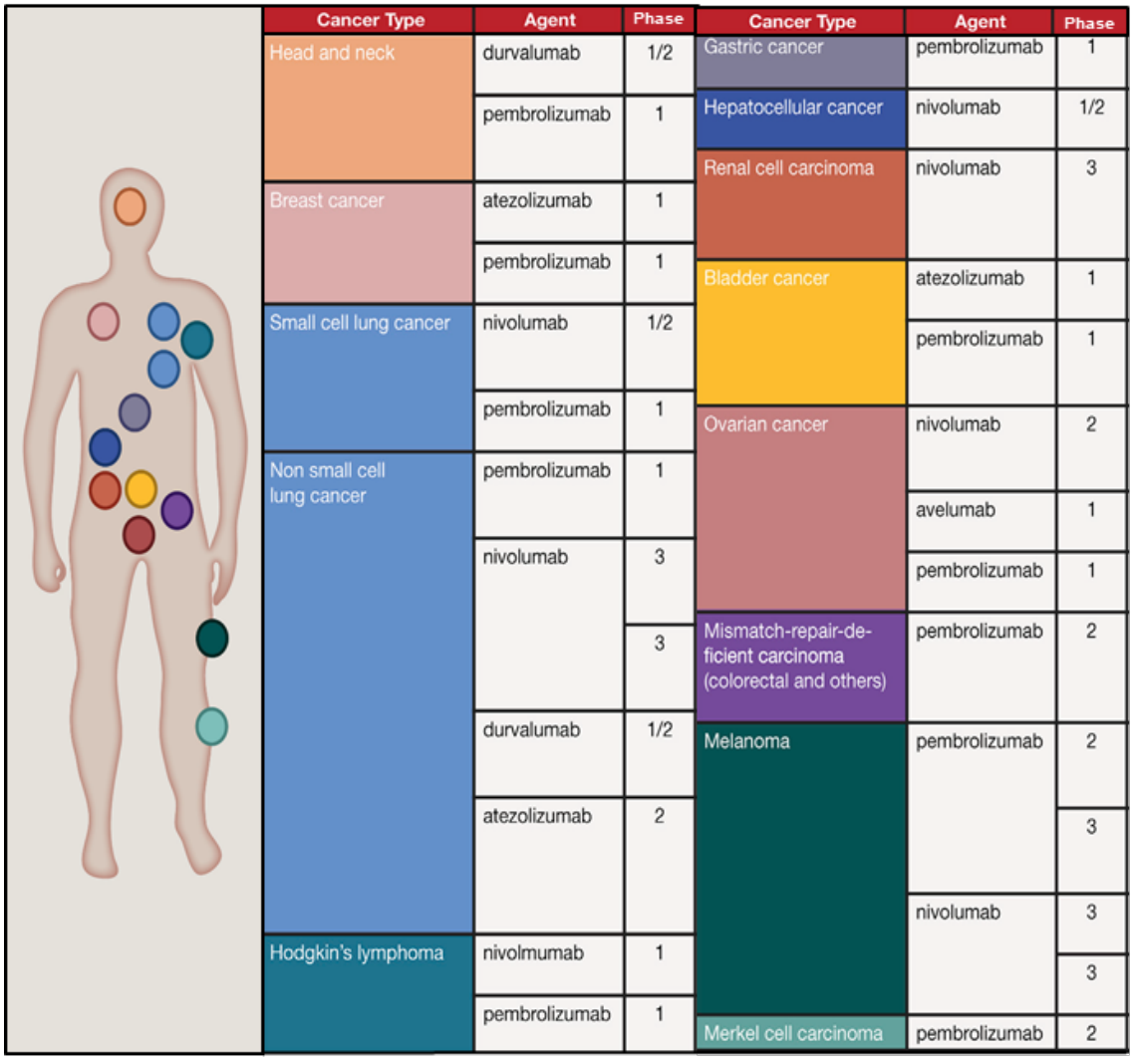

Cancer Type	Agent	Phase
Head and neck	durvalumab	1/2
	pembrolizumab	1
Breast cancer	atezolizumab	1
	pembrolizumab	1
Small cell lung cancer	nivolumab	1/2
	pembrolizumab	1
Non small cell lung cancer	pembrolizumab	1
	nivolumab	3
		3
	durvalumab	1/2
	atezolizumab	2
Hodgkin's lymphoma	nivolmumab	1
	pembrolizumab	1

Cancer Type	Agent	Phase
Gastric cancer	pembrolizumab	1
Hepatocellular cancer	nivolumab	1/2
Renal cell carcinoma	nivolumab	3
Bladder cancer	atezolizumab	1
	pembrolizumab	1
Ovarian cancer	nivolumab	2
	avelumab	1
	pembrolizumab	1
Mismatch-repair-deficient carcinoma (colorectal and others)	pembrolizumab	2
Melanoma	pembrolizumab	2
		3
	nivolumab	3
		3
Merkel cell carcinoma	pembrolizumab	2

Figure 7. Existing therapeutic mAbs anti-cancer treatment use across a range of cancer types. *Nivolumab, Pembrolizumab: being therapeutic anti-PD1 mAbs and Atezolizumab, Avelumab, Durvalumab: being therapeutic anti-PDL1 mAbs (Adapted from Callahan et al[16], 2016)*

More recently, the **Cemiplimab** (2018, Libtayo-Regeneron pharmaceuticals), another human mAb anti PD-1 has been approved for patients affected by cutaneous squamous cell carcinoma disease (Lu et al[17], 2020).

Concerning mAb-targeting PD-L1, two human/humanized IgG1 received the US approval for bladder cancer treatment: **Atezolizumab** (2016, Tecentriq-Roche) and **Durvalumab** (2017, Imfinzi-MedImmune-AstraZeneca).

In cancer treatment, monoclonal antibodies targeting checkpoint inhibitors are applied in second-line and often in association with another therapy. Monoclonal Ab therapies are commonly combined with conventional chemotherapy or other immunotherapies. Depending on the cancer type and clinical phase trials, some monoclonal anti-PD-1 antibodies can be used as monotherapy, but most of the time they are associated with Ipillumab targeting CTLA-4 protein. Some trials combine the two anti-PD1 mAbs Nivolumab or Pembrozilumab to strengthen the wanted effect or proceed in several phases, the first one with mAb combination and a second monotherapy phase (Institut national du cancer). All those clinical assays are obviously cancer and patient-dependent.

Patients cured with monoclonal antibodies against PD-1/PD-L1 showed incredible survival rates in comparison with standard second-line chemotherapy such as Docetaxel (Lu et al[17], 2020). For a decade, new mAbs from different companies have been approved by the FDA, and thanks to their promising results they continue to be developed by pharmaceutical company as it is the case in Sanofi R&D departments. They develop and test new mAbs against PD-1 with different conformation and antibodies conjugation to improve cancer treatment by immunotherapies (chapter 1.3.1).

1.1.4. PD-1/PD-L1 blockade checkpoint inhibitors

The crystal structure of PD-1 (also known as CD279) has been reported by Lin et al[18] and Lazar-Molnar et al[19] in 2008, and recently characterized by Zak et al[20] (2017), who also investigated the interactions between PD-1 and clinical monoclonal antibodies. Figure 8 shows PD-1 interactions with Pembrolizumab and Nivolumab, two therapeutic mAbs studied in this thesis.

PD-1 has two natural ligands: PD-L1 (B7-H1, CD274) and PD-L2 (B7-DC, CD273). PD-1 proteins are Ig-like transmembrane receptors expressed at the surface of activated T-cells. PD-1 is a **monomeric receptor** of 288 amino acids (aa) (Zak et al[20], 2017). It is composed of an extracellular domain, Ig-like of 147aa, which interacts and induces signal transduction to an intracellular domain. The cytoplasmic domain of 97aa has two tyrosine motifs in its tail, an immune-receptor tyrosine-based inhibitory motif (ITIM) and an immune-receptor tyrosine-based switch motif (ITSM) (Francisco et al[21], 2010).

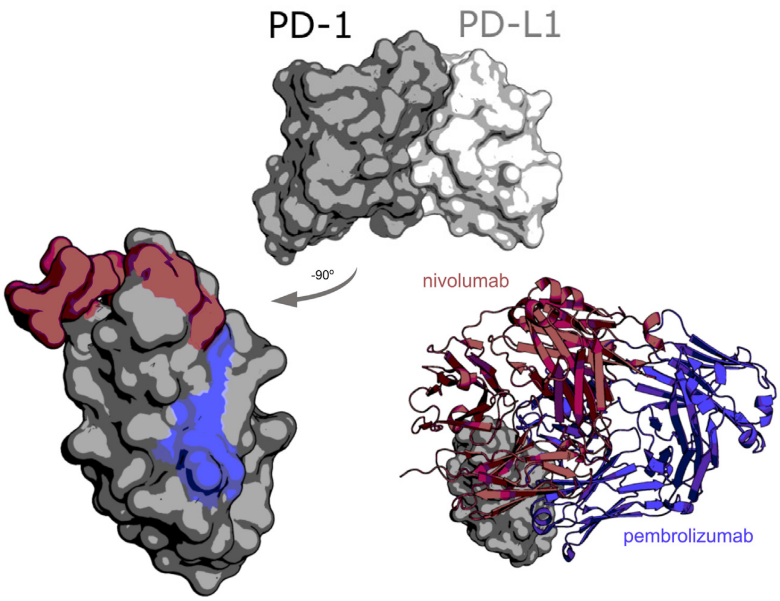

Figure 8. PD-1/PD-L1 molecular structure and interactions with clinical antibodies. *Structural basis for blocking the ligation of PD-1 (grey) and PD-L1 (white) by therapeutic mAbs, Nivolumab (brick-red) and Pembrolizumab (purple). (adapted from Zak et al[20], 2017).*

PD-1 is present on T-cells, NK cells, B-cells and monocytes, upon their activation (Agata et al[23], 1996). In particular, PD-1 is not only highly expressed on T-cells after their activation on "exhausted" T-cells (T-cells with a progressive loss of their effector function)(Francisco et al[21], 2010). PD-1 is not expressed or at barely detectable level on resting primary T-cells. However, they start to appear two hours after their activation (Riley[22], 2009). It is still not clear yet if there is a correlation between the level of PD-1 expression and its function on T-cell inhibition.

The couple of programed cell death receptors PD-1/PDL-1 has been highly reported and studied in literature. They are the main targets of therapeutic medication campaigns (for review see: June et al[24], 1987; Mullard et al[25], 2013). However, a few information is available about the organization of such receptors at the surface of these cells and more particularly during the course of their activation. **It was thus obvious to extend the use of microscopy tools to decipher the checkpoint inhibitors PD1-PD-L1/antibodies interactions and nano-organization at the single-molecule level. In combination with high content screening approach, quantitative super resolution microscopy will provide relevant information for the selection of the best antibodies in the early phases of the project when a large number of molecules can be generated and displaying different formats (nanobodies, mono/bi/tri-specific antibodies, etc.).**

1.1.5. Super-resolution microscopy in immunology: quantification of the nanoscale organization of T-cell membrane receptors

Imaging technologies have largely contributed to our understanding of spatial and dynamic organization of T-cell receptors at the immunological synapse, providing biological insight to T-cell activation mechanisms. Diverse techniques such as immunohistochemistry, electron microscopy and fluorescent microscopy have provided accurate details, both at the cellular and molecular levels (Balagopalan et al[26], 2011). The two last decades have witnessed the unprecedented evolution of **fluorescence microscopy** in terms of labeling efficiency and

achievable spatial resolution, illustrated by two Nobel price awards for the discoveries of GFP (Osamu Shimomura, Martin Chalfie and Roger Tsien, 2008) and super-resolution microscopy (Stefan W. Hell, Eric Betzig and William E. Moerner, 2014). It is today possible to investigate **T-cell receptor organization and dynamics at the nanoscale using super-resolution microscopy.**

Pentcheva-Hoang et al[27] (2007) and Yokosuka et al[28] (2012) used diffraction-limited fluorescence microscopy and TIRF microscopy (described in chapter 2) with quantitative image analysis (i.e. **colocalization** and **clustering analysis**), to investigate the location and kinetic of PD-1/PD-L1 interaction at the immunological synapse. They showed how this couple regulates T-cell activation.

Investigation on T-cell surface receptors using super-resolution microscopy

receptor	SMLM methods	authors	year
TCR	STED-dSTORM	Rossboth and al	2018
TCR	SIM-LSM-dSTORM	Hu and al	2016
Lat	PALM-dSTORM	Williamson and al	2011
TCR-CD45	PALM-dSTORM	Razvag and al	2018
TCR-CD45	LSM-PALM	Ponjavic and al	2018
CD2-CD45	LLSM-dSTORM	Wäldchen and al	2020
TCR-CD3	dSTORM	Pageon and al	2016
CD19	dSTORM	Nerreter and al	2019
TCR	LLSM	Jillian Rosenberg and al	2020

Figure 9. List of publications which investigated T-cell surface receptors using super-resolution microscopy.

Since then, TCR receptor behaviors have been extensively investigated over the past decade using fluorescence microscopy (Rossy et al[29], 2012; Roh et al[30], 2015; Ma et al[31], 2020; Meddens et al[32], 2018). With the advent of super-resolution microscopy, and single molecule localization microscopy (SMLM) in particular, scientists recently precisely described T-cell receptors dynamics (Figure 9). Several T-cell membrane receptors (CD3, CD45, CD2, Lat, etc.) and intracellular signaling proteins (Lck, etc.) playing a key role in T-cell activation signaling, have been recently studied (Figure 9). However, there is still no study of PD-1 receptor organization and dynamics by super-resolution microscopy.

For practical reasons of SMLM limitations, most of the studies were performed on T-cells seeded on coverslips using either standard coating (Poly-L-Lysine, Fibronectine, etc.) or supported lipid bilayers combined with specific ligands (e.g. ITAM-1, CD3 or PD-L1) mimicking the immunological synapse. Coating-free methods allowed high-resolution imaging of the immunological synapse between two cell types using mechanical or microfluidic devices (Jang et al[33], 2015).

More recently, the 3D nanoscale organization and dynamics of T-cell membrane receptors has been investigated by Ponjavic et al[34] (2018) and Wäldchen et al[35] (2020) by combining advanced light-sheet and super-resolution microscopies.

These publications describe the temporal and spatial organizations of T-cell membrane receptors, revealing new insight of biological mechanisms with either new sequence of events (kinetic studies) or specific nanoscale organizations of receptors. Receptor organization was reported to be heterogeneous, encompassing a broad range of cluster sizes (Figure 10): oligomers, protein islands, nano-clusters to micro-clusters (Feher et al[36], 2019). Ground-breaking super-resolution approaches revealed to be an outstanding boost to T-cell membrane receptors research.

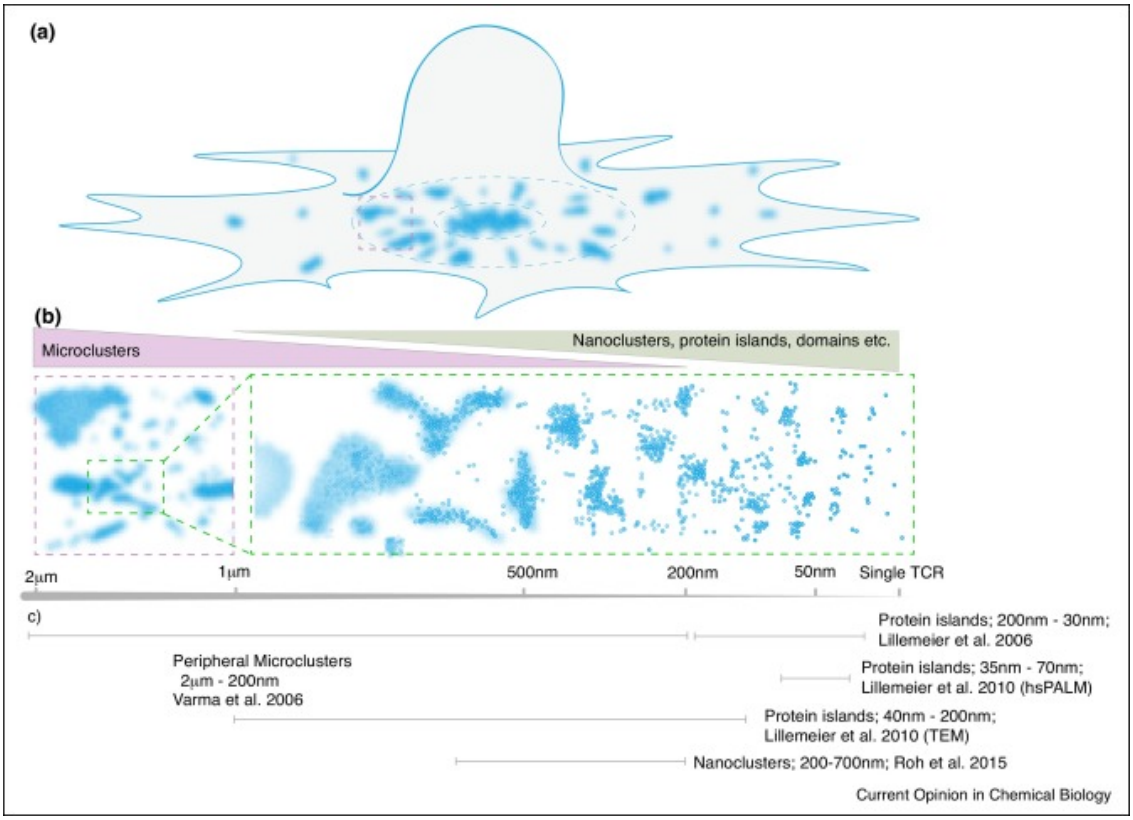

Figure 10. Multi-scale organization of T-cell receptors. *(a) Schema of an activated T-cell spread onto a coverslip surface. T-cell activation induces TCR aggregation, increasing towards the center of the cell called canonical supramolecular activation clusters (SMACs) of TCR. The SMACs include a peripherical part (outer ring) and a central part (inner ring) separated by 1-10µm. (b) This area presents different size of TCR-clusters, ranging from micrometer-scale with TCR peripheral micro-clusters, to nanometer scale with protein island, nano-clusters and domains. Such organization have been reported by high and super-resolution microscopy. Each blue spot represents a single molecule localization. (Adapted from Feher et al[36]. 2019)*

1.2. CHAPTER 2: Optical Super-Resolution Microscopy

1.2.1. Fluorescence microscopy

1.2.1.1. Principle of fluorescence

For several decades, scientists have been able to observe various biological systems, ranging from whole organisms (small animals, embryos, etc..) down to micrometer-sized sub-cellular biological structures (cellular organelles). While advances in microscopy have allowed to better investigate small biological structures, there are still some physical and biological barriers preventing our understanding of the precise role of proteins in the immune system. By binding a fluorescent probe to a protein of interest, fluorescence microscopy brings contrast and, more importantly, specificity, enabling the discrimination between molecules, proteins, and organelles of interest and their surroundings. Thanks to the ability to provide a specific signature of any biological component, fluorescence microscopy has become the most widely used technology in biology and medicine to study the complexity of the organization of proteins in live and fixed samples.

The capacity of fluorescence microscopy to individually separate biological structures lies in the ability to accurately and specifically tag a structure of interest with a small fluorescent probe. Each fluorescent probe has a unique molecular energy signature. The principle of fluorescence is based on the various electronics state of electrons of a fluorescent probe, as illustrated in the **Jablonski diagram** (Figure 11.a). The excitation of a fluorescent molecule is due to the absorption of a photon with a given energy, bringing this molecule from a "stable" state, the fundamental electronic state S_0, to an "excited" state S_1 or S_2. The photon's energy (E) is inversely proportional to the wavelength (λ) of the incident photon, and is given by:

$$E = h\nu = h\frac{c}{\lambda}$$

where ν is the light's frequency (in Hz), h is Planck's constant (h=6.626×10−34J.s) and c is the speed of light in vacuum. This excited state being molecularly unstable, after several nanoseconds, the electron relaxes form this upper state to its ground state. To return to its electronic ground state, the molecule emits photons with a lower energy than the absorbed photons, resulting in the observation of unique **fluorescence spectra** that corresponds to the vibrational and electronic energy states of the molecule. Each fluorescent molecule is characterized by a unique absorption and emission spectrum (Figure 11.b Alexa Fluor 647's spectrum). The energy difference between the excited and emitted photons is called **Stokes Shift** (expressed in units of wavelength). In a less common scenario, a fluorophore can also move from a singlet excitation states S_1 or S_2 to different metastable state T_n, called a triplet state. The lifetime of electrons in this state is longer than in singlet states, lasting from few nanoseconds to several minutes. The relaxation of electrons from the triplet state T_n to its ground state S_0 is the origin of the process of **Phosphorescence**.

It is possible to perturb this cycle of photon absorption and emission, for example via a chemical reaction between fluorescent molecules and their environments, which is the foundation of the dSTORM approach, a localization-based super-resolution microscopy technique (Chapter 1.2.3.1). Every fluorescent molecule can reach a maximum number of absorption/emission cycles before **photo-bleaching**. This phenomenon irreversibly disrupts and ends the fluorescent lifecycles by preventing the absorption of new photons. It limits the total amount of photon a fluorophore can emit, called the photon-budget. Some dyes are

more resistant to photo-bleaching than others, making them suitable for specific fluorescent microscopy approaches (chapter 1.2.3.2-3).

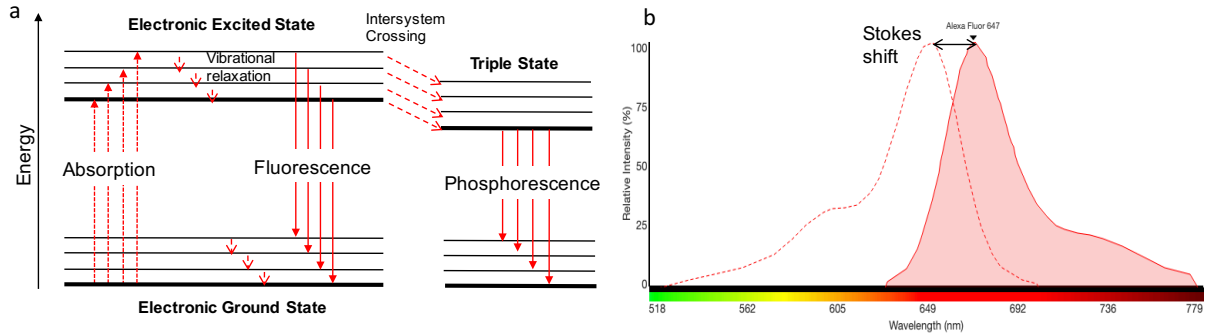

Figure 11. The Principle of fluorescence. *(a) Jablonski Diagram representing the fluorescence timeline and the different energetic levels in which a molecule can transit through. (b) The excitation (dotted line) and emission (solid red line) spectra of the Alexa Fluor 647 dye. The loss of energy of a fluorescent molecule due to the vibrational relaxation and internal conversion results in a wavelength shift of the emission spectrum (the Stokes Shift).*

Many different fluorescence dyes exist, covering a wide range of the visible spectrum, from the near-UV to the far-red (400 to 700 nm). These dyes can be easily attached to a protein of interest (either genetically or using fluorescent antibody) on fixed or living cells, providing structural specificity and contrast in biological samples. Lasers, light emitting diodes (LEDs) or fluorescence lamps, are commonly used in combination with optical filters and objective lenses to illuminate and collect the fluorescent of biological samples with high specificity.

1.2.1.2. Resolution limit

Resolution is a common metrics to determine the capacity of microscope to resolve sample details. In fluorescence microscopy, resolution is limited by the diffraction barrier discovered by E. Abbe more than a century ago.

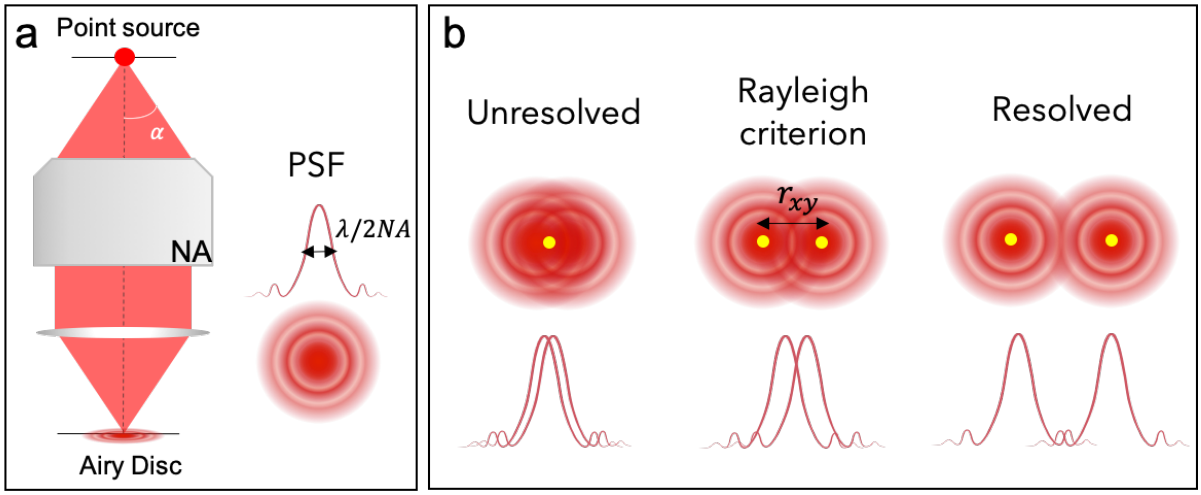

Figure 12. Resolution in fluorescence microscopy. *(a) The numerical aperture NA of an optical system determines the ability of an optical system to collect a fraction of the emitted photons through a collection angle α. The image of point source at the focal plane of an optical system is a 2D Airy pattern called the point spread function (PSF). (b) The resolution of an optical system is defined by the Rayleigh criterion, the ability to distinguish two close emitting point sources.*

The observation of a fluorescent dye through a microscope objective can be modeled as a point source emitting light waves. The **diffraction of light** phenomenon, established by Huygens and Fresnel, is the reconstruction of these waves onto the image plan through a finite aperture. The resulting 2D image of the diffracted waves coming through the optical system is called **Airy disc** (Figure 12.a). It is an interference pattern composed of one high intensity central disc surrounded by several circles with decreasing intensities. This pattern is also called **Point Spread Function** (PSF), which is the image of a point source through a given optical system. The image of a complex object made of several point sources can be mathematically modeled in 2 and 3 dimensions as the convolution between the object and the PSF (Figure 13).

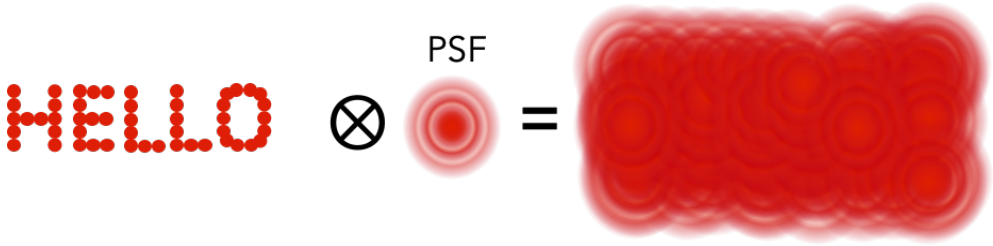

Figure 13. Image of a fluorescent object of interest through an optical system. *The image of an object of interest, composed of multiple fluorescent point sources, through an optical system, can be mathematically modeled as the convolution between the object and the PSF of the optical system.*

The capacity of an objective to collect efficiently a fraction of the emitted photons depends on the objective collection angle, called the **Numerical Aperture** (NA) (Figure 12.a), defined by:

$$NA = nsin\alpha$$

Where n is the refractive index and α is the half-angle of the cone of light that enters the lens. Both the Numerical Aperture (NA) and the emission wavelength (λ) determine the spatial resolution. The lateral **spatial resolution** of an objective in the image plane r_{xy} defines its capability to separate two point sources close to each other. It is defined by the **Rayleigh Criterion**[37] (Figure 12.b) by:

$$r_{xy} = 0.61\frac{\lambda}{NA}$$

Similarly, the axial resolution r_z, which defines the capacity of an optical system to separate 2 points sources in the axial direction, is defined by:

$$r_z = \frac{2\lambda}{NA^2}$$

Optical microscopy is not isotropic, axial resolution being always worse than lateral resolution (3-4 times for high NA objectives). As an example, the best achievable lateral resolution for GFP molecules ($\lambda \approx 510\text{nm}$) with a 1.4 NA objective is 220nm, and 520nm for the axial resolution. This limit prevents the optimal investigation of complex 3D biological samples.

1.2.1.3. Improving axial resolution, why and how?

In cell biology, there is a whole world below 200 nm, made up of organelles, macromolecular complexes or nano-structures, which conventional microscopy cannot

resolve (Figure 16). Over the years, scientists have developed different approaches to overcome this limit of resolution, more especially in the axial dimension, allowing investigating complex biological samples in 3D.

In fluorescence microscopy, the most popular sectioning technique is the **confocal microscope**. It uses a pinhole conjugated to the image plane to reject out-of-focus light, improving by 2-fold the axial resolution (Figure 14.e). Using a point scanning excitation, it allows deep imaging of thick samples by collecting serial optical sections. However, it requires high intensity light leading to photo-bleaching and radiation damages. Point scanning techniques are usually slow, a difficulty resolved by **spinning-disks**, which use an array of pinholes allowing to significantly increase the imaging speed. Alternatively, **multiphoton microscopy** improves the axial resolution without the need of a pinhole and provides a great depth penetration with less photo-toxicity on live cells imaging (Denk et al[38], 1990). Thanks to a 2 and 3-photon effect based on advanced pulsed laser excitation sources, it reduces the effective excitation to very small focal volume (Figure 14.f). However, in addition to the slow imaging speed of point scanning, it is complex and more expensive.

A well-known optical technology which highly improve contrast is the **total internal reflection fluorescence microscopy** (TIRF) (Axelrod et al[39], 1984). By choosing the critical angle of a collimated excitation beam where the light is totally reflected at the interface between the coverslip and the sample (which needs to be with a refractive index lower than the glass), an evanescent wave is created. This evanescent wave only excites the fluorophores located at less than about one hundred nanometers above the glass coverslip, drastically improving the contrast. The TIRF angle and related penetration distance of the evanescent wave can be precisely controlled by positioning the beam in the back focal plane of the objective. TIRF microscopy is widely used to observe membrane proteins of living adherent cells. However, it does not permit the imaging of biological structures above 200 nm distance from the coverslip (Figure 14.b).

Oblique microscopy, also called **HILO** for Highly Inclined Laminated Optical Sheet (Tokunaga et al[40], 2008), uses the same principle as the TIRF microscopy. By slightly moving the beam in the back focal plane of the objective within the widefield area, it creates an oblique light-sheet of a few micrometers thick (depending on the angle and width of the collimated beam), improving the contrast and reducing the out-of-focus light compared to the **wide-field** illumination (Figure 14.a, c). It is well suited to monitor biological samples within few microns' distance from the coverslip.

Light sheet microscopy (LSM) or **selective plane illumination microscopy (SPIM)** is a 3D imaging technique that traditionally uses two objectives, one to create an excitation light-sheet perpendicular to the optical axis, the other one for the detection of fluorescence (Figure 14.d). It offers good contrast and reduced photo-bleaching and photo-toxicity compared to wide-field and confocal illuminations. It permits high-quality 3D live imaging of large samples. SPIM is commonly achieved with two or more objectives, but recent approaches, such as soSPIM, use only one objective (chapter 1.2.1.3).

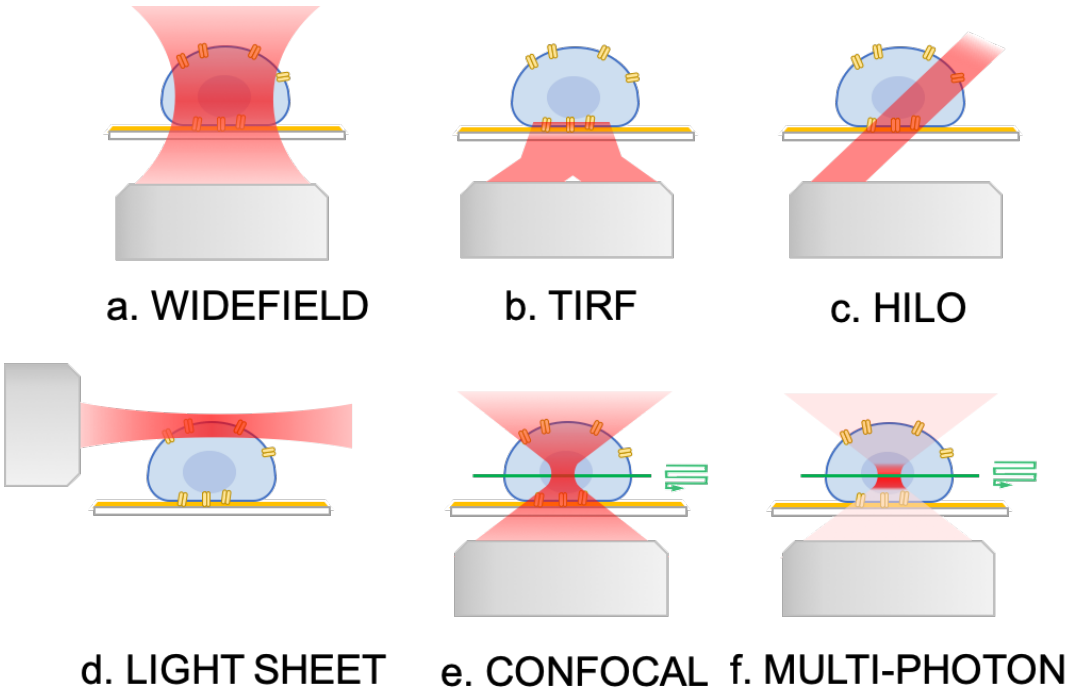

Figure 14. Main illuminations techniques used in fluorescence microscopy. *(a) WideField microscopy, (b) Total Internal Reflection Fluorescence (TIRF) microscopy creates an evanescence wave and allow the excitation of dyes to a few hundreds of nanometers above the glass-coverslip surface. (c) HiLo or Oblique illumination creates a thin and oblique light sheet that allows imaging 1-2 µm above the glass-coverslip surface. (d) Light sheet, or selective plane illumination microscopy (SPIM) separates the excitation and detection path using 2 objectives, enabling imaging of large samples with improved sectioning. (e) Confocal microscopy is a point scanning technique that uses of a detection pinhole, allowing only excited light from the focal plane to reach the detector. (f) Multiphoton microscopy confines the excitation volume by using multi-photon excitation.*

1.2.1.4. soSPIM: single objective selective plane illumination microscopy

The **single objective selective plane illumination microscopy (soSPIM)** (Galland et al[41], 2015) system, created in the host lab in collaboration with the MechanoBiology Institute lab in Singapore, provides a simplified version of SPIM. It uses a single objective both for the excitation and the detection of the fluorescence, by combining micro-wells flanked with 45° micro-mirrors with a laser beam–steering unit. Using a single high NA objective reduces considerably the complexity of standard light sheet microscopes (Figure 15. a). A light sheet is created by the reflection of the excitation light onto the mirrors and propagates into the micro-wells across the biological sample. Synchronizing the displacement of the excitation beam and the objective, allows to perform 3D imaging of a whole sample as well as SMLM (Figure 15.c, d). The dimensions of the micro-mirrored-well can be adjusted (from 20µmx20µm to millimetric size) allowing imaging samples of various sizes, such as isolated T-cells, cell aggregates, organoids or embryos (Figure 15.b).

In the present work, we used the soSPIM technology combined with super-resolution microscopy to gather complementary information on T-cell receptors nanoscale organization at a single cell level that our TIRF-based HCS-SMLM cannot access.

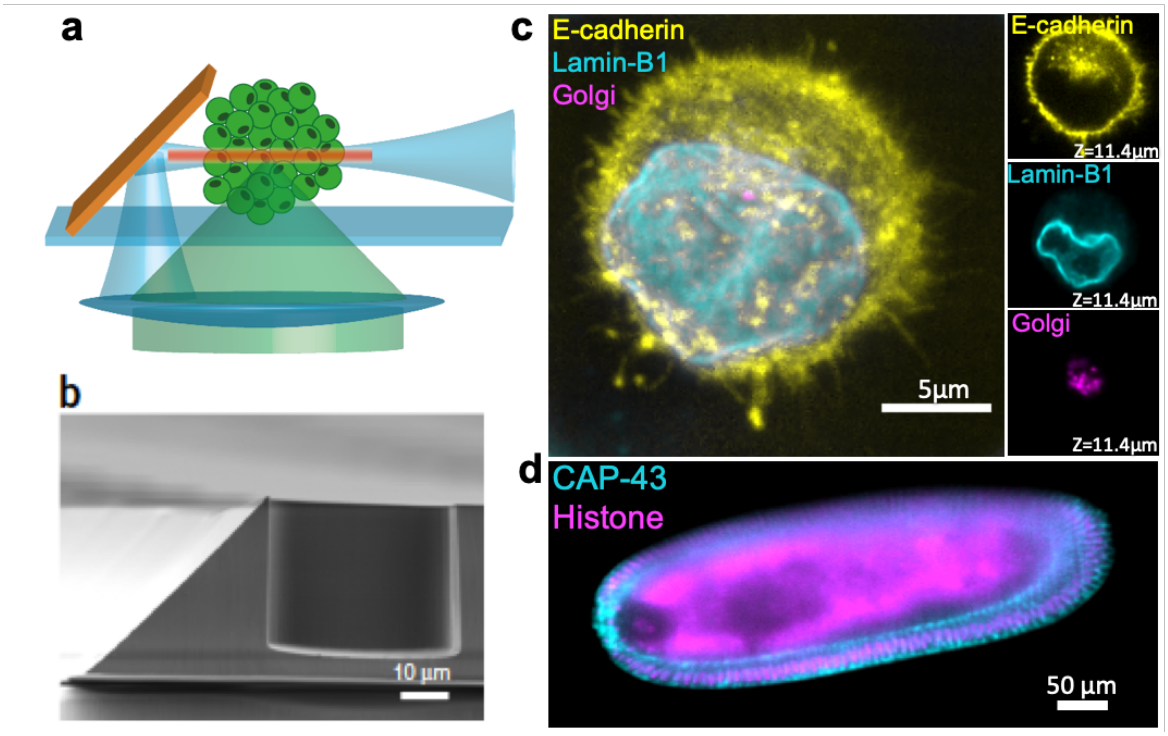

Figure 15. Principle of the soSPIM and its 3D imaging capabilities. *(a) Schematic representation of the soSPIM system. The excitation light source is reflected onto 45° mirror creating a thin light sheet illuminating the sample perpendicularly to the image plane. This geometry enables 3D-volume imaging by simply synchronizing the movements of the objective and the excitation beam. (b) Scanning electron microscopy image of a polymeric microcavity with a 45° micro-mirror. c) 3D multicolor acquisitions (maximum intensity projection) of a single cell expressing labled for E-cadherin–GFP, Lamin-B1–AlexaFluor647, GM130-AlexaFluor568 within a 22x22µm^2 microwell and (d) an embryo labeled for Histone-mCherry and CAP43-Venus within a few millimeters-size well (Adapted from Galland et al[41], 2015)*

1.2.1.5. Beyond the diffraction limit

By far the most spectacular advance to circumvent the diffraction barrier was the advent of **super-resolution microscopy**, also called **nanoscopy**, awarded by the Nobel prize in chemistry in 2014 (Schermelleh et al[42], 2019). Three major families of techniques have been developed allowing to circumvent the diffraction limit: **stimulated emission depletion** (**STED**; Hell&Wichmann[43], 1994), **structure illumination microscopy** (**SIM**; Gustaffson[44], 2000) and **single molecule localization microscopy** (**SMLM**; Betzig et al[45], 2006; Hess et al[46], 2006; Rust et al[47], 2006; Heilemann et al[48], 2008; Jungmann et al[49], 2014).

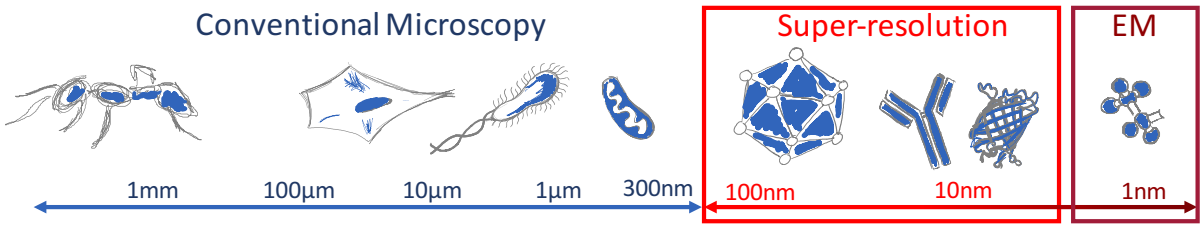

Figure 16. Size scale of different biological micro-organisms and nano-structures*. Representation of biological samples imaged using conventional and standard microscopy versus super-resolution microscopy. Super-resolution microscopy is able to image nanoscale-structures such as viruses, small molecular-complexes or even isolated proteins by overcoming the diffraction limit.*

Super-resolution microscopy successfully overcame the diffraction limit of conventional microscopy by an order of magnitude, bridging the gap between light-microscopy and electron microscopy (Figure 16).

1.2.2. Single Molecule Localization Microscopy (SMLM)

Amongst super-resolution technique, **SMLM** is the most resolutive. It offers the capability to monitor the nanoscale organization and dynamics of biological structures down to 10 nm resolution with single protein accuracy. Single molecule localization microscopy relies on the cumulated stochastic localization of sparsely distributed isolated fluorophores, rendered fluorescent by photo-activation, photo-switching or transient binding (Chapter 1.1.3). The position of each isolated fluorescent emitter can be computationally estimated with a nanometric precision. By sequentially switching on (fluorescent) and off (non-fluorescent) all the fluorophores, and cumulating their estimated position, it is possible to reconstruct a super-resolution image. Several historical acronyms of SMLM exist in the literature. The main ones are the **PALM** (**photo-activated localization microscopy)** (Betzig et al[50], 2006; Hess et al[46], 2006), the (d)**STORM** ((direct) **stochastic optical reconstruction microscopy**) (Rust et al[47], 2006, Van de Linde et al[51], 2011), and the (DNA/u)-**PAINT** (**point accumulation for imaging in nanoscale topography**) (Jungmann et al[52], 2014, Giannone et al[53], 2013).

1.2.2.1. Principle of SMLM and Localization mechanism

When single emitters are imaged through a microscope, appear as **PSF**. To determine their positions, individual PSF are usually fitted by a bi-dimensional Gaussian function, providing both their position and their intensity (Figure 17.B). This principle was developed and used before the advent of super-resolution microscopy for single-particle tracking (Sibarita[54], 2014). However, while it is straightforward to precisely resolve and track few emitters and assess their dynamics using sparse labelling, there is another challenge which is to image small densely labelled biological structures of interest (Möckl et al[55], 2014, Figure 13, 17.A). Indeed, if all the fluorescent probes emit simultaneously, PSFs will overlap with each other's and won't be able to be optically resolved, preventing reliable Gaussian fitting.

Under-labeling the biological structure of interest to reach single molecule density will result in its incomplete reconstruction. To overcome this issue, single molecule localization-based super-resolution microscopy, such as PALM or (d)STORM, initially employed the properties of some fluorophores under specific conditions to rapidly photo-switch between fluorescent and non-fluorescent states. It allows only a sparse subset of fluorescent molecules to emit for a short duration, so that they can be digitally localized. Repeating this process a large number of times until all the molecules have been localized, makes it possible to reconstruct a super-resolution intensity image by "simply" pooling all the localizations. The photo-switching kinetic, or blinking kinetic, defined by the fluorophores off-state/on-state duration ratio impacts the quality of the final reconstruction (Sauer and al, 2013). The ideal camera frame rate to capture enough of emitted photons per image needs to match this blinking kinetics which depends to the SMLM approaches (Chapter 1.2.3). Single molecule localization microscopy requires simple instrumentation setups with good sectioning and sensitivity to detect single molecules (e.g. TIRF or HILO), as well as dedicated labeling strategies and algorithms.

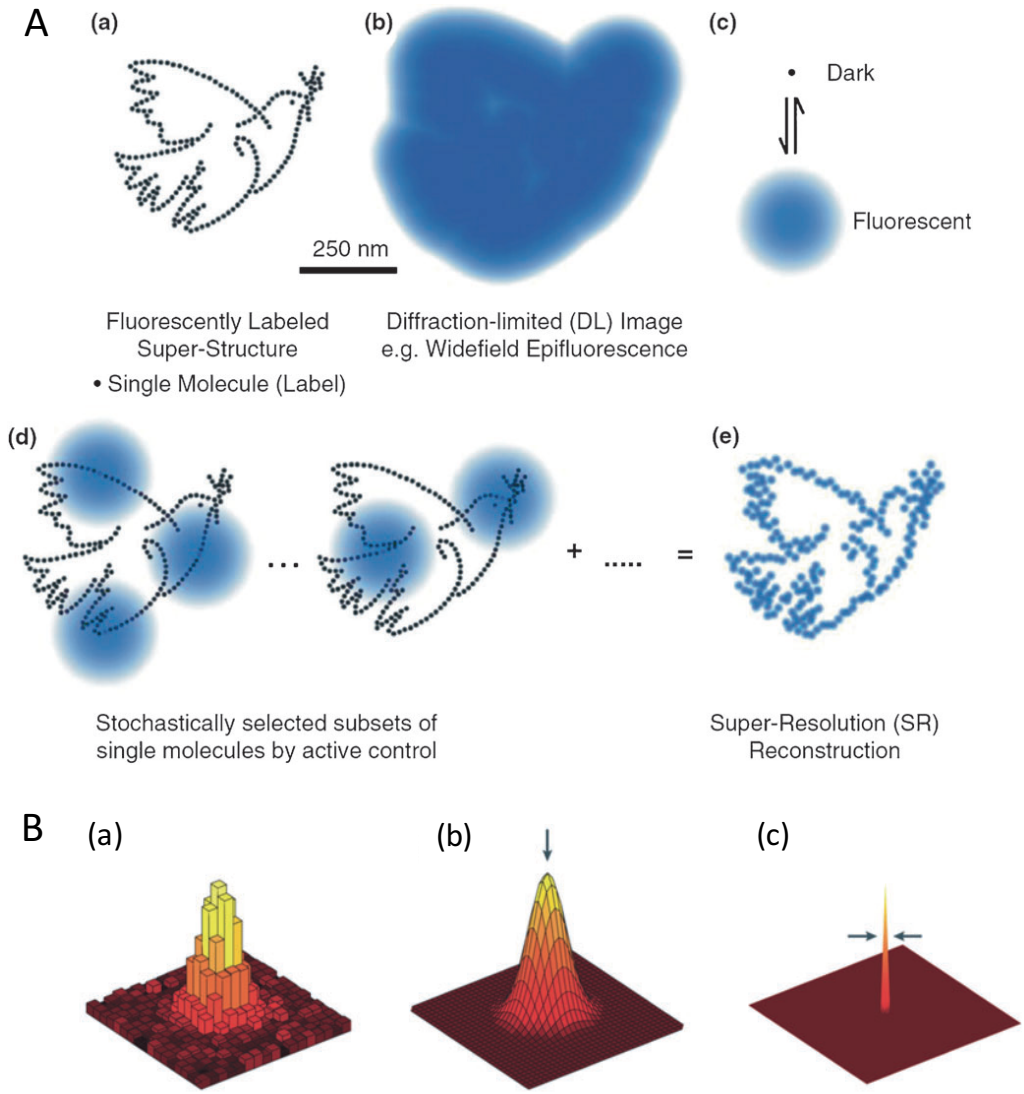

Figure 17. Principle of single molecule localization microscopy*. A. (a) Structure of fluorescent probes representing La Paloma de la Paz (Picasso, 1961) and (b) its resulting diffracted-image through a standard microscope. Optical blur prevents the shape of the Paloma to be identified. (c) By stochastically switching the molecule between their fluorescent state (ON-state) to their dark state (OFF-state) so that fluorescent molecule subset is sparsely distributed in space (d), the center of each individual fluorescent molecule can be accurately localized to finally reconstruct a super-resolution image. B. For the localization process, the PSF of each fluorescent emitter (a) is usually fitted by a 2D Gaussian model (b) to retrieved precisely its center (c). (Adapted from Möckl et al[55], 2014)*

1.2.2.2. Resolution in SMLM

In conventional diffraction limited, the experimental resolution can be estimated by PSF Gaussian fitting by:

$$r_{xy} = FWHM = 2\sqrt{2ln2}s \approx 2.3s$$

Where s represents the standard deviation of the Gaussian. Resolution in SMLM is directly linked to the accuracy to "localize" the center of each PSF, introducing the concept of localization precision. It can be estimated experimentally by fitting the distribution of a large series of localization of the same fluorescent emitter. It is however not sufficient to describe

the quality of a super-resolution image. Deschout et al.[56] (2014) introduced two distinguishable but linked concepts: the **localization precision** and the **localization accuracy** (Figure 18). The localization precision σ can be analytically described by:

$$\sigma = \frac{s^2 + p^2/12}{N} + \frac{8\pi s^4 b^2}{p^2 N^2}$$

Where s is the standard deviation of the PSF Gaussian fit (described above), p is the camera pixel size, N is the number of detected photons, and b is the background photon count per pixel (Thompson et al[57], 2002). The localization precision can be simplified by the following estimation:

$$\sigma_x \approx \frac{s}{\sqrt{N}}$$

It defines that for an objective with a given NA (defining s), the number of detected photons per localization event is the main parameter affecting the localization precision: the more photons are detected per single molecule localization event, the more precisely the position of the single molecule is determined. This simplification ignores certain parameters that may affected the localization precision, such as the image sampling or the fluorescent background that can drastically degrade the reconstruction quality. Moreover, and to a lesser extent, the different algorithms used to localize single molecules and to compute super-resolution images can also affect the final quality of SMLM images (Mortensen et al[58], 2010, Sage et al[59], 2019). As an example, using Alexa 647, one of the best fluorophores for dSTORM-SMLM, it is possible to reach ~9 nm localization precision for 1,000 localized photons and 1.4NA objective, representing a resolution of ~21 nm.

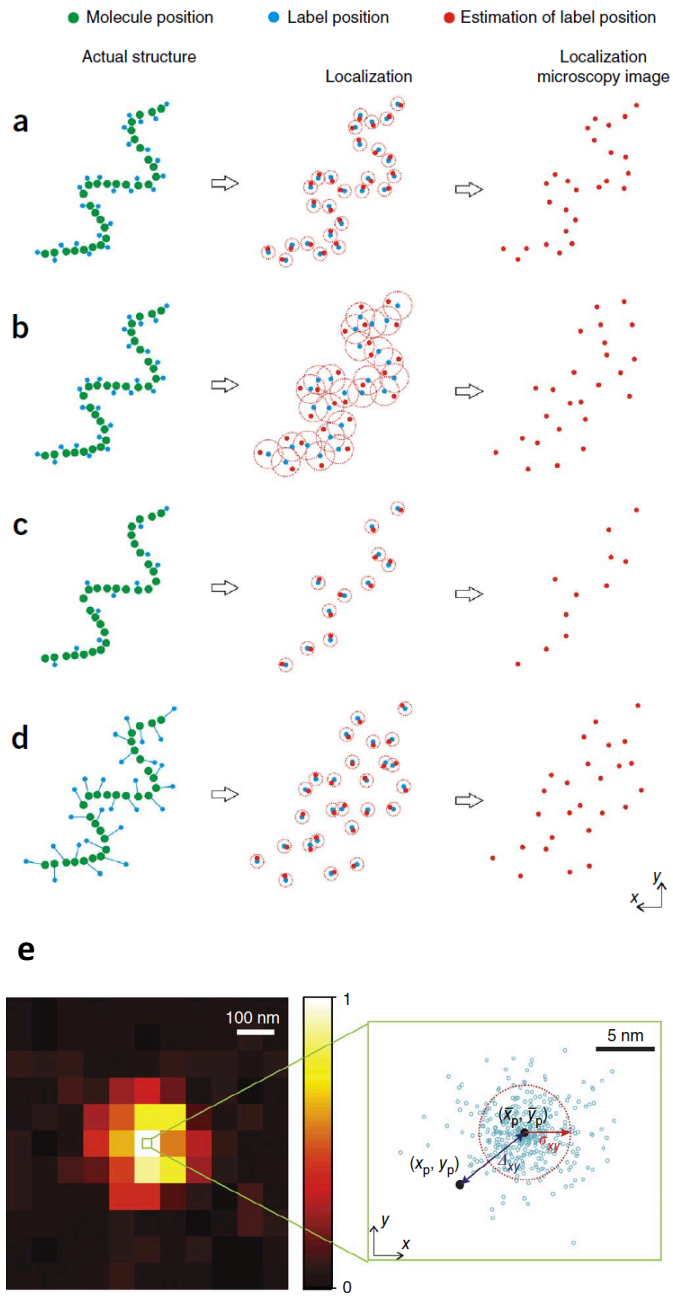

Figure 18. Resolution in single molecule localization microscopy. *(a-d) The label density and label size and its displacement (the distance of the label from the structure of interest) influence the localization precision and the resolution of the super-resolution image of the labeled structure of interest. The original structure of interest is represented in green dots, the actual structure observed in the reconstructed SR images consisted of estimated positions (red dots) of the labels (blue dots). The red circles represent the localization precision. (a) The resulting SR image represents faithfully the structure of interest when the localization precision is high, the label density is sufficient and the total labelling size is small. On the contrary, the resolution of SR images decreases due to a lower localization precision (b), lower label density (c) or bigger labelling size (d). (e) Schematic representation of the parameters influencing the resolution in SMLM. The successive localizations of one fluorescent molecule generate a cloud of localizations confined in an area defined by the localization precision (σ_{xy}). This localization area is shifted from the real position (x_p,y_p) of the tagged protein by a distance given by the labeling size (linker length) which define the localization accuracy (Δ_{xy}). (Adapted from Deschout et al[56], 2014)*

1.2.2.3. 3D SMLM

In its initial implementation, SMLM microscopy does not discriminate the axial position of single emitters. Several techniques have been developed to determine the axial position of each localized single molecule. They either rely on multiplane imaging (bi-plane, Juette et al[60], 2008; Multifocus microscopy, Abrahamsson et al[61], 2013), PSF-shaping (astigmatism, Huang et al[62], 2008; double-helix, Pavani et Piestun[63], 2008; etc.) or interferometric imaging (iPALM, Shtengel et al[64], 2009; SELFI, Bon et al[65], 2018). By exploiting the evanescence light, another advanced technique is based on the detection of the nearfield supercritical emission (SAF), which permits the access of the absolute depth of the fluorophores relatively to the coverslip (Bourg et al[66], 2015). The most popular and straightforward approach is based on astigmatism. It usually uses a cylindrical lens introduced in the detection path of the microscope to shape the PSF in a non-symmetric manner depending on its axial position. The PSF displays a round shape when the emitter is in focus, whereas it elongates along one axis

or its perpendicular depending if the emitter is located above or below the focal plane. It is therefore straightforward to numerically retrieve the axial position by analyzing the astigmatic PSF shape after calibration. Astigmatism-based 3D SMLM combined with HILO illumination allows localizing single molecules up to 1µm above the coverslip with axial precisions reaching a few tens of nanometers.

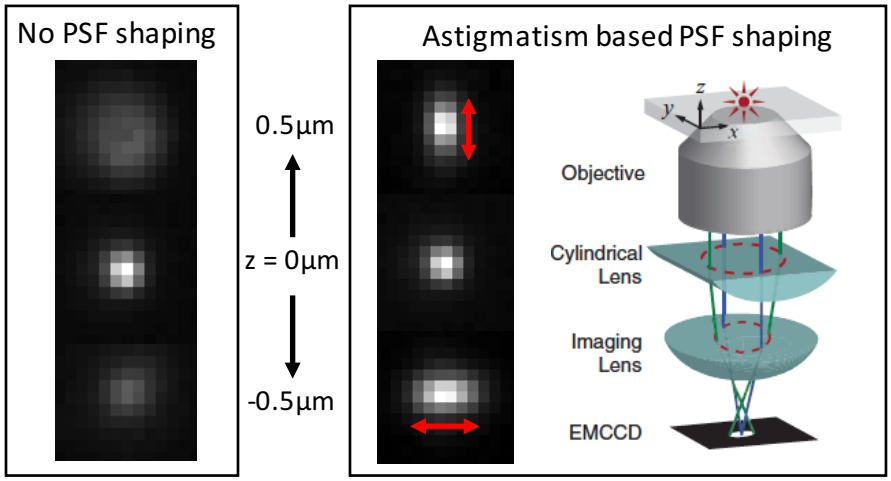

Figure 19. Astigmatism-based 3D single molecule localization. *In absence of aberration, the PSF of a microscope is symmetric, preventing its axial localization (left). Introducing a cylindrical lens in the detection path of the microscope allows inducing astigmatism. The PSF is then deformed in a non-symmetric manner depending on its axial position relative to the focal plane, allowing three-dimensional single molecule localization (right) Adapted from Huang et al.*

1.2.2.4. Labeling strategies for SMLM

Labeling strategies to target a protein of interest are crucial for high quality quantitative SMLM images (Kaplan&Ewers[67], 2015). First, in order to be faithful to the actual structure of the object of interest, **the labelling density** needs to be high enough to permit the localization of each individual protein and resolve entirely the structure of interest. Second, the **labelling size** is a critical point. Indeed, the size of a standard antibody being around 10 nm, the conjugation of a primary with a secondary antibody can reach 20 nm. This can be bigger, or in the same range than the localization precision, leading to bias in the final SMLM image resolution (Figure 18). To overcome this issue, there are different types and size of antibodies and antibodies conformations suitable for different SMLM techniques, such as Fab antibodies, fluorophore conjugated primary antibodies, nanobodies or streptavidin.

In this project, we use specific clinical human primary antibodies, preventing the use of several combination of antibodies such as nanobodies, Fab antibodies or conjugated primary antibodies. This is mainly due to the human species and the functionality of this therapeutic antibodies.

1.2.2.5. Real-time localization and tracking

SMLM has reached a mature stage, becoming today a routine tool used to investigate biological questions at the nanoscale. But it is still full of pitfalls (see: SMLM concept and labelling strategies) and remains a computationally intensive technique. In particular, Gaussian fitting used to precisely extract the position of the fluorophore requires intensive processing. Indeed, a typical SMLM data reconstruction workflow can represent several tens of thousands of images to acquire and analyze in order to extract up to a million of

localizations. Several algorithms and open source software offer solutions to analyze SMLM data. Two papers (Sage et al[59], 2015; Small et Stahlheber[68], 2014) benchmarked a large number of existing methods and compared them on different factors: accuracy, time processing, noise model, fitting approach, etc. Various techniques exist such as low-pass filtering, band-pass filtering, watershed, and wavelet transform for single molecule detection. For the localization step, most of them use fitting the PSF with Gaussian or alternative models. These studies showed that simple Gaussian fitting is sufficient to accurately localize low-density single molecule dataset, contrary to high-density dataset computation which highly depends on the model of the PSF. Most of existing techniques process SMLM data off-line, making the overall pipeline very time consuming when aiming at analyzing a large number of cells to assure robustness to the biological effect observed.

One alternative solution, introduced by Kechkar et al[69] (2013), is based on exploiting "a trous" **wavelets** described in Izeddin et al.[70] in 2012 to reliably detect single molecules events. It has the advantage to well discriminate single molecule fluorescent signal from noise or background, to offer very good single molecule localization accuracy and to be very efficient in term of processing time. The fine determination of each localized molecule coordinates is performed by Gaussian fitting initialized from the coordinates determined by the wavelet segmentation. By exploiting GPU and CPU resources as well as multithreading, the software allows real time single molecule localization that can be performed in parallel with the acquisition (Figure 20) at any frame rate, offering unprecedented speed compared to off line processing solutions, without compromising the localization accuracy.

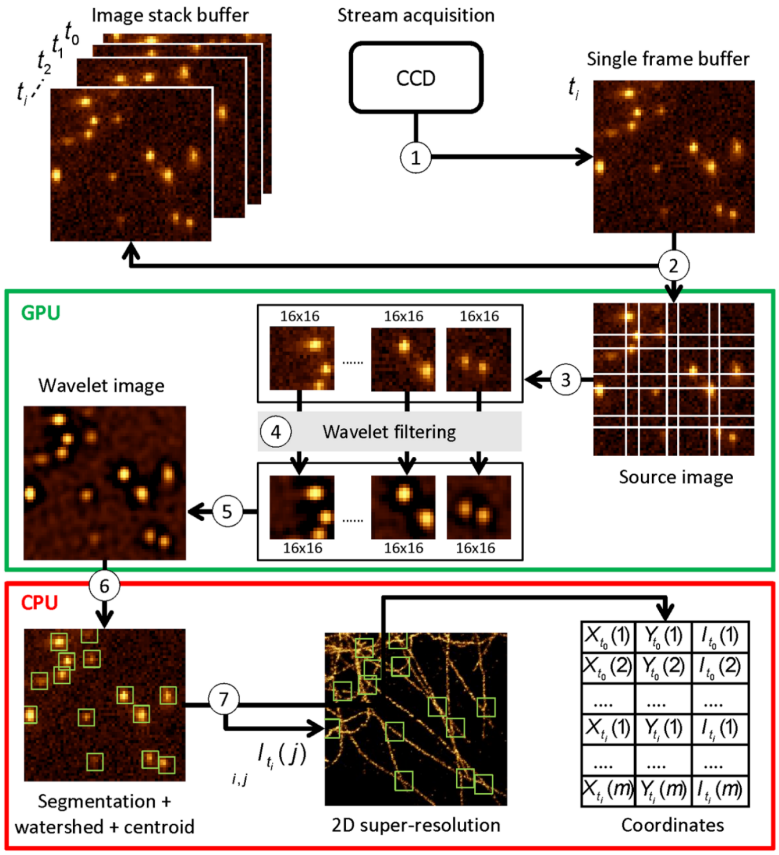

Figure 20. Real-Time localization and analysis workflow of WaveTracer software. *The parallelization of single molecule localization of emitter spot on GPU/CPU allows users to perform SMLM acquisition and reconstruction in real-time. (Adapted from Kechkar et al[68], 2013)*

WaveTracer is a user-friendly module developed as a plugin of MetaMorph acquisition software (Figure 20). It makes it possible to compute the localization and the super-resolution

image reconstructions **online**, in real-time during the acquisition streaming. WaveTracer also offers advanced features, such as automatic drift correction from fiduciary markers, astigmatism-based 3D localization, and single molecule tracking. These functionalities will be extensively exploited in this project, more especially for the HCS part.

1.2.2.6. Drift correction

SMLM is extremely sensitive to the microscope environment. Indeed, the reconstruction of a super-resolution image of a biological structure requires several tens of thousands of images, which can represent between a few minutes to about hour of continuous acquisition, depending on the single molecule regime. During this long acquisition time, micrometer range **mechanical drifts**, mostly due to small temperature changes, corrupt the super-resolution image (Figure 21), leading to the misinterpretation of the reconstructed object of interest (Balinovic et al[71], 2019).

As a consequence, drift correction needs to be fully integrated to the SMLM acquisition and reconstruction workflow. The most popular method is to use fiduciary markers absorbed on the glass coverslip, located in the acquisition field of view. Their positions are tracked during the SMLM acquisition, and used for drift correction. Nano-diamonds (Hsiao et al[72], 2016) and fluorescent beads are commonly used in SMLM. Tetraspeck beads are high intensity multicolor fluorescent microspheres, easy to manipulate and widely used in the field. However, their strong fluorescence and bleaching can be limiting factors. Nano-diamonds are chemically robust, photo-stable and fluorescent on the whole visible spectrum. Nevertheless, they are more complex to use since they tend to form aggregates.

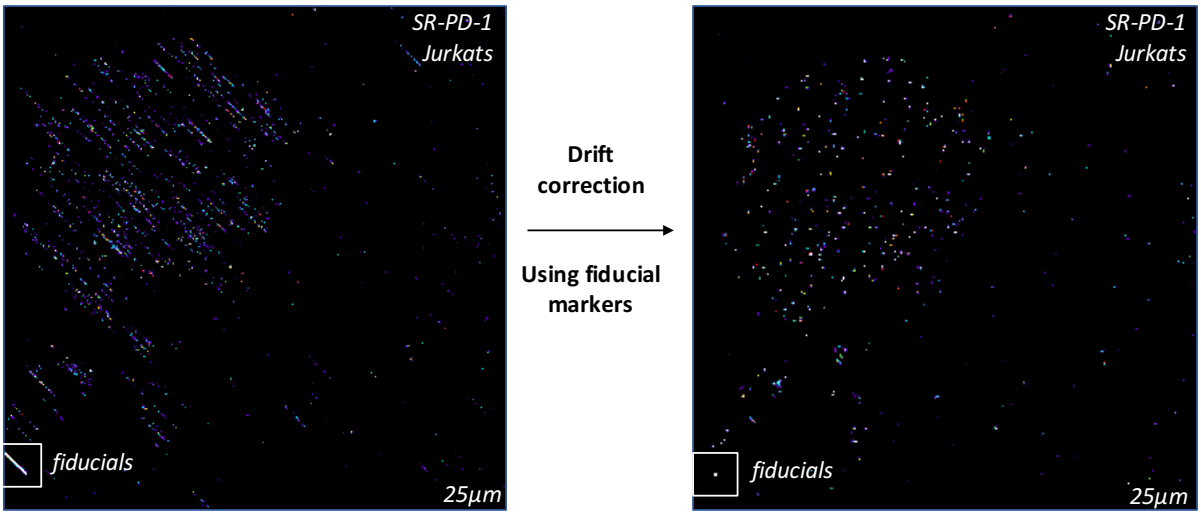

***Figure 21. Fiducial-based drift correction in SMLM**. Example of super-resolution reconstruction of PD-1 membrane receptor on Jurkat cell (dSTORM, 15.000 frames, 25 µm-size), before (left) and after (right) drift correction using one fiducial markers (white square, 100nm-Tetraspeck).*

Axial drifts also occur during the acquisition, shifting the focal plane and resulting in out of focus molecules. Axial drifts cannot be corrected off-line by post-processing. Integrated optical autofocus systems, such as the Nikon Perfect Focus System (PFS), allows stabilizing the microscope in the axial direction with more less than 50 nm precision, allowing keeping the single molecule signal in-focus, even in TIRF mode. In the particular case of the soSPIM technique, when lateral and axial drifts are correlated, online 3D registration is mandatory. I developed a solution to allow soSPIM-based 3D SMLM (Chapter 3).

1.2.3. SMLM techniques

1.2.3.1. Direct stochastic optical reconstruction microscopy (dSTORM)

A couple of years after the first publication of PALM (Betzig et al[50], 2006) and STORM (Rust et al[47], 2006), a simplification of the STORM imaging technique called dSTORM (for direct STORM) was introduced by Heilemann et al[48]. in 2008. While original STORM technique requires specific dyes, **dSTORM** allows any Alexa dye, already broadly used in fluorescence microscopy, to blink with a kinetic compatible with single molecule localization microscopy. It relies on the use of **dSTORM buffers** combined with high intensity lasers, in order to favor long-lived triplet states of excited fluorescent molecules (chapter 1.2.1.1). dSTORM imaging is fast compared to other SMLM approaches, with a typical integration time between 5 to 50ms. Some factors can influence fluorophores photo-switching kinetics, such as the intensity of the excitation beam and the chemical properties of the imaging buffer. Unfortunately, high intensity lasers lead to partial fluorescent molecule photo-bleaching. A recent publication demonstrates that more gentle illumination strategies should be adopted to limit the amount of irreversibly photo-bleached molecules in the early phases of the acquisition (Diekmann et al[73], 2020). This issue, specific to dSTORM imaging, is fluorophore dependent, increasing the difficulty of finding compatible dyes for multicolor dSTORM.

The imaging buffer is key for dSTORM. It is commonly composed of an oxygen scavenger and thiol to favor the transfer and the stabilization of fluorophores to triplet states. This enables stochastic relaxation to ground state of subset of fluorophores, permitting few fluorophores to emit at once and thus single molecules localization. Standard buffers are enzymatic-based, made of glucose oxidase or pyranose oxidase, catalase, glucose and MEA (primary thiols) in PBS or Tris buffers (Dempsey et al[74], 2011; van de linde et al[51], 2011; Beghin et al[75], 2017; Olivier et al[76], 2013; Nahidiazar et al[77], 2016). Recently, Hartwich et al[78] (2018) reported a new chemical sulfite-based buffer which presents better assets than enzymatic-based ones.

However, dSTORM imaging buffers have limitations. Firstly, its chemical composition (Appendix) is not compatible with live imaging. Secondly, it lacks of stability over the time due to oxygen reaction, leading to a limitation time of SMLM acquisition, a major issue for single-molecule-based high content screening.

For the labelling, different types and size of antibodies exist (1.1.2.4), but the use of a couple primary/secondary antibodies is the most straightforward way to target a protein of interest. There are several commercially-available secondary antibodies coupled to conventional dyes, covering a large wavelength spectrum. Alexa Fluor-647 is so far the best dye to perform dSTORM. Multicolor imaging is possible, with the condition to choose different dyes with well-separated emission spectra, as well as non-interfering antibody species. However, only a few of them can be efficiently used simultaneously, making two-colors and three-colors dSTORM imaging challenging. The Alexa-532/Alexa-647 couple seems to be a good candidate in our hands (Beghin et al[75]). Image acquisitions are usually done sequentially (Bates et al[79], 2007), one color at a time, allowing the optimization of the acquisition parameters per dye. Simultaneous acquisition, combined with spectral unmixing approaches (Bossi et al, 2008; Baddeley et al[80], 2011; Lampe et al[81], 2012) or new spectral methods (Xu et al[82], 2018) are also possible, at the expense of more sophisticated microscopy setups and analysis software.

1.2.3.2. DNA-PAINT/uPAINT: transient labelling approaches

PAINT technique, for **Point Accumulation for Imaging Nanoscale Topography**, is another family of single molecule localization microscopy based on transient binding of a

fluorophore to a target of interest. This alternative approach allows the repeated localization of fluorescent molecules at high photon count, without the requirements of intense lasers or imaging buffers. **DNA-PAINT** aims to decouple the standard protein labelling by using primary antibodies and a pair of complementary DNA-strand conjugated to a fluorescent dye (Jungmann et al[52], 2014, Schnitzbauer et al[83], 2017). First, single DNA-strand antibodies (docking strand), are used to tag the proteins of interest, then complementary DNA-strands coupled to organic dyes (imager strands), are added into the solution for SMLM imaging. This process enables the stochastic transient labeling of the tagged proteins, and by extend permits the infinite localization of molecule targeting the same protein. DNA-PAINT overcomes photo-bleaching and lack of stability issues of dSTORM. Unfortunately, it remains a slow technique (with about 200ms exposure time per frame), an important limit for single-molecule-based high content screening.

In contrary to DNA-PAINT, **uPAINT**, for universal PAINT, is based on standard primary and secondary antibodies (Gianonne et al[53], 2012). It relies on the live recording of the permanent binding of secondary antibodies to the extra-cellular membrane proteins in living cells. A low concentration of antibodies is added with the cells in the solution to promote low density labeling of membrane proteins. Combined with oblique illumination to reject out of focus light collection from non-attached dyes, uPAINT permits single molecule localization and tracking. Using specific dyes resistant to photo-bleaching such as ATTO, SeTau or QD dyes, single particles tracking of fluorescent antibodies is possible over several frames, until bleaching, accessing nanoscale molecular dynamics.

1.2.3.3. Photo-activated localization microscopy (PALM)

PALM (photo-activated localization microscopy) technique (Betzig and Hess[46,50], 2006) relies on **photo-activatable fluorescent proteins**. These fluorescent proteins, derived from the GFP, have the properties to reversibly (or irreversibly) change their absorption and emission spectra upon absorption of 405 nm light. They are genetically encoded directly on the sequence of the protein of interest. Once stochastically activated upon very low intensity of 405 nm to be in single molecule regime, they emit for a short period until they bleach (or revert back to their non-activated state). This process of single molecule activation/imaging/bleaching is repeated until all the proteins are imaged to reconstruct the super-resolution intensity image.

Compared to immuno-labelling strategies used for dSTORM, they have a high level of specificity and are compatible with live imaging and single protein tracking. However, the expression of the fluorescent protein of interest requires cell transfection or electroporation, and is usually associated to protein over-expression that may affect the biological readout. Moreover, fluorescent proteins are usually less bright compared to organic fluorophores, leading to a lower localization accuracy.

Several types of fluorophores can be used for PALM (Figure 22.a). The **Photo-activatable fluorescent proteins** (PAFP) which switch non-reversibly from non-fluorescent (OFF) to fluorescent (ON) states until bleaching (e.g. mCherry, PA-GFP, mKate). **Photo-convertible fluorescent proteins** (PCFP) initially emit fluorescence in their basal state, and non-reversibly photoswitch to a different color upon photo-activation. The most popular PCFP are mEos (mEos 2, mEos 3.2, mEos 4; Zhang et al[84], 2012) and Dendra2. Finally, **reversely photo-switchable fluorescent proteins** (RSFP) can be reversibly switched between ON and OFF states (e.g. Dronpa, mGeosM, etc.). The 405nm absorption commutes the dyes, while the imaging light commutes the dye back to the non-fluorescent state.

PALM being compatible with live samples, it is possible to track individual localized fluorescent molecule until bleaching (Figure 22.b). This technique, called **sptPALM** (for single

protein tracking combined with PALM) (Manley et al[85], 2008) allows to decipher both the nanoscale organization and dynamics of biomolecules, providing a unique quantitative insight on the interaction with other partners. Protein dynamics are commonly investigated by computing the diffusion coefficient from individual tracks (Rossier et al[86], 2012; Nair et al[87], 2013; Floderer et al[88], 2018; Sibarita et al[54], 2014). The diffusion coefficient D is extracted for the **mean square displacement** (MDS) analysis, which quantifies the area r^2 explored by a single molecule over time t. It is calculated from linear fits of the first points values of the MSD curves, using the following equation:

$$MSD(t) = < r^2 > = 4Dt$$

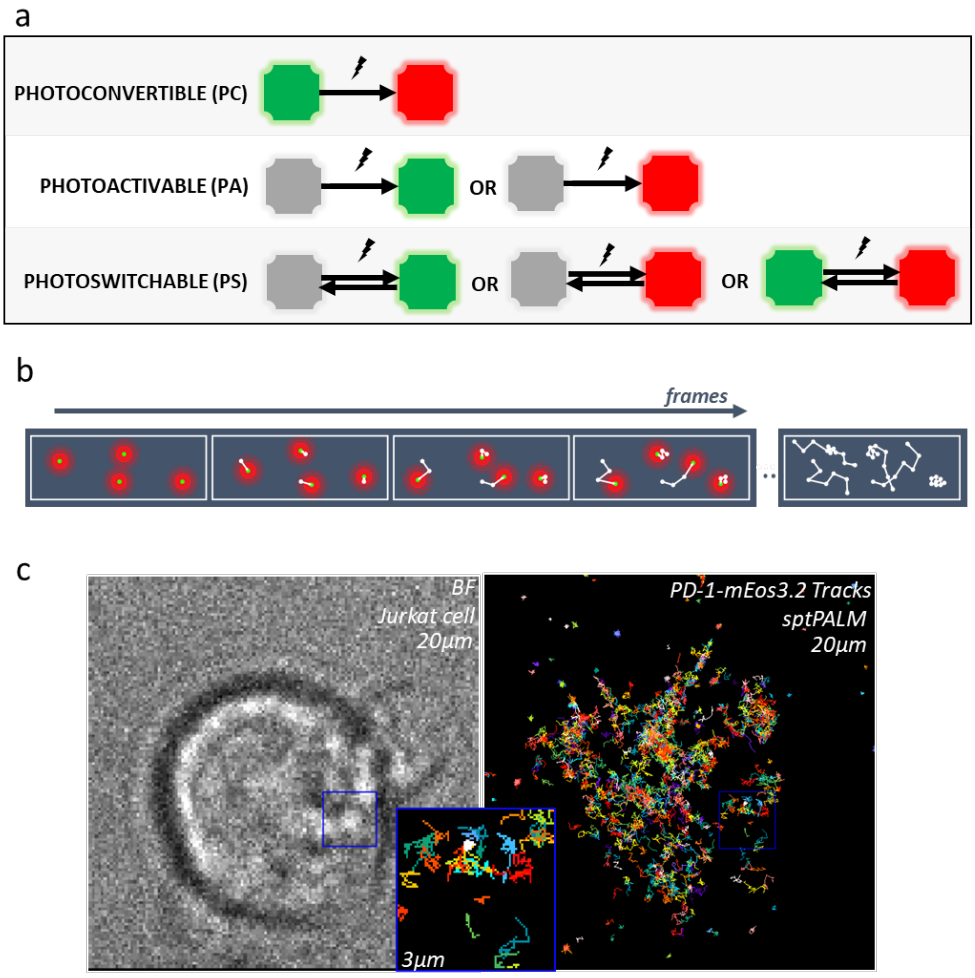

Figure 22. Principle of (spt)PALM. *(a) Different type of fluorophores used for (spt)PALM. Probes are either photoconvertible, photoactivable or photoswitchable. (b) Principle of single protein tracking PALM. Localized single molecules are connected on adjacent frames allowing reconstructing their trajectories. (c) Example of sptPALM acquisition of photoactivable PD-1-mEos3.2 proteins. sptPALM enables the tracking of individual PD-1 protein fused with mEos3.2 fluorescent protein in Jurkat cells. (images 20µm-size; 20ms; 4000 frames; Tracks length [10-1000]).*

1.2.3.4. Why is SMLM suitable for immunotherapy applications?

SMLM techniques have been extensively used over the last decade to investigate the nanoscale spatial organization of T-cell membrane receptors (Figure 9, chapter 1.1.5). In 2011, Williamson et al[89] quantified the Lat receptors distribution on T-cell surface using PALM and dSTORM imaging. T-cell receptors and the CD3 complex organization and dynamics upon T-cell activation were investigated at the immunological synapse by few teams (Rossboth et al[90];

Hu et al[91]; Pageon et al[92], Rosenberg et al[93], Ponjavic et al[34]) using dSTORM and (spt)PALM techniques, but also using other super-resolution microscopy techniques such as SIM and STED. Several other T-cell receptors (e.g. CD45, CD2, etc.) have been also investigated using SMLM imaging, but none of them belong to the list of immunotherapy potential targets. Using dSTORM, receptor clusters size, cluster distribution and their molecular density have been studied and compared at the membrane of resting and activated T-cells. sptPALM approaches have been also used several times to study receptors interaction (Ponjavic et al[34], Razvag et al[94]), allowing to better understand their intrinsic mechanisms and implication upon T-cell activation. Recently, the combination of advanced lattice light-sheet microscopy with SMLM permitted to observe membrane receptors at the whole T-cell surface, and to map the 3D spatial organization of T-cell receptors on fixed and living cells (Wäldchen et al[35], Rosenberg et al[93], Ponjavic et al[34], Hu et al[91]).

All SMLM techniques can be applied to study T-cell membrane receptors at the nanoscale level. sptPALM and uPAINT are well-suited and complementary approaches for high density single particle tracking. dSTORM and DNA-PAINT are ideal to investigate the nanoscale spatial organization and clustering properties of fixed T-cells membrane receptors with the best possible resolution (Rossboth et al[95]). DNA-PAINT, and qPAINT (Jungmann et al[96], 2016) in more particular, is more suited than dSTORM for advanced quantification (Simoncelli et al[97]) and is not limited in time due to the buffer. However, as mentioned before, it requires 10 times longer integration time and has not yet been used to study T-cell membrane receptors. All these techniques are compatible with HTS/HCS, each of them having pros and cons.

1.2.4. Quantitative analysis of single molecule localization microscopy data

Localization-based super-resolution microscopy has brought a new type of data in microscopy, called point cloud data, creating a new field of research for their analysis. Indeed, SMLM output is a list of molecular coordinates, while other microscopy techniques provide pixel-based images as output. While it is still possible to reconstruct pixel-based images from the point cloud data and to use regular image analysis tools, it has been demonstrated that the direct analysis of point cloud patterns is more precise than pixel-based images.

Protein clustering, aggregation, oligomerization, internalization, diffusion, etc. are examples of quantitative parameters that can be computed from the molecular coordinates and trajectories, which directly relates to underlying biological mechanisms. Numerous analytical methods have been developed over the past years to quantify molecules organization and dynamics. The methods I will present below are those that I used for this thesis.

1.2.4.1. Analysis of protein dynamics using PALMTracer

PALMTracer is a module integrated as a plugin of MetaMorph software. It has been developed in the Lab, by Jean-Baptiste Sibarita, Adel Kechkar and Corey Butler. It integrates off-line single molecule localization (Izeddin et al[70], Kechkar et al[69]) and tracking (Racine et al[98], 2006) algorithms to process and quantify multidimensional SMLM data. This software is a versatile tool, able to compute and export localization, tracking and diffusion data, as well as to represent them in 2D and 3D, using color-coding depending of localization depth, intensity, number of localizations, diffusion coefficients, etc.

Raw data stacks of single molecule sequences can be analyzed, localized, tracked, filtered and saved as coordinates files. It supports the import of WaveTracer localizations files and integrates a powerful user-friendly batch analysis mode. PALMTracer includes 2D and 3D

visualization options both for localization and trajectories, including density maps, 3D projections and Z-stacks, imaging plane, and multi-plane stacks.

1.2.4.2. Segmentation and clustering using SR-Tesseler

SR-Tesseler (Levet et al[99], 2015) is an open-source software dedicated to the segmentation and quantification of SMLM data from point cloud data. The principle of SR-Tesseler is to create polygons around each localization, subdividing the space into a mosaic of regions called **Voronoï diagram** (Figure 23.a).

In contrary to other methods (e.g. Delaunay triangles), Voronoï tessellation is based on individual localizations, with one polygon per single molecule, making this technique better suited to quantify single molecule properties and neighborhoods. The area of each polygon defines the local density of localization and their neighborhoods. Applying a color code to this feature allows a clear visualization of local density (Figure 23.a,b). SR-Tesseler allows objects segmentation to quantify proteins clustering based on the local density (Figure 23.c). The segmentation thresholds can be either manually adjusted or automatically determined. Finally, clustering features like morphological clusters descriptors (area, size, circularity, etc.), the number of localizations per cluster, the localization density, etc. can be extracted in a .csv file for each SMLM dataset.

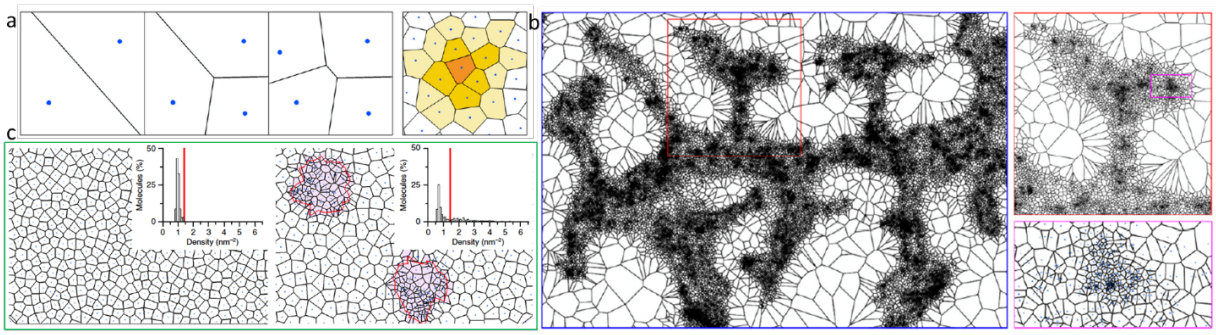

Figure 23. SR-Tesseler: principle of Voronoï diagram construction. *(**a**) Voronoï polygons of only two seeds are delimited by their perpendicular bisector. When a new seed is added, the previous section is cut by the bisectors computed between the previous seeds and the new one. The Voronoï diagram is designed by repeating this process for each new seed. Each seed can be defined and color-coded by its area representing the local density. The 5 medium-orange and 11 light-orange polygons are defined as the first-rank and second-rank neighboring polygons of the original and centered seed (dark-orange). (**b**) Three different levels of a Voronoï diagram built from an experimental GluA1-mEOS2 PALM data set, showing a dendrite (blue), a spine (red) and a nanocluster (magenta). (**c**) SR-Tesseler automatically comptes clusters by segmentation of the Voronoï diagram based on the first-rank density. (Adapted from Levet et al[98], 2015)*

1.2.4.3. Interest of combining SMLM and High-Content Screening

Localization-based super-resolution techniques are multi-parametric. Performing SMLM imaging requires mastering multiple parameters: labeling density, integration time, laser intensities, SNR, imaging buffer, drift correction, SR metadata analysis, etc. These parameters need to be adapted for each technique to ensure optimal single molecule acquisition and localization. As an example, dSTORM and PALM are particularly sensitive to molecules photo-bleaching, an effect controlled with the adjustment of illumination parameters. Single particle tracking experiments, i.e. sptPALM or uPAINT, does not require all the molecules to be localized, as long as there is an enough amount of trajectories to asses protein dynamics with robust statistics. In the contrary, dSTORM, PALM and DNA-PAINT, are used to analyze protein structure and spatial nano-organization, and where each detection influences the final quantification. This means that the acquisition and analysis parameters

must be standardized to provide robust and un-biased quantifications. Finally, SMLM is long and usually requires lots of manual interventions, making it fastidious to investigate several different biological conditions with enough statistics. In this context, there is a real advantage to combine SMLM with high content screening. It allows the normalization of single molecules acquisition quality for all the conditions enabling faithful comparison of SMLM features. However, individual parameters adjustments are not possible at such large-scale acquisitions. To avoid any single molecules artifacts on images, HCS-SMLM experiments must ensure a single molecule regime compatible with all the cells and biological conditions using the same acquisition parameters.

1.3. CHAPTER 3: High Content Screening (HCS)

1.3.1. HCS in pharmacology: drug screening approaches for therapeutic Abs characterization

1.3.1.1. Therapeutic Ab development: goal and strategies

In parallel to chemical molecules, Sanofi develops antibodies to specifically meet the therapeutic needs of patients not covered by current treatment. Among diverse targets, Sanofi focuses its activity on the antibody development against key actors of the T-cell activation process, targeting the most promising co-stimulatory or co-inhibitory T-cell surface receptors.

Antibodies are produced in the Biological Research department, and functionally characterized by the Integrated Drug Discovery (IDD) department. The different research and development phases result in the selection of antibodies having good binding and functionality properties towards the target of interest, good behavior under different stress conditions (high, low temperature, pH, aggregation…), before being tested on animals. The early phases of therapeutic antibody certification take place during the phase I, II and III clinic trials on humans.

Until the clinical trials, the IDD-department checks and confirms the antibody functionalities using diverse **immuno- or non-immuno-specific** methods. These cellular-based experiments, described in the next section, are employed multiple times in the different mAb development phases.

1.3.1.2. HCS-drug screening methods: large scale characterization

In my project, the therapeutics antibodies we are interested in, block the interaction between a pair of checkpoint inhibitors, leading to an immune response and cytotoxic T-cell activity to kill tumors cells. In the tumor environment, the TCR expressed on T-cells recognizes tumor-associated antigens presented by the Antigen Presenting cells (dendritic cells, macrophages, etc.) leading to T-cell activation via the intracellular signaling cascade (1.1.1.2). This results in a massive production of Interleukin IL-2 and Interferon gamma cytokines, which modulate the immune response. In this context, **IL-2, TNFa and IFNg** cytokines influence T-cell proliferation and promote their activation. After several days, the more the T-cells are numerous, the more cytokines are produced, creating a cytotoxic activity against cancer cells.

Sanofi's screening department (IDD) has adapted protocols to mimic this biological context in order to evaluate several tens to a hundred of new therapeutics antibodies in **384 multiwell plate**. For this purpose, they perform two kinds of experiments: mixed leucocyte reaction and T-cell activation experiments, to control individually, or in combination, the antibody functionality, efficacy and physical properties.

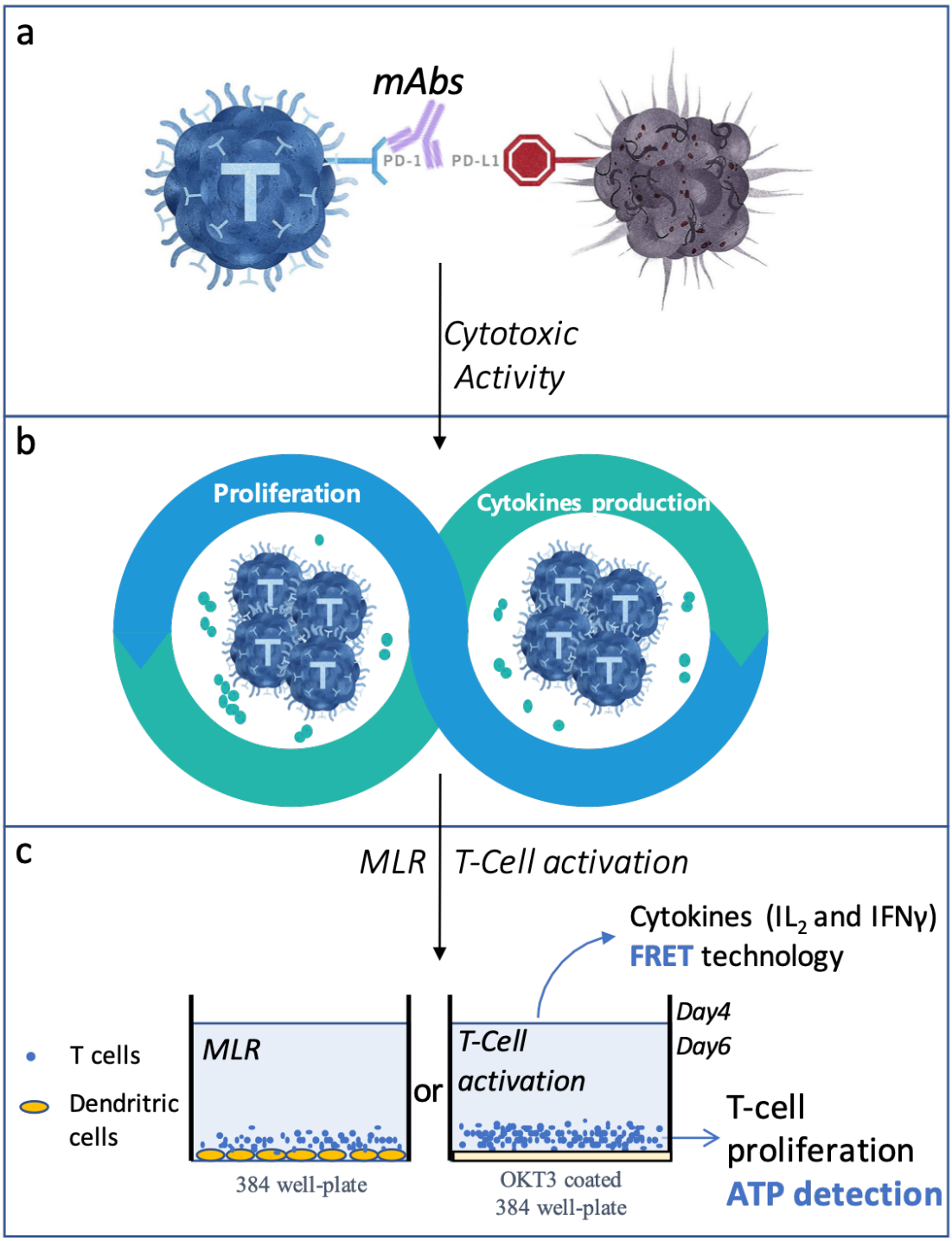

Figure 24. Schema of MLR and T-cell activation drug screening experiment for mAbs characterization. *(a) Introduction of individual or combination of therapeutic mAbs to be tested on T-cells activated either by OKT3 coating or by the presence of dendritic cells (APC cells, mimicking tumor cells) which express PD-L1 to their surface (image inspired by Roche). (b) Depending of the efficacy of mAbs tested, the checkpoint inhibitors interaction is blocked triggering a full T-cell activation. It leads to a cytotoxic activity resulting in T-cell proliferation and massive cytokines production. In this context, MLR or T-cell activation experiments are done to evaluate the functionality of mAbs. (c) For both types of experiments, 4 and 6 days later, cytokines rates are determined by FRET technology from supernatants, and the final number of T-cells are measured by ATP detection as the indicator of T-cell proliferation.*

The **Mixed Leucocyte Reaction experiment**, called MLR, mixes two immune cell types, T-cells and dendritic cells (APC cells, mimicking tumor cells) to encourage a cytotoxic activity from T-cells. Both cell types are isolated at Sanofi from the blood of two different healthy

human donors. In this assay, antibodies will specifically bind the T-cell receptors of interest, blocking the interaction with their ligand present on dendritic cells. After 4 days in presence of dendritic cells, T-cells upon an activation start proliferating and producing IL-2 cytokines, and after 6 days INFy and TNFa. The cytokines rate is measured by **FRET** technology (**Fluorescence Resonance Energy Transfer**) from well supernatants recovered after 4 and 6 days. The proliferation is measured by ATP detection on the remaining cells in wells. Since dendritic cells are not dividing cells, the proliferation measurement only concerns T-cells (Figure 24).

A second type of experiment is made to evaluate the antibodies properties on activated T-cells alone. Here, human resting T-cells are activated by functional **anti-CD3 antibodies** (**OKT3**), instead of being mixed with dendritic cells. Then, the same readouts are applied at Day 6, as previously described (Figure 24).

For both experiments, each antibody is evaluated in triplicate on three different human lymphocyte donors to assure the robustness of the observed effects. Typically, between 30-70 antibodies and combinations are tested simultaneously. Each screening campaign allows to compare antibodies with each other and with benchmark antibodies or internal Sanofi entities. All the results provide an overview of the antibodies effect on T-cell response (individual and against dendritic cells), determining the fate of potential candidates.

Thereby, Sanofi characterizes new antibodies at large scale level through two biological features: The **T-cell proliferation** and **Cytokine rate** measurements. Then, mAbs which do not correspond to the specifications are removed, whereas the potential candidates are kept and will go into further evaluation thus continuing its journey in research and development. The decision is not easy to take on antibodies with same potency combining their physico-chemical properties, their functionality, immunogenicity risk, etc., meaning **that more information is needed to conclude on the real interest of some antibodies.** These current assays give global information at the cellular level; however, it lacks a **fine antibody characterization at the molecular level. A better mAbs characterization will help to understand if and how they impact the spatial organization of T-cell receptors and secondly of signaling proteins or how they are influenced by lymphocyte behavior.** Such information can be addressed by nanoscopy solutions compatible with HCS. Indeed, localization-based single molecule microscopy technologies and emerging quantitative analysis solutions reached the required maturity to be used in the pharmaceutical field, bringing unprecedented new type and amount of quantitative information on the nanoscale molecular organization and dynamics.

1.3.2. HCS, HTS and microscopy

High content screening (HCS) methods have been widely applied for drug discovery and development in biological research. High throughput screening (HTS) is closely linked to HCS approaches. Where HTS implies the tests of thousands of compounds in parallel to sort the best conditions and to enhance data robustness, HCS is an image-based approach which increases the amount of quantitative data by enlarging the number of conditions to be tested. HCS and HTS are used in routine in pharmaceutical companies for drug screening applications.

These methodologies, combined with advanced fluorescence microscopy, increase the image acquisition rate by ten-fold, enlarging the quantity and the variety of data collected from the measured samples. They have been extensively used for small molecule and antibody drug discovery as well as for the cell biology understanding, cell behavior, differentiation, dynamism, molecular function or toxicology (Bullen[100], 2008).

To answer these biological questions, commercially available systems use conventional optical technology, such as widefield, confocal spinning disk or phase contrast microscopy. “All-in-one” HCS-HTS systems presented by companies provide laboratories with stable, opaque and complete solutions for living cell assays, including cells monitoring, image acquisition, analysis, as well as other advanced functionalities (e.g. 3D, plate holders, incubators, or automatic liquid dispensers). However, none of these commercial solutions integrates single molecule-based super-resolution approaches. Indeed, optical super-resolution microscopy has not yet been applied to the drug discovery field. This is primarily due to the complexity of the acquisition and analysis pipeline, lack of automation and dedicated datamining software.

1.3.3. State of the art HCS-SMLM approaches

SMLM techniques, such as dSTORM, PALM and DNA-PAINT, are time-consuming and low throughput. They usually require user expertise and extensive manual intervention for the acquisition analysis and datamining, making them fastidious to use for the investigation of a large number of samples under various biological conditions. For this reason, most of biological studies using SMLM are still performed at the single cell level with a limited number of conditions. To overcome this limit, several groups have developed custom approaches that integrate HCS-HTS in the SMLM pipeline in order to significantly increase the acquisition and analysis workflow.

A review by Pereira et al[101] (2015) showed the interest of combining high content screening with nanoscopy. They presented an “easy-to-implement” protocol to perform high-content 3D multicolor SR imaging on a standard microscopy setup, but did not address data storage, analysis and data visualization issues. Holden et al[102] (2014) successfully accomplished high throughput PALM imaging, allowing large-scale imaging of hundreds of cells, but considering only one condition. HCS-SMLM correlative techniques have been also introduced, but still with the need of user manual intervention. Cells are manually selected at low resolution on a first microscope and the SMLM acquisitions are performed on the identified cells using a second microscope (Gunkel et al[103], 2014; Flottman et al[104], 2013). Yasui et al[105] (2018) recently introduced an automated single molecule dynamics screening system integrating artificial intelligence for automated cell-searching and auto-focus stabilization. This system, called AiSIS, allowed single particle tracking experiments of 1,600 living cells plated on a 96-multiwell plate support in one day. More recently, Barentine et al[106] (2019) developed a SMLM-HTS imaging platform able to perform fast high-speed 3D multicolor SMLM imaging of more than 10,000 nuclei in one day, with a success rate of 99.8% of target field of views (FOVs) acquired. However, despite their outstanding ability to produce huge amount of SMLM data, their pipeline does not integrate any automated quantitative analysis and datamining solutions. Other approaches proposed automated solutions for multicolor quantitative super-resolution microscopy. For example, Almada et al[107] (2019) developed the NanoJ fluidics system to automatize a five-color experiment; Klevanski et al[108] (2020) published a new method enabling automated multiplexed super-resolution imaging using a fully automated microscopy system including a non-invasive solution exchange. While the automation of the staining gives a real asset in the super-resolution imaging workflow, none of these approaches allows multiple biological conditions to be acquired and analyzed.

We can see a trend to develop automated solutions to improve super-resolution microscopy workflow and to reduce user interaction with the sample for faster image acquisition and less biases. However, all these methods usually focused on a specific problem and a dedicated SMLM technique. They most of the time do not address storage, quantitative

analysis, visualization and datamining issues, which are central to any HCS-HTS pipeline. However, very promising results drastically address some of the intrinsic limit of SMLM as a good step forward drug screening and molecule discovery at the single molecule level.

1.3.4. When high content screening meets single molecule localization microscopy

In 2017, our team published a HCS-SMLM[75] imaging platform, an integrated functional fully automatic solution for drug screening at the nanoscale. It is compatible with 96-wellplate standards and integrates an HCS-based acquisition and analysis software. Using a mix of commercial and freely available software, it can be installed on traditional SMLM setups as an upgrade toward HCS-SMLM.

Our HCS-SMLM imaging platform proposes an automated workflow which streamlines the acquisition and data analysis by generating a database "online", during the super-resolution acquisition. It computes automatically the molecule coordinates and trajectories of a large number of fixed or living cells, without the need of user interaction. The platform includes the full automation of a standard inverted motorized microscope, with all the necessary devices to perform single molecule-based super-resolution acquisitions, as well as online data-analysis, metadata extraction and datamining (Figure 25). Several existing or developed on purposed software were integrated to the pipeline to permit SMLM acquisitions and analysis to be performed in an HCS fashion. I initially joined the lab to work on this project with the goal to develop the HCS acquisition software.

1.3.4.1. HCS-SMLM acquisition workflow

The HCS-SMLM software is the brain of the HCS-SMLM platform. It comes with a Graphical User Interface (GUI) as a plugin of MetaMorph software, and handles all the acquisition parameters to perform automatic super-resolution acquisition in a high content screening fashion. It supports any multi-wellplate format or coverslip, and allows a direct interactive visualization of the plate layout, selected wells and fields of view. It controls all the necessary software modules, including custom ones (WaveTracer) and MetaMorph plugins (Multidimensional Image Acquisition), as well as all the microscope devices (illumination devices for SMLM and wide-field, filter cubes, motorized stages, etc.). The HCS-SMLM workflow is described in Figure 25, and its specifications in Appendix.

Metadata computation and organization

Metadata are quantitative data computed during the HCS-SMLM pipeline. During each SMLM acquisition sequence, WaveTracer plugin (1.2.2.5) computes automatically "on the fly" the super-resolution images and localization data (Kechkar et al[69], 2013). Two types of data are generated: i) the super-resolution images of 2D (and 3D when required) intensity and trajectories (when required); ii) ASCII files containing the localization coordinates, trajectories, MSD and diffusion coefficients. These data are processed in less than a minute per SMLM stack thanks to WaveTracer's multithreading, GPU and CPU. Overall, depending of the SMLM techniques (dSTORM, PALM, DNA-PAINT), the acquisition and the online analysis lasts between 4 to 20 minutes per field of view, without any manual intervention. Other quantitative descriptors, such as clustering and dyes photo-physical properties, can be extracted directly from the localization and tacking files. These additional metadata are computed automatically offline by SR-Tesseler software (1.2.4.2).

Database construction and data mining

All the images and metadata are automatically saved and organized in a well-defined arborescence to form a database that can reach several hundreds of GB. This database is then imported by Single Molecule Profiler (SMP), a free software developed for this project, which organizes all the SMLM metadata in a functional SQL database compatible with CellProfiler Analyst (CPA, Jones et al[109], 2008; Dao et al[110], 2016). Metadata are organized along the multiwell plate layout and linked with a unique ID.

Devoted to datamining HCS data, CPA is a freely available software with a simple interface enabling the visualization of single-molecule quantitative data in an intelligible manner using histogram, scatterplot or heatmap representations.

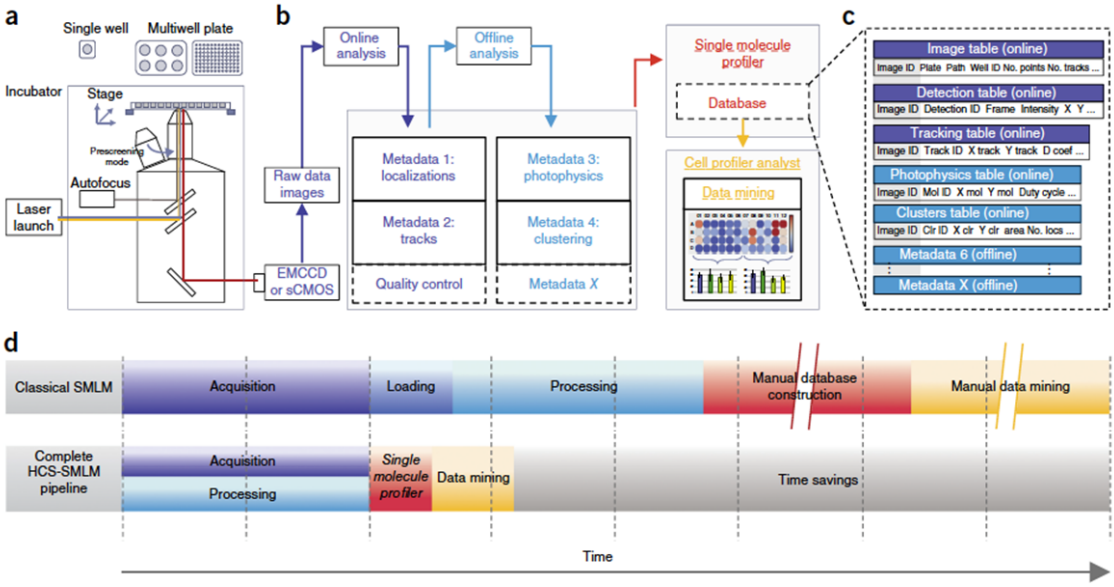

Figure 25. Complete HCS-SMLM pipeline. *(a) SMLM data are acquired on a conventional inverted microscope, equipped with an autofocus device and a fully motorized stage (X, Y, Z) under TIRF illumination for optimal single-molecule imaging. Several acquisition strategies can be chosen, with or without pre-screening mode, which use a low magnification objective. (b) Metadata used for the datamining process are computed on-line during the acquisition (red) and off-line after the acquisition (dark blue). Off-line metadata are computed directly from the on-line metadata, so that there is no need to reload the raw images. (c) HCS-SMLM metadata are automatically exported from the hierarchy tree of files in an ASCII database format composed of one table, called image table, which contains the image data information, and a few tables containing the SMLM metadata. Image and metadata tables are linked through a unique ID. (d) Benchmarking between HCS-SMLM and traditional SMLM procedure: A huge amount of time is saved compare to manual acquisition by parallelizing the SR acquisition and post-processing SR computations, and using SMP module and appropriate SQL-based data mining. (adapted from Beghin and al).*

1.3.4.2. Examples of HCS-SMLM applications

3D super-resolution dSTORM imaging of a complete 96-wellplate

As proof of concept, in 2017, we automatically acquired 3D dSTORM images of fixed cells on a complete 96-wellplate. Hundreds of images of microtubules labeled with Alexa-647 were imaged sequentially in an HCS fashion, without any user intervention except for the cell selection before launching the screen. The entire screen was achieved in 8 hours, including image reconstructions and online metadata extraction. The database contained 500 GB of raw images, 200 million single-molecule localizations, and 70 GB of metadata files (Figure 25).

As explain in 1.2.3.1, dSTORM buffers have a limited lifetime, rendering fluorophores blinking less efficient with time for SMLM. The photo-physical properties metadata analysis indicated a decrease of single molecule blinking quality after 10 hours of acquisition, imposing

a limit of a dSTORM screening acquisition duration under these conditions. Off course, the 96-wellplate must be perfectly sealed to avoid contact between oxygen and dSTORM buffer, which would reduce its efficacy and decrease that limit.

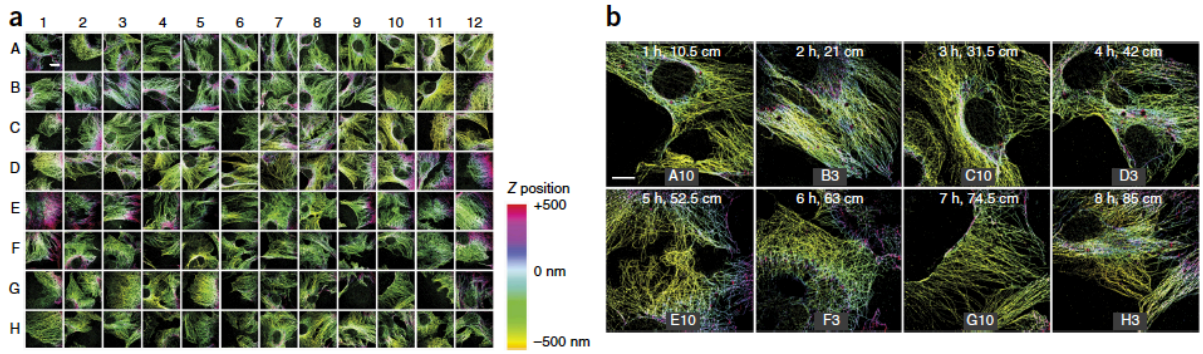

Figure 26. 3D dSTORM SMLM on 96-multiwell plate using HCS-SMLM*. (a) 96 astigmatism-based 3D dSTORM images (20.5x20.5 µm FOV, 40 nm/px) of Cos-7 cells' microtubules, automatically acquired without human manual intervention by HCS-SMLM. The total acquisition has been held within 8h, including the localization and the reconstruction. The color coding indicates the Z-position. Scale bar, 5 µm. (b) Gallery of 3D dSTORM images with a regular time interval of 1 h between each image. Scale bar, 8 µm. Z-scale applies to (a) and (b). (adapted from Beghin and al).*

We performed similar HCS-SMLM experiments using DNA-PAINT. While DNA-PAINT was not impacted by the buffer time limitation, it required much longer exposure time (200 ms VS 10 ms for DNA-PAINT and dSTORM respectively). Consequently, for the same HCS-SMLM acquisition duration, only sixteen 3D-DNA-PAINT images were acquired compared to hundreds of images for a dSTORM experiment. Recently Jungmann's lab introduced new optimized-fast DNA-PAINT approaches which exchange 10 to 100-fold faster than classical DNA-PAINT using periodic DNA sequences or FRET-based imager. These new approaches would facilitate automated super-resolution microscopy opening interesting HCS-SMLM perspectives (Strauss et al[111], 2020; Schueder et al[112], 2019).

Quantification of membrane-receptor dynamics

We validated the capacity of our HCS-SMLM platform to quantify receptor dynamics in an HCS context thanks to its capability to collect automatically single protein tracking data. To achieve this goal, we successfully performed a dose-response sptPALM experiment of cross-linkers antibodies on membrane receptors' mobility: a gradient of polyclonal anti-SEP Ab was mixed on living transfected Hela cells expressing SEP::GluA1::mEos2 (Figure 27). We used diffusion coefficient and clustering metadata to quantify the impact of cross-linker Ab concentration on SEP receptor nanoscale organization and dynamics. Quality control read-out was performed using the homogeneity of single molecules signal and dynamics, and the cell viability. This study validated our HCS-SMLM platform to be a powerful tool for nanoscale investigation of protein organization and dynamics, paving the way for new drug discovery assays at the single molecule level.

a

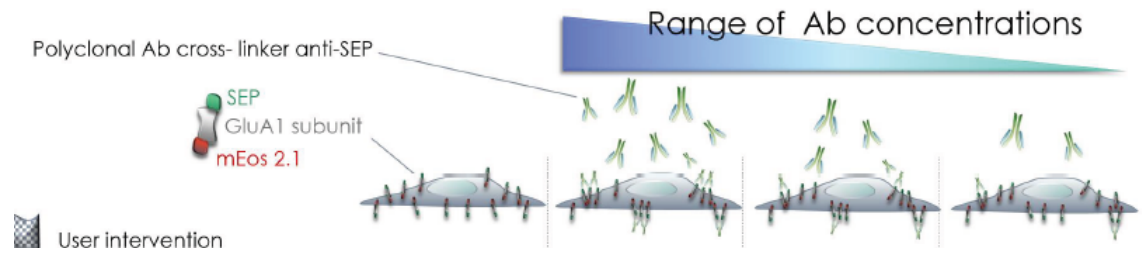

b

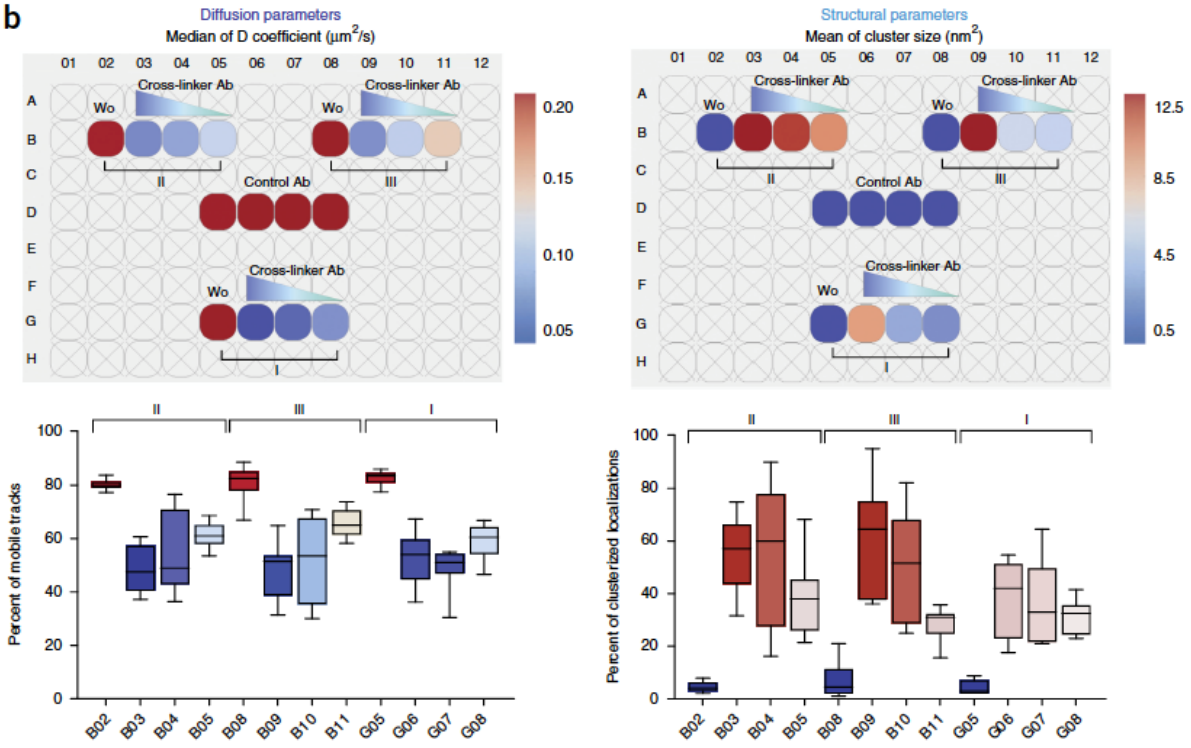

Figure 27. Quantification of dose response effect of Ab cross linker on single proteins mobility. *(a) Induced clustering of membrane receptors was obtained using crosslinker polyclonal anti SEP antibody. 3 concentrations of Ab were tested (1/100, 1/300, 1/1000) and 3 types of acquisition sequence were processed (I. Sequential acquisition; II. Serial acquisition; III. Random acquisition). (b) Graphics representing diffusion and structural parameters of resulting metadata. Heat maps showed perfect correlation between Ab concentration and medians of D coefficient (µm²/s) as well as means of cluster size (nm²). (Adapted from Beghin and al).*

THESIS OBJECTIVE

The HCS-SMLM imaging platform is a versatile and evolutionary tool for drug screening applications which can be applied to various biological applications. Previous work described in the last chapter confirmed its ability to provide qualitative and quantitative information on protein spatial organization and trafficking at the nanoscale level.

Currently, in Sanofi there is a need to align capacities which lead to the selection and nomination of the best candidate to development in a research project. Indeed, screening campaigns for antibodies can generate a large amount of actives. How these compounds interact with their target in living cells is often not yet well characterized. For example, the mechanisms regulating the blockade of T-cell responses by the co-signaling receptors need to be better understood, especially when these receptors are undetectable on naive or resting human T-cells and induced by T-cell engagement in an immune response. Understanding how the spatial organization of receptors and signaling proteins is regulated and how it determines lymphocyte activation and cell fate decisions has become a 'holy grail' for cellular immunology.

In this context, the main goal of my thesis project was to realize the proof of concept that single molecule localization microscopy combined with high content screening approach would improve the comprehension of the mode of action of therapeutic antibodies and their role in immune T-cell activation. The HCS-SMLM would permit to access finer and more precise readouts at the single molecule level, such as proteins spatial nano-organization or trafficking; events undetectable by commercially available HCS-HTS systems which only furnish global readouts. Such information was requested to better understand the differential efficacies of therapeutic candidates targeting PD-1 receptors expressed on T-cells.

The nano-spatio-temporal organization of checkpoint inhibitors after mAbs ligation will help in understanding how it triggers complete lymphocyte activation and how home-made antibodies are acting compared to the benchmark antibodies used today in the clinic or in *in vivo* studies. Here, the use of quantitative super-resolution microscopy will help in the precise delineation of their immunological functions, paving the road for antibody optimization as well as maximizing their functional efficacy. These studies would provide new insights for home-made mAbs characterization for drug commercialization purpose.

This work was a collaborative project between Sanofi's Integrated Drug Discovery department (IDD) and the Quantitative imaging of the cell team of IINS. It aimed at combining both expertise in immune drug screening approaches in immuno-oncology field with quantitative super-resolution microscopy in order to **characterize therapeutic mAbs/receptor pairs nanoscale organization and trafficking at the T-cell surface using HCS-SMLM.**

To answer the thesis problematic, two main Super-resolution-based imaging methods developed in Jean-Baptiste Sibarita's team have been used: 1) The HCS-SMLM imaging platform and 2) 3D-SMLM-soSPIM technique.

First, the HCS-SMLM method was used for the standardized and quantitative evaluation of multiple therapeutic antibodies targeting PD-1 T-cell membrane receptors. Its ability to extract and compare efficiency clustering and dynamics features on several compounds has already been proved. However, the current workflow required several improvements and optimization to access the biological questions such as the automation of the clustering analysis.

Second, where the HCS-SMLM methods brings single-molecule microscopy to a higher quantitative and temporal dimension, the soSPIM technology (described in 1.2.1.4) highly increases the imaging depth capacity. Indeed, 3D astigmatism-based TIRF microscopy applied by our HCS-SMLM approach is restricted to hundreds of μm above the glass-bottom accessing only partially T-cell membrane receptors organization. Thus, soSPIM allowed 3D membrane receptors imaging of an entire T-cell under SMLM conditions. It permitted to image T-cells receptors in more physiological manner without bias of any kind of support or coating. Thus, it provided additional and complementary information to 2D/3D HCS-SMLM experiments. In this context, the 3D-sub-diffracted mapping of receptors of interest required imaging and dedicated software developments.

Both methods exist and have been published (Beghin et al[75], Galland et al[41]). In this context, to assess therapeutic antibodies targeting PD-1 receptors, the HCS-SMLM and soSPIM workflow required further developments regarding T-cells culture, activation and imaging protocols, as well as software developments and pipelines optimization. Technological and biological developments I addressed along my PhD thesis are described in this script.

2. PROTOCOLS AND MODEL DEVELOPMENT

The elaboration of new protocols for immuno-staining and imaging requires the comparison of several biological conditions to be tested in duplicate or triplicate. Multi-well plates (96, 384 or 1,536) are standard supports used in pharmacology which allow significant time saving compared to single condition coverslips. They permit to screen multiple conditions in a single acquisition workflow, and drastically reduce the volumes of reagents necessary for imaging, enabling to save precious and expensive antibodies and imaging buffers.

The main goal of my thesis project is to implement a functional HCS-SMLM platform to test multiple conditions. 96-well plates are the smallest format used in big pharma for drug screening applications. I developed most of the protocols on these 96-well plates. These protocols can be directly adapted to coverslips or larger multi-well plates (Appendix).

2.1. Protocols and model development

2.1.1. Jurkat cells, a human T-lymphocyte cell line

Human primary T-cells are precious and expensive cells extracted from the blood of human donors, and isolated and frozen in vials for use. Various studies done on human healthy donors have shown inter-donor T-cell variations in their capacity to trigger immune responses following activation (Longo et al[113], 2012; Dempsey et al[114], 2014). However, these cells do not proliferate and cannot be "cultivated". We therefore used a Jurkat cell line as T-cell model, which is an immortalized line of human T-lymphocyte cells.

This Jurkat cell line is able to proliferate and to be cultivated over weeks, making them a good simple model for this thesis project. I learned how to manipulate cells in suspension as I am the only one using such cells in the Institute. I adapted the culture protocols to my environment and developed the activation protocols necessary for my experiments. These protocols needed to be robust and reproducible for high content screening experiments.

T-cells are non-adherent cells, contrary of all standard cells used in the labs. They have a round shape and a variable size depending of the cell line. The diameter of Jurkat cells varies between 10 to 20 µm, whereas human primary T-cells are twice smaller, ranging between 7 to 9 µm. Jurkat cells grow in suspension and form clusters of floating cells in the growing culture medium. Healthy growing Jurkat cells are perfectly round and create cells bunches. When isolated or organized in small clusters in the medium, they have some difficulties to grow properly. They are really sensitive to the cell confluence (not lower than $0.2x10^6$ cells/mL and not higher than $3x10^6$cells/mL) and need to be carefully manipulated in order to avoid involuntary activation.

2.1.2. Jurkat cell adhesion

Non-adherent T-cells are commonly fixed on the glass-coverslip via protein coating to be imaged by SMLM using TIRF or HILO illumination. Different kinds of coating exist, some allow T-cell imaging in their resting states (PLL, Fibronectin, etc.), whereas other types of coating have functional properties reproducing immune system interactions (Abs coating).

During the first months of my thesis, I investigated the best way to fix and immobilize Jurkat cells on the glass-bottom of 96-well plates. SMLM imaging requires high-quality 0.17mm thick glass-bottom to be compatible with high numerical aperture objectives. I used a 1.5H coverslip coated and uncoated 96-well plates from Matek Industry (P96G-1.5-5-F).

I first tried to trap them in a "sandwich PAD" of Poly-L-Lysine (PLL) or Agarose (2% and 4%) without success, since this process either killed the cells or did not fix them properly. Then, I tried different well-known coating methods such as a monolayer of Matrigel, Fibronectin and PLL. If Matrigel was really difficult to manipulate in comparison with

fibronectin and PLL, only PLL efficiently allowed to attach the cells to the glass-bottom of the wells. Using transmission light time-lapse imaging, I monitored during several hours the cells behavior on these three types of coatings with a negative control (non-treated glass-bottom). While cells remained alive in all conditions, most of them could not resist to aspiration steps required for the fixation protocols. I observed that only around 1/3 of the cells remained fixed on Matrigel and Fibronectin conditions, in comparison with PLL condition which kept a large number of cells per camera field of view (FOV) attached. Finally, no cells remained on the plastic control condition.

I also compared industrial Poly-D-Lysine (PDL) pre-coated 96-well plates to manual PLL coating on uncoated 96-well plates (Ref. Sigma PLL P2636- mol wt 30,000-70,000). Surprisingly, the industrial PDL coating did not allow to maintain cells on the surface after the fixation and washing steps, and a stable cell seeding could only be obtained after several hours of contact in comparison to about few minutes for manual PLL coating. Unfortunately, the best protocol consisting in manual PLL coating, was not reproducible, whereas immune-staining protocols required more than ten washing steps. This made it necessary to find a more robust protocol to adhere cells onto the coverslip. As a consequence, I decided to evaluate higher molecular weight of PLL (Ref. Sigma PLL P4707 - mol wt 70,000-150,000) to increase the cell interaction. This high molecular weight PLL coating allowed to immobilize Jurkat cells over several washing steps and in a reproducible manner.

Using this final seeding and coating approaches, I managed to seed correctly the cells on the glass coverslip during several tens of minutes, including several steps of washing. I used this protocol to analyze the PD-1 spatial nano-organization by super-resolution imaging and in HCS-like experiment (Appendix).

2.1.3. Jurkat cell activation protocol

We used Jurkat cells as T-cell model to investigate the mechanism of action of PD-1/therapeutic antibodies interaction. It has been reported that Jurkat cells do not, or barely express PD-1 receptors at their membrane surface unless they are activated (Petrovas et al[115] 2009, Yang et al[116], 2008). Contrary of primary T-cells, it seems that Jurkat cells are less responsive to co-stimulatory signal generated by CD28 receptor ligation. It has been questioned if these cells are suitable for the studies of co-stimulatory and co-inhibitory signals due to their infinite cell-cycle (Riley et al[22], 2009). Other studies revealed that the ligation of PD-1 on Jurkat cells, activated by anti-CD3, leads to an inhibition of IL-2 secretion in opposition to controls (Latchman et al[117], 2001), meaning that these cells respond to checkpoint inhibitors, and are therefore suitable for the studies undertaken in this project.

In order to go further with the investigation of PD-1/therapeutic antibodies interactions, I needed to better understand T-cell activation pathways, how they can be properly activated and how the PD-1 receptor expression is modulated. To achieve this goal, I conducted several experiments in order to establish simple, robust and reproducible T-cell activation protocols applicable to Jurkat cells compatible with the single molecule localization microscopy experiments.

Checkpoint inhibitor receptors are induced following *in vitro* T-cell receptors engagement. As described in the introduction, functional anti-CD3 and anti-CD28 antibodies are classically used to activate human primary T-cells. I first performed some preliminary experiments to confirm the efficacy of both antibodies on Jurkat cells activation.

2.1.3.1. Activation of Jurkat cells by CD3 coating

I performed a first assay to validate the Jurkat cells culture protocol using the Vi-CellXR system (Beckman Coulter) which automatically counts and provides viability features information. Jurkat cells' viability, mortality rate and proliferation rate were monitored at each passage during 2 weeks of culture. For 4 passages, I obtained an average of 97.37% of cells viability, a doubling time of 20.7 hours (corresponding to the value found in Cellausorus database), and a diameter of 12.76 µm. These values confirmed that cells were in good condition, validating my culture protocol.

I also evaluated standard T-cell activation protocols on Jurkat cells with the anti-CD3 +/- anti-CD28 coating. Functional antibodies anti-CD3 (clone OKT3) +/- anti-CD28 (clone CD28.2) both at 5 µg/mL have been coated in a 12-well plate with plastic culture treated as negative control. Both antibody clones have been characterized in Sanofi's lab and their activating properties have been confirmed on human primary T-cells. The Jurkat cell cultured on either culture-treated plastic (resting state) or on the two types of activation coatings were followed up for 8 days in culture (Figure 28).

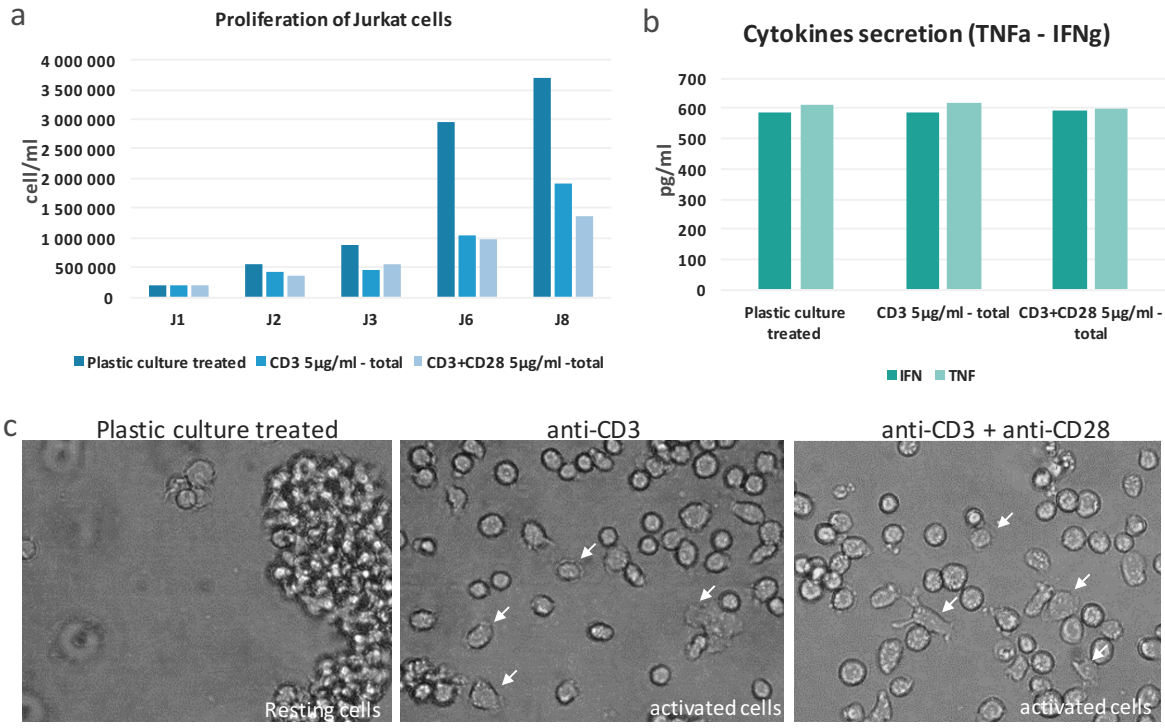

Figure 28. 8-days evaluation on Jurkats's behavior under activation protocols. *Activation of Jurkats T-cells during 8 days using an activating coating consisting of anti-CD3 (5µg/mL) +/- anti-CD28 (5µg/mL). Jurkat cells were observed on plastic culture treated wells as control. (a) Characterization of cells proliferation. (b) Cytokine (TNFa, IFNg) secretion rate measured from supernatants of each condition recovered each culture day. (c) Examples of brightfield image for each condition, white arrow presenting activated Jurkat cells spreading onto the bottom of the plate.*

As observed on an 8-days follow-up, the number of Jurkat cells increased over all conditions (Figure 28.a). However, the lowest cell proliferation rate obtained with antibodies coating conditions were unexpected. We indeed expected a positive difference of proliferation between activated Jurkat cell on anti-CD3 +/- anti-CD28 coatings and resting cells growing on plastic. An increase of these values was also expected on the double activating anti-CD3 + anti-CD28 condition compared to the single anti-CD3 activation, since the double anti-CD3 + anti-CD28 activation is supposed to strongly increase T-cell activation (Figure 28.a).

We hypothesized that since the Jurkat cells are immortalized T lymphocyte cell lines that naturally proliferate in contrast to primary T-cells, their activation may not impact their proliferation (Riley et al[22], 2009). In contrast, the cell morphology clearly changed after activation by anti-CD3 coatings. White arrows on Figure 28.c shows examples of strongly activated cells presenting morphological changes with a complete spreading on the coating. On the contrary, resting cells remained round, in suspension and clustered as expected.

What about the secretion of cytokines which is also expected following T-cell activation? The results indicated that no induction of TNFa or IFNg cytokine secretion was obtained on this experiment compared to the media alone (Figure 28.b). This suggests that the number of cells per well was not sufficient to express enough cytokine to be detectable by the HTRF assay kit. To verify this conclusion, I held a second experiment on a 96-well plate where I measured the cytokine rate of different Jurkat cell densities and under different activation protocols. I seeded Jurkat cells through a gradient of different densities (12,5kC/25kC/50kC/100kC in 200µL) per well, either on poly-L-lysine coated, anti-CD3 coated (5 or 10 µg/ml) or non-coated wells (Figure 29.a). In parallel, I compared two activation protocols: the first one using the already evaluated anti-CD3 coating, and the second one with direct addition of anti-CD3 in the culture media with suspended cells. After four days of incubation, the cytokine rate has been measured from 100µL of supernatants. The results revealed that IL-2 cytokines were only detected on anti-CD3 coated activation conditions (Figure 29.b). Moreover, by comparing the anti-CD3 concentrations as well as the tested cell densities, I concluded that coating by only 5µg/mL of anti-CD3 is sufficient to activate Jurkat cells, and that a minimum density of 50k cells per well is required to detect a proper cytokine rate.

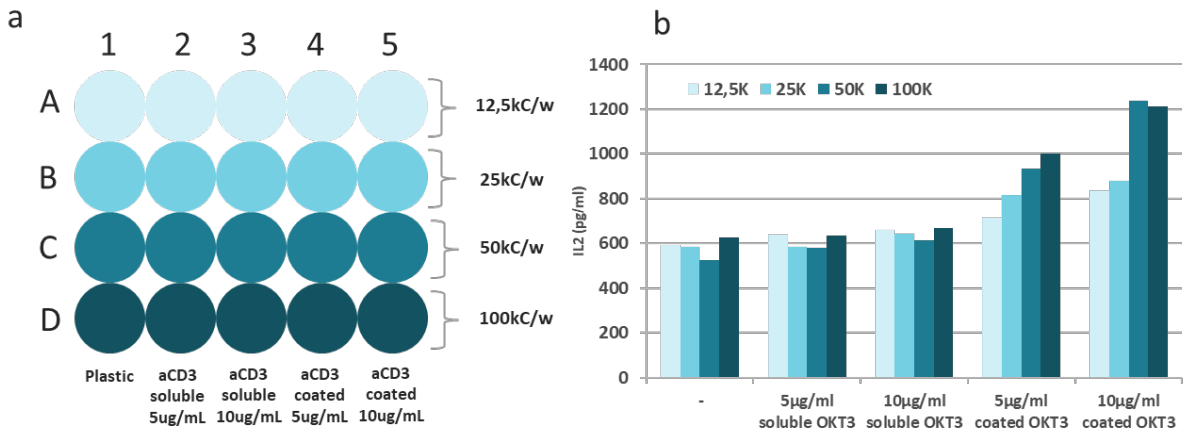

Figure 29. Measurement of IL2 secretion from a 96-well plate experiment. Study of the best cell densities and activating protocols to promote sufficient Cytokine secretion detectable by the Pherastar reader (BMG), a system used in Sanofi to characterize mAbs functionality. (a) Plate map testing gradient of cells density per well, [12.5/25/50/100] thousands of cells per well, over 4 activating conditions, and without activating reagents as control. The activating antibody used was anti-CD3 (OKT3 clone) antibody evaluated at two different concentrations 5µg/mL or 10µg/mL either in solution or coated on plastic wells. (b) After 4 days, 100uL of supernatant was taken from each well and the IL2 cytokine rate was measured for each condition.

Other parameters can be measured to provide more quantitative information on T-cell activation. Calcium release is one of them. Upon T-cell activation, the engagement of the TCR with a tumor-associated antigen of an antigen-presenting cell leads to an immune system activation and induces an intracellular signaling cascade (see Introduction). It results in a cytoskeleton reorganization and a huge increase of intracellular calcium (Ca2+) level (Ostergaard et al[118], 1987; Valitutti et al[119], 1995), which can be used to measure the level of T-cell activation. Several techniques exist to perform such measurement. I used both HCS-

FLIPR calcium assay and ratiometric calcium imaging experiments. They both detect in real time the calcium release by measuring the specific fluorescent intensity shown by the binding of probes to any intracellular calcium molecule present in the cellular cytoplasm. The more the cells are activated, the more the intracellular calcium concentration increases, and the higher is the fluorescent signal.

2.1.3.2. Calcium 5+ assay via FLIPR HTS

I used the high-throughput Cellular Screening-FLIPR platform to quantify the activation of Jurkat cells by addition of anti-CD3 +/- anti-CD28 antibodies in comparison to well-known cellular positive and negative controls. The FLIPR system measures the intracellular calcium release by cells in real time and simultaneously over 384-well plates. It allows the analysis of the compound efficacy in kinetic mode by reagents injections (=events) at precise doses and given times during the live acquisition. Defined reagents were distributed by an automatic pipetting arm system. This automatic workflow permitted the simultaneous comparison of tens of different conditions. Two controls are classically used: i) the Ionomycin is an effective calcium ionophore which triggers a transmembrane calcium influx leading to a strong increase of the intracellular calcium concentration; ii) the Ethylene Glycol Tetraacetic Acid (EGTA) is a chelator molecule trapping divalent cations with a selectively for Ca+ ions. Ionomycin is a non-physiological positive control which can induce a full saturation of the calcium probe, corresponding to 100% "T-cell activation state", whereas EGTA is a non-physiological negative control blocking all Ca2+ ions present in the solution, corresponding to a 0% T-cell activation state. Phytohemagglutinin (PHA- lymphocyte cell cycle stimulator), Thapsigargin (blocking the ability of the cell to pump calcium into the sarcoplasmic and endoplasmic reticula) and anti-CD3 +/- anti-CD28 (physiological T-cell activators) are effective ways to induce lymphocyte activation leading to a calcium release.

Reagents tested (triplicate):	**Cf**
Ionomycin	10μM
EGTA	2mM
PHA	100μg/mL
Thapsigargin	1μM
Anti-CD3 +/- anti-CD28	10/5/2,5/1,25/0,612 μg/mL +/- aCD28 10μg/mL
Anti-PD-1 (Nivolumab)	10μg/mL
Anti-TNP (Nivolumab isotype control)	10μg/mL

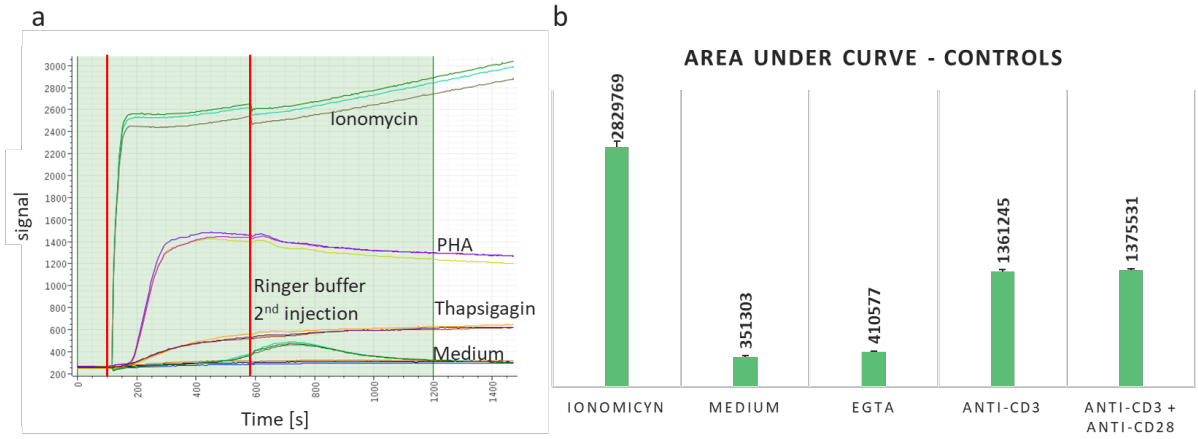

Figure 30. Jurkat cell activation study using Ca5+ on HTS-FLIPR platform. Jurkat cells, labelled with a calcium probe (Ca5+), are activated using different positive/negative controls which modulate the calcium flux released overtime. (a) Ca5+ intensity signal measured overtime (in seconds). Different reagents have been injected automatically on top of cells 4 seconds after the experience started (red line). Each curve corresponds to the Ca5+ fluorescence intensity of one well (i.e. conditions in triplicate). Immediate positive responses from Jurkat cells to Ionomycin, Thapsigargin and PHA are obtained with clearly different modes of action shown by the curve shape. (b) Average of the area under curve (AUC) for each condition.

In a preliminary experiment, the capacity of Jurkat cells to respond to the control molecules was checked. After labelling with a calcium probe, the application of negative and positive controls on top of Jurkat cells, seeded in a PLL-coated 384-well plate, gave the expected results on calcium signal intensity (Figure 30).

In a second phase, a range of anti-CD3 concentrations was injected, and a dose-response experiment was achieved showing a rapid signal increase followed by a slight decrease, as expected (Figure 31). The more the anti-CD3 concentration increases, the more the fluorescent signal rapidly occurs (delay shortened), and higher is the peak response, until a top reached at 5-10 µg/mL. These differences were less visible using the area under the curve calculated on the 0-1200 second period. The time point to obtain the maximal fluorescent signal is reached at 4 min after the injection of anti-CD3 antibody to the cell suspension, meaning Jurkat cells present activation signs rapidly, only a few minutes after CD3 ligation. When a second injection of anti-CD3 at the highest concentration of 10 µg/mL was performed, the intracellular calcium signal did not increase significantly, and no second abrupt increase was obtained except for the curve started at 0.6 µg/ml anti-CD3. These results showed that 5µg/mL of anti-CD3 should be sufficient to fully activate Jurkat cells. Interestingly, the addition of 10 µg/ml of anti-CD28 to the different concentrations of anti-CD3 gave almost the same intensity responses (Figure 31.c), meaning that anti-CD28 does not result in intracellular calcium changes in Jurkat cells. It seems that the anti-CD28 does not affect Jurkat cell activation, confirming our previous data demonstrated in culture experiments.

Finally, we tested the impact of Nivolumab, the antibody blocking the checkpoint inhibitor PD-1 on calcium signaling. As expected, like its isotype control, Nivolumab does not activate alone Jurkat cells, neither modifies the anti-CD3 response, secondarily injected (Figure 31.b).

In conclusion, these results confirmed that Jurkat cells could be systematically activated by a functional anti-CD3 antibody. The final concentration of 5ug/mL was sufficient to reach a strong intracellular calcium flux, and there is no need for additional co-stimulatory signal from anti-CD28.

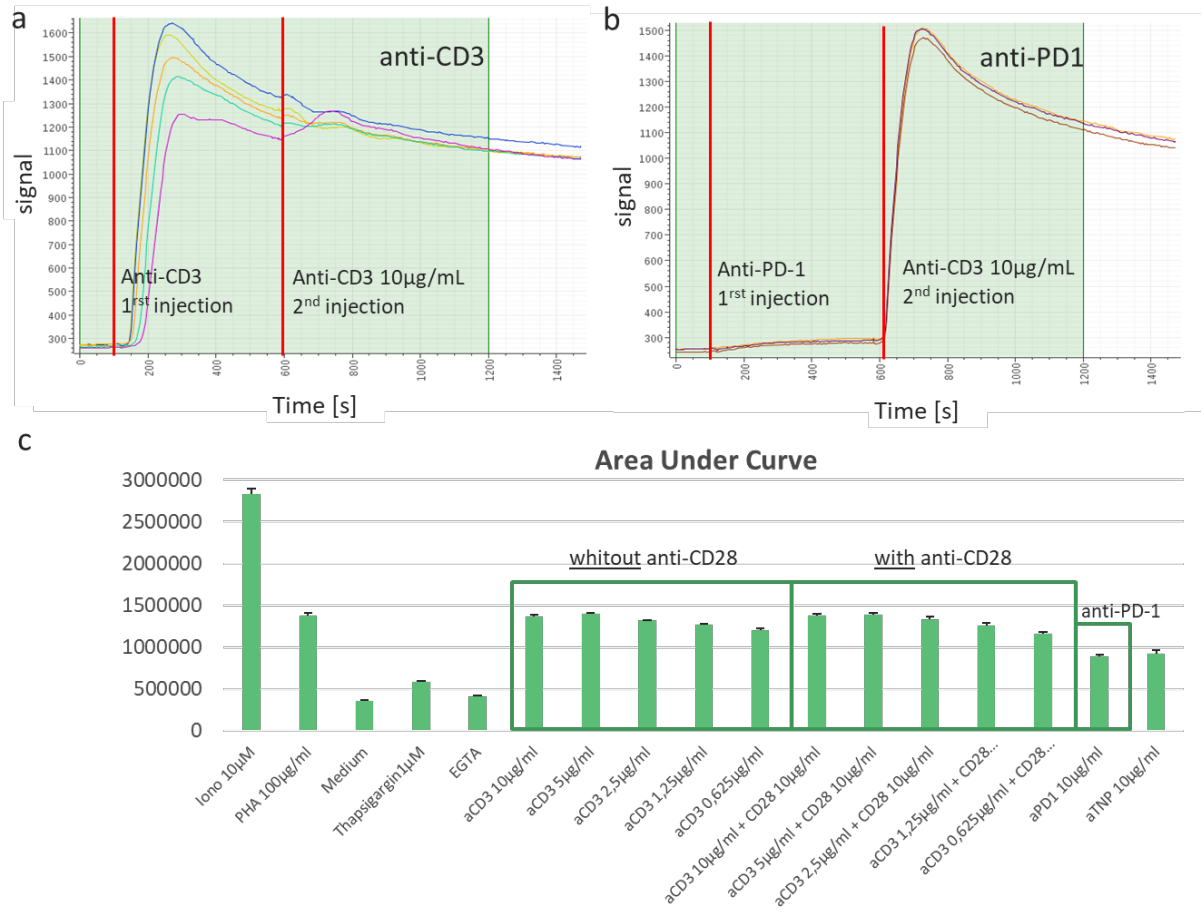

Figure 31. Jurkat cells activation by anti-CD3 mAbs using Ca5+ on HTS-FLIPR system. (a) A gradient of concentration of anti-CD3 [0.6, 1.2, 2.5, 5, 10]$\mu g/mL$ +/- 10$\mu g/mL$ of aCD28 Abs was tested. (b) The therapeutic anti-PD1 mAb Nivolumab and its isotype control were *also* tested to control their effect on Jurkat cell state. Reagents were injected automatically on top of cells 4 seconds after the experience started (red line), and a second injection of anti-CD3 at 10$\mu g/ml$ was applied after 10 minutes to directly compare the activating capacity of each reagent to the most common activating protocols (second red line). (c) Graphs representing the average area under curve for each condition.

2.1.3.3. Calcium imaging using Fura2 via video-imaging

After the investigations done on Jurkat cells at a large-scale level using the HTS-FLIPR system, further experiments were conducted using a video-imaging system which provides single cell information of the calcium concentration on individual cells (Partiseti et al[120], 1994). The video-imaging system is composed on a standard inverted microscope which integrates an x100 objective and sCMOS camera controlled by MetaFluor software. During the experiment, reagents were distributed using a 1mL-pipet on top of PLL-immobilized Jurkat cells labelled with Fura2 calcium probe. The same reagents used for FLIPR experiments were tested (Figure 29). As previously obtained from FLIPR experiments, individual cell activation by positive and negative controls were conformed to the expectations (Figure 32). The analysis of the Jurkat cell behavior under anti-CD3 antibodies stimulation showed a slight but significant increase in individual calcium signal, which was not modified by addition of anti-CD28 antibody (Figure 32.b, c). The analysis taking into account all the evaluated cells confirmed the good consistence of the results between the HTS-FLIPR platform and the video-imaging system (Figures 31.c and 32.c).

To conclude, Jurkat cell line is a good model as the cells were able to reproduce the activation characteristic known for primary T-cells. We used it for the PD-1 characterization by SMLM.

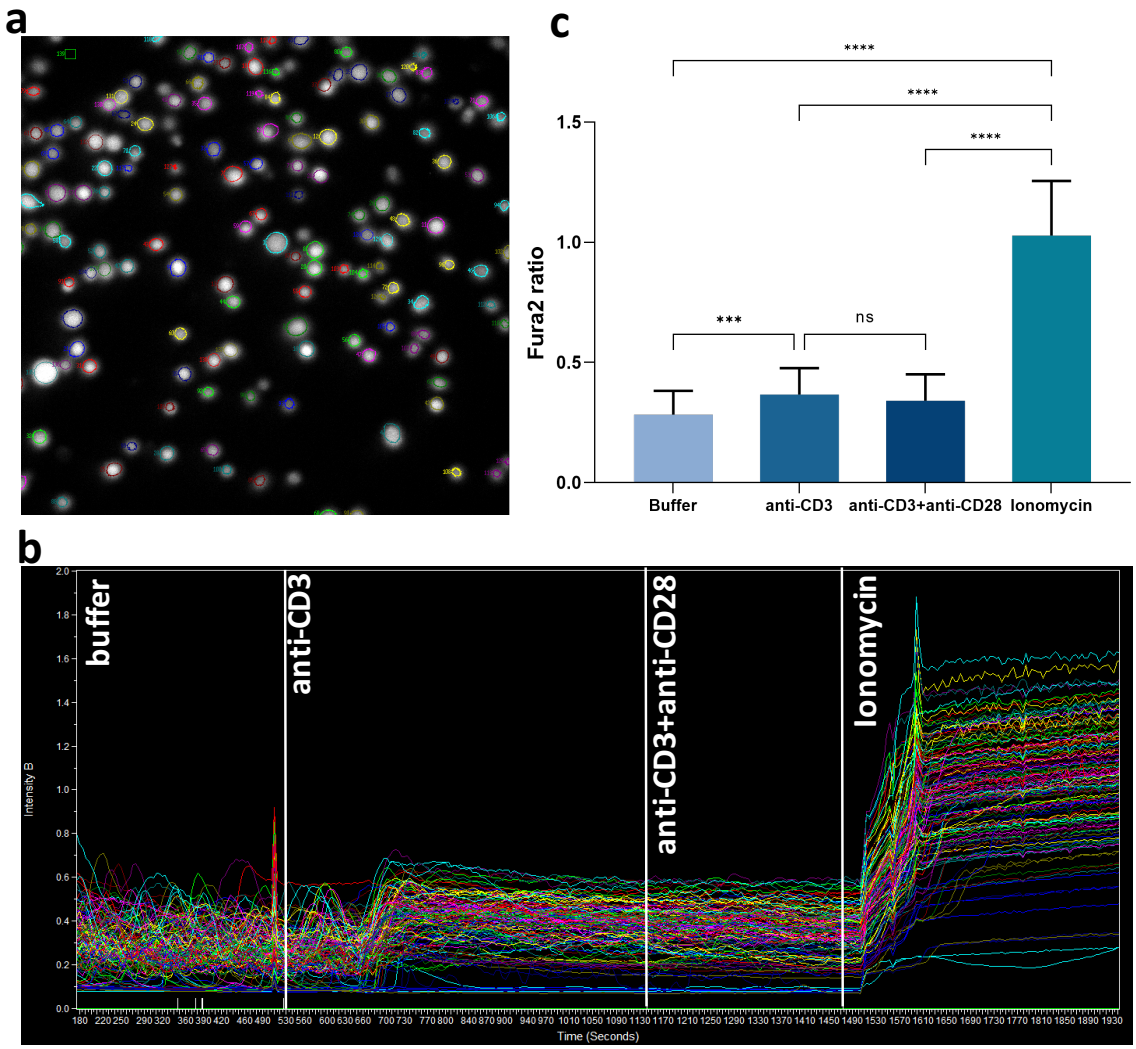

Figure 32. Calcium imaging of individual Jurkat cells using Fura2. *(a) Jurkat cells are first labeled with Fura2 probe, then seeded onto PLL-coated coverslips and imaged via a video-microscope following reagent addition. (b) Online analysis and calcium flux release was measured during live acquisition using MetaFluor software. Each curve represents one cell of the field of view. (c) Graph shows the average Fura2 ratio obtained from resting Jurkat cells in buffer (basal state, n=138, for 6min), after activation by 10µg/mL anti-CD3 (n=123, for 6min) and then 10µg/mL anti-CD3 + 10µg/mL anti-CD28 (n=123, for 5min), in comparison to Fura2 ratio provided by Jurkat cells stimulated by 10µM Ionomycin (n=138, for 8min). Image: 0.2fps. P values were calculated using non-parametric Kruskal-Wallis tests.*

2.1.4. Investigation of the PLL Effect on Jurkat cells

Two recent papers published in 2018, investigated the effect of Poly-L-Lysine coating on T-cell activation. They showed that PLL coating could induce primary T-cell activation and membrane receptors immobilization (Ponjavic et al[34], 2018, Santos et al[121], 2018). This last point highlighted that PLL coating, by preventing receptors to freely diffuse at the surface of T-cell membrane, could induce some bias in the quantification of the PD-1 dynamics by TIRF microscopy (Chapter 3). Since all my further staining and imaging protocols required the seeding of Jurkat cells on PLL surface, I investigated the impact of the PLL on the Jurkat cell activation state. I repeated the FLIPR calcium assay, described previously, on 4 different types

of PLL/PDL (industrially and manually coated at various concentrations). I performed a second experiment, where Jurkat were dropped on different types of PLL/PDL to monitor its effect on cell calcium signal intensity in real time.

The comparison of all the "medium" (buffer) conditions between manually PLL coated 384-well plates and the 384-well plate without coating (culture-treated plastic), showed no apparent cell activation. In contrary, the industrial PDL-coated-384-well Greiner plate induced only a slight cell activation (Figure 33). However, as Jurkat cells were seeded several minutes before imaging, we might have missed any activation effect. So, a second experiment was carried-out, where cells were dropped onto the 4 same 384-well plates in well-containing either ringer buffer, Ionomycin or EGTA for the positive and negative controls (Figure 34). The response to Ionomycin resulted in strong intracellular Ca2+ flow in all the plates as expected, even if we observe larger cell response dispersion for the 384-well plate without coating. In the presence of ringer buffer, the 384-well plate with 5µg/ml PLL and the 384-well plate without coating condition presented a very low Ca2+ level, similar to EGTA treated condition (Figure 33). These signals were slightly higher under 100µg/ml PLL and Greiner PDL-Coated plates, but not significant in comparison to the signals given by the Ionomycin condition. All taken together, these results indicated no activation signals observed from Jurkat cells in contact with different types of PLL coatings.

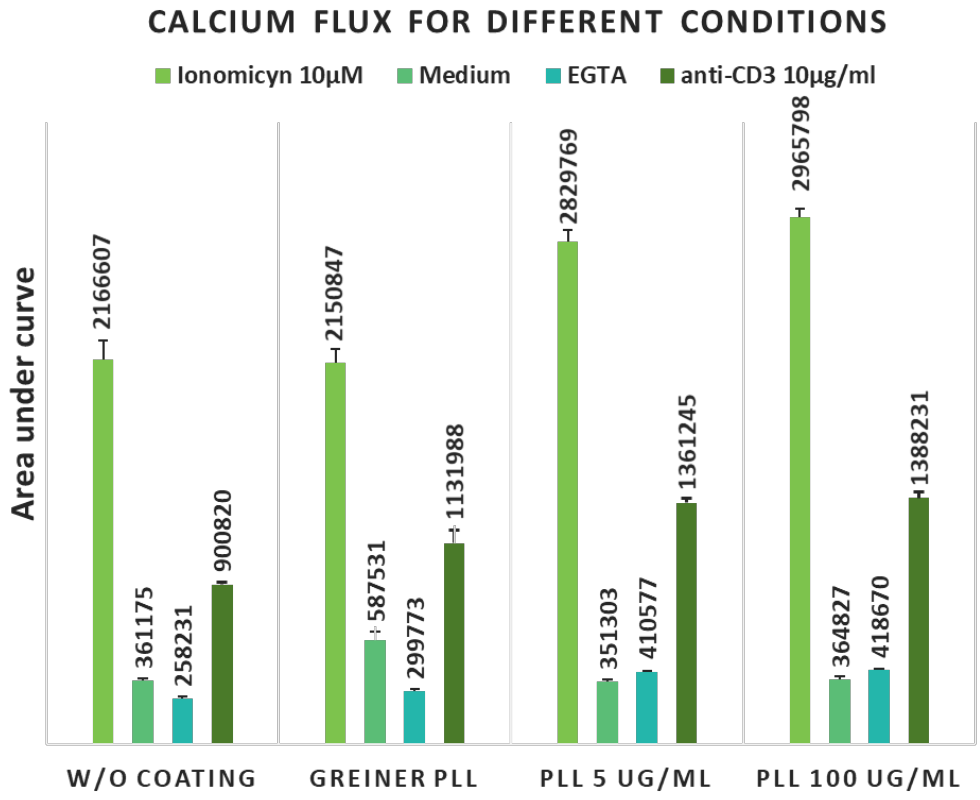

Figure 33. Effect of Poly-L-lysine-coating on Jurkat cells activation measured by HTS-FLIPR Ca5+ assay. *4 types of 384-well plates were used, either industrially PLL-coated (Greiner), manually coated at 5µg/mL vs 100µg/mL or not coated. 4 reagents were tested, Ionomycin and EGTA as positive and negative controls, respectively, anti-CD3 mAbs or medium.*

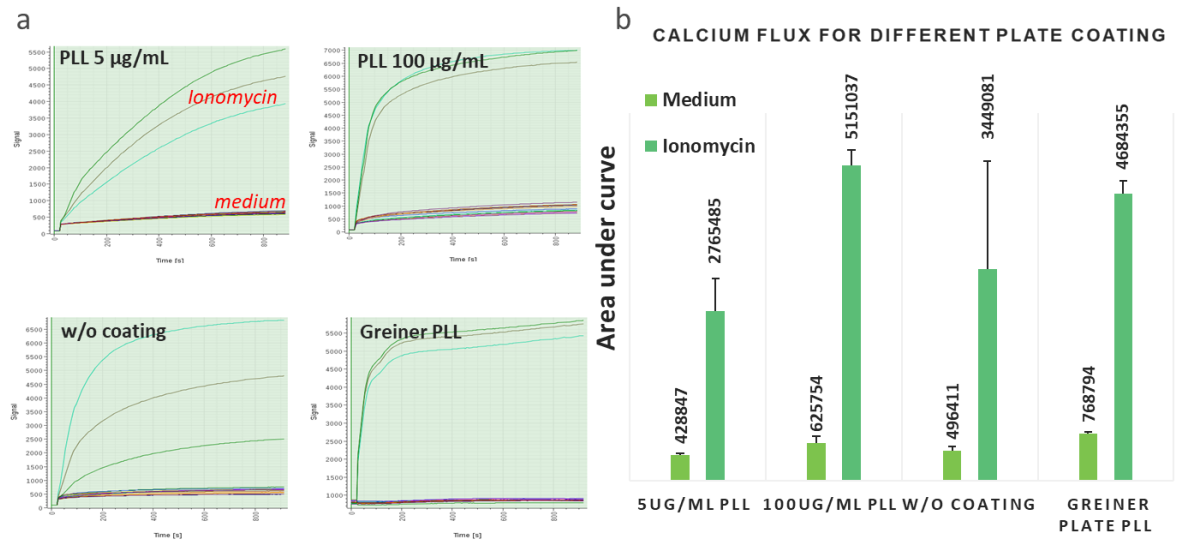

Figure 34. Cell dropping and calcium imaging using Ca5+ on HTS-FLIPR system. *Jurkat cells were dropped into wells from 4 types of 384-well plate (industrial PLL pre-coated, manual PLL coated at $5\mu g/mL$ or $100\mu g/mL$ or not coated). (a) Each well contained either medium or Ionomycin. Each curve represents the Ca5+ fluorescence intensity of one of the 384 wells (i.e. conditions in triplicate). Immediate positive responses from Jurkat cell to Ionomycin can be observed, whereas cells dropped into the medium did not release calcium. (b) To quantify those results, we measured the average of the area under curve (AUC) for each condition.*

To conclude this part, I characterized the Jurkat T-cell activation on anti-CD3 coating and evaluated the effect of poly-L-lysine to anticipate the requirement of the imaging protocols. I validated the Jurkat cell culture, seeding and activation protocols on 96-well plates. I defined two types of coating protocols: 1) an anti-CD3-based activator coating for Jurkat cells activation, which induced intracellular calcium release and IL2 secretion, and should induce the apparition of PD-1 receptors at the cell surface as shown for human primary T cells; 2) a manually PLL coating for the immobilization of Jurkat cells at a resting state at the bottom of the wells for imaging purpose.

2.2. Protocols for SMLM of PD-1 receptors on Jurkat cells

2.2.1. PD-1 receptor labeling strategies

Antibodies, either primary or secondary, are characterized by their type, specificity and affinity to the target of interest. The **specificity** is the accuracy of detection of a target, protein/antigen, avoiding the detection of non-specific proteins. The **affinity** is the binding strength of an antibody to its protein antigen. These properties are essential in imaging because they allow the precise visualization of a protein of interest, while limiting the non-specific labeling leading to background and possible bias in the quantification. This can be a major issue when the density of protein of interest is low, which is the case of T-cell receptors.

2.2.1.1. Therapeutic vs standard primary mAbs

We choose to investigate the PD-1 receptor as a first target. We selected two mAbs anti-PD-1, the Nivolumab and the Pembrolizumab, to study mAbs/receptor behaviors at the nanoscale. Both of them are well-known and well-described in the literature, especially in medicine and clinical assays. Petros Fessas et al[122] (2017) compared the molecular, preclinical, and early clinical studies of both antibodies. Both mAbs target epitopes of PD-1 with high affinity and high specificity. They are both from the same igG4 subclass and are quasi-identical

apart from their variable region. They both showed T-cell activation results and similar early clinical pharmacokinetics data. All these studies allowed us to compare our results with other indirect biological experiments, as well as Sanofi drug screening experiments (Introduction). Several studies performed on PD-1 and associated therapeutic mAb used fluorescence microscopy (1.1.5), but to our knowledge, none have been achieved with super-resolution microscopy.

I first privileged the use of Nivolumab to develop the imaging protocols for SMLM. Indeed, over and above its functionalizing effect on T-cell receptors, this mAb will be used both for its functional properties to address the biological question, or only for its binding function to perform classical fluorescence microscopy via primary-secondary antibodies. In a second time, for the HCS experiments (Chapter 4), I evaluated the Pembrolizumab and compared it with the Nivolumab to quantify any potential effects of therapeutic antibodies on the nanoscale spatial organization and dynamics of PD-1 receptors. In parallel, I used two commercial Abs described for immune-staining applications with non-apparent functional effect as controls (mouse anti-human PD-1, rabbit anti-human PD-1).

2.2.1.2. Labelling strategy for SMLM

In order to monitor the effect of therapeutic antibodies on the nanoscale organization of T-cell membrane receptors, we investigated different labeling strategies adapted to SMLM.

For dSTORM imaging, I initially considered small dyes such as Fab antibodies (50kDa), rather than secondary antibodies (150kDa) coupled with Alexa dyes to improve the resolution of the super-resolution images. However, preliminary studies showed that Fab antibodies lead to some unspecific signal when used at the same concentration than AlexaFluor647 (A647). Conditions using non-therapeutic primary indirectly bound by a standard secondary Abs labelled with A647 have therefore been preferred rather than directly conjugated Abs. Considering that fewer dyes are attached to a single primary Ab conjugated than a single primary Ab attached with several fluorescent secondary Abs, conjugated Abs could provide less localizations per protein, decreasing the dSTORM imaging quality. Nanobodies (15kDa), which could be another labelling possibility, were not considered because such Abs targeting human species are rare or non-existing.

For DNA-PAINT imaging, the use of therapeutic antibodies as primary antibodies couldn't be considered because DNA-PAINT dyes matching with human species are not commercially available. Therefore, we used standard anti-PD-1 Abs from mouse.

For uPAINT imaging, the Nivolumab batch used has been conjugated in the lab with Atto647. We choose the Atto647 dye since it is more photo-stable compared to A647, making it more appropriate for such single molecule tracking experiments. The functionality of this new Ab Nivolumab-Atto647 has been controlled through imaging experiment (labeling efficiency) as well as on its biological property in MLR experiments in Sanofi's lab (Introduction).

Finally, for sptPALM experiments, we used two plasmids coding for human PD-1 and mEos3.2: the mEos probe being linked to PD-1 either at the Nt (mEos-Nt-PD1) or Ct (mEos-Ct-PD1) part of PD-1. Both plasmids were internal to Sanofi (specifically developed for the project) and were not commercially referenced. As preliminary transfection experiments demonstrated a lower rate of cell transfection with mEos-Nt-PD1, I used essentially the human PD-1-Ct-mEos3.2 construct.

2.2.1.3. Optimization of the immuno-staining protocols

Non-specificity of biological event is mostly caused by antibodies binding to the wrong target. Hundreds of immuno-staining protocols exist, each of them being suitable for a specific

biological application, a specific target of interest and a specific fluorescent microscopy technique. A given protocol can lead to poor results and unspecific signals when applied in a different biological context or different microscopy approach. The main parameters which vary from one protocol to another are: i) the incubation time of antibodies, ii) the incubation temperature, and iii) the Abs concentration. To optimize staining protocols and avoid non-specificity, the main recommendations are:

- The use monoclonal Abs as much as possible.
- The blockade of non-specific sites using bovine serum albumin (BSA) with or without biotin or another blockade solution.
- The use of detergent (e.g. TWEEN20, Triton, etc.) can be employed to remove extra antibodies attached to the coating or the glass-bottom of the imaging support.
- Avoiding cross-reactivity from different antibody species, especially in the case of multicolor imaging implying multiple labeling.
- The removal of secondary antibody aggregates before their application on cells (strong centrifugation).
- Reducing the auto-fluorescence coming from the medium or the cells by using adapted imaging buffer, cell membrane clarification protocols, or photo-bleaching.
- Increase the number of washing steps as much as possible to avoid non-specific fluorescence.
- The choice of adapted secondary antibodies fluorophores to prevent the overlapping between excitation and emission spectra.
- Avoiding the incubation of antibodies on cells under extreme conditions of duration, temperature and concentration.

I struggled a lot with non-specific signals coming both from therapeutic antibodies and immuno-staining protocols. Indeed, I used to incubate a too high concentration of primary antibodies over a too long incubation time on my cells at 37°C. The combination of those extreme conditions ended to string non-specific signals on the Jurkat cells, corrupting the single-molecule analysis.

In addition, months after validating the staining protocols, it turned out that the OKT3 antibodies used as a coating for Jurkat cells activation degraded within few months. This unusual degradation generated a strong unspecific background coming from its affinity with anti-Human A647 Abs (Figure 36). I tried several solutions to prevent A647 to non-specifically bind to the coating or to remove them after the staining. I first tried different concentrations and incubation times of several blockade solutions such as BSA, milk, western blot buffer. Second, I tested the combination of BSA +/- 5% of Goat serum, which is the same species as the anti-Human A647 Abs. Finally, I tested different reagents to remove extra Alexa disposed onto the coating such as Triton +/- 0.01% of SDS. None of these conditions succeeded in reducing efficiently the background signal compared to the negative control without A647 incubation (Figure 35). The best option I found was to use a new OKT3 vial for each experiment. The remaining non-specific signal may lead to some issue in the quantitative analysis of SMLM data.

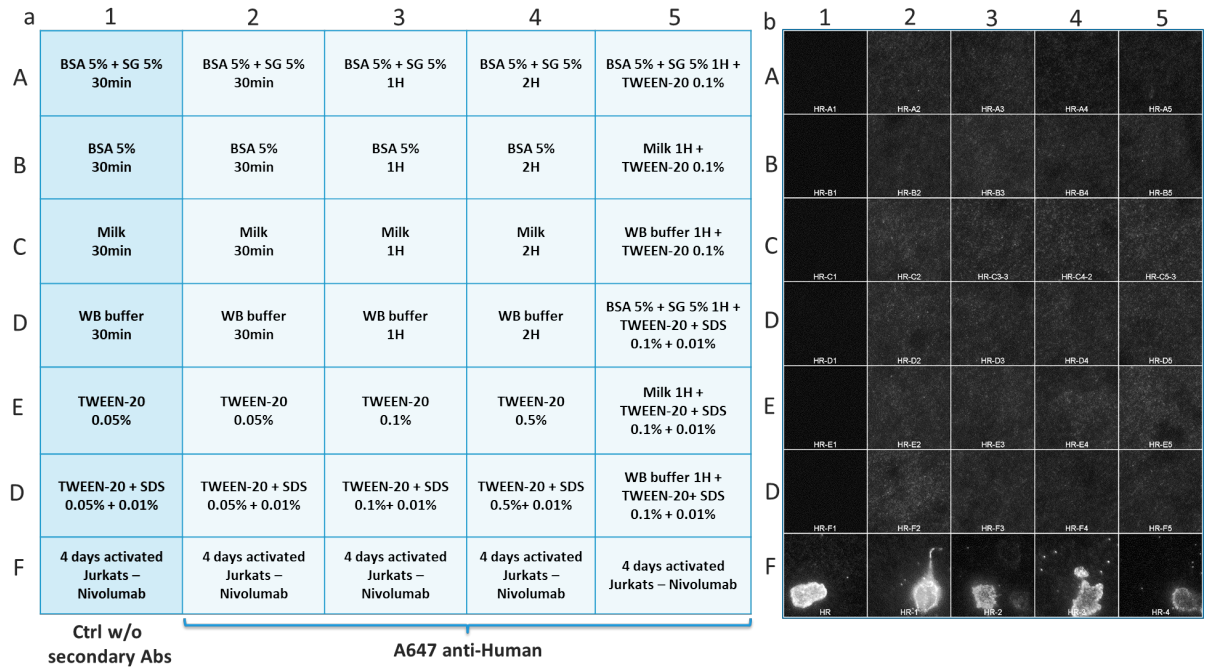

Figure 35. Development of new blockade protocols*. To overcome background issues due to A647 affinity with anti-CD3 Abs coating, different blockade solutions were tested: PBS-BSA +/- of goat serum (SG), Western Blot blockade buffer (WB buffer) or Milk at various incubation times on wells containing Jurkat cells activated by adhesion for 24h onto CD3 coating on a 96-well plate. (a) After blocking steps, wells were incubated with 1/10000 of A647 for 1h at RT and then wells were rinsed 3 times with PBS or TWEEN-20 +/- SDS at various concentrations. (b) Representative images of each condition defined in (a) with negative control on the left column and positive control at the bottom row (TIRF images, 635 laser, 256*256pxl).*

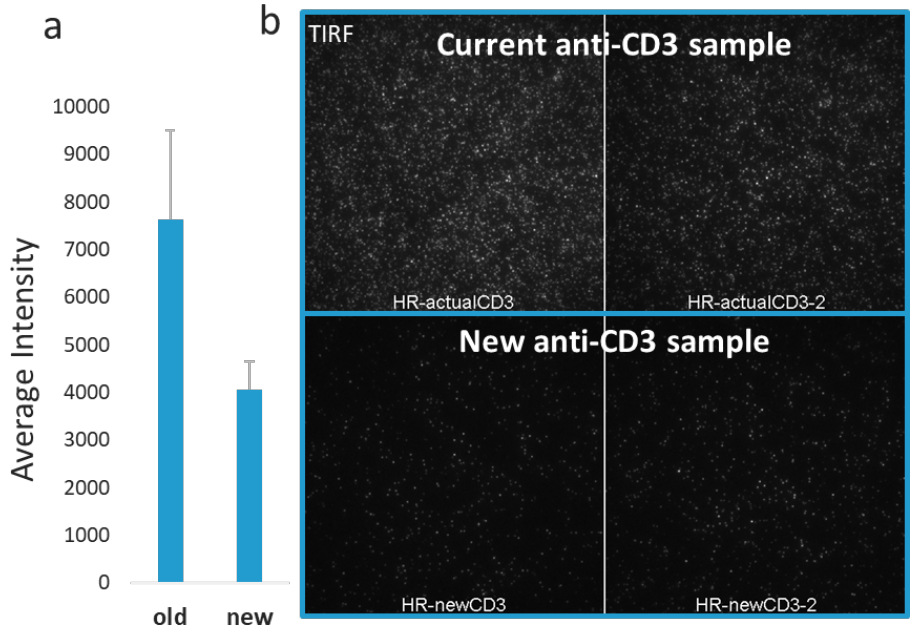

Figure 36. Background investigation*. Wells were coated with anti-CD3 Abs from new non-opened samples and a 2 months old sample. After a blocking step using PBS-BSA 5% for one hour, A647 anti-Human were incubated for one hour at RT. (a) Average intensities measured from images in (b). TIRF images using 635 laser, (256*256pxl). The average intensity of the background signal from a coating made with a fresh and new anti-CD3 sample is almost 2-fold lower than the old one. The high background signal may be linked to the degradation of the anti-CD3 Abs occurring over time.*

In addition to optimizing the labelling protocol, it is crucial, for each experiment, to validate the fluorescence signals obtained from the structure of interest with several negative and positive controls. Different preliminary control experiments were required for my study, i.e. specificity, imaging and T-cell activation protocols. Isotype controls were exploited as negative controls of the specificity of primary Ab (Figure 37). An isotype control is a primary Ab that lack specificity to the target but matches the host species, the class and subclass (isotype) of the tested primary Ab, and which is used at the same working concentration as the primary antibody. Its use allows to brings to light the fluorescence resulting from non-specific Fc receptors binding and other non-specific cellular proteins. To control the specificity of secondary antibodies, cells are stained using only the secondary Abs without any primary Abs (Appendix).

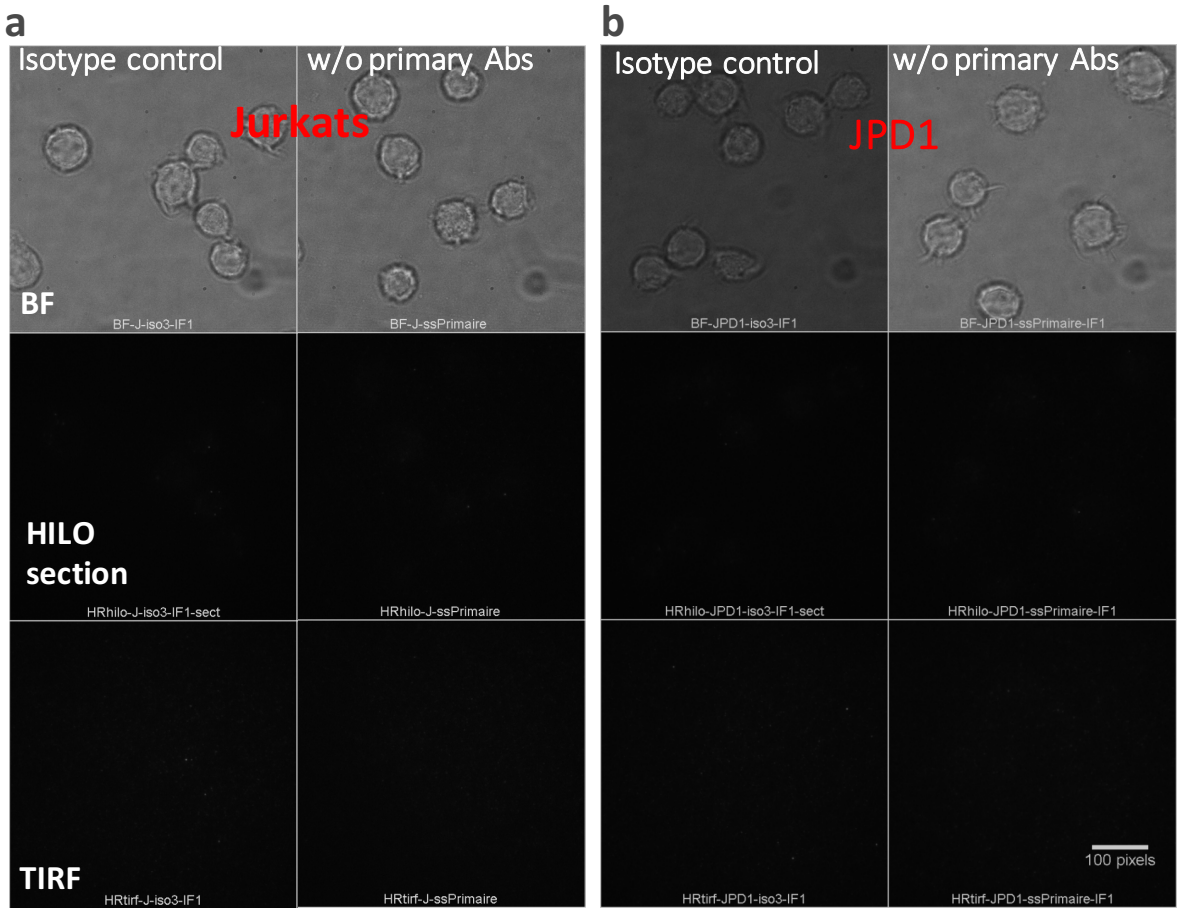

Figure 37. Control of immunostaining protocols*. The immunostaining protocol was applied to native Jurkat cells (a) and to a Jurkat cell line expressing human recombinant PD-1 at their surface (JPD1) (b). Cells were stained following the protocols described in Appendix. To control the specificity of primary antibodies, isotype control was used instead of primary antibodies (left panel). To control the specificity of secondary antibodies, cells were stained without primary antibodies (right panel). Bright-Field images (top), high resolution images (635 laser, 512*512pxl) (middle), and high-resolution images of cells at the glass-coverslip interface (bottom) were acquired respectively in Bright-Field, HILO and TIRF illumination (635 laser, 512*512pxl).*

2.2.2. Protocols for PD-1 and CD3 receptors fluorescence imaging

As a model and control, I used the well-known and widely described **CD3 T-cell membrane receptor**. The cluster of differentiation CD3 is a member of the complex TCR-CD3, which plays a key role in T-cell activation by generating downstream intracellular signaling events. Its nanoscale organization has been reported in the literature using several microscopy techniques, ranging from classical fluorescence microscopy to SMLM (Introduction, Figure 9).

Publications reported that CD3 is randomly and homogeneously distributed on the membrane at the resting state of T-cells (Rossboth et al[95], 2018). It aggregates at the immunological synapse, forming clusters upon T-cell activation. Such protein aggregation process appears between 10 min to 8 hours after T-cell activation through TCR/CD3 activation using functional Ab coating or functionalized SLB (20 min – Rossboth et al[95], 10 min – Pageon et al[92], 8h – Zhong et al[123]). All these studies were performed using high resolution TIRF microscopy, and dSTORM and PALM single molecule-based super-resolution microscopy (Figure 9).

I used this well-studied model as a control to validate my culture and staining protocols for SMLM microscopy on T-cell membrane receptors. The fluorescence signal obtained on the CD3 receptors on resting Jurkat cells was then compared to the signal obtained for PD-1 receptor (Figure 38, 39). Similarly, CD3 clustering during the early step of Jurkat cell activation was used as positive control of T-cell membrane receptor clustering, and compared with PD-1 cluster analysis (Chapter 4).

The PD-1 model development has been initially tested on a commercial **PD-1 recombinant Jurkat cell line (JPD1),** which constitutively overexpresses PD-1 at the membrane before being tested on activated Jurkat Jurkat cells for which the PD-1 expression is induced by cell activation. Indeed, JPD1 cell line express natively PD-1 in the resting state, making these cells easier to use in routine for the development of the quantitative super-resolution imaging pipeline.

In order to validate the first step of culture and staining protocols, I compared the fluorescent signal obtained for the staining of CD3 on resting Jurkat cells, with PD-1 receptor on resting JPD1 cells and after 4 days of Jurkat cell activation (Figure 38, 39). The protocols described in the Appendix included all the details on the different coatings, cell viability and seeding, immune-fixation and immune-staining (Appendix). Once the best conditions determined, super-resolution microscopy and quantitative analysis of the nanoscale organization were performed on CD3 and PD-1 receptors.

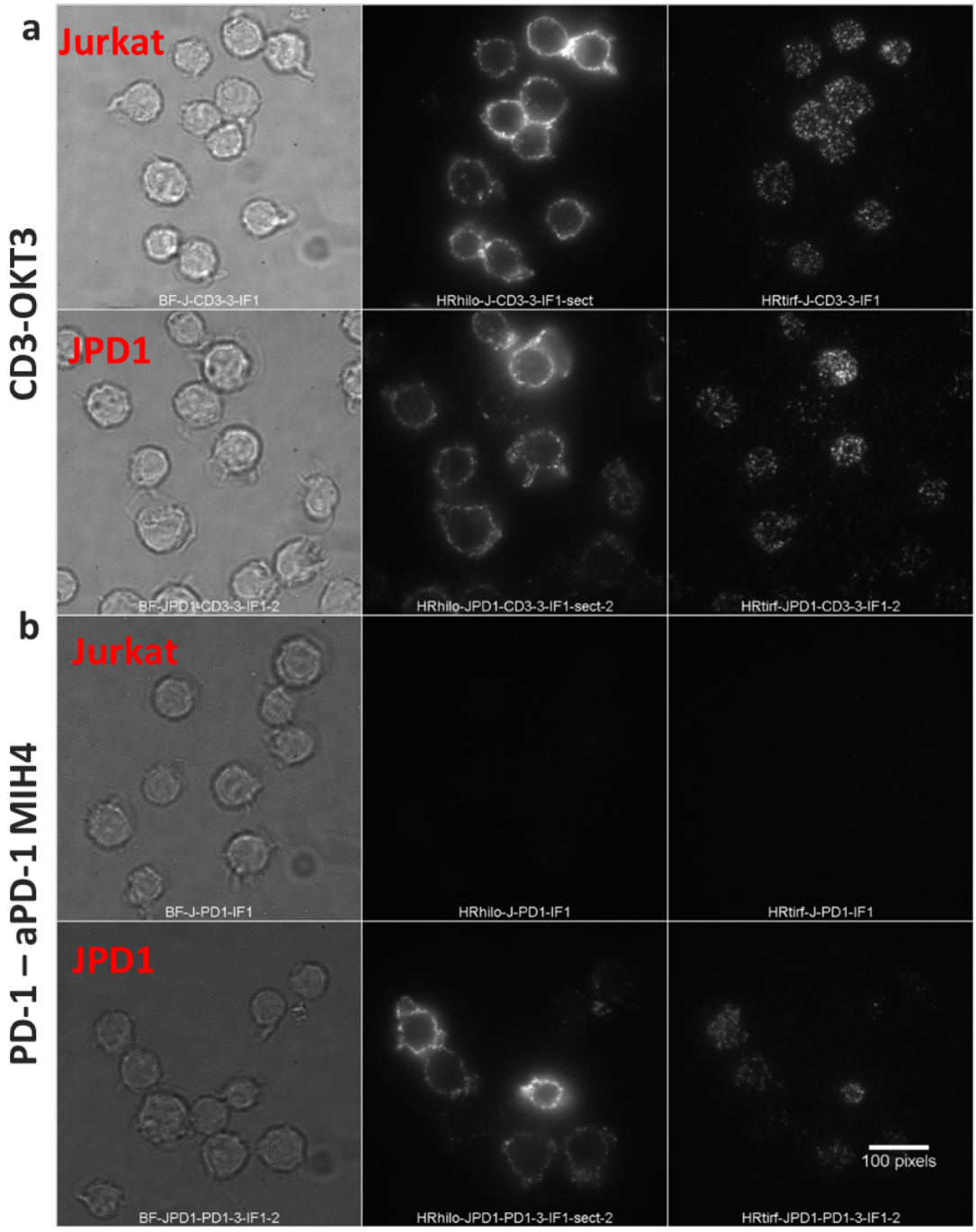

Figure 38. Visualization of PD-1 and CD3 receptors at the Jurkat cell surface. *Native Jurkat cells and PD-1 recombinant Jurkat cells (JPD1) were seeded on PLL and stained by anti-CD3-OKT3 and anti-PD-1 clone MIH4. (a) CD3 receptor distribution at the membrane surface was similar for both cell types. (b) Resting Jurkat cells did not express PD-1 in contrary to JPD1 cell line. Bright-Field images (left), high resolution images (635 laser, 512*512pxl) (middle), and high resolution images at the glass-coverslip interface (right) were acquired respectively using Bright-Field, HILO and TIRF illumination (635 laser, 512*512pxl).*

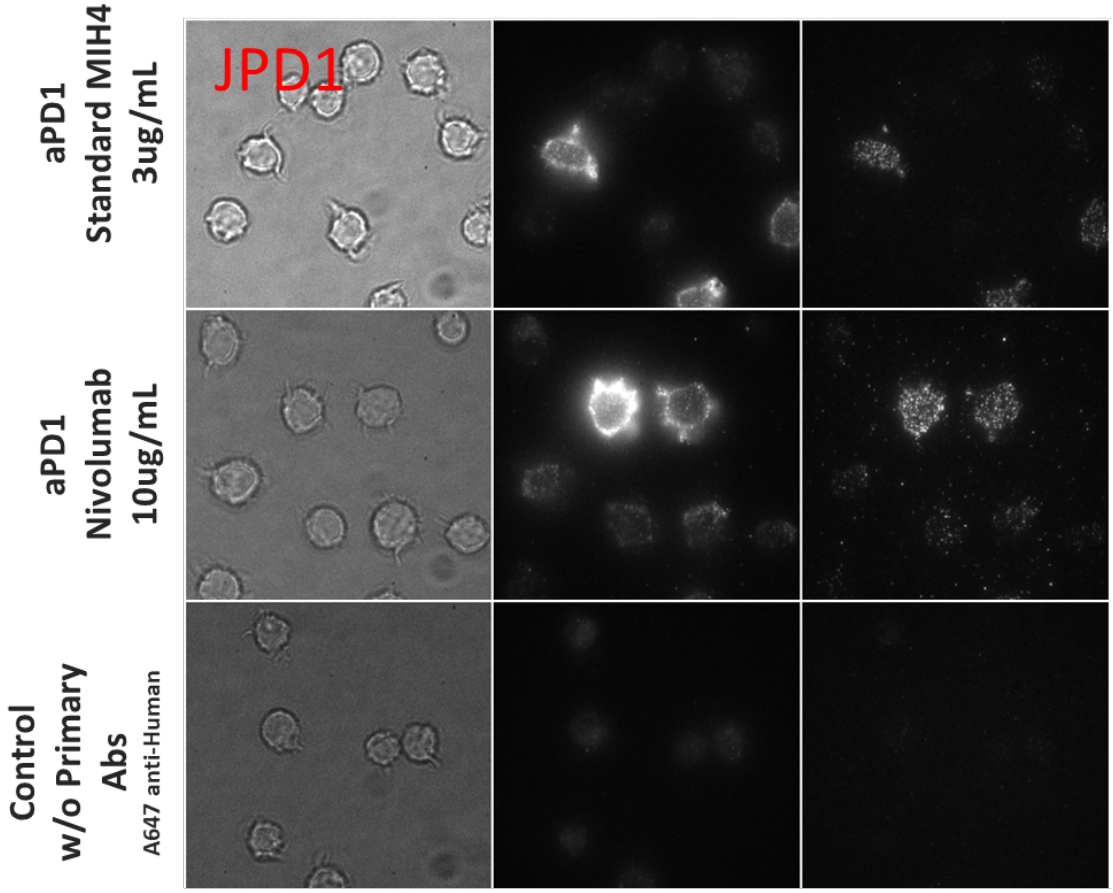

Figure 39. Detection of PD-1 receptors on JPD1 using standard vs therapeutic anti-PD-1 Abs. PD-1 receptors on the PD-1 recombinant cell line (JPD1) were stained by Nivolumab, a functional antibody, or by anti-PD-1 MIH4 Abs. PD-1 receptors distributions are similar using both type of Abs and present homogeneous and random distributions of receptors at the JPD1 membrane (right panel). Bright-Field images (left), high resolution images (635 laser, 512*512pxl) (middle), and high-resolution images at the glass-coverslip interface (right) were acquired respectively using Bright-Field, HILO and TIRF illumination (635 laser, 512*512pxl).

3. 2D & 3D Jurkat PD-1 receptor organization and dynamics at the single cell level

Checkpoint inhibitors of the immune response, PD-1 receptor, plays key roles in immune tolerance, auto-immune diseases as well as tumor progression. A better understanding of its mechanism of action would lead to new pharmacological approaches and more efficient treatments. The literature is rich on this topic, but only a few studies have been done so far on the function of PD-1 receptor at the membrane level. In my project, prior doing HCS-SMLM, I investigated the spatial nanoscale organization and dynamics of PD-1 receptor, at the single cell level using several SMLM approaches. PD-1 organization at the membrane of Jurkat cells was first investigated on fixed cells, in 2D and 3D by dSTORM and DNA-PAINT super-resolution microscopy techniques. Then, I explored sptPALM and uPAINT single particle tracking methods to quantify the PD-1 dynamics on living Jurkat cells. After PD-1 nanoscale organization and dynamics characterization, I investigated the impact of the therapeutic mAb Nivolumab on fixed and living Jurkat cells. We used these results to calibrate potential readouts for the high content screening experiments of anti-PD-1 therapeutic mAbs.

This chapter describes the single cell quantitative analysis of PD-1 nanoscale organization and dynamics by SMLM, at the basal cell surface by TIRF illumination, and at the whole cell level using light-sheet illumination.

3.1. Study of PD-1 receptors spatial organization using SMLM

3.1.1. Characterization of PD-1 expression at the membrane surface of Jurkat cells

As explained in the Introduction and Chapter 2, PD-1 receptors are expressed on the surface of activated T-cells. The kinetics of PD-1 expression on Jurkat cells is not plainly described in the literature. Some publications described a PD-1 expression observed on primary T-cells after a few hours to a few days of activation (Francisco et al[21], 2011; Iwai et al[124], 2017). On the other side, Yang et al[116] (2008) reported that 70% of the Jurkat cells express PD-1 receptors after 48 hours of activation. Investigating PD-1 expression kinetics on our cellular model was primordial prior SMLM quantitative analysis. This study was conducted in 96-well plate, in which Jurkat cells were activated between 30 minutes to 96 hours (4 days) via anti-CD3 coating. Cells were then fixed and PD-1 receptors labeled using Nivolumab as primary anti-PD1 mAb combined with A647 as secondary fluorescent mAb (Appendix). Here, Nivolumab was used only as a detecting Ab. The same staining procedure applied to Jurkat cells seeded for 96 hours on a non-activating coating (PLL coating), resulted in the absence of PD-1 expression at the membrane surface (data not shown), confirming the signal specificity. High-resolution TIRF (HR-TIRF) image analysis revealed different levels of receptor expression (Figure 40.a). To compare the level of expression between the different incubation times, I measured the average fluorescent intensity for each cell detected from brightfield images (circles in Figure 40.a). For this analysis, at least 14 cells were evaluated by time point. Interestingly, PD-1 receptors were detectable on Jurkat cell surface 4 to 8 hours after activation by the anti-CD3 coating. Then, a slight decrease in PD-1 expression could be observed between 12 to 24 hours, followed by a plateau until 96 hours. This kinetic of PD-1 expression at the Jurkat cell surface was non-linear, certainly due to the heterogeneous expression observed at each time point (Figure 40.b), as illustrated on HR-TIRF images (Figure 40.c).

I then investigated several activated cells from the same experiment by 2D dSTORM, and analyzed them to identify the clusters and extract the number of localizations per cluster, clusters area (nm^2) and the cluster density (cluster/μm^2) per cell. The statistical analysis of these parameters demonstrated no significant difference between all the time points (1-4

days of activation) on the number of localization and cluster area. However, a strong variability was observed on the cluster density parameter (Figure 41). These results indicated that the Jurkat cells were able to respond to the anti-CD3 coating by increasing PD-1 expression at their surface. Surprisingly, PD-1 expression was highly heterogeneous between Jurkat cells. In particular, a proportion of Jurkat cells did not express PD-1 receptors at their membrane or did not responded to the anti-CD3 coating. One potential explanation is that, as an immortalized cell line, this Jurkat cell line proliferates constitutively which could impact its ability to express PD-1. These observations strongly suggested the need to work later with primary T-cell for validation.

In summary, these first experiments indicated that activated Jurkat cells could be imaged from 8 hours to 4 days after activation, and that there was a global heterogeneity of PD-1 expression on activated cells. From these results, further experiments were conducted on 24 hours and 4 days activated Jurkat cells to determine the PD-1 nanoscale receptor organization, and measure the therapeutic mAbs effects on cells, considering these two-time points as an early and late activation phase, respectively.

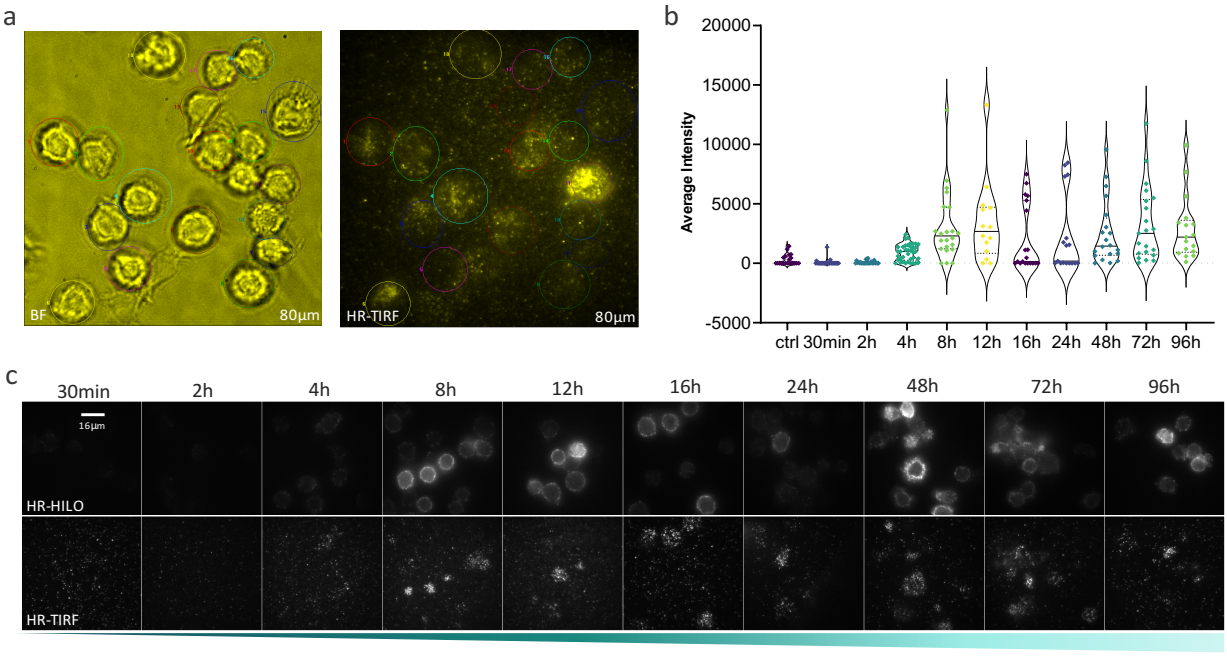

Figure 40. PD-1 expression time-scale on activated Jurkat cells. *Jurkat cells were seeded on an anti-CD3 coating in a 96-well plate between 30 min to 4 days before fixation. (a) Example of resulting bright field (BF) and high-resolution TIRF (HR-TIRF) images of the same FOV (80µmx80µm, Nivolumab-A647). Cells were manually segmented from the BF images. Then, ROI were duplicated on the HR-TIRF images and the average intensity of each cell analyzed (b). (c) Time evolution image gallery of PD-1 expression from 30 min to 4 days. The first line represents the HR-Hilo images of the middle of the cell. The second line represents HR-TIRF images of Jurkats membranes (Nivolumab-A647).*

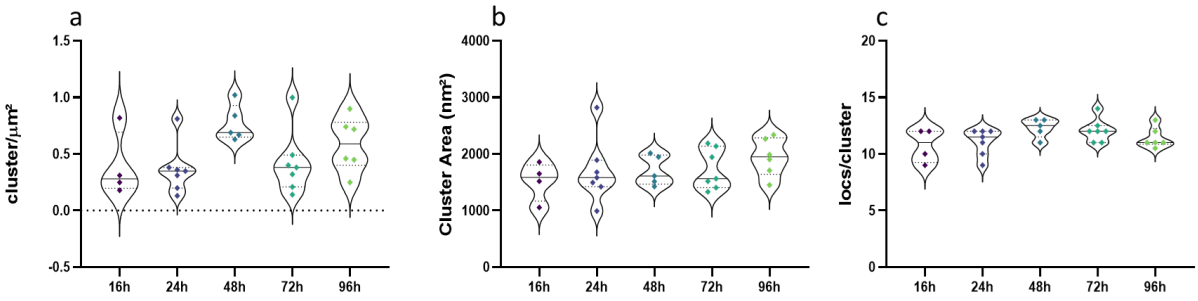

Figure 41. Quantitative analysis of PD-1 clusters on 2D dSTORM images of Jurkat cells at various activated states. *Jurkat cells were seeded on an anti-CD3 coating in a 96-well plate from 16h to 4 days before fixation. dSTORM imaging was performed for each activation time, followed by single molecule localization and cluster analysis. (a-c) Three clustering features were investigated: the number of clusters per µm² (left), the cluster area in nm² (middle) and the number of localizations per cluster (right). Each point represents the median of one cell cluster distribution. Dark lines represent medians obtained from all cells for each condition. (n=6, 4 days; n=7, 3 days; n=5, 2 days; n=7, 24h; n=3, 16h). (dSTORM: 635 Laser, 15,000fr, 50fps).*

3.1.2. 2D&3D quantification of PD-1 spatial organization by dSTORM

On these experiments, PD-1 receptors were first imaged using 2D dSTORM to characterize their spatial nano-organization at the membrane of activated Jurkat cells, hundreds of nanometers above the coverslip using TIRF microscopy. Following 2D dSTORM acquisition, single molecules were localized using PALMTracer software, and the resulting localization coordinates were analyzed by SR-Tesseler software for cluster quantification (Introduction). Practically, PD-1 clusters were segmented using a threshold based on the local localization density, and clustering features were extracted for each cell (Figure 42.d,e). There is two ways to measure the size of clusters of localization in SR-Tesseler software. It can be measured either using the principal component analysis (PCA) based on the localization distribution, or directly from the segmented polygons area (Figure 42.e). To standardize the quantification, we focus our clustering analysis using the second option. 2D dSTORM images revealed isolated and randomly distributed PD-1 clusters of homogeneous size (Figure 42). We measured clusters with a median value of 10-15 localizations per cluster, and a diameter of 35-60 nm per cluster, proving more structural information of PD-1 receptors organization than classic fluorescent microscopy (Figure 42.c, d, zoom).

To deeper characterize PD-1 organization, I performed astigmatism-based 3D dSTORM, providing access to PD-1 membrane receptors at up to 1µm above the coverslip. The resulting images globally revealed a similar organization pattern of PD-1 compared to 2D dSTORM data. We could however notice some cavities (white arrows, Figure 43) inside the Jurkat cells, which were probably due to membrane ruffling onto the activator coating (Ponjavic et al[34], 2018). These observations were made on native Jurkat cells (Figure 43-right) and on the Jurkat cell line constitutively expressing human PD-1 (JPD1) (Figure 43-left).

In order to better understand PD-1 organization upon cell activation, I conducted experiments aiming to observe the impact of anti-CD3 activation on the spatial re-organization of PD-1 receptor. We expected PD-1 receptors to present specific patterns of organization upon cell activation, such as receptors aggregation surrounding CD3 clusters upon cell activation. To this end, multicolor imaging experiments were carried out to image both CD3 and PD-1 receptors on this recombinant cell line. To induce JPD1 activation, CD3 receptors were recruited by antibody cross-linking via primary and secondary antibodies complexes for 30 minutes on the living cells. Different ratio of secondary antibodies A532 over unconjugated anti-CD3 mAb (2 or 4 times) were used for JPD1 cells activation (data not

shown). dSTORM super-resolution imaging was performed on PD-1 receptors and overlayed with high-resolution TIRF images of CD3 (Figure 44). Unfortunately, dSTORM reconstruction of CD3-A532 acquired for this experiment did not reach the required quality to be analyzed. However, HR-TIRF images were sufficient to conclude on the spatial organization of PD-1 according to CD3 clusters, showing no apparent co-localization, clusters formation or PD-1 re-organization upon Jurkat cells activation. Images revealed no particular receptors aggregation or clustering around CD3 clusters induced by crosslinking. PD-1 cluster density seemed lower in CD3 clustering area which could also explain the presence of cavities observed in 3D dSTORM images. All these observations were supported by the qualitative analysis of 8 cells.

To confirm such observations, I conducted SMLM experiments on living cells to access finer kinetics and possibly observe any changes on PD-1 receptor nanoscale organization upon T-cells activation. I used single particle tracking technique, such as sptPALM, to capture PD-1 receptors dynamic behavior upon cell activation in real time (data not shown).

Altogether, these results validated the immunostaining and acquisition protocols for 2D and 3D dSTORM imaging of PD-1. Both 2D and 3D dSTORM reconstructions of JPD1 cells on an activating coating showed similar well-distributed homogeneous single-molecule clusters. The labeling density looked appropriate to detect PD-1 clusters, despite a weak number of localizations per cluster. We validated these imaging protocols for further HCS-dSTORM experiments.

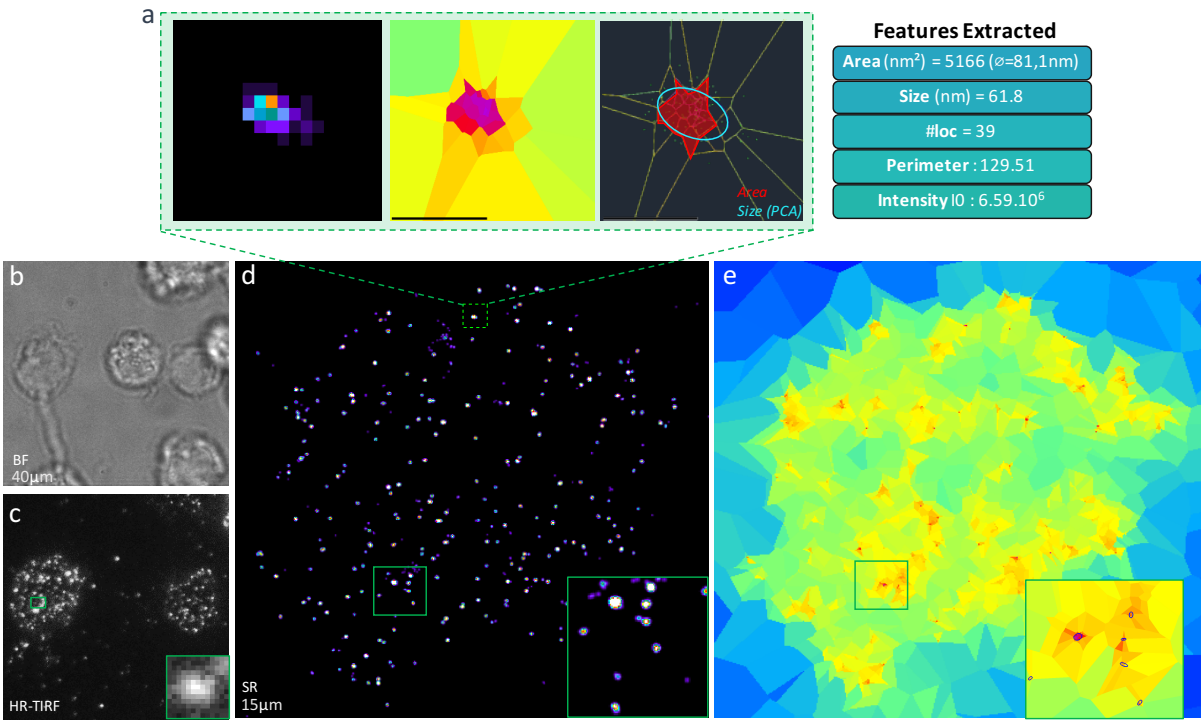

Figure 42. ***SR-Tesseler quantification of PD-1 nano-clusters.*** *Examples of PD-1 nano-clusters analysis using SR-Tesseler software based on Voronoï-Tesselation. (a) Zoom of a single cluster acquired by 2D-dSTORM. The cluster area is computed from the Voronoï polygons segmented using a density factor threshold of 2. Diameter = 81 nm; #loc = 39; Intensity (sum of integrated intensities of localization contain in one cluster) I_0 = 6.59x10^6. (b) Bright-field image (40µmx40µm). (c) HR-TIRF corresponding image (Nivolumab-A647). (d) 2D-dSTORM super-resolution reconstruction (15µmx15µm). (e) Localization density map computed from the Voronoï analysis. The zoom in the green ROI represents the same area for each image. (dSTORM: 635 Laser, 15,000fr, 50fps).*

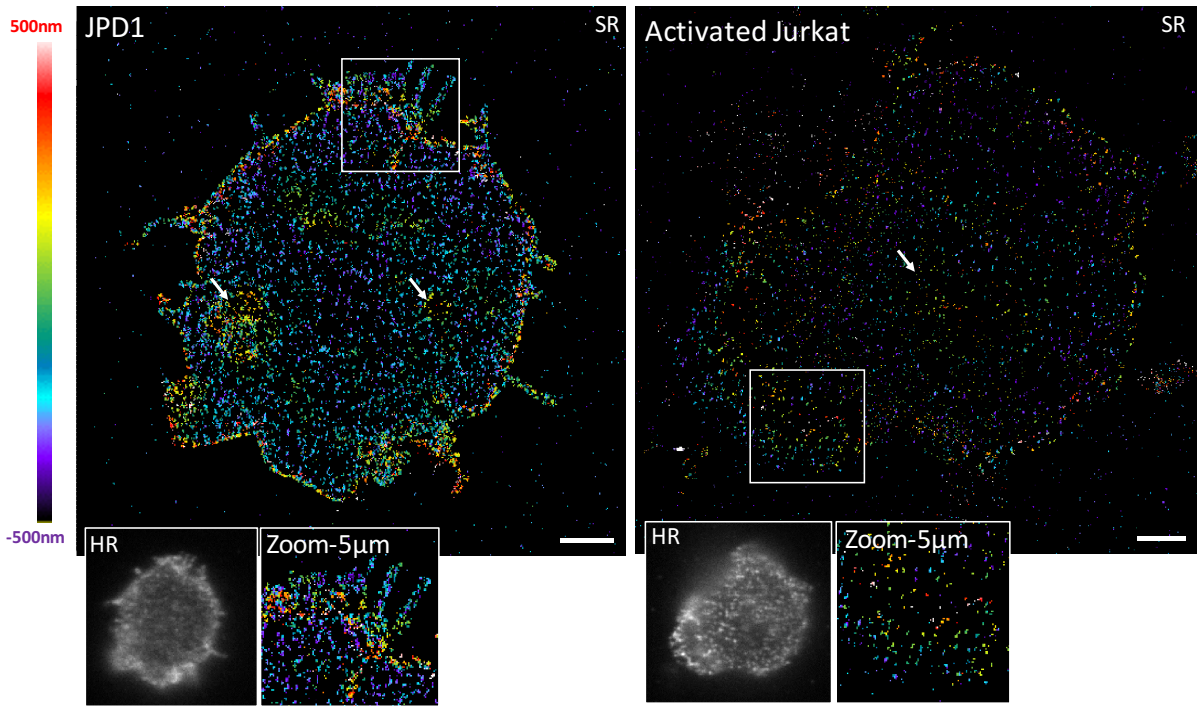

Figure 43. 3D dSTORM reconstruction of PD-1 at the membrane surface of Jurkat and JPD1 cells. *Example of astigmatism-based 3D dSTORM reconstruction of PD-1 on a JPD1 cell seeded on PLL (left) and activated Jurkat cell after 24h (right). Images are Z-color-coded. (Scale bar: 2µm; 3D dSTORM: 635 Laser, 15000fr, 50fps).*

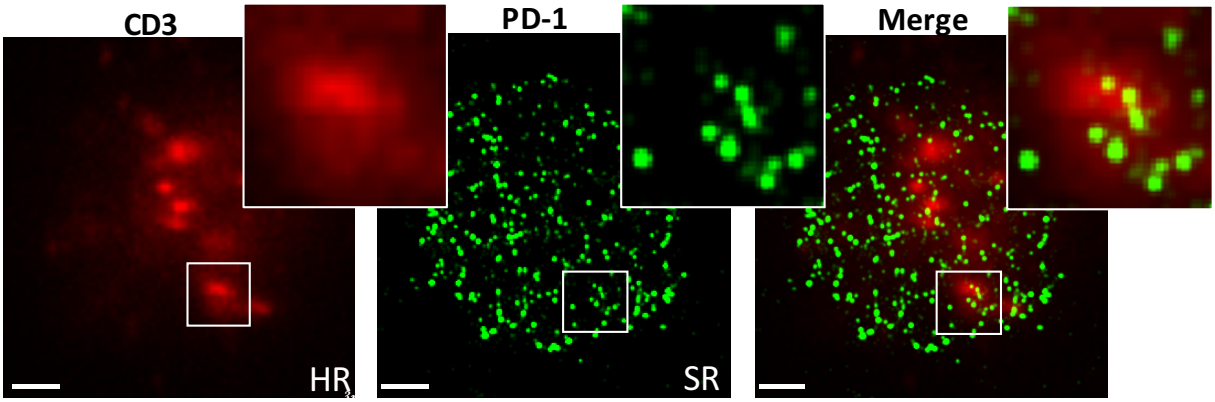

Figure 44. HR and dSTORM imaging of PD-1 and CD3 receptors on JPD1 cell membrane. *Example of 2D dSTORM imaging of PD-1 on JPD1 cell. PD-1 was labeled using Nivolumab-A647 and CD3 labeled trough a cross-linking approach with complex of antibodies (2µg/mL of anti-CD3, 4µg/mL unconjugated secondary Abs and 4µg/mL of A532 Abs). Cross-linking was used to induced CD3 clustering and T-cell activation. HR-TIRF of CD3 image (left), dSTORM image (middle) and merged (right). (Scale bar: 2µm; dSTORM: 635 Laser, 15,000fr, 50fps).*

3.1.3. Quantitative analysis of the impact of Nivolumab on the PD-1 spatial re-organization on living Jurkat cells

I here investigated the impact of therapeutic mAbs directed against PD-1 on PD-1 receptors nanoscale organization, with the goal to extract some key quantitative parameters as a potential readout for the screening of new mAbs. Living activated Jurkat cells were incubated during different times with therapeutics mAbs. Experiments were performed on 96-well plates to investigate several conditions in parallel, in a single HCS-like workflow. The anti-PD1 Nivolumab mAb was used at 5µg/mL concentration and incubated between 3 min to 2 hours with living Jurkat cells previously activated for 24h on an anti-CD3 coating. After cell

fixation, 2D dSTORM super-resolution microscopy was performed. As a reference of PD-1 organization, 24h-CD3 activated Jurkat cells were fixed before incubation with Nivolumab, representing the basal state of PD-1 receptors (post fixation conditions). Following the previously described workflow, PD-1 receptor single molecules were localized and analyzed for clustering for each cell using PALMTracer and SR-Tesseler software, respectively (Figure 45).

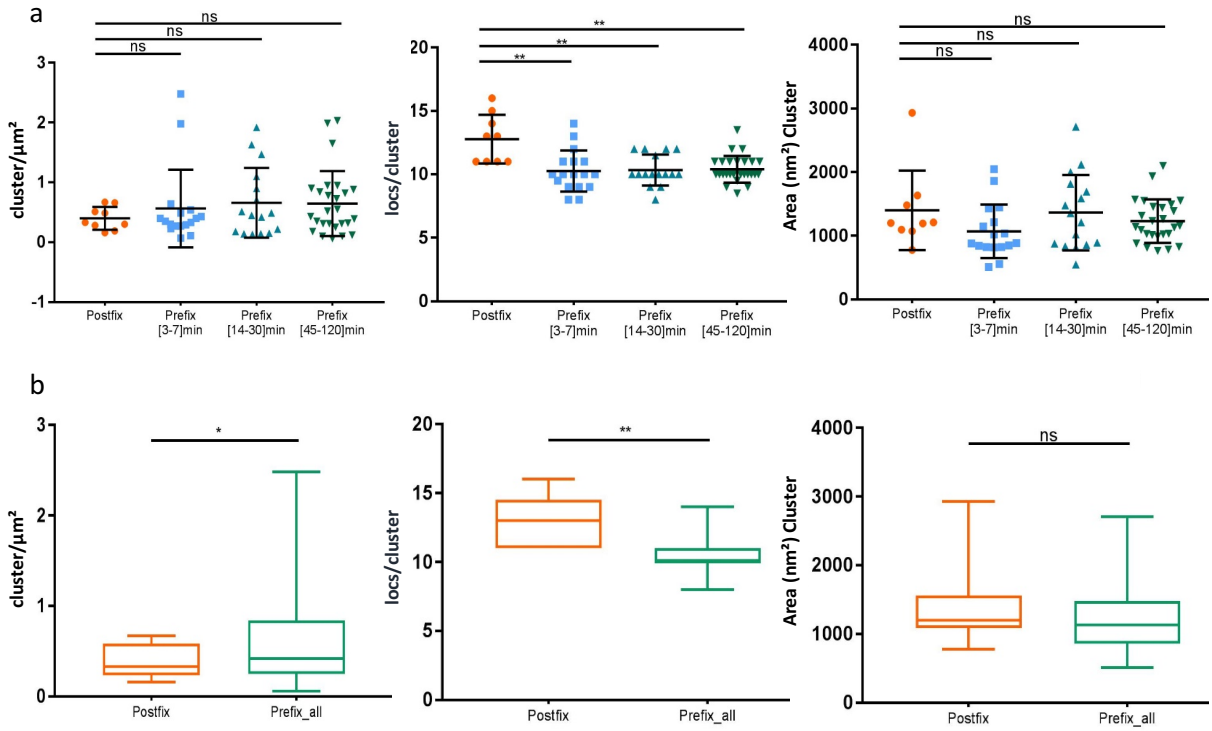

Figure 45. Quantitative analysis of the effect of Nivolumab on PD-1 clustering by 2D dSTORM on activated Jurkat cells. *Clustering features extracted from PD-1 clusters: a) cluster density (#clusters/µm^2), b) number of localizations per cluster (#locs/cluster) and c) cluster area (nm^2). Each point represents the median of one cell's cluster distribution for each condition. A Welch t-test (parametric test) was used to measure the significance between the reference (Postfix) and the conditions (Prefix, Nivolumab effect). Upper panels: clustering features comparison of the negative control and different Nivolumab (5µg/mL) incubation time conditions (n=9, ctrl; n=17, [3-7] minutes; n=16, [14-30] minutes; n=26, [45-120] minutes). Lower panels: all conditions of living activated-Jurkat cells with Nivolumab have been taken together and compared with the Postfix control. Data obtained from 3 experiments. (dSTORM: 635 Laser, 15,000fr, 50fps).*

The effect of Nivolumab on 24h CD3-activated Jurkat cells was studied for three time points: early (3-7min), medium (14-30min) and late (45-120min). Surprisingly, only the number of localizations per cluster was impacted by the Nivolumab treatment, with a significant decrease for the three time points in comparison with the postfix Nivolumab incubation. In contrast, there was no significant difference, neither on the cluster density nor on the cluster area (Figure 45, upper panels). However, at the whole population level, i.e. pulling all the Nivolumab conditions together, therapeutic mAbs treatment on activated Jurkat cells seemed to induce an increase of clusters density, and a decrease of the number of localizations per cluster compared to PD-1 distribution found in the absence of Nivolumab (Postfix condition, PD-1 basal state) (Figure 45, lower panels). In summary, while no or small significant differences were found on the cluster density and cluster area, suggesting no or low clustering effect of Nivolumab binding to the PD-1 receptor, a clearer diminution of the number of localizations per cluster was observed, suggesting potential PD-1 receptor internalization.

3.1.4. Conclusions

To conclude, our preliminary quantitative analyses used to investigate the effect of Nivolumab on PD-1 nanoscale organization at the surface of activated Jurkat cells, revealed very weak effect of Nivolumab. Nevertheless, since clear observations are essential in the context of HCS, the evaluation of a higher number of conditions is necessary hopping it might highlight relevant features. To this end, several activated cell states, anti-PD-1 antibodies and longer incubation times has been tested in further HCS-like experiments.

3.2. Single particle tracking of therapeutic antibodies/receptors pairs by SMLM on living Jurkat cells

dSTORM super-resolution is limited to fixed cells, which precludes dynamics analysis. As previously mentioned, single particle tracking techniques permit live-cell imaging, providing access to receptors' dynamics at the cell surface. They allow the real-time monitoring of the effect of Nivolumab/PD-1 binding on PD-1 diffusion, enabling possible therapeutic mAb signature. To tests this hypothesis, we conducted proof of concept experiments of sptPALM and uPAINT. I developed and validated all the labeling and imaging protocols to perform both single particle tracking experiments on living Jurkat cells.

During my PHD thesis, I developed several electroporation protocols for Jurkat cells transfection. These cells are known to be difficult to transfect, so I had to adapt existing electroporation protocols for my conditions. Preliminary electroporation experiments using plasmids encoding for PD-1-GFP or GFP-PD-1 fusion proteins, leaded to high cell mortality rates and a low percentage of transfected cells (Lonza System-Appendix), confirming that Jurkat cells are very sensitive. Neon system from Invitrogen, on the contrary, provided a higher ratio of fluorescent cells, a much better cell viability, and was easier to use (Appendix). We used this system to produce Jurkat cells expressing PD-1-mEos3.2 (C-terminal) fusion protein and perform sptPALM experiments.

In order to measure PD-1 mobility, PD-1-mEos3.2 Jurkat cells were adhered in a resting state to PLL-coated coverslip. A first round of sptPALM acquisitions was carried out on several cells, from which PD-1 receptors diffusion coefficients was extracted (Figure 46.a). Then, Nivolumab or its Isotype control were added (at 5 µg/mL and 2.5 µg/mL concentrations, respectively) for different time points, and serial acquisitions were performed on cells during 30 minutes (e.g. cell01-t0, cell02-t0, cell03-t0, cell01-t1, cell02-t1, cell03-t1, etc.), giving a total of 5 time points with approximately 5 min of intervals between each acquisition (Figure 46.a). These time-lapse experiments permitted to investigate a broad range of incubation times, allowing gathering quantitative statistics on PD-1 diffusion as a function of Nivolumab incubation time.

Sequential acquisitions were handled automatically via the HCS-SMLM software I developed, which supports any types of plates, avoiding variability between cells and time points.

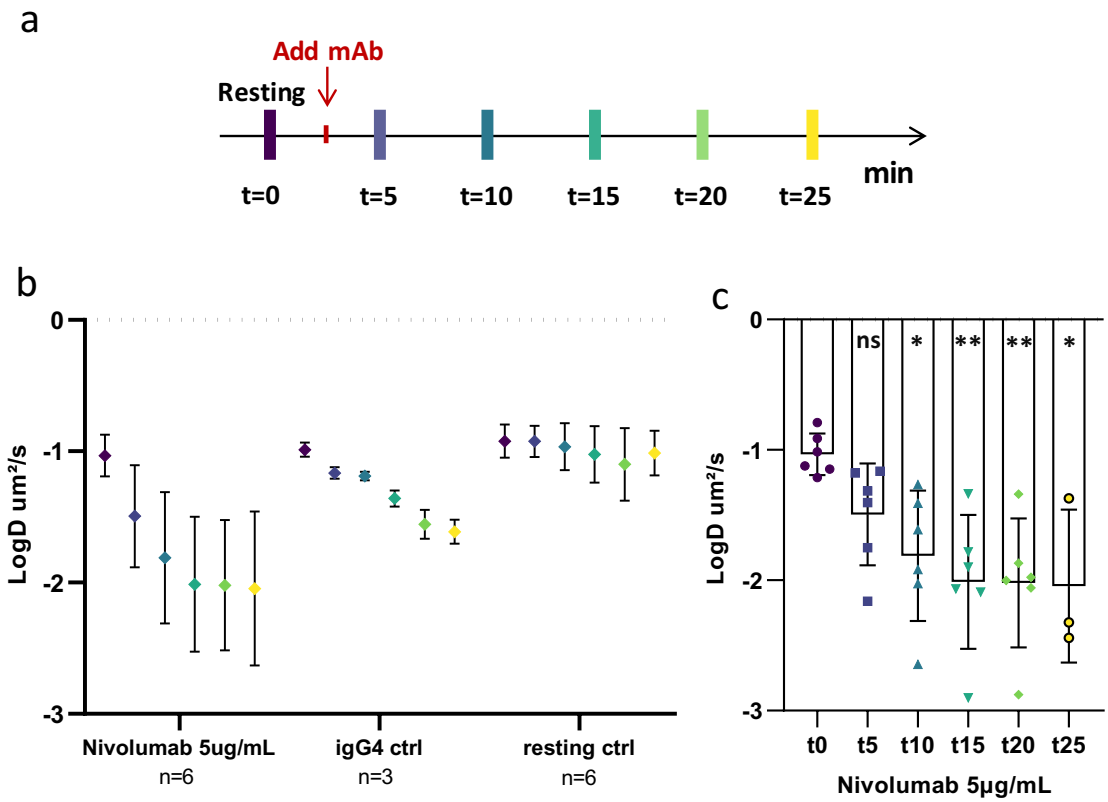

Figure 46. Effect of Nivolumab on PD-1-mEOS3.2 receptor membrane dynamics by sptPALM on Jurkat cells. *(a) sptPALM time-lapse sequence performed on manually-selected cells after addition of 5µg/mL of Abs in the media. 5 sptPALM acquisitions were performed every 5 minutes on each selected cell, to measure the kinetics of PD-1-mEos3.2. (b) Quantitative analysis of PD-1 diffusion coefficients (Log10 of D(µm²/s)) on 3 conditions: i- addition of 5µg/mL Nivolumab (n=6), ii- addition of 2.5µg/mL IgG4 isotype control Ab (n=3), and iii- no Ab addition as negative control (n=6). (c) Effect of Nivolumab on PD-1 diffusion coefficient on data normalized by the sum of the diffusion coefficient distribution of the negative control. Kruskal-Wallis tests (non-parametric). (sptPALM: TIRF, 405-561 laser, 4000fr, 50fps)*

Graphs of Figure 46 display the median of PD-1 receptors diffusion coefficients D(µm²/s) on resting PD-1-mEos3.2 Jurkat cells incubated with Nivolumab IgG4 mAb, the negative IgG4 isotype control or media. Overall, these results indicated that Nivolumab mAb seems to significantly impact PD-1 receptors mobility. Indeed, a significant decrease of PD-1 mobility was observed between the resting state t0, and t15 until its immobilization, i.e. 15 minutes after Nivolumab incubation. According to the brightfield images (data not shown), the Jurkat cells looked still healthy and living after 30 minutes' acquisition. However, we could observe slight morphological changes or coating detachment, probably due to the 405 laser, known for its photo-toxicity.

These results demonstrated that sptPALM can provide relevant quantitative insight of the nanoscale receptor reorganization upon activation, which could be of great interest for this study. However, many questions arose, and it will be interesting to investigate in the future PD-1 behaviors upon Jurkat activation, as well as the effect of Nivolumab/PD-1 binding prior Jurkat activation. Moreover, experiments should be reproduced with Pembrolizumab to qualitatively compare both mAbs effects. In conclusion, receptors diffusion analysis obtained by sptPALM microscopy could bring an efficient read-out to compare mAbs and/or completing the information provided by dSTORM imaging.

Complementary to sptPALM, which is used to monitor receptors dynamics, we also considered uPAINT, an alternative single-particle tracking approach, to follow the functional

mAbs rather than their targets in non-transfected cells. To achieve this goal, we collaborated with Eric Hosy and Matthieu Sainlos from IINS, to conjugate Nivolumab mAb with Atto647, an organic fluorophore known for its high photo-stability and well-adapted for single particle tracking experiments. This project is still in progress, but the first results were very encouraging and provided similar kinetics than PD-1 via sptPALM experiments (data not shown).

3.3. 3D PD-1 receptor nanoscale spatial organization on a whole T-cell by DNA-PAINT imaging combined with light-sheet microscopy

All the results shown previously on PD-1 receptor nanoscale organization were performed by TIRF microscopy. TIRF microscopy provides access to T-cell membrane receptors at only a few hundreds of nanometers above the interface between the cell and the coverslip, requiring cells adhered onto the coverslip. In order to have a more complete vision of PD-1 receptor nanoscale organization, I started investigating the 3D nanoscale organization of PD-1 receptors at the entire non-adherent T-cell surface, in collaboration with Hisham Forriere in the team. This is a non-trivial methodological development, for which no commercial solution exists. To achieve this goal, we improved the soSPIM technology developed in the lab (Galland et al[41]. 2015) to be able to perform automatic 3D super-resolution acquisitions. Light-sheet microscopy allows imaging cells in suspension, in a coating-free environment more physiological for non-adherent cells.

3.3.1. Upgrading the soSPIM technique for in-depth 3D-SMLM

Micro-mirror chips are essential for the soSPIM technique. These chips are molded by imprinting a master mold in a UV-curable polymer (NOA 73 and MYpoly134). Nano-diamonds (i.e fluorescent beads) mixed in the polymer in appropriate concentration (≈1–10 nano-diamonds per FOV) were used as fiducial markers for image registration. For our application, we used the soSPIM chips containing thousands of 22x22x40 μm^3 or 40x40x40 μm^3 well-arrayed micro-wells flanked with 45° micro-mirrors, in which Jurkat cells are allowed to grow (Figure 48.A). We developed and adapted the immune-staining protocols to perform single molecule-based super-resolution imaging on PD-1 and CD3 receptors on fixed Jurkat cells in the soSPIM chips (Appendix). By adding depth information to the soSPIM system, we were able to perform astigmatism-based 3D-SMLM and to localize molecules across 1 µm around each focal plane. Therefore, the acquisition of an entire 10-15µm thick Jurkat cell with 300 nm Z-intervals, required several tens of optical sections.

SMLM acquisitions can require several minutes of acquisition for a single plane depending of the single molecule technique. Typically for a total of 5,000 frames, 1–2 minutes are necessary in dSTORM, while more than 15 minutes are required in DNA-PAINT. This can represent more than 12h of continuous acquisition to carry out DNA-PAINT imaging on 50 planes under these conditions, making it a real challenge for the soSPIM technique. I addressed some of the technical challenges during my PhD thesis, notably on the nanometric stabilization protocol and automatic acquisition pipeline.

First, inherent spatial drifts occurring over time have a significant impact on soSPIM-SMLM acquisitions (Figure 47). Indeed, in the soSPIM architecture, the excitation beam is reflected on a 45° micro-mirror to create the light-sheet perpendicular to the optical axis. This specific geometry results that axial and lateral drift from the sample induces in a shift of similar amplitude between the light-sheet and the focal plane of the objective. Consequently, a post-processing axial and lateral drift correction, as for conventional SMLM, doesn't work. Real-

time nanoscale drift correction is mandatory to be able to perform long term SMLM acquisition on soSPIM, as required for this project.

Second, the multiplane acquisition workflow needs to be fully automatized to perform optimal whole-cell 3D-SMLM. To achieve these goals, I developed an automatic real-time 3D registration and acquisition software integrated in the existing acquisition workflow.

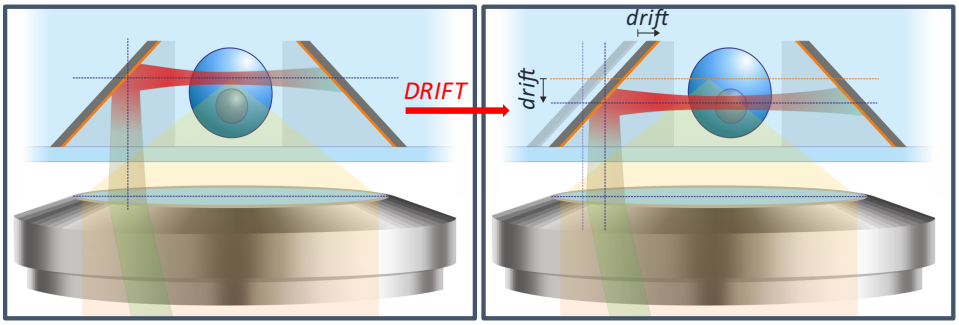

Figure 47. Impact of the spatial drift on the light-sheet position for the soSPIM.
Due to the specific geometry of the soSPIM, lateral and axial drifts of the sample induce shifting the light-sheet outside of the focal plane of the objective.

This software, called **ZTrack**, is a VB.NET and C# program that comes with a user-friendly graphical user interface, and operates as a plug-in of MetaMorph acquisition software. It handles light-sheet and sectioning parameters (calibrations, Z steps, registration, etc.), by controlling a nanometric XYZ piezo-stage (Mad City Labs Inc.) and the streaming acquisition (Appendix).

Figure 48 describes the ZTrack software automatic drift correction workflow performed online for each plane. The real-time drift correction is performed using astigmatism-based 3D localization of fiducial markers embedded in the polymer surrounding the micro-wells, in which the cells of interest are immobilized. The drift is estimated for each frame during the streaming acquisition process, and the stage displaced upon conditions to compensate for the drifts (see detailed workflow below, Figure 48.B and Figure 49). To avoid unnecessary communication with the stage, parameters can be set to define the conditions to perform feedback correction. After each plane acquisition sequence, the image stack is saved into a database and the stage plus the light-sheet are displaced to the next plane, until the whole cell has been acquired in 3D.

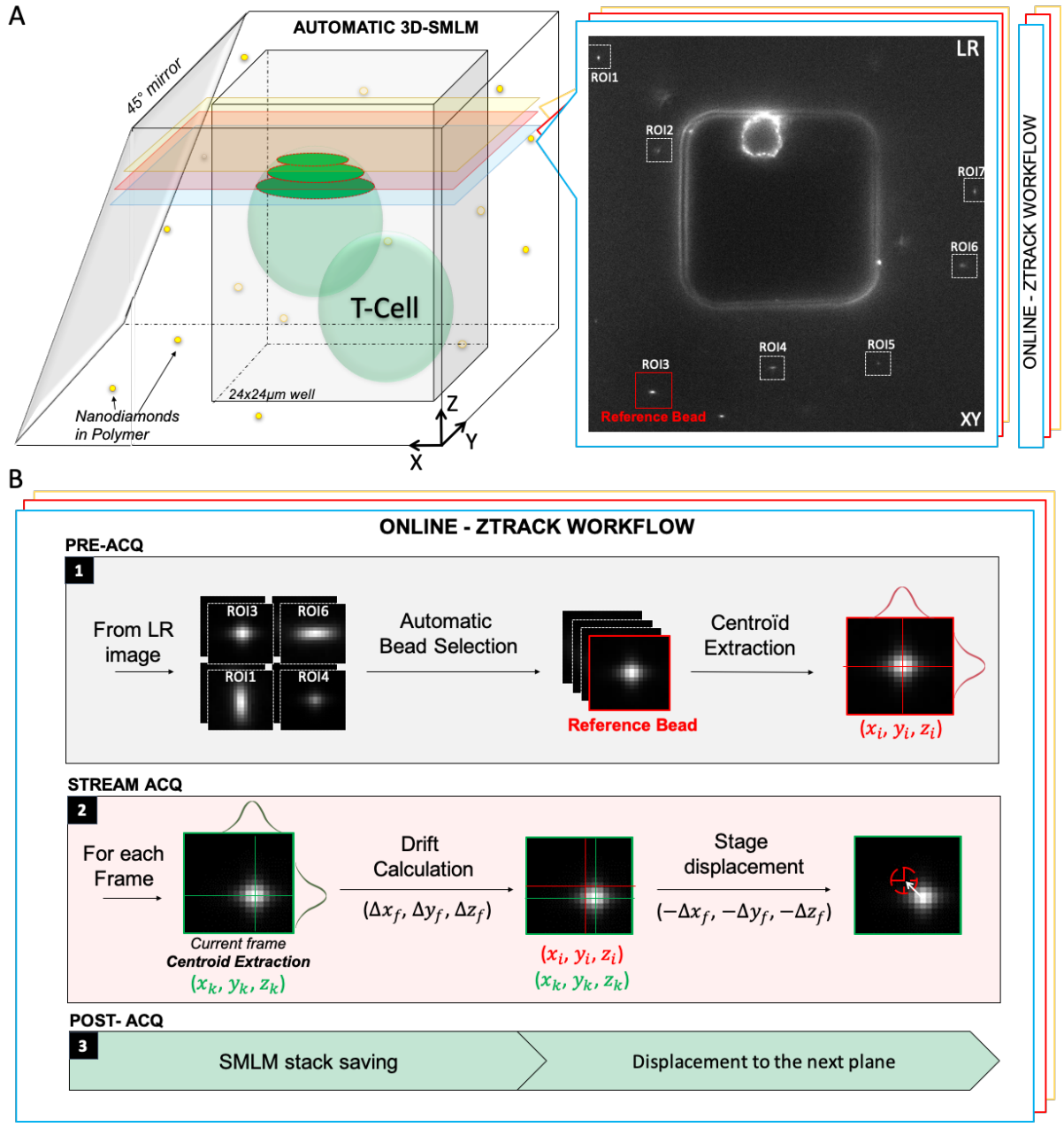

Figure 48. ZTrack automatic pipeline for 3D T-cell soSPIM-SMLM acquisition. *ZTrack software handles the automatic 3D acquisition workflow by controlling: the X,Y,Z stage position and the acquisition. (A) The drift correction is assessed online during the acquisition, by localizing fiducial markers embedded into the polymer surrounding the micro-wells. B.1) Before the acquisition, a reference bead among tens is selected from a Low-Resolution (LR) images of the plane and its centroid is extracted. B.2) During the SMLM streaming acquisition, the current drift is estimated from the reference and current bead coordinates, and is compensated to keep the light-sheet at the focal plane. B.3) After each SMLM plane acquisition, the stack is automatically saved into a database before moving to the next plane.*

3.3.2. ZTrack automatic acquisition workflow

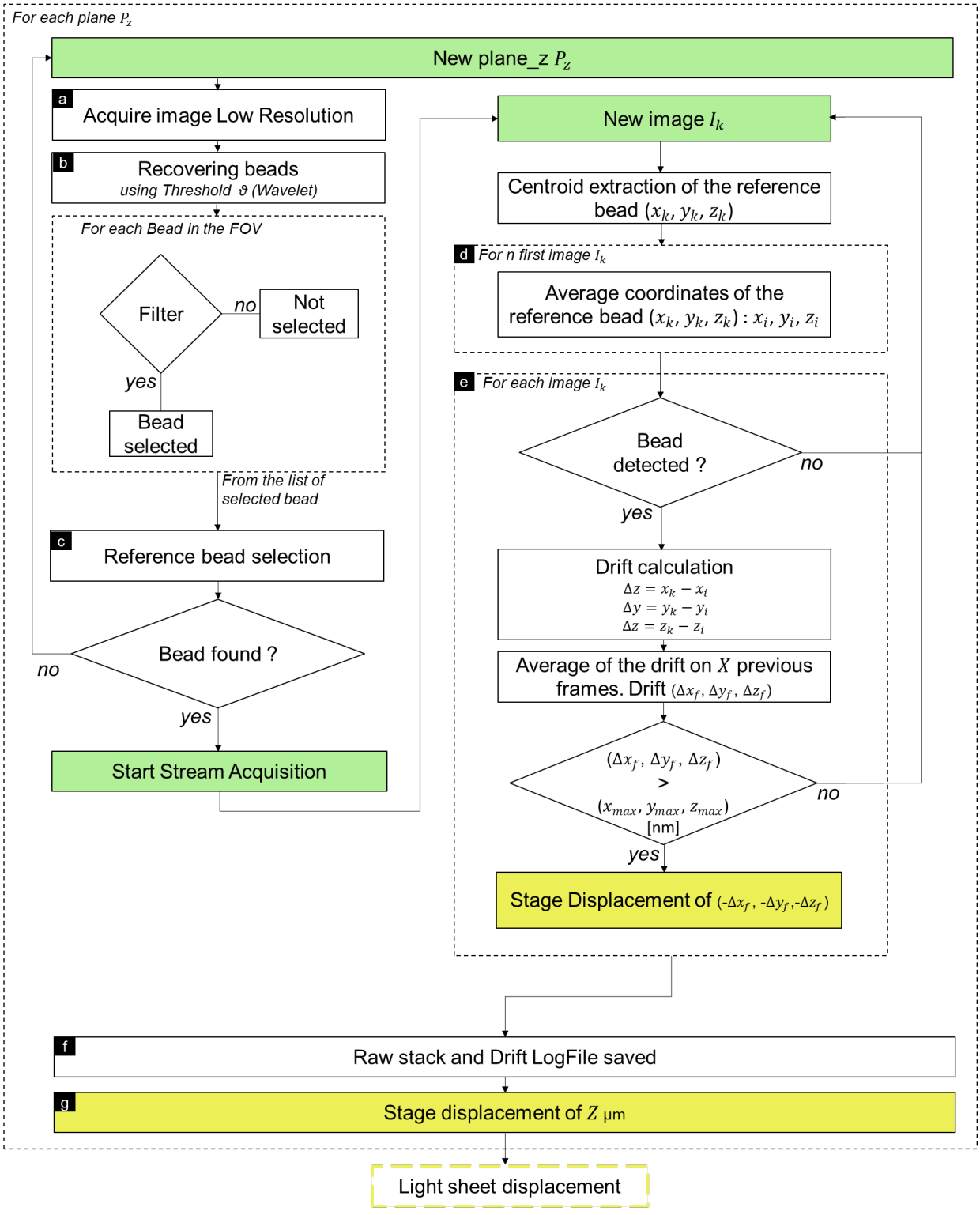

***Figure 49. ZTrack algorithm flowchart**. Flowchart of ZTrack algorithm performed online during the acquisition, for each frame and each plane of the 3D SMLM acquisition.*

The following text describes in details the ZTrack algorithm, for each plane and each frame (Figure 49):

Once the acquisition and drift correction parameters defined (Appendix) the light-sheet and the focus are positioned. The following process is repeated until the end of the whole cell acquisition, for each *plane_z* (P):

a. A low-resolution image is acquired (Figure 48).
b. All fluorescent bead present in the image are automatically localized using a combination of a trous" wavelets segmentation (threshold ϑ) and 2D Gaussian fitting (1.2.2.5). Then, the localized beads are filtered using three key parameters based on the Gaussian fitting features: the standard deviation (σ_x, σ_y) and the mean square error (MSE). The resulting beads are then individually evaluated and classified using a score based on their Gaussian fitting features: MSE, circularity (ratio σ_x/σ_y) and integrated intensity. Finally, the best scored bead is used as a reference for the acquisition.
c. **If** a bead has been selected as reference, **then** the streaming acquisition is launched. **Else** the current plane is not acquired and the next plane is processed.
d. The "initial" coordinates of the reference bead (x_i, y_i, z_i) are calculated by averaging its coordinates from the first n frames. Then, a "reference" ROI of 15 pixels-size is created around the (x_i, y_i, z_i) coordinates.
e. For each image frame (I_k) of the stream acquisition:
    - The centroid of the reference bead (x_k, y_k, z_k) is extracted.
    - **If** no bead is detected, the next steps are skipped.
    - **Else**: The distance (i.e. drift: Δx_f, Δy_f, Δz_f) between the current position of the reference bead (x_k, y_k, z_k) and its "initial" coordinates (x_i, y_i, z_i) is calculated.
    - **Correction option 1: If** the drift (Δx_f, Δy_f, Δz_f) exceeds the defined limits (x_{max}, y_{max}, z_{max}) in nanometers, **Then** the stage is displaced of ($-\Delta x_f$, $-\Delta y_f$, $-\Delta z_f$) to compensate the current drift.
    - **Correction option 2:** Every X frames, the stage is displaced of ($-\Delta x_f$, $-\Delta y_f$, $-\Delta z_f$) to compensate for the current drift. The current drift (Δx_f, Δy_f, Δz_f) can be averaged over multiple frames.
f. At the end of acquisition, the raw single molecule image stack and a log-file are automatically saved in the head directory to complete the database.
g. The stage is displaced automatically to the next *plane_z*.

At the end of the multiplane acquisition, the database automatically created online, contains for each acquired plane: the reference ROI (.rgn) containing the reference bead, the diffraction-limited image acquired before the single molecule acquisition, the raw single molecule images stacks and a log file. This log file includes, for each frame, several information: the coordinates of the reference bead, its localization features (σ_x, σ_y, MSE, etc.), the current position of the stage and the current drift (Δx_f, Δy_f, Δz_f).

The final 3D-SMLM image reconstruction of the entire cell is computed using PALMTracer and Thunderstorm software, for single molecules localization and 3D-SMLM reconstruction respectively. It is important to notice that ZTrack software is used essentially to keep the light sheet and the focal plane aligned all along the acquisition. For optimal reconstruction, it remains necessary to correct for residual drift occurring within each SMLM plane acquisition, which is easily done using the resulting log files, as well as to re-align planes between each other's.

3.3.3. Benchmarking of ZTrack

ZTrack benchmarking, conducted by Hisham Forriere, was performed to evaluate ZTrack efficiency in correcting axial and lateral drifts with a sufficient precision to avoid light-sheet illumination derives. We first compared ZTrack with the integrated Nikon Perfect Focus System (PFS), a laser-based system designed to correct axial drifts in real time with about 50nm precision (factory specifications). It is important to keep in mind that there is no existing solution to correct for lateral drifts, which is mandatory for long term soSPIM-SMLM acquisitions. We acquired nano-diamonds embedded into the polymer for 2H under standard SMLM acquisition conditions. Drifts were compensated either using ZTrack or the PFS, and compared without any corrections. Figure 50 shows that without registration, the system could drift more than 750 nm after only 6,000 frames (10 min), illustrating that real-time drift correction is necessary in our microscope to perform 3D-SMLM. After real-time correction, we could observe that both axial and lateral drifts were properly corrected using ZTrack. As expected, if the PFS was able to compensate axial drifts, it did not permit lateral drift corrections. We then evaluated and compared the precision of the drift correction of the PFS and ZTrack. ZTrack correction was slightly better compared to the PFS, with 29.6nm accuracy against 38.1nm respectively. ZTrack lateral drift correction accuracy was 14.6nm. These results confirmed the efficiency of ZTrack in the soSPIM-SMLM acquisition workflow.

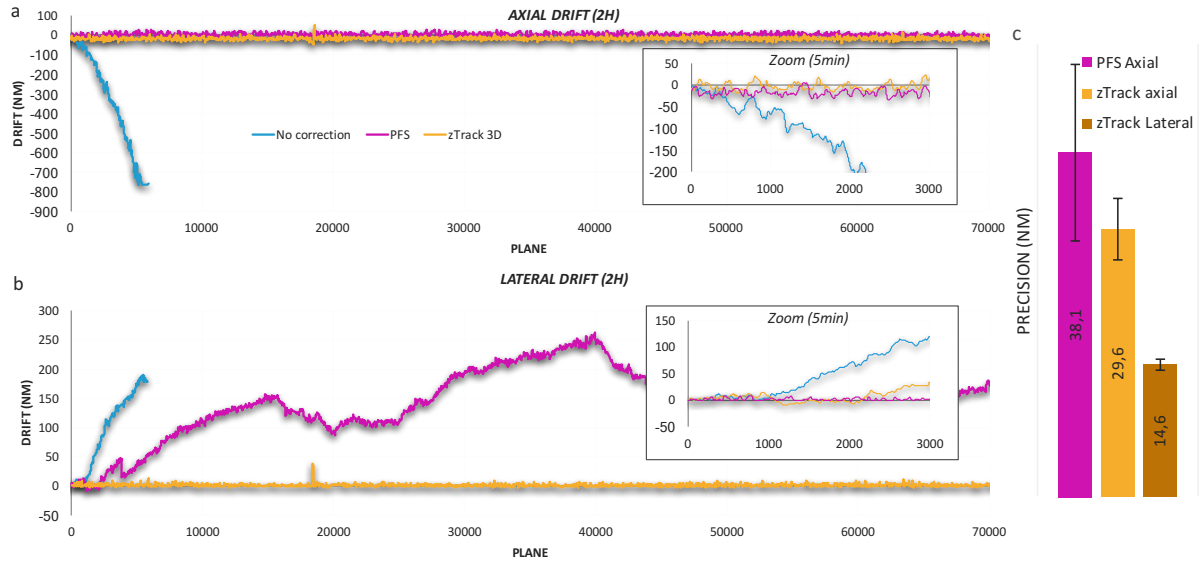

Figure 50. ZTrack benchmarking. *Examples of axial (a) and lateral (b) drifts recorded over 2h of acquisition (at 10 fps). Drifts were either compensated in real time using ZTrack (yellow) or the Nikon PFS (pink), or not compensated (blue). (c) Drift correction precision (nm) of ZTrack and Nikon PFS.*

3.3.4. 3D nanoscale PD-1 imaging of an entire Jurkat cell

We successfully managed to acquire and reconstruct the 3D nanoscale organization of PD-1 on the recombinant cell-line JPD1 using DNA-PAINT combined with soSPIM (Figure 51). It displays a homogeneous distribution of PD-1 nano-clusters over the whole cell membrane. This experiment required more than 13h of continuous acquisition, performed automatically without any human intervention. 21 optical sections, with a plane-to-plane distance of 500 nm, were used to acquire the 10 µm-thick suspended Jurkat cell. For each optical plane, 22,500 frames of single molecule events were acquired at 10 fps (100 ms exposure time), representing a total of 664GB for the whole acquisition, from which more than 330,000 single molecules were localized in 3D.

I presented here, the capabilities and requirements for soSPIM to probe the 3D nanoscale organization of proteins in depth at the single-molecule level. It involved an aberration-free astigmatism-based 3D localization combined with a computerized method for real-time mechanical drift correction and automated acquisition. This project is ongoing and further images acquisition and analysis will be carried-out. The 3D clustering analysis of PD-1 receptors structures over the cell membrane, and the spatial distribution of the clusters will be realized using a 3D version of SR-Tesseler. These results will be quantitatively compared with 2D-SMLM data acquired by TIRF. soSPIM-based SMLM will complete or confirm the information obtained by HCS-SMLM about PD-1 clustering.

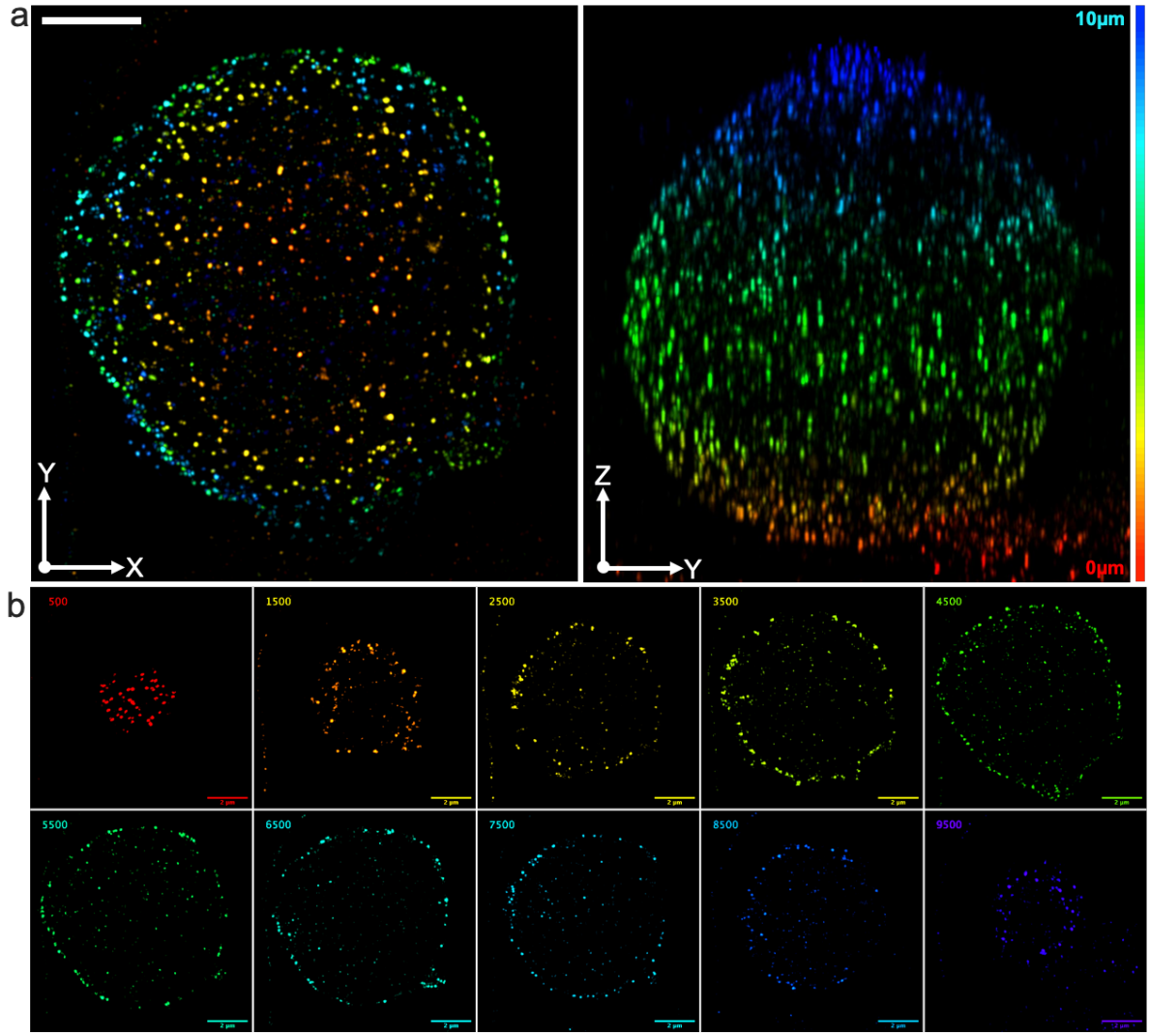

Figure 51. 3D DNA-PAINT of PD-1 membrane receptors on a suspended Jurkat cell using soSPIM*. (a) XY and ZY projections of PD-1 nano-clusters of JPD1 cells (recombinant Jurkat cell line). (b) 50nm thick optical sections (a) at 1µm intervals. The color codes for the depth, from 0 to 10µm. The PD-1 nano-clusters reconstruction was obtained from 21 optical planes separated by 500nm steps. 22,5000 frames were acquired at 10ps for each plane, representing a total of 13h25 of continuous acquisition performed automatically using soSPIM system and ZTrack. (Scale bar:2µm)*

3.4. Conclusion

To conclude this chapter, I performed single molecule localization microscopy on fixed and living JPD1 Jurkat cell lines using the protocols developed in Chapter 2. I characterized the PD-1 spatial organization on fixed CD3-activated Jurkat cells, in 2D and 3D, by dSTORM-TIRF, at the interface between the glass coverslip and the cell. PD-1 membrane receptor

quantifications revealed a pattern of sparse and isolated nano-clusters of homogenous area (35-60nm diameter) and localization density (10-15 localization per cluster). These results also revealed a cell-to-cell heterogeneous cluster density distribution, confirming previous experiments reporting a variability of PD-1 expression at the membrane of Jurkat cells depending on the cell and its activation state.

I then studied the effect of Nivolumab, a therapeutic mAb targeting PD1 receptor used in clinic for cancer therapy, first on PD-1 nanoscale organization at the cell membrane surface, second on PD-1 receptor dynamics. PD-1 nanoscale organization was investigated on fixed cells by mixing the therapeutic mAbs with Jurkat cells for different incubation time. PD-1 dynamics on living transfected Jurkat cells were measured using sptPALM and uPAINT single particles tracking techniques. All together, these first promising results showed that i) we could confirm some differences between Jurkat cells incubated with and without Nivolumab on 24h activated cells, and ii) Nivolumab at 5μg/mL seems to immobilize PD-1 receptors after 15min incubation.

However, it clearly appears that new biological conditions are required to find an efficient readout in order to clearly be able to quantify more precisely mAbs efficacies in a high content screening approach. We used our HCS-SMLM quantitative platform to study PD-1 receptors nanoscale organization by 2D dSTORM, under several activation conditions and in a single and fully-automatic workflow. These results and all the experimental details are described in the next chapter.

Finally, we successfully performed the proof-of-concept experiment that it is possible to investigate the nanoscale topography of PD-1 receptor at the entire suspended T-cell level. Even if this work is still ongoing and exploratory in the framework of this study, the new developed instrument should bring interesting insight to the nanoscale organization of therapeutic receptors under more physiological conditions.

4. HCS-SMLM: a single molecule-based high content screening platform for therapeutic Abs

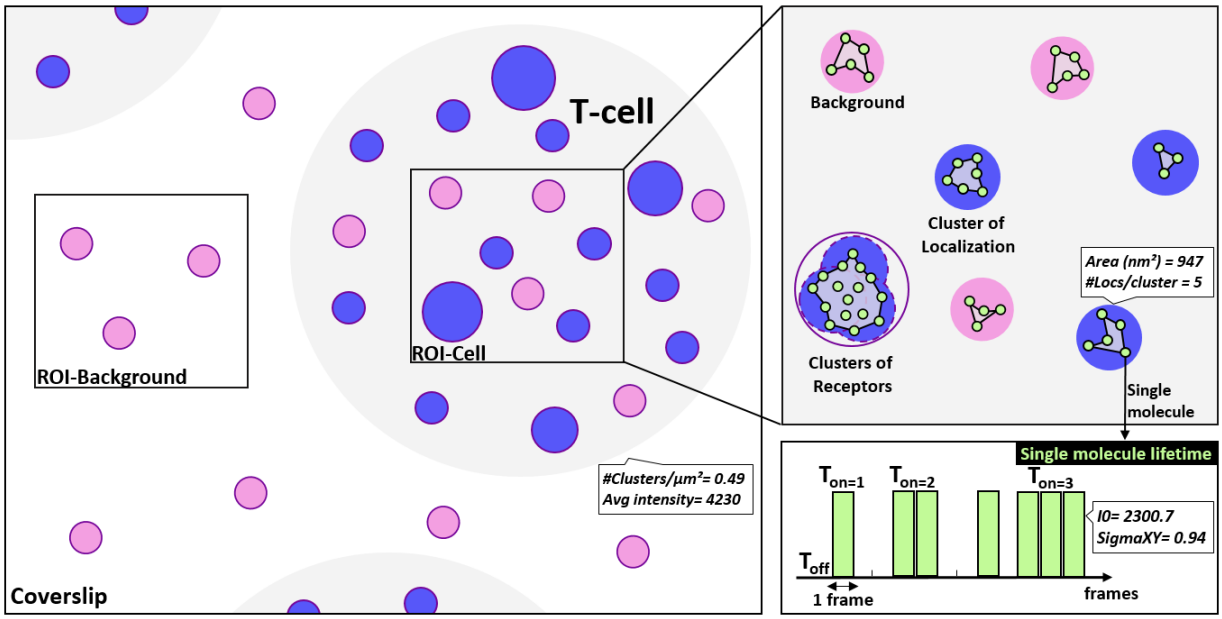

Figure 52. Schema of the cellular and molecular structures and parameters used for T-cell membrane receptors quantification. *Super-resolution image reconstructions display clusters of localization distributed all over the images. These clusters can be background (small pink clusters), isolated receptors (small purple circles) or clusters of receptors (large purple clusters). All these clusters can be statistically distinguished by their size and their number of localizations per clusters.*

In this chapter, I characterized different structures at the cellular and molecular levels, which I quantified using several quantitative parameters, or features, using single molecule localization microscopy data. Images are composed of multiple Jurkats cells acquired under different conditions, PD-1 or CD3-tagged. Each cell expresses various number of receptors at its surface, revealed using single molecule localization microscopy under TIRF illumination. These receptors appear as clusters of single molecule detections. These clusters have different sizes (Area in nm^2) and are composed of single molecule detections (#localizations/cluster). They are distributed at the cell surface with a certain density (cluster density in #clusters/μm^2). Each localized molecule has specific characteristics extracted from the Gaussian fitting localization process (coordinates, integrated intensity, σ_{xy}), which can be used to evaluated the quality of SMLM acquisitions. In this work, we use the term of "cluster of localizations" to define a group of localizations. A cluster of localizations can represent a single receptor as well as an aggregate of receptors, or "cluster of receptors". Clusters of receptors will usually statistically differ from single receptors by their higher number of localizations per cluster and their bigger size. Background signal (pink circles in Figure 52), also characterized by small clusters of localizations homogeneously distributed in the image, can be characterized and used as reference to discriminate single isolated receptors.

4.1. Optimization of the HCS-SMLM software and acquisition

4.1.1. HCS-SMLM software platform for clustering analysis and data navigation

I adapted the existing analysis pipeline developed in Beghin et al[75] to improve data navigation through the PD-1 clustering features, and statistical analysis. The existing pipeline permitted reformatting metadata files of any type into a MySQL database readable for Cell Profiler Analyst (CPA) software. Nevertheless, this process was too slow to navigate into huge volumes of data. To overcome this limit, I developed several new tools, which I integrated into

the HCS-SMLM pipeline to improve the clustering analysis and facilitate data navigation. The HCS-SMLM software includes now several new post processing functionalities such as: database cleaning, filtering, background filtering and global statistics (Figure 53). These steps are described below:

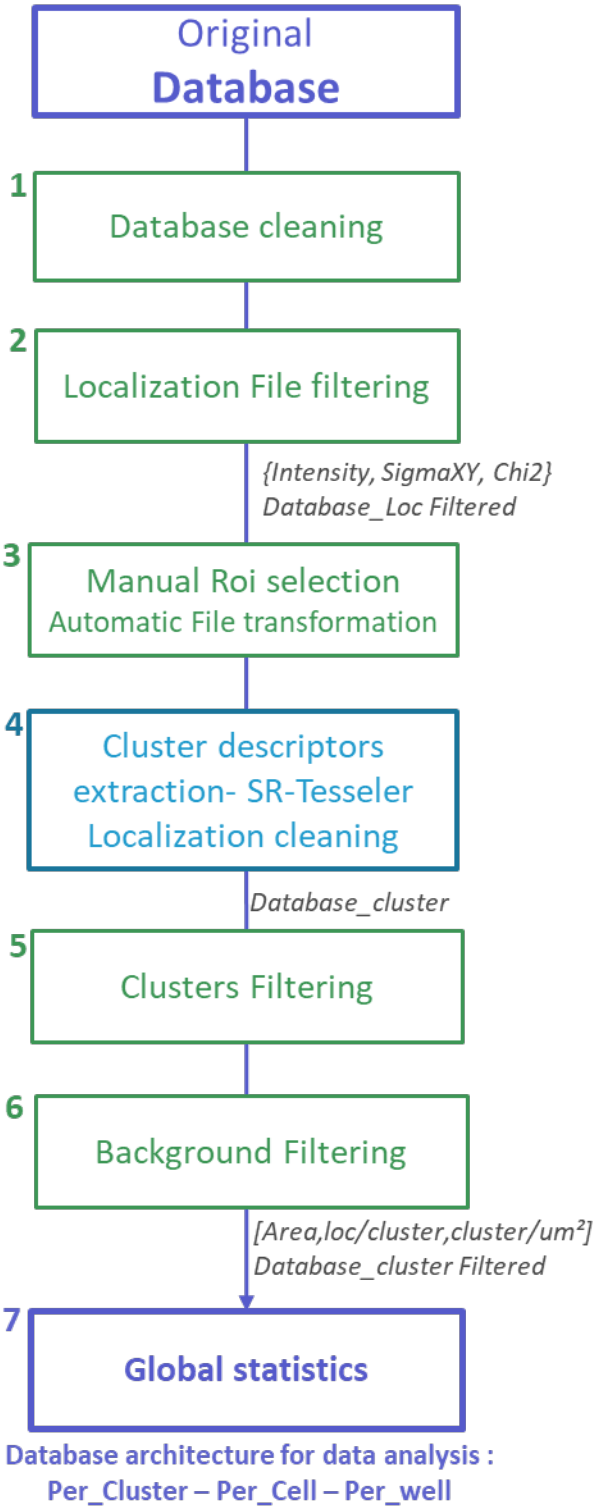

Figure 53. The clustering analysis pipeline

1-Database cleaning: The database can contain non-registered images due to the absence of fluorescent beads in the field of view. Since they are not usable for further quantification, they are automatically deleted from the arborescence files.

2-Localization file filtering: I integrated several filtering steps into the pipeline, allowing filtering of individual localizations using Gaussian fitting parameters, i.e. the standard deviations (σ_x, σ_y), the mean square error (MSE) and the integrated intensity (I_0). This step allows to concentrate the analysis on the best localizations by filtering artifacts such as aggregates of fluorophores, fluorescent beads, auto-fluorescent background, biological wastes, etc.

3-Manual ROI selection and automatic file transformation: To take into account the heterogeneous expression of PD-1 at the cell membrane and the strong background, I integrated i) a cell segmentation step, allowing individual cell analysis, and ii) a background filtering step (Figure 54). For these steps, ROIs on cells and background need to be manually defined from each Bright-Field and HR-TIRF images using ImageJ's ROI-tool-manager. Cells ROIs are tagged either PD-1 positive or PD-1 negative (PD-1+ or PD-1-), depending on the fluorescence intensity (Figure 62.a). All the ROIs information are automatically converted and saved into individual ROI-files in a SR-Tesseler format for further cluster segmentation.

4-Cluster descriptor extraction via SR-Tesseler: From the cleaned and localization-filtered database, cluster segmentation is automatically processed using SR-Tesseler software macro routine overall the arborescence file. Clusters are segmented for each cell and their clustering features (localization density, cluster size, cluster area, #localization/clusters, cluster intensity, etc.) were automatically extracted and saved for each image into .csv files.

5-Cluster Filtering: It is possible to select a sub-population of clusters of interest by filtering the 3 clustering features: cluster area, #localization/cluster and cluster density (#cluster/μm^2) per cell ROI.

6-Bakcground Filtering: As illustrated in Figure 54.a, the more the Jurkat cells express PD-1 at their surface, the less the background signal impacts the PD-1 clustering quantification. But for cells expressing low level of PD-1, the background can bias the clustering analysis. Figure 54.b confirms this by showing significant differences of cluster density values between PD-1+ cells and the background, in contrary to PD-1**-** cells which shows similar cluster densities than the background. To account for the background localizations, a normalization step is required. Unfortunately, un-mixing background signals from isolated PD-1 receptors signal was not impossible. We therefore simply corrected the cluster density and the average intensity of each cell by subtracting the average cluster density and intensity of the background of the same well.

7-Global Statistics: The final step consists in computing and exporting the global statistics of clustering and image metadata, into two text files in the main directory, providing three levels of analysis: *per_condition*, *per_image* or *per_object*. The first file contains the mean, the standard deviation and the median values for each cell. The second file contains the average values per well, i.e. statistics per condition. In order to easily navigate into the database, I developed a graphical interface allowing to visualize all the SMLM features. For each condition, the histogram of every clustering or localization descriptors can be plotted by cells or by clusters for each well.

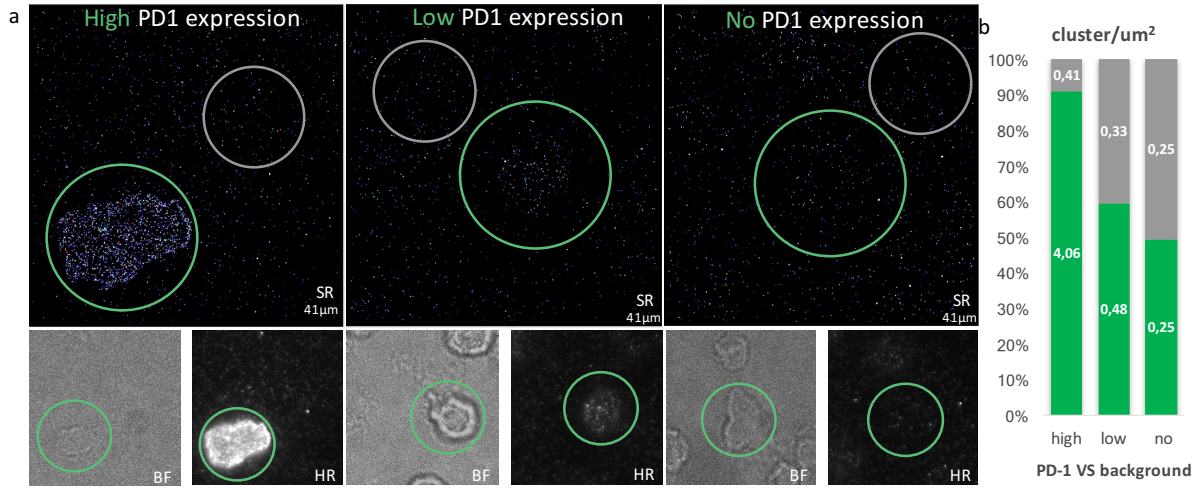

Figure 54. Impact of the background on the quantification of PD-1 expression. *(a) Super-resolution reconstructions (SR), bright-field (BF) and high-resolution TIRF (HR) images of activated Jurkat cells with three different levels of PD-1 expression (from left to right, high, low and no PD-1 expression, 41µm-size). (b) Ratio of PD-1 to background cluster density, calculated from ROI in (a). White numbers represent the cluster density values obtain from cells (green) and the background area (grey).*

4.2. Proof of concept: clinical therapeutic mAbs anti-PD-1 characterization by HCS-SMLM

As explain in Chapter 2, CD3 receptor is an ideal positive control of clustering. Its ability to cluster upon T-cell activation has been described in the literature using standard fluorescence microscopy and single molecule-based super-resolution microscopy.

4.2.1. CD3 receptor as a reference for PD1 characterization

CD3 receptors are highly expressed on resting Jurkat cells, and homogeneously distributed at the cell membrane when cells are seeded onto a PLL coating (Figure 55.a). The level of CD3 expression is stable among the cell population (data not shown). HR images acquired using TIRF illumination indicated no particular aggregation or clustering of the receptors, which was coherent with the literature. To induce a physiological CD3 clustering, I stimulated cells by seeding them on a functional anti-CD3 coating for 15 min, as described previously. This ensures the TCR-CD3 complex recruitment at the cell membrane (Appendix). Following cell fixation, we observed the formation of CD3 receptor clusters, mostly in the center of the cell (Figure 55.b). Finally, I introduced a third level of “artificial” CD3 clustering by antibody cross-linking. The principle of antibody cross-linking is to bridge several anti-CD3 antibodies all together via an anti-Fc antibody, in order to create complex of anti-CD3. These anti-CD3 complexes, when in solution, will promote the recruitment of CD3 receptors on the cell surface, creating CD3-clusters. Figure 55.c illustrates a high level of clustering induces by crosslinking, showing big protein islands at the Jurkat cell surface. The image segmentation performed using SR-Tesseler shows a clear reorganization of the number and sizes of clusters compared to the other conditions (Figure 55, bottom panels).

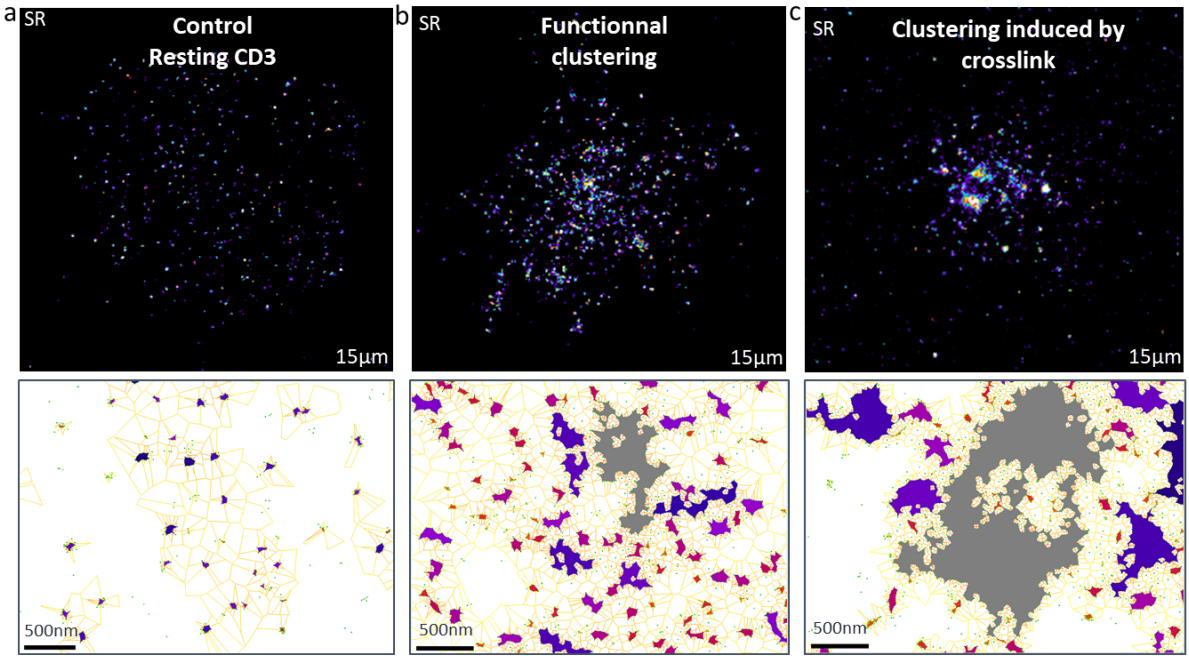

Figure 55. Three levels of CD3 receptor clustering. *(a-c) Top: Representative super-resolution images of (a) CD3 on resting Jurkat cells, (b) CD3 clustering induced by OKT3 coating, and (c) CD3 clustering induced by antibody cross-linking. (Top) dSTORM images of CD3. (Bottom) Clusters are segmented and color coded for the size using Voronoï-tessellation diagram (SR-Tesseler).*

To characterize these different CD3 receptor clustering patterns, I used the 3 quantitative parameters introduced earlier: the number of clusters per µm^2 (cluster density), the number of localizations per cluster (#locs/cluster), and the area of each cluster (area) (Figure 56). Interestingly, spatial organizations of CD3 on resting and PD-1 on activated cells were similar for the 3 parameters: cluster density (1.17+/-0.79 and 0.75+/-0.32 cluster/µm²), number of localization per cluster (10.6+/-1.65 and 9.5+/-1.18 locs/cluster) and cluster area (1322+/-194.12 and 1116+/-614.09 nm^2), for each cell. All the parameters slightly increased for CD3 when cells were functionally activated by OKT3 coating (2.05+/-0.43 cluster/µm², 15.8+/-2.46 locs/cluster and 2690+/-747.75 nm^2). Finally, all parameters strongly increased in the case of anti-CD3 cross-linking condition (3.79+/-0.70 cluster/µm², 50.4+/-12.10 locs/cluster and 8417+/-1903.64 nm^2). These results revealed CD3 clusters sizes, clusters densities and amount of localization 1.5-fold and 3-fold higher upon activation via coating or cross-linking (respectively) than for the resting conditions.

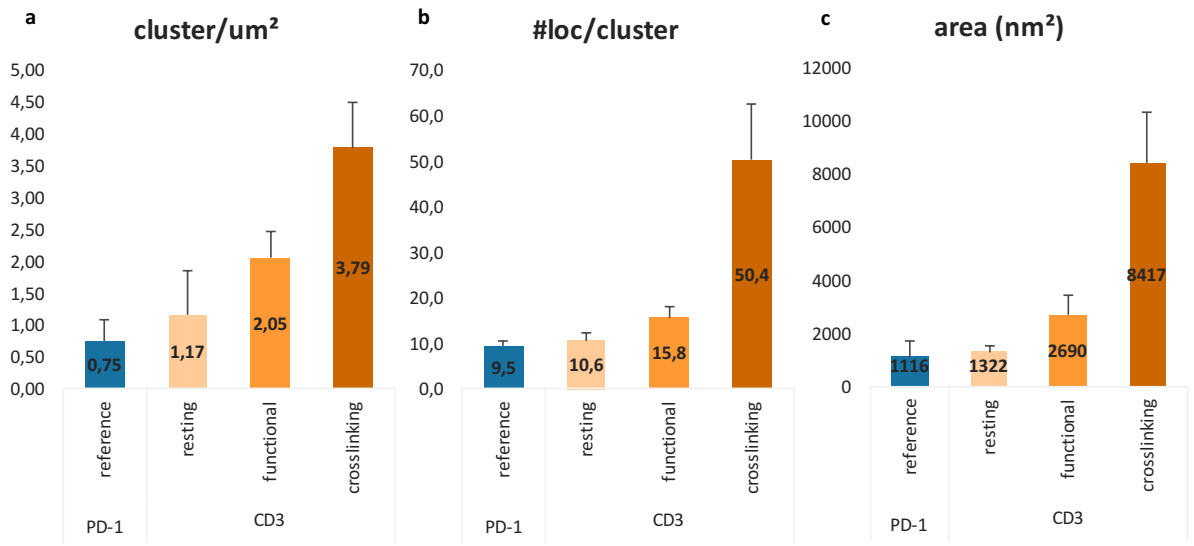

Figure 56. Comparison between CD3 and PD-1 clusters*. (a-c) Quantitative comparison of three clustering parameters (number of clusters per cell, number of localizations per cluster, cluster area (nm²) between CD3 receptors on resting Jurkat cells (n=10), CD3 receptors on Jurkat cells activated by OKT3 coating for 15min (functional, n=8), CD3 receptors on Jurkat cells activated by antibody cross-linking for 30min (n=3), and PD-1 receptors on activated Jurkat cells by OKT3 coating for 24h (n=5*).

T-cell activation induced a clear CD3 spatial reorganization. Depending on the mode of activation, the triggered CD3-dependent signaling pathways lead to different patterns of CD3 receptor nanoscale organization at the membrane surface. Whereas, the increase of clusters area and number of localizations per cluster is the signature of receptors clustering, the increase of cluster density upon T-cell activation suggests a receptor recruitment at the Jurkat cell surface. For the functional condition performed using an anti-CD3 coating, the number of clusters slightly increased by about two-fold compared to the resting condition (2.05+/-0.43 VS 1.17+/-0.69). This suggests that some intracellular pools of CD3 could have been recruited at “the contact zone”, mimicking an immunological synapse. In contrast, the significant increase of cluster size, number of clusters and number of localizations for the anti-CD3 cross-linking condition, could indicate that the receptors were recruited from all over the cell to the contact zone, increasing massively the total number of receptors/clusters at the imaged membrane. It would be interesting to verify if it happens only at the contact zone or all over the cells surface by 3D-SMLM (chapter 3.3).

However, we need to be cautious with the biological interpretation, since bias can be induced by the imaging protocols. Indeed, the primary and secondary antibodies, as well as the immunostaining protocols differ for the different conditions. Moreover, the permeabilization process used for the functional condition (Appendix) was performed before staining, which could allow the staining of intracellular CD3 proteins. However, whereas the fixation was done after anti-CD3 labelling, the “protein island” induced by the cross-linking condition could be the result of fluorophore aggregates coming from antibodies specifically added in this protocol. It is therefore difficult to confirm such hypotheses since TIRF method does not permit to image the whole T-cell surface. Still, the surprising result of this analysis is the small difference observed between the resting and the functional activation states (Figure 55 & 56). Additional quantifications need to be performed to better characterize T-cell receptor clustering.

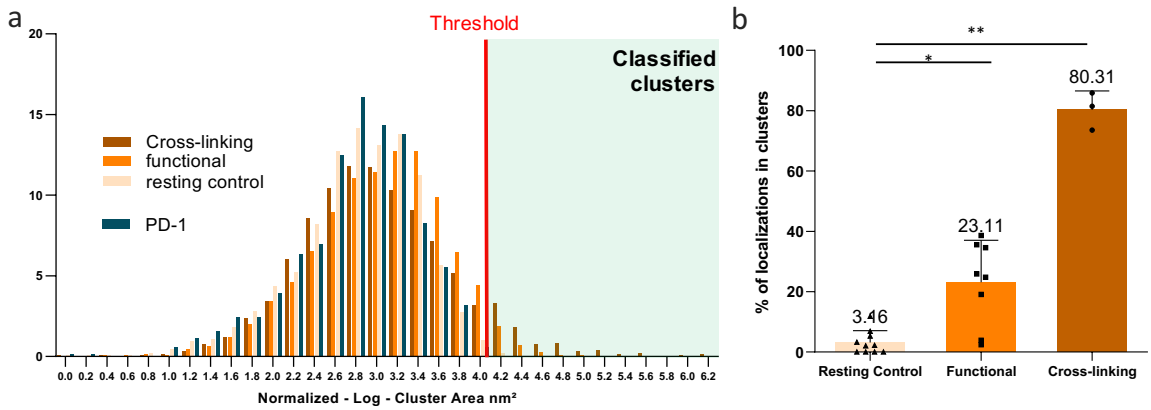

Figure 57. Analysis of the percentage of localization contained in clusters of receptors. *(a) Normalized distributions (Log transform) of the cluster area for CD3 and PD-1 conditions: CD3 on resting Jurkat cells (n=10), CD3 on Jurkat cells activated via OKT3 coating (n=8), CD3 on Jurkat cells activated via antibody cross-linking (n=3), and PD-1 on activated Jurkat cells (n=5). "Large" localization clusters, representing potential clusters of receptors, were classified using a threshold measured form the CD3 resting condition cluster area distribution (red line). (b) The number of localizations in each class of clusters allows estimating the percentage of molecules contained in clusters of receptors. Distributions were normalized with CD3-resting condition, P-values were calculated using Kruskal-Wallis test.*

Instead of taking into account all the localization clusters, I focused the analysis on the "large" clusters, which are clusters statistically larger than the ones in the resting state. We can estimate this sub-group of clusters to be clusters of receptors, since I already proved that there was no cluster formation at Jurkat resting state. To do this, the distribution of all the localization clusters area was computed for the three CD3 conditions, and a threshold based on the resting condition was defined to separate clusters of CD3 receptors from isolated CD3 receptors. The threshold, calculated for each experiment, was defined to 95% of the cumulative frequency distribution (Figure 57.a), to 11,231 nm² for this experiment. Then, for each cell, the total number of localizations contained in this sub-population of clusters was calculated, and divided by the total number of localizations in all the clusters. Using this parameter, we could estimate that 23% of the localizations were clustered for the cells functionally activated by an anti-CD3 coating, compared to 80% for the cells activated by cross-linking, and only 3% for the resting cells (Figure 57.b). It is important to note that these values are not physiological, they just provide quantitative insight on the level of receptor clustering.

As expected, the number of localizations contained in large clusters of receptors increased with the level of activation, in agreement with the Voronoi images (Figure 55). Per cell, the average number of large clusters only represent a small portion of the total number of clusters for each condition (1 cluster, resting; 18.38 clusters, functional; 42 clusters, cross-linking condition), which entirely justifies the need of advanced statistical analysis of the SMLM quantitative features. In comparison with the initial analysis of cluster size, number of clusters and number of localizations, this new parameter is more representative of the receptor clustering. Even if not biologically relevant, it provides a finer readout to discriminate clustering conditions via SMLM, that can be used in the framework of HCS-SMLM.

This pilot analysis of clustering patterns demonstrated that HCS-SMLM can decipher CD3 spatial organization with respect to the cell activation. However, no similar organization could yet be demonstrated for PD-1.

4.2.2. Experimental condition setting for HCS-SMLM experiment

Until now, I demonstrated that the expression of PD-1 was induced at the cell surface following activation, without any obvious specific pattern reorganization. In order to differentiate therapeutics mAbs action on PD-1 receptor, I searched for an efficient read-out able to discriminate for any change that could occur in the PD-1 nanoscale organization. To achieve this goal, I screened several conditions covering two activation time points (24 hours and 4 days, Chapter 3) and a kinetic of anti-PD1 contact with Jurkat cells (from 15 minutes to 24 hours) with two well-known therapeutic mAbs, the Nivolumab and Pembrolizumab (Chapter 2), at two mAbs concentrations (0.5 and 5 µg/mL) (Figure 58.a).

The first idea was to compare the effect of both clinical and functional anti-PD1 mAbs with a standard anti-PD-1 antibody used for PD-1 detection in immuno-fluorescence applications. Unfortunately, all the PD-1 immuno-staining assays performed on 96-well plates were not convincing due to the weak PD-1 signal obtained at the membrane of activated Jurkat cells compared to Nivolumab labelling (data not shown). More experiments would have been required to find the good anti-PD1 mAb, or the right immune-staining protocols allowing faithful imaging of PD-1 receptor at the cell surface.

Finally, I compared all these conditions with the native PD-1 receptor distribution induced at the cell surface, i.e. PD-1 distribution obtained on CD3-activated fixed Jurkat cells, and then revealed by anti-PD1 mAb. All the protocols employed for imaging, specificity and clustering controls are described in the appendix.

Each condition was done at least in duplicate, leading to a total of 30 conditions including controls (CD3 conditions have been screened separately (Chapter 4.2.3)). To increase our capacity of SMLM acquisition, we integrated an innovative beam shaper (Asphericon ©) in the optical path of the setup, providing a homogeneous illumination on the entire FOV (Stehr et al[125], 2019). It allowed to increase by two-fold the number of cells per FOV, improving the total HCS-SMLM acquisition time in the time limit of dSTORM (Appendix). The number and the choice of conditions have been carefully studied to respect the buffer dSTORM lifetime of 10h (Beghin et al[75]). To respect this time limitation, the plate was divided into two subparts which have been screened sequentially.

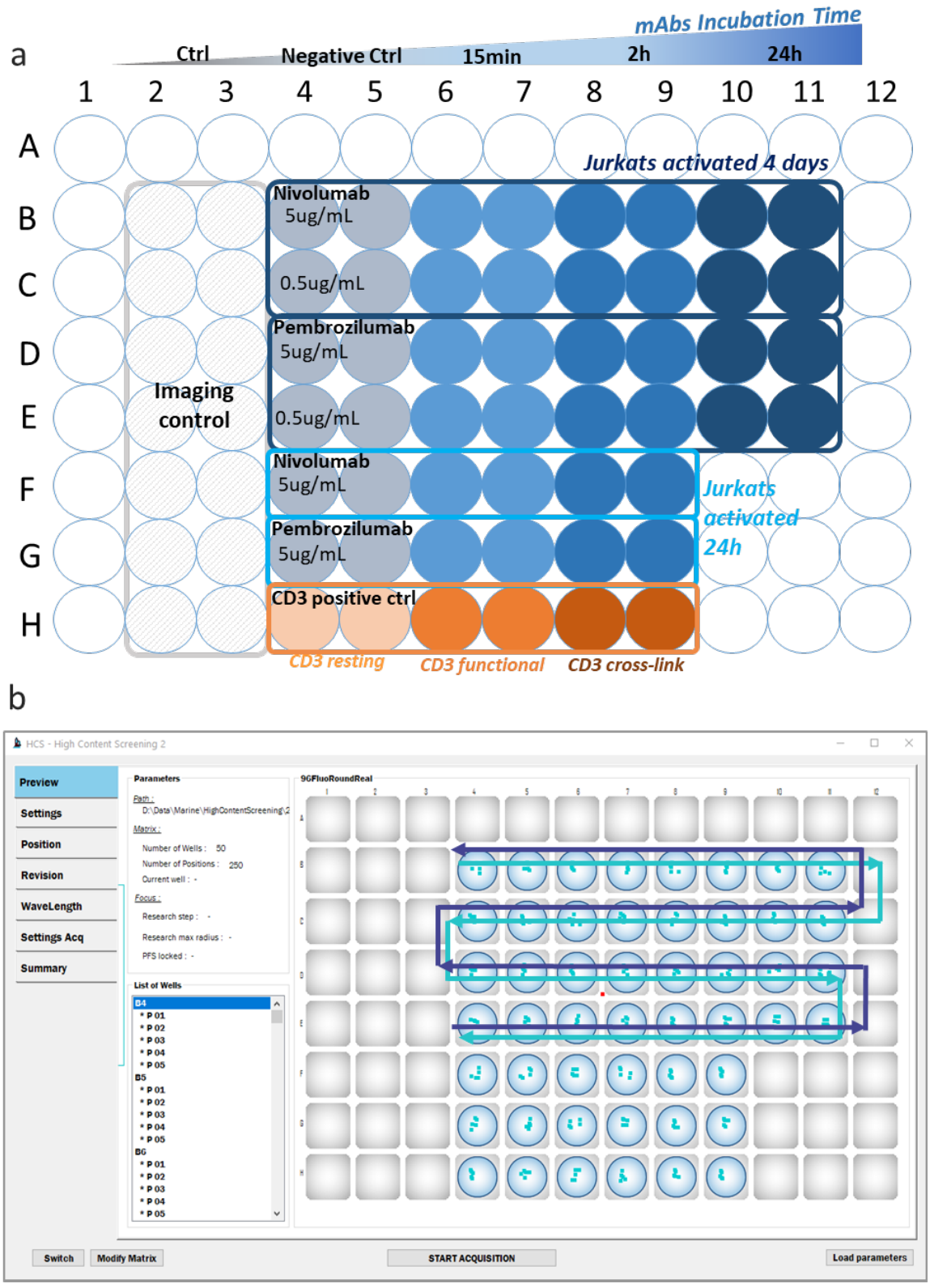

Figure 58. 96-well plate experimental layout for the characterization of therapeutic mAbs effect on PD-1 spatial nanoscale organization. *(a) Plate layout with multiple conditions: incubation of Nivolumab [0.5µg/mL-5µg/mL], Pembrolizumab [0.5µg/mL-5µg/mL] on 4 days activated Jurkat cells for [15 min, 2H, 24H] before fixation. Incubation of Nivolumab [5µg/mL], Pembrolizumab [5µg/mL] on 24h activated Jurkat cells for [15 min, 2H] before the fixation. Three CD3 conditions were used as reference to control the clustering effect of T-cell receptors. (b) Graphical user interface of the HCS-SMLM software which allows handling the automatic HCS-SMLM acquisition of each selected position (each blue square represents one position). The blue line shows the path followed for the acquisitions. The localization files and reconstructed SR images were automatically computed using WaveTracer and saved into a database during the 96-well plate acquisition.*

4.2.3. Automatic acquisition and analysis pipeline

Once all the parameters (Appendix) defined on the HCS-SMLM interface, the whole acquisition was launched (Figure 58). Before each acquisition, the dSTORM buffer was carefully prepared and disposed into the wells. The wells were filled to the top, and a large rectangular coverslip was used to hermetically seal the wells to avoid air bubbles. The software automatically handled the single molecule acquisition sequences, fields of view after fields of view, with up to five fields of view per selected well. For each FOV, two HR-TIRF images at two different wavelengths (WGA-488 and PD-1-A647 or CD3-A647), as well as a bright-field image were taken before the single molecule acquisition sequence. Before launching the SMLM acquisition in TIRF mode, a “pumping phase” of few seconds in widefield mode was achieved to synchronize the fluorophores into their triplet state (10,000 frames, 42 fps, 64 x 64 μm^2 FOV). This experiment has been conducted in a "snake mode" and "series-plate mode". The “snake mode” ensures a minimum stage displacement between the wells. The “series-plate mode” consists in acquiring only one FOV position per each well, then looping to the next FOV position of each well by following the invert path, until the end of all the positions (e.g. A1-P01; A2-P01; A3-P01; … AnP01; AnP02; … A3-P02; A2-P02; A1-P02; A1-P03; …). It was particularly important in the case of dSTORM to avoid bias due to the imaging buffer degradation over time, and its potential impact on the quantifications. The total screening time of the whole plate for the two subparts acquired separately was 15h30. After the suppression of unusable data, manually (out of focus) or automatically (non-registered, less than 7%), the whole database size including raw image stacks was 513GB, representing 165 FOV, and 949 analyzed cells. The database contained:

- 1 raw single molecule image stack (64 μm*64 μm size, 10k frames, 42 fps)
- 1 bright field image
- 1 HR-TIRF image of PD-1 or CD3 receptors
- 1 HR-TIRF image of WGA-cell membrane
- 1 registered SR image
- 1 registered localization file

Following the guidelines of the clustering analysis workflow described earlier, the database was automatically transformed for metadata extraction and quantification (Figure 53). Localization files were filtered using Chi^2 [0.7;1] and σ_{xy} [0.6;2] to remove aggregates, background and auto-fluorescence. Clustering data were extracted automatically from all the segmented cells via SR-Tesseler software. Finally, the clusters containing less than 5 localizations were filtered-out, and the global statistics were computed automatically and saved into two separated .txt files. At the end, this HCS-dSTORM experiment resulted in a complete database of localization and clustering metadata (including more than 15 different features). This experiment successfully validated the overall HCS-SMLM acquisition and analysis workflow.

4.2.1. HCS-SMLM experiment specificity and quality control

I controlled the quality, specificity and background of the single molecule signals of PD-1 and CD3 experiments acquired by HCS-dSTORM.

First, no fluorescence intensity signals from HR-TIRF images of isotype controls conditions were observed in comparison to Nivolumab, Pembrolizumab and OKT3 reference

conditions. These controls confirmed the specificity of PD-1 and CD3 signals and validated the experiment (Figure 59).

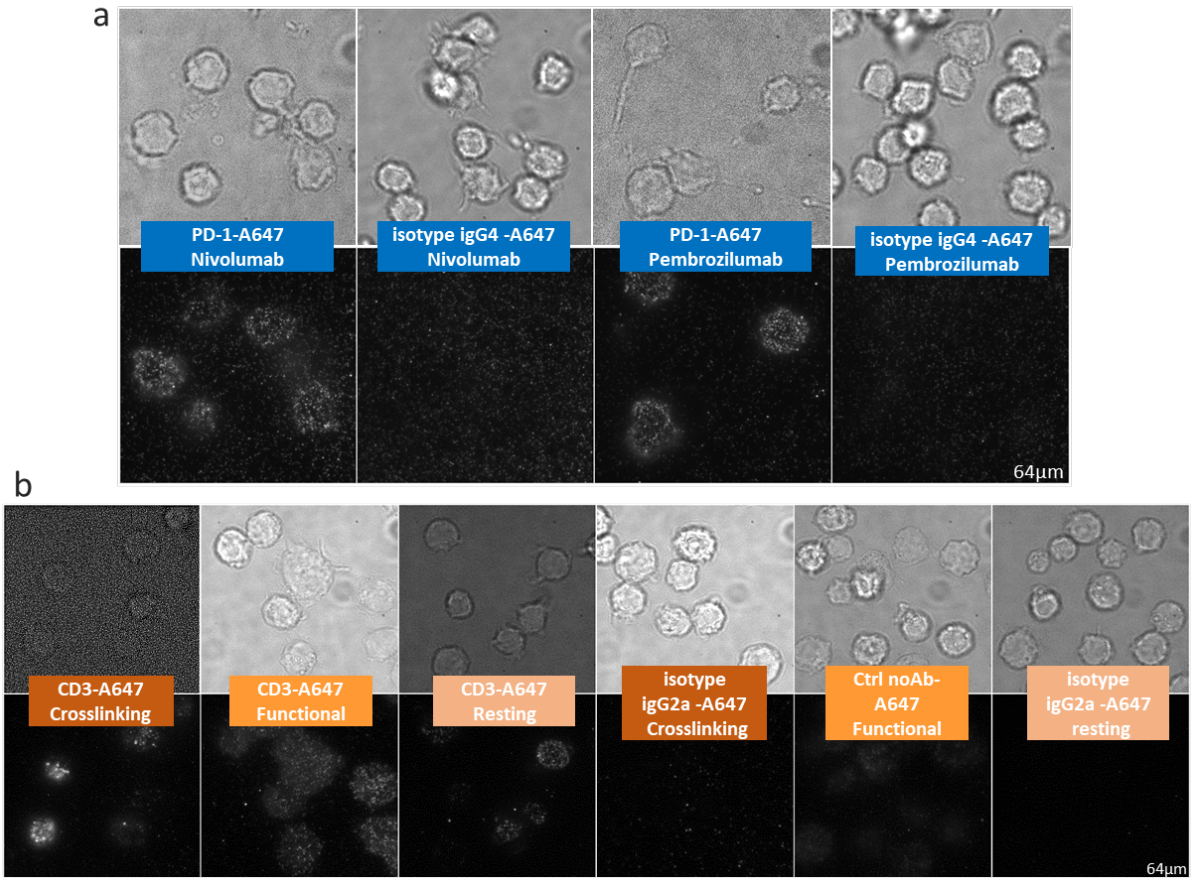

Figure 59. Specificity of CD3 and PD-1 signals. *(a) TIRF images of 4 days-activated Jurkat cells using the anti-PD1 Nivolumab IgG4 mAb (5 µg/mL), the anti-PD1 Pembrolizumab IgG4 mAb (5 µg/mL), and their IgG4 isotype controls (5 µg/mL). (b) TIRF images of the three CD3 conditions (cross-link, functional and resting) with the anti-CD3 mAb OKT3, the IgG2a isotype mAb, and without any primary Ab. All the TIRF images (64x64 µm) are displayed using the same intensity-scaling for comparison.*

In order to validate both screening acquisitions, I controlled the overall quality of the single molecule signals in the wells C5-F4 (Figure 60). These two wells are two PD-1 activated reference conditions (F4:24h activated; C5: 4 days activated), and have been acquired in the two separated screening acquisitions. For each well, three images were analyzed after sequential acquisition from +1h to +6h after the dSTORM buffer sealing (C5_1, T+1h; C5_2, T+3h; C5_3, T+6h; F4_1, T+1h; F4_2, T+2h30; F4_3, T+4h30). The analysis compared background signal and cell signal.

These results indicated homogeneous single molecule integrated intensity (3820+/-2318.83) and size (σ_{xy}, 0.96+/-0.1) across the images. In addition, cells clustering analysis revealed similar values of number of localization per cluster (22.67+/-30,14) and cluster area (880+/-1065.83 nm^2). The homogeneity of σ_{xy} values is also explained by the filtering step (Figure 60.b). As an example, 69% of the localizations of C5_2 remained after filtering. Here, the single molecule signal and clustering parameters extracted from the cells presented homogeneous values, validating the reproducibility of the HCS-SMLM acquisitions all along the screening process, and the limited impact of the dSTORM buffer degradation overtime.

The same analysis was performed on the background regions (Figure 60). It resulted in very similar results for σ_{xy} (0.96+/-0.1 vs 0.94+/- 0.08), integrated intensities (3820+/-2318.83 vs 4217.3+/-2498.17), number of localization per cluster (22.67+/-30,14 vs 19.35+/-29.72), further validating the robustness of the HCS-SMLM acquisition workflow. Surprisingly, the

cluster area in cells were bigger than background's clusters (880+/-1065.83 vs 396+/-682.83 nm^2).

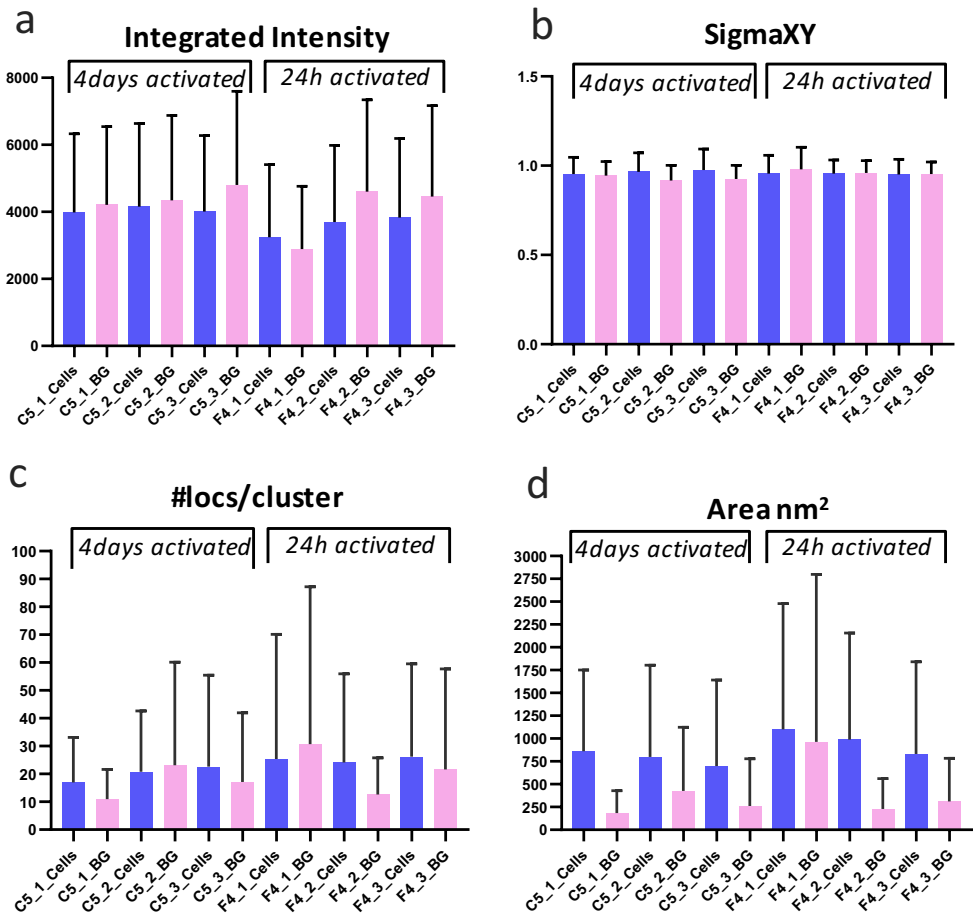

Figure 60. Quality control of the single-molecule signal. *(a-e) Comparison of single molecule signals and clustering features computed for each image from the background (pink) and the cells (purple). (a-d) Dyes photo-physic and clustering features average values obtained from 6 PD-1 reference images (C5: 4 days activated/F4: 24h activated): (a) Integrated intensity and (b) σ_{xy}, (c) number of localizations per cluster and (d) cluster area. (C5_1, n=6; C5_2, n=8; C5_3 n=8; F4_1, n=6; F4_2, n=6; F4_3 n=4).*

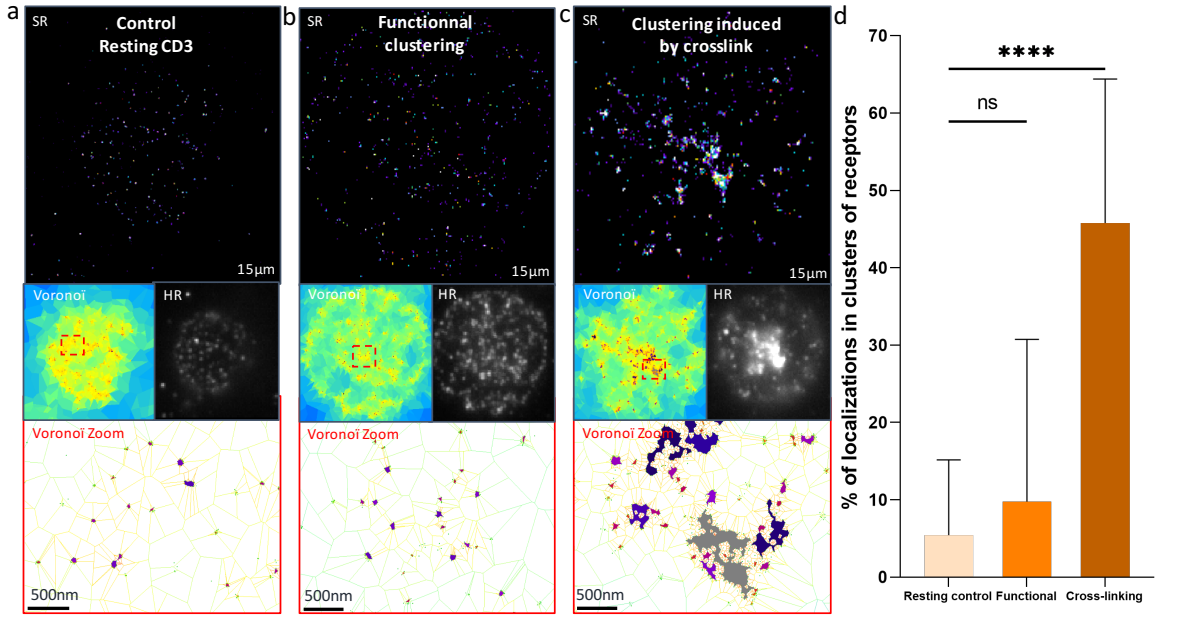

Figure 61. HCS-SMLM experiment of CD3 receptor clustering. *(a-c) Three representative illustrations of CD3 nanoscale spatial organization: (a) resting Jurkat cells, (b) activated Jurkat cells induced by OKT3 coating, and (c) activated Jurkat cells induced by antibody cross-linking. Nano-clusters were segmented and analyzed using Voronoï-tessellation (SR-Tesseler, Level et al. 2015). Bottom images are 500 nm wide zooms of the Voronoï images showing the cluster segmentation. (d) Percentage of localizations contained in large clusters of each cell. Distribution were normalized with the control; P-values were calculated using Kruskal-Wallis test.*

Finally, I controlled CD3 receptors clustering used as positive controls of membrane receptors clustering. “Large” CD3 clusters of receptors were identified using a threshold (11773 nm^2) based on the CD3 resting condition. Similarly, PD-1 clusters of receptors were identified based on PD-1 reference condition (6396 nm^2). Unfortunately, CD3 functional conditions did not revealed any significant difference as previous experiments (Figure 57). Indeed, the percentage of localizations contained in large clusters was higher, but not significant compared to the resting condition (Figure 61.b). This may be explained either by the variability of Jurkat cell behaviors, or by a problem of activation time. As shown in Figure 61, clusters seem to be more concentrated toward the center of the cells, and a longer activation onto the coating would perhaps have been necessary to induce larger cluster formation. In any case, cross-linking condition positive controls were validated, enabling PD-1 spatial nanoscale organization quantifications.

As a final control, we compared PD-1 clustering features obtained from HCS-dSTORM with single cell experiments. The clustering features extracted from cells under the same condition (PD-1 reference on 24h activated Jurkat) differed for the cluster density (0.75 clusters/μm^2 vs 1.08 clusters/μm^2), cluster area (733.67 nm^2 vs 1039.9 nm^2), and number of localizations per cluster (7 vs 21.3). Several reasons could explain such differences making difficult to compare the experiments. First, the acquisition and analysis workflow was not identical (number of frames per acquisition, filtering step, background normalization). Second, the clustering analysis is sensitive to the heterogeneity of T-cell activation and PD-1 expression level at the membrane. Indeed, in a single cell experiment, the analysis is only focused on the manually chosen cell of interest, whereas in the HCS approach, the amount of data allows taking into account this variability.

To summarize, quality control of HCS-SMLM experiments is important to guaranty the quality of the data all along the acquisition process. It allows the standardization of the experiments and precludes for potential bias in the analysis.

4.2.2. Quantitative results of the HCS-dSTORM experiment

Jurkat cells were manually classified into PD-1+ and PD-1- cells according to their PD-1 expression level. The integrated intensity values were calculated for each ROI and the background subtracted. For all PD-1 conditions, the average integrated intensities of PD-1+ cells of activated cells was 5-fold higher than PD-1-cells, and 39-fold higher than resting cells seeded on PLL (Figure 62.d). The huge standard deviation confirmed once again the important variability of PD-1 expression level on activated Jurkat cell population. Figure 62.c indicates the proportion of PD-1+ and PD-1- cells per well on 4 days and 24 hours activated cells. This percentage was homogeneous among the wells, and quite similar between Jurkat cells activated for 24 hours and 4 days, confirming our previous results on the PD-1 expression kinetic (Figure 41-Chapter 3). This manual analysis revealed that an average of 62% of cells expressing PD-1 (PD-1+ cells) after 4 days or 24 hours activation (Figure 62.d). It is a small proportion, but we have to keep in mind that these cells are immortalized human T-lymphocytes that continue to divide. Using the background integrated intensity as a reference, I was able to classify the cells automatically. In contrast with the manual classification, an average of only 49% of cells per well were defined PD-1+ for a similar number of PD-1- cells (41 versus 38%) with 10% of false positive (Figure 62.d). For further experiments, I would recommend the use of the automated PD-1 process because it provided an objective and accurate segmentation, and improves the cluster analysis automation.

Since the goal of this work is to determine if the therapeutic anti-PD-1 mAbs, Nivolumab and Pembrolizumab, impact PD-1 receptor nanoscale spatial organization, I focused the analysis on PD-1+ cells. Each condition exhibited a minimum of 9 PD-1+ cells, which was a sufficient to provide a robust quantitative analysis.

In this context, the data extracted from the HR-TIRF images provided valuable information used for cells classification, but did not provided access to the same level of information offered by super-resolution microscopy. Interestingly, the average intensity of HR images for each cell barely correlated with the cluster density obtained by SMLM cluster analysis (Pearson Coefficient = 0.6). Super-resolution provided more quantitative insight on PD-1 spatial organization at the T-cell membranes than classic fluorescent microscopy.

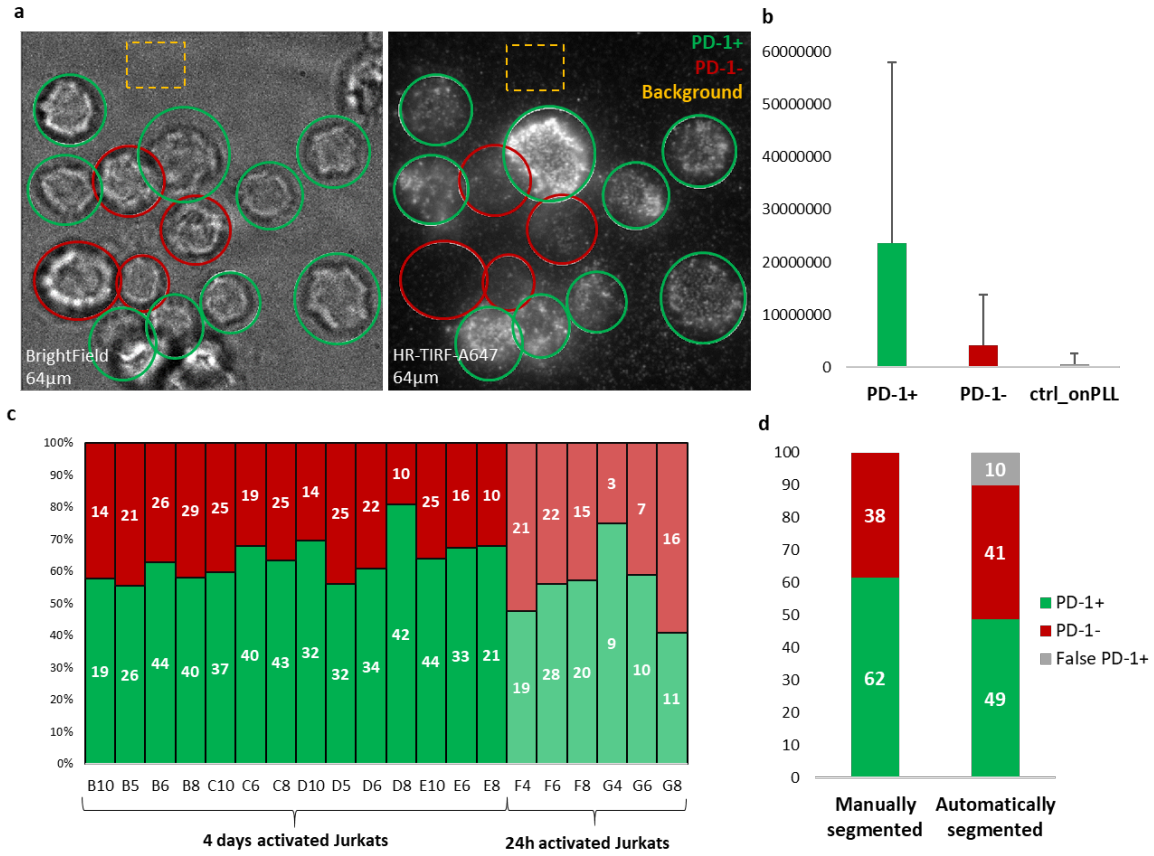

Figure 62. Analysis of PD-1 expression in Jurkat cells. *(a) Bright-field (left) and HR-TIRF images (right) of 4 days-activated Jurkat cells. Cells were manually segmented using circular ROIs on the bright-field images and tagged individually as PD-1+ in presence of fluorescent signal (green), or PD-1- in absence of fluorescence signal (red). The selected ROI were copied on the HR images to extract quantitative image features for each ROI (i.e. cells). (b) Average integrated intensity of PD-1+, PD-1- cells, and non-activated (resting) cells. (c) Each column represents the proportion of PD-1+ versus PD-1- cells per well for 24 hour and 4 days activation conditions. (d) Average proportions of PD-1+, PD-1- and false PD-1+ cells for all the conditions, depending on whether the cells have been segmented manually or automatically.*

The Figure 63 summarizes the quantitative analysis of PD-1 nanoscale organization by HCS-dSTORM. Heat-maps correspond to several clustering features extracted for each condition, with each value representing the average of medians calculated for PD-1+ cells.

The PD-1 expression and nanoscale organization induced by the incubation with PD-1 therapeutic mAbs were compared with the native spatial distribution in the absence of therapeutic mAbs. All the quantitative parameters showed that the native nanoscale organization of PD-1 receptor remained unchanged between 24 hours and 4 days activation time, excepted for the % of localizations contains in large clusters of receptors, which can be explained by the heterogeneity of activation of early activated Jurkat. The similarities with PD-1 native condition suggest that once expressed at the cell surface, its spatial organization do not change until PD-1 receptor is engaged into an interaction with its ligands or with a mAbs.

After incubation with therapeutic mAbs, both the cluster density and cluster area increased for the 4 days of activation condition compared to the 24h condition, for all the tested anti-PD-1 mAbs. The clustering parameters for the 24h activation conditions strongly fluctuated, suggesting that PD-1 receptors linked to Nivolumab or Pembrolizumab did not reach an organizational equilibrium, representative of an activation heterogeneity. Surprisingly, cells incubated 2h with anti-PD-1 therapeutic mAbs exhibited an overall decrease compared to others incubation times. Stronger differences were observed for cells activated 24h compared to cells activated 4 days. This suggests that more time points could be

interesting to investigate in a future experiment, in order to better understand what specifically happens around the 2h incubation time.

A deeper analysis revealed a significant difference in the cluster density between Nivolumab and the native PD-1 control conditions (Figure 64.a). The cluster density increased when cells activated 4 days were incubated with Nivolumab, for all concentrations and all incubation times (Figure 64.c). As expected with cluster density values, the less cells were activated, the less they expressed clusters at their surface. However, even if a similar effect could be observed between the control and the early activated cells, it was not significant (Figure 64.d). In parallel, Jurkat cells incubated with Pembrolizumab did not revealed any significant differences in the cluster densities compared to their negative controls at 4 days activation time (Figure 64.b, e). These results suggest that Pembrolizumab does not impact PD-1 cluster density. However, we could observe a clear increase trend for the 24h activation time condition, indicating a different mechanism between Pembrolizumab and Nivolumab.

Altogether, these results suggest that the cluster density parameter can be used a as read-out in Abs functions to discriminate between both therapeutics mAbs and control conditions. This raises the hypothesis that therapeutic anti-PD-1 Abs could prevent PD-1 receptors internalization compared to the native condition. Another possible explanation for the cluster density increase, could be that anti-PD-1 mAbs lead to recruitment of PD-1 at the cell surface, which could come from sub-membrane vesicular pools (Williamson et al[89], 2011).

Another interesting parameter to consider is the percentage of localizations contained in larger clusters of receptors (4.2.1), which pointed out clear differences for the different incubation and activation times (Figure 65). The results indicated a 2 to 4-folds higher concentration of localizations in large receptor clusters when Nivolumab and Pembrolizumab were incubated with living cells, compared to the PD-1 native control. However, such increase was only observed following 4 days activation (Figure 65.b, d). In contrast, we could observe a clear, but non-significant, decrease of this fraction of localizations on early activated cells after anti-PD-1 incubation with both mAbs, suggesting that antibodies/receptors ligation impacts PD-1 clustering.

Several other parameters displayed interesting differences between Nivolumab and Pembrolizumab. Indeed, whereas Nivolumab had a significant impact on the percentage of localizations contained in large clusters, the cluster density and the cluster area when cells were activated for 4 days, the effects of Pembrolizumab were more pronounced for the 24h activation time, confirming the potential different mechanism between Pembrolizumab and Nivolumab.

Finally, when compared with the CD3-induced clustering positive control condition (Figure 63, ctrl+), a moderate functional condition, and cross-linking condition, it seems that PD-1 receptor organization induced by therapeutic mAbs was closer to the CD3 resting and functional conditions for all the quantitative parameters. As anti-PD-1 therapeutic mAbs are described to prevent the inhibition of the T-cell immune response, a formation of PD-1 clusters, signature of activation, might be expected. However, our results suggest that their mode of action are different.

To summarize, tested anti-PD-1 mAbs, Nivolumab and Pembrolizumab, induced a nanoscale spatial reorganization of PD-1 receptors, leading to their clustering. Nivolumab induced a clearer PD-1 receptor clustering compared to Pembrolizumab for the same 4 days activation condition. Both mAbs didn't significantly changed PD-1 receptors nanoscale organization after 24h activation, compared to 4 days activation. Finally, the cluster density and percentage of localizations contained in cluster parameters, seem to be potential activation signatures for both anti-PD-1 mAbs.

4.2.3. Conclusions

Even if this first HCS-SMLM experiment of receptor clustering helped to decipher the clustering ability of receptors when bound by mAbs, a major question remains: can clustering analysis provide efficient read-outs to evaluate and characterize anti-PD-1 mAbs? This proof-of-concept HCS-SMLM experiment conducted on Nivolumab and Pembrolizumab demonstrated that nanoscale clustering analysis can efficiently highlight differences in PD-1 nanoscale spatial organization. Despite these promising results, no clear conclusions can be drawn. This experiment being conducted only once, it has to be repeated a few times, including a detailed kinetic, to support the first conclusions, and before testing potential anti-PD-1 candidates developed by Sanofi R&D's department. This first analysis will allow future investigations to be performed discarding some of the conditions, such as anti-PD-1 concentration of 0.5 μg/mL, which indicated no particular changes on PD-1 spatial organization. Beyond these conclusions, this first proof of concept validates all the protocols developed during my PhD as well as the HCS-SMLM automatic workflow, from cell culture to data quantification.

aPD-1 mAb screening			conditions PD-1				CD3
Jurkat Activation	therapeutic mAbs (C°f)		ctrl-	15min	2H	24H	ctrl+
% localization in clusters							
4days	Nivolumab	5 µg/mL	3.21	16.28	8.97	13.70	5.43
		0.5 µg/mL		14.73	9.46	14.95	9.76
	Pembrozilumab	5 µg/mL	6.64	12.79	11.87	11.62	45.76
		0.5 µg/mL		9.56	12.21	5.71	
24h	Nivolumab	5 µg/mL	15.38	11.24	7.64		
	Pembrozilumab	5 µg/mL	16.30	12.23	6.31		
cluster density (cluster/µm²)							
4days	Nivolumab	5 µg/mL	0.64	2.00	1.60	1.83	1.59
		0.5 µg/mL		1.68	1.63	2.19	0.68
	Pembrozilumab	5 µg/mL	1.08	1.57	0.83	1.84	1.05
		0.5 µg/mL		1.31	1.14	1.40	
24h	Nivolumab	5 µg/mL	0.65	0.92	1.02		
	Pembrozilumab	5 µg/mL	0.43	1.04	1.30		
Cluster Area (nm²)							
4days	Nivolumab	5 µg/mL	843.02	1120.99	948.68	933.40	1599.82
		0.5 µg/mL		1121.38	1062.78	1287.01	1080.85
	Pembrozilumab	5 µg/mL	1039.88	946.94	764.95	1028.54	2169.98
		0.5 µg/mL		1041.73	1155.99	954.25	
24h	Nivolumab	5 µg/mL	879.49	842.72	785.15		
	Pembrozilumab	5 µg/mL	798.97	788.56	652.13		
nbr_locs/cluster							
4days	Nivolumab	5 µg/mL	18.48	17.64	17.01	18.03	18.29
		0.5 µg/mL		19.25	19.02	19.81	17.20
	Pembrozilumab	5 µg/mL	21.33	19.84	18.73	21.08	23.33
		0.5 µg/mL		19.41	18.33	18.15	
24h	Nivolumab	5 µg/mL	20.47	17.55	16.28		
	Pembrozilumab	5 µg/mL	18.17	16.55	14.55		
localization density/nm²							
4days	Nivolumab	5 µg/mL	0.027	0.019	0.022	0.023	0.013
		0.5 µg/mL		0.022	0.021	0.018	0.018
	Pembrozilumab	5 µg/mL	0.025	0.024	0.040	0.026	0.012
		0.5 µg/mL		0.024	0.020	0.023	
24h	Nivolumab	5 µg/mL	0.028	0.026	0.025		
	Pembrozilumab	5 µg/mL	0.028	0.025	0.028		
cluster intensity							
4days	Nivolumab	5 µg/mL	67694	67055	61774	71031	54662
		0.5 µg/mL		74342	69851	68883	56821
	Pembrozilumab	5 µg/mL	81390	76020	77853	76028	62731
		0.5 µg/mL		62156	58781	66688	
24h	Nivolumab	5 µg/mL	70006	61378	57114		
	Pembrozilumab	5 µg/mL	67149	62571	51744		

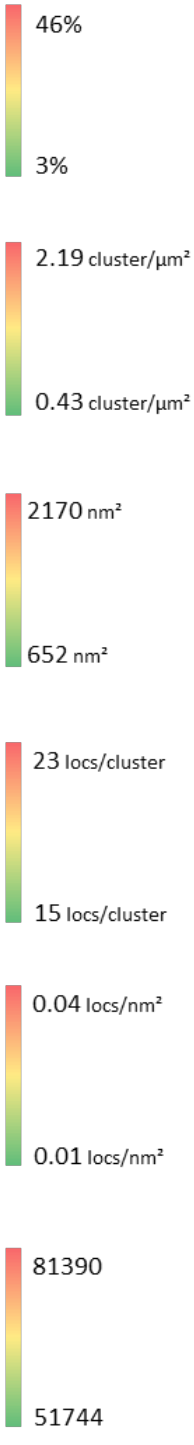

Figure 63. Heat-map of SMLM quantitative results of PD-1 clustering features. *Heat-map representing 6 clustering features for each condition: % of localization contained in large clusters, cluster density, cluster area, number of localizations per cluster, localization density, and cluster intensity. Each value represents the average of medians calculated from PD-1+ cell's cluster distribution. Values were color-coded between the minimum and maximum value of each array. Arrays describes all tested PD-1 conditions, including the negative control (w/o anti-PD-1 treatment, ctrl-). As positive controls (ctrl+), CD3 conditions were displayed on the right from the top to the bottom: resting, functional, cross-linking.*

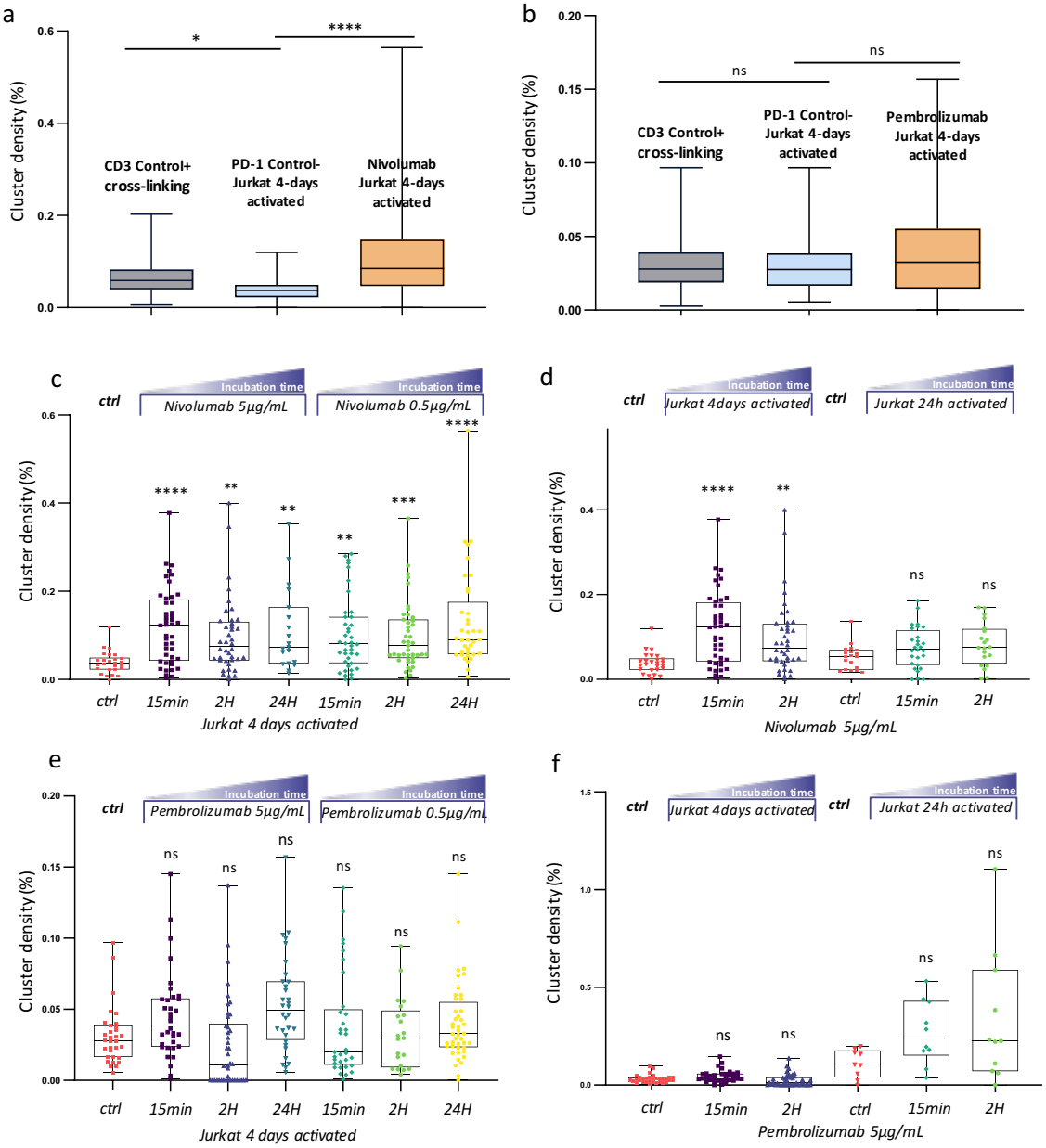

Figure 64. Cluster density (#cluster/µm²) of PD-1 after Nivolumab and Pembrolizumab treatment. *(a-b) Comparison of PD-1 cluster density of 4 days activated Jurkat cells between CD3 cross-linking, native PD-1 negative control, and all the PD-1 conditions for Nivolumab (a) and Pembrolizumab (b) treatments. (c-e) Comparison of PD-1 cluster density of 4 days activated Jurkat cells between 5µg/mL and 0.5µg/mL of Nivolumab (c) and Pembrolizumab (e) treatment. (d-f) Comparison of PD-1 cluster density of 4 days and 24h activated Jurkat cells between 5µg/mL (d) Nivolumab and (f) Pembrolizumab conditions. Each distribution was normalized with the PD-1 reference control (ctrl, red values); P-values were calculated using Kruskal-Wallis test.*

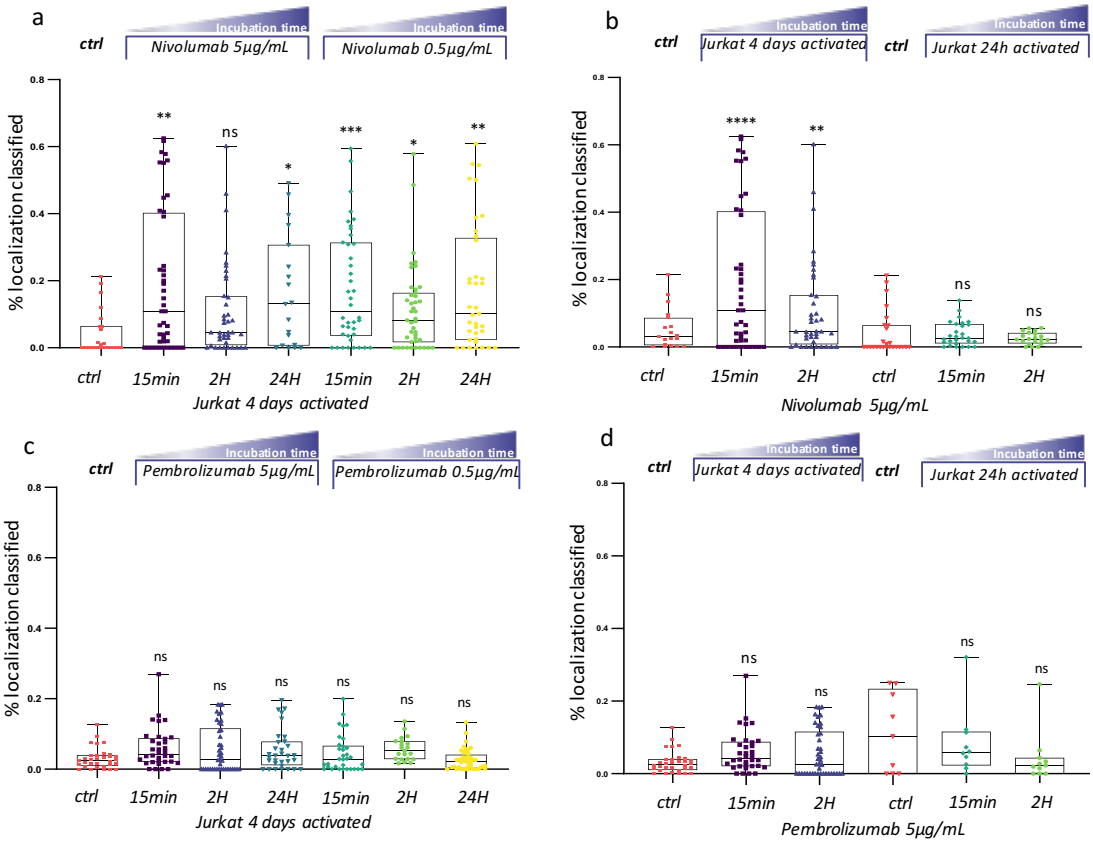

Figure 65. % of localizations contained in PD-1 clusters after Nivolumab and Pembrolizumab treatments. *Comparison of the % of localization in clusters of receptors of 4 days activated Jurkat cells incubated with 5µg/mL and 0.5µg/mL of Nivolumab (a) and Pembrolizumab (c) conditions. Comparison of PD-1 cluster density of 4 days and 24h activated Jurkat cells incubated with 5µg/mL Nivolumab (b) and 5µg/mL Pembrolizumab (d) conditions. Each distribution was normalized with the PD-1 reference control (ctrl, red values); P-values were calculated using Kruskal-Wallis test.*

5. DISCUSSION

My PhD thesis work follows the Beghin et al[75] 2017 initial publication. It aims at providing the proof of concept that HCS-SMLM can be used for drug-screening applications, by using the nanoscale spatial organization of key receptors as a quantitative read-out.

5.1. HCS-SMLM: optimization and perspectives

Prior studies have noted the importance of introducing super-resolution microscopy to HCS/HTS approaches (Barantine et al[106], 2019). Indeed, single molecule-based super-resolution microscopy already proved its ability to revolutionize biology by allowing the characterization of the nanoscale organization and dynamics of proteins. However, this process remains slow, complex, and usually requires lots of manual manipulations. It is a multi-step and multi-parametric operation which is limited to tens of cells per day and often undergoes acquisition-to-acquisition variability. This variability of SMLM experiments acquired over weeks or months, in addition to the high-level expertise required to perform such imaging and subsequent analysis, may impact the final quantification. On the contrary, combining HCS/HTS methods with SMLM ensures the same SMLM quality over all the conditions, by acquiring and analyzing images in a single workflow using identical settings. It is one of the major advantages of the HCS-SMLM method described here.

SMLM imaging is especially sensitive to inappropriate acquisition settings that could lead to artifacts, impacting images quality and analysis. In the context of HCS-SMLM, the side effect is that for all conditions, targeted proteins and antibodies must match and provide equivalent labeling density and blinking properties under the same conditions (i.e. dSTORM buffer, laser intensities, number of frames, camera frame rate, etc.). The HCS-dSTORM experiment described in this thesis as a proof of concept, notably presented a large portion of single molecules with short lifetime. These results are likely to be related to too high laser intensities. As suggested recently by Diekmann et al[73] (2020), one approach to reduce the amount of photo-bleached A647 over the acquisition would be to decrease laser intensities during the “pumping” phase. Optimizing imaging speed and excitation intensity might improve SMLM experiment quality included in an HCS pipeline.

For now, the HCS-SMLM workflow does not allow adjustment of acquisition parameters for individual or multiple conditions. We are considering integrating such functionalities to be able to either adjust SMLM settings specifically, or to use the settings themselves as read-outs to investigate SMLM properties (De Zitter et al[126], 2019). For example, integrating several read-outs into online SMLM parameter adjustment could be used to study the blinking properties of different fluorophores or different dSTORM buffers under several SMLM settings by varying laser intensities, camera frame rate, illumination type or combinations during the acquisition.

Continued efforts are needed to make HCS-SMLM more accessible. However, dSTORM turns out to be one of the most complex SMLM techniques in terms of stability over the time required for HCS-SMLM acquisitions. As explained in the introduction, DNA-PAINT revealed many advantages as it does not suffer from photo-bleaching, does not have imaging buffer life-time limit, can be quantitative, and has been recently shown to be able to reach acquisition speeds equivalent to dSTORM (Strauss et Jungmann[111], 2020; Schueder et al[112], 2019). Thus, it facilitates multiplexing as well as SMLM automatization, offering a good alternative to HCS-dSTORM. However, in the context of this thesis project, one main limitation is the use of human therapeutic antibodies, which prevented us the use of standard DNA-PAINT probes anti-mouse or anti-rabbit. To this end, we started a collaboration with Jungmann’s Lab in order to generate anti-human probes suitable for DNA-PAINT imaging.

(spt)PALM approach demonstrated in this thesis its high capabilities to provide interesting quantitative insight of the nanoscale receptor organization and dynamics. For now,

such approach is principally used for single cells imaging mainly due to the transfection protocols which provides a limited quantity of viable and transfected cells. But we can imagine the use of a stable Jurkat cell line expressing PD-1-mEos3.2, which would render this technique one of the most suitable method to perform quantitative and automated SMLM microscopy in a HCS fashion.

Another alternative could be to employ different fluorescent probes such as the photo-activable Janelia probes which don't require specific imaging buffer to perform single molecule imaging, and are also compatible with living cells imaging and single particle tracking.

In spite of the many advances in the field, there remains abundant room for further progress in improving HCS-SMLM acquisition pipeline.

Generally, I did not observe strong variability from well to well between the same condition in terms of cells density and fluorescence intensity. However, I could identify inhomogeneous background signal probably due to washing variability. If Abs are not well rinsed, it leads to an increase of the final background signals. Several solutions could be applied to solve inter-well variability and background issues. We recently demonstrated in our lab that salmon sperm combines with Dextran sulfate used as a blockade solution could resolve strong Abs non-specificity (Appendix). Other options could be to avoid anti-CD3 coatings responsible for the background issues by changing the way Jurkat cells are activated: either in suspension through anti-CD3 and anti-CD28 antibodies (alone or attached to micrometer-sized beads) or using supported lipid bilayers (SLB). SLB is a technique widely used in the field of T-cell imaging. It is cell membrane mimic interface which would provide a large range of possibilities in terms of T-cell functionalizing. It would allow, for example, to modulate its composition by increasing the density of anti-CD3 or adding T-cell membrane receptors ligands such as PD-L1. It would represent a valuable asset for our HCS-SMLM pipeline as it accesses to actual needs of potential users.

Another improvement would be the integration of a pipetting robot that would improve the pipeline by guaranteeing standardized immune-staining protocols. Beyond to be time savings, it would permit finer and more precise and reproducible incubation times of Abs, and a better control of the washing steps, a critical issue with non-adherent cells. Such a system would ease the reproducibility of HCS-SMLM experiments and render it more accessible. An ideal setup would integrate a pipetting machine directly on top of the microscope enabling many options (Klevanski et al[108], 2020): dSTORM imaging using fresh buffers, real-time DNA-PAINT probes washing and incubation (Exchange PAINT), live Abs incubation for living cell imaging, etc.

In our current HCS-SMLM pipeline, an automatic cell pre-selection before the acquisition and/or automatic post-processing cell segmentation would complete the automation of the whole workflow. For now, positions are manually selected before the HCS-SMLM acquisition, and after the acquisition, cells are manually segmented from the transmitted-light images before clustering feature extraction and statistical analysis. Both manual steps are time consuming and are based on users' subjective choices that may induce bias in the final quantification.

Selecting the positions manually is time consuming and must be taken into account in HCS-dSTORM experiments to respect the imaging buffer lifetime. As an example, it took me from 1h to 2h, so $^{1}/_{10e}$ of total buffer lifetime, to manually select more than 200 different positions for this proof of concept. A first option could be to pre-select the cells manually,

using a lower magnification objective via the pre-screening mode already implemented in the software I developed (Beghin et al[75], 2017). A second option would be to pre-select positions on the microscope before sealing the plate with the dSTORM buffer. Using appropriate calibrations, the pre-selected positions can be saved and retrieved after the 96-well plate removals from the microscope. These two options are already available in the HCS-SMLM, and will be considered for future HCS-SMLM experiments. Unfortunately, I did not have yet the opportunity to try these functionalities, because the HCS experiment described in this thesis has been run the days before the first France's lockdown due to covid-19.

Another limit of our current approach concerns the selection of the individual quantitative parameters to use for classification. It often relies on manual gating from reference positive and negative controls, similar to how we proceed in research labs with single-cell analysis. Our approach would definitively benefit from bioinformatics automatic supervised and unsupervised clustering that would allow the automatic comparison and classification of the various conditions based from the tremendous amount of data that we collect automatically (Rosenberg et al[93], 2020). These new methods could reveal unexpected new clusters of information based on non-physiological or cross-combination features, and would certainly help to decipher new finer and more robust read-outs.

More generally, it would be interesting to integrate machine and deep learning approaches in the HCS-SMLM workflow. Training deep learning networks with specific images, and patterns would for example enable the automatic cell segmentation and classification of bright-field and fluorescent images to improve the clustering analysis pipeline.

Finally, one last major limitation of single molecule-based super-resolution microscopy is the drift occurring during the acquisition. Here, I obtained 93% of successful registration for the HCS-dSTORM experiment, where images containing beads were selected manually before acquisition. In a fully automatic mode, getting rid of the assumption of fluorescent beads presence in the FOV would be a plus. To this end, it would be interesting to implement a fiducial-free registration algorithm in the HCS-SMLM pipeline, based directly on the localization coordinates and cross-correlation-based algorithm. This type of approach is widely used in this field by existing software or company (Ovesny' et al[127], 2014; Wang et al[128], 2014; ©Abbelight). This ongoing project already shown encouraging results and will be implemented in the future HCS-SMLM software. However, for this method to work efficiently, and avoid potential artefacts, one must require a very dense labelling with well identified structures, which was not the case of our biological models under our experimental acquisition conditions.

Beside the HCS approach, we demonstrated the 3D nanoscale imaging of whole T-cells to be a fruitful area for further investigations. Our soSPIM-based approach and the evolution I brought with the development of ZTrack, represents a very promising investigation tool, offering biologists a wide range of possibilities. It allows for example to perform co-culture experiments and to image the immunological synapse between different types of cells, such as dendritic cells/T-cells, or B-cell/T-cell conjugates with nanoscale single molecule precision. It is compatible with most SMLM techniques, such as DNA-PAINT and (spt)PALM on fixed and living cells, giving complementary functional information to the HCS-SMLM method. While my work was focused on the optimization of the system to perform 3D automatic acquisitions, it remains possible to integrate HTS acquisition automation in the soSPIM acquisition, since the microchip offers intrinsic screening capabilities. Combining soSPIM with HCS would make it possible to investigate new biological processes, not possible in TIRF illumination. Combining together the HCS-SMLM and SMLM-soSPIM methods, would bring new insight to the

comprehension of T-cell membrane nanoscale receptor organization. Unfortunately, it will be at the expense of time consuming and a more complex experimental acquisition and analysis workflow.

5.2. HCS-SMLM, an imaging platform for immunotherapy applications

Why HCS-SMLM instead of HCS-HR? Does super-resolution bring new insights in the characterization of T-cell membrane receptors? Is single molecule-based super-resolution microscopy important to understand complex underlying mechanisms of immune cells receptors?

Commercially available HCS-HTS systems furnish global and general readouts, such as fluorescence intensity, morphological features, etc. In addition, "obscure" features obtained using filters and convolutions (e.g. texture features) are created to extract further information, which, like deep learning approaches, provide non-contextual and non-physiological readouts. However, in contrary to SMLM, they are not explicitly usable to explain behaviors or phenomena observed. Throughout my research project, I have been able to demonstrate that SMLM gives out more quantitative information of immune cell-membrane receptors than classic fluorescent microscopy. Moreover, it provides a very fine read-out compared to bulk microscopy, and the access to a large number of quantitative parameters, from which we only used a small fraction during this pilot experiment.

The advanced quantitative microscopy techniques I used during my PhD helped to improve our comprehension of the modes of action of therapeutic antibodies on targeted PD-1 receptors. They permit the observation of their subcellular trafficking and nanoscale spatial organization, enabling the understanding of the induced signaling pathways at the single molecule level. I succeed to demonstrate the functional proof of concept that the HCS-SMLM approach, we developed in the Quantitative Imaging of the Cell team, could provide essential information requested to differentiate efficacy of therapeutic candidates. To achieve this proof of concept, I used and improved the HCS-SMLM platform on a model based on two therapeutic mAbs used in the clinic for cancer immunotherapy: Nivolumab and Pembrolizumab. One of the main questions raised by the checkpoint inhibitor model was: is mAbs function reduced by blocking the PD-1/PD-L1 ligation, or does it induce deep changes on T-cells such as receptor reorganizations and intracellular signaling, maintaining cellular activation? To answer such question, despite no preconceived answers could be found in the literature on the subject, we investigated differences between both the mAb's effect on PD-1 organization and dynamics at the membrane of Jurkat cells. This study undertaken using the HCS-SMLM imaging platform was acknowledged by first promising results. Despite its exploratory nature, this proof of concept revealed significant differences between Nivolumab and Pembrolizumab, in the cluster density and the number of receptors present in large clusters. We did not necessarily expect any differences between both mAbs, since both antibodies are competitors of PD-1 receptor binding to PD-1 ligand: PD-L1. However, the fact that they do not recognize the same domain on PD-1 receptors can generate functional differences. Nivolumab binds partially to the PD-L1 binding site on the PD1 receptor, whereas Pembrolizumab covers it entirely. In addition, Pembrolizumab remains functional in Fab format, as opposed to Nivolumab which only displays functional effects in IgG format, and therefore could potentially bind to two PD-1 receptors. This leads to the hypothesis that Nivolumab is able to recruit and/or immobilize more receptors at the membrane, whereas Pembrolizumab could be internalized more rapidly.

This research has brought up many questions that further need to be investigated. Indeed, these first hypotheses could be drawn from the present HCS-dSTORM experiment, which needs to be reproduced several times before final conclusions. Further improvements of the analysis pipeline are recommended to provide robust control of SMLM quality over an entire 96-well plate. We can also expect from the cluster analysis to explore finer readouts for mAbs nanoscale characterization. In addition, motivated by our preliminary promising study of PD1 dynamics, further experimental investigations on PD-1/mAbs dynamics will be carried out by sptPALM or uPAINT combined with HCS. Receptor diffusion analysis already provided clear read-outs in comparison to the controls, and single protein tracking techniques present high potentials, and might be the best approach for mAbs characterization.

5.3. Perspectives & Technology Transfer

Once the proof of concept was validated on Pembrozilumab and Nivolumab, the initial project aimed to use the HCS-SMLM as a screening platform to compare the modes of action of potential mAbs candidates targeting PD-1 created by Sanofi. However, for the sake of time, we could not go further than the proof of concept. Once the previous results will be reproduced, protocols and methods developed during this PhD will serve to screen up to tens of conditions in a 96-well plate format. The nanoscale spatio-temporal organization of checkpoint inhibitors after mAbs ligation will help in understanding how it triggers complete lymphocyte activation and how our antibodies are acting compared to the benchmark antibodies used today in the clinic or in *in vivo* studies. We can expect these studies to provide new insights for homemade mAbs characterization for drug commercialization purpose.

The present study lays the groundwork for promising future research for cancer immuno-therapies by investigating either co-stimulatory or co-inhibitory targets. The determined clustering patterns provided by HCS-SMLM are expected to be different between agonist (co-stimulatory) and antagonist (co-inhibitory) receptors. Indeed, agonist receptors are more likely leading to receptors clustering upon T-cell activation (e.g. CD28, OX40, etc.). Thus, their study by HCS-SMLM could enable a drastically clearer read-out in therapeutic mAbs effect in terms of clustering and dynamics. Further model development work will have to be conducted in order to determine the clustering and dynamic patterns of such receptors.

Finally, we began with a Jurkat cell line as a simplified biological model. However, for further experiments, donor samples will be employed in order to decipher more realistic cellular mechanisms of action and resistance phenomena. Reproducing HCS-SMLM experiments on primary T-cells would confirm the first results achieved on the Jurkat model and conclude on the therapeutic mAbs mode of action *in vivo* in humans. Ultimately, we aim to integrate the results obtain from technical immune approaches in Sanofi into the HCS-SMLM analysis (MLR and T-cell activation experiments). The SMLM quantitative analysis will be correlated to the T-cell behavior by measuring their proliferation and cytokine secretions as the signature of T-cell activation.

In conclusion, despite its exploratory phase, the success of this proof of concept project may lead to a potential technology transfer between the research institute and Sanofi. Our HCS-SMLM platform will help exploring and improving the comprehension of the mode of action of new therapeutic antibodies and their role in immune T-cell activation. The generated SMLM metadata will provide an essential database for the internal development of Immuno-Oncology therapeutic antibodies. Finally, we could imagine the HCS-SMLM platform to be used as a new prognostic tests dedicated to the immune-oncology field. Besides, the HCS-SMLM platform is a versatile tool which can be applied to various biological

applications. To this end, the technology will be also transferred in the Bordeaux Imaging Center of the Bordeaux University Campus, for making it available to the research community.

APPENDIX: *Protocols*

Jurkat cell culture protocol: Jurkat cells vial (ATCC, Clone E6-1, TIB-152) is thawed in a 37°C-water bath then the cellular suspension is removed and placed in a tube containing 15mL complete medium. Following gentle homogenization using a pipet, the cells are centrifuged at 800 rpm for 10min, the resulting supernatant is aspirated and the cells pellet is re-suspended with 10ml of warm complete RPMI (at least 30min at 37°C). After cell counting, 1.5 million of cells are mixed in a final volume of 12mL of warm complete RPMI and deposited in T75 flasks. Finally, flasks are settled lie down at 37°C with 5% of $C0_2$ in the incubator and cells are allowed to grow for 3 or 4 days. The same procedure is applied for the culture of JPD1 Jurkat cell line.

Culture medium for native Jurkat cells: The culture medium used to cultivate the Jurkat cell line is based on RPMI 1640-1X supplemented with Phenol Red, GlutaMAX™ and HEPES (Thermofisher, 72400047). 1% of Penicillin-Streptomycin and 10% of inactivated foetal bovine serum (FBS) are added to fully complete the RPMI medium (complete RPMI). Before mixing, FBS is warm up on water bath for 45 minutes at 56°C in order to inactivate the complement which could perturb or activate T-Cells.

Culture medium for human PD-1 recombinant Jurkat cell line (JPD1): The same complete RPMI medium is used and mixed with complementary selective reagents: RPMI-1X (Thermofisher, 72400047) supplemented with 1% of Penicillin-Streptomycin, 10% of inactivated FBS, 200µg/mL of Hygromycin B (Thermofisher, 10687010), 500µg/ml of Geneticin (Gibco, 15140-122), 1mM Sodium pyruvate and 0,1mM MEM NEAA (Gibco, 11140-050).

Thawing primary cells protocol: 45mL of X-vivo15 medium (Lonza, BEBP02-061Q) is warmed up in water bath during 30min. The human isolated CD3 primary T-Cell vial is quickly thawed in the water bath and cells are diluted in the 45mL of X-vivo15 medium. T-Cells are gently homogenized using a pipet and then centrifuged at 1500rpm for 10min. The supernatant is removed and the cells are re-suspended in warm X-vivo medium. The final volume of medium is calculated to obtain the wanted final concentration of cells.

General uses applied for immune-staining protocols: The osmolarity of Phosphate Buffered Saline (PBS) solution in contact with living cells is adjusted to 300-330mOsm. After addition of any reagents (PBS included) or Abs to the seeded cells in multi-well plate, each well is gently mixed with pipet. In case of soSPIM experiments, for a better homogenization of reagents or antibodies into the micro-wells, gentle mix steps are performed with 1ml-pipet several times. Each liquid injection is carefully proceeded to avoid cells detachment into wells. Finally, each well never stay completely dry.

Activating coating protocol: an anti-human CD3 coating for T-Cell activation is performed on the top of imaging glass-bottom support using the functional mouse monoclonal antibody OKT3 (clone OKT3 - eBioscienceTM - #16-0037-81). 100µL/well of 5µg/mL OKT3 diluted in PBS is deposited in a glass-bottom 96w plate (Matek- ref P96G-1.5-5-F) and incubated either at 37° for 3 hours or overnight at 4°C. Afterwards, coated wells are washed 3 times with warm or ambient PBS. Then the wells are filled with 300µL/well of PBS and kept at 37° until cells seeding (the plate can be left at 4°C up to 24h before seeding).

PLL coating protocol: To induce non-adherent cells adhesion we used a Poly-L-lysine coating (Sigma PLL P4707 - mol wt 70,000-150,000) on top of our imaging glass bottom support. 100ul/well of 5µg/mL PLL is deposited in a glass-bottom 96w plate. Then, the plate

is incubated at 37° for 45 min. Afterwards, coated wells are washed 3 times with warm or ambient PBS. Similarly, the wells filled with 300µL/well of PBS can be kept at 37° until cells seeding or at 4°C up to 24h before seeding.

Cells seeding protocol: After PBS removal from the coated wells of the glass-bottom 96w plate, 60-70k of Jurkat cells are seeded in 200µL/well of complete RPMI. The cells are allowed to settle at 37° from 30 minutes to 1h before receptor clustering, fixation or immune-staining steps. The incubation time varies depending on the experiment protocol. In case of incubations lasting several days at 37°C, wells surrounding the wells of interest must be filled with water to prevent liquid evaporation.

Supernatants recovery protocol: 100µL of the supernatant is gently taken from each well of interest of the 96w plate – only liquid at the upper state of the wells is removed to avoid taking any cells. Each supernatant sample is deposited into a well of a non-protein-binding 384w plate (Greiner, 781900). Then the 384w plate containing the supernatants is carefully closed with a plastic film, and frozen at -20° until its sending to Sanofi's lab for cytokine measurement.

Prefix immunostaining: In case of Prefix experiment, cells are incubated with a blocking solution composed of warm complete RPMI+3%BSA w/o Biotin (Roth, ref 0163.4-200g) for 30min at 37°C+5%C02 in incubator. Then the medium is removed and primary Abs diluted in complete RPMI medium are deposited in wells and let at 37°C+5%C02 for various incubation time, before the fixation. Afterwards, wells are washed 3 times, once with warm RPMI and two times with warm PBS. The cells are now ready for further staining steps except that the primary Abs staining step is avoided.

Fixation: The supernatant is taken from each well to let only 50uL of media remaining. 100µL of warm PFA4%+sucrose diluted in PBS (300-330mOsm to match with T-Cell osmolarity) is added on each well and gently mixed with 1ml-pipet. Then, the 96w plate is set for 10min at 37°C in an adapted incubator/hoven. Afterwards, wells are washed 2 times with PBS and quenched by 100µL/well of 150mM of Glycine (Euromedex, ref 26-128-6405-C) for 5min at RT before washing 3 times in PBS. In the case of an intracellular labelling, a permeabilization step is further required: after PBS removal, 0.3% of Triton-X100 (Sigma, ref T9284) is added and gently mixed for 20min at RT. Finally, fixed samples are washed 3 times with PBS.

Standard immunostaining protocol: Once cells seeded on the appropriate coating are fixed (cf previous steps), cells are incubated in blocking solution with 150µL/well of PBS-BSA5% (Sigma, ref A9647) for 1H at RT. 120µL/well of primary antibodies mixed with PBS-BSA2% is added on the wells for 1H at RT in the dark, followed by 3 washing steps with PBS-BSA2%, with 5min intervals of resting time between each washing step. Then, 120µL/well of secondary Abs diluted in PBS-BSA2% is deposited on cells for 1H at RT in the dark and then washed 3 times with PBS.

Post-fixation: After staining steps, a post-fixation step is carried out by adding 100µL/well of 4%PFA+sucrose for 5min at 37°C. Wells are then washed 2 times with PBS and 100µL/well of 150mM of Glycine is added for 5min at RT. After washing 3 times in PBS, the sample is wrapped in an aluminum foil and store at 4°C before imaging. The post fixation protocol is performed for both long term storage and to prevent the imaging of unbound fluorophores diffusing within the media during the SR acquisition.

Drift correction: For post-acquisition drift correction and membrane detection, 100µL/well of 1:1000 of Tetraspeck beads is deposited per well for 10min incubation at RT (Tetraspeck T7279, LifeTechnologies). Additionally, 1:1000 of Alxea-488 labelled WGA in PBS can be added with fluorescent beads.

dSTORM Pyranose switching buffer: The 3 separated solutions (Base (B) + MEA (M) + Pyranose (P)-Table below) that made up the Pyranose buffer were prepared in advance and aliquoted for -20°C storage. The pH of MEA and Base solutions was verified and adjusted to be 7.5pH using a pH-meter. Before dSTORM imaging, aliquots were allowed to thaw and the final imaging buffer was mixed as followed: 1mL B + 120µL P + 120µL M for a single mounted coverslip or 330µL B + 40µL M + 40µL P for one well of a 96w plate.

1/ BASE = B	2/ MEA (2M) = M	3/ PYRANOSE = P
45 ml TRIS 1X pH 8 (Euromedex EU0111)	1.136 g MEA (Sigma M6500)	200 µl TCEP 1M (Sigma C4706)
5 ml Glycerol (Sigma G5516)	5 ml dH_2O	100 µl Catalase (Sigma C3515)
5 g glucose (Sigma G8270)		50 mg Pyranose oxidase (Sigma P4234)
		22,5 ml dH_2O
		1,25 ml KCl 1M (Sigma P9333)
		1 ml TRIS 1X pH 7.5 (Euromedex EU0111)
		25 ml Glycerol (Sigma G5516)

CD3 cross-linking protocol: Once cells are seeded (after 30/60min) on PLL-coated multiwell plate (cf previous steps), cells are incubated with a blocking solution composed of warm RPMI+3%BSA w/o Biotin for 30min at 37°C+5%C02 in incubator. The blocking solution is removed and a mix of primary and secondary Abs diluted in warm RPMI is deposited on top of Jurkat cells for 30min in the incubator. The mix is composed of 2µg/mL of anti-human CD3 mouse antibody (OKT3, BioscienceTM - #16-0037-81), 4µg/mL of Alexa647-labelled goat anti-mouse antibody (Invitrogen, A-21235) and 4µg/mL of unconjugated goat anti-mouse antibody (Jackson ImmunoResearch, 115-005-071). Before fixation step, the medium is removed and the wells are washed carefully 3 times, a first time with RPMI, the two-last time with PBS. Cells are fixed and prepared for SMLM imaging.

CD3 functional clustering: 50-70k Jurkat cells are dropped in complete RPMI medium on each well of ~~a~~ OKT3-coated 96-well plate (cf previous steps), and let to seed in the incubator for **exactly** 15min to allow receptors to aggregate into clusters. After 15min, cells are fixed and permeabilized with 0,3% of Triton-X100 for 20min at RT. Following my standard immune-staining protocol, cells are stained using 2µg/ml of primary rabbit anti-human CD3 antibody (Abcam, ab135372) and 2µg/ml of A647-labelled goat anti-rabbit antibody (Invitrogen, A-21244) as secondary antibody. Then, cells are postfixed and prepared for SMLM imaging.

soSPIM protocol: Chips are washed firstly with ethanol and secondly 3 times with PBS. Micro-wells are covered with 1mL of 5µg/mL of Poly-L-Lysine (Sigma PLL P4707) for 45min at 37°C, then washed 3 times with PBS. Between 200-400µL of 500K/mL of Jurkat cells in complete RPMI are deposited in the center of each well, like one drop of liquid above the

micro-wells. Cells are allowed to seed for 15min in incubator. After 15min, the liquid excess is aspirated and another subset of 500K/mL Jurkat cells is deposited on top of wells. This step is repeated until the density of cells per well is sufficient (2/3 cells per 24*24μm microwells, 5/6 for 40*40μm microwells). Cells are allowed to seed during at least 2 hours for a complete adhesion. Before fixation, cells not contained in micro-wells are removed and washed with complete RPMI by aspiration/injection with a pipet. For the fixation, the excess of RPMI is aspirated and 1mL of 2%PFA+sucrose in PBS (300-330 mOsm) is deposited for 10min at RT. Wells are washed 3 times with PBS and quenched by 1mL of Glycine (150mM) for 10min at RT. After 3 washing steps with PBS, the petri-dish is incubated with 1mL of PBS-BSA 3% + 0.1 mg/mL Sheared Salmon Sperm DNA (Thermofisher AM9680) + 0.1% (wt/vol) Dextran sulfate (Sigma D4911) as blocking solution for 1H30 at RT. Then, a drop of 200-300μL/w of primary antibodies [1:300 of anti-PD-1 (14-99969-80, Invitrogen)] diluted in PBS-BSA2% + 0.1 mg/mL Sheared Salmon Sperm DNA is added on top of microwells overnight at 4°; followed by 3 washing steps with PBS-BSA-2% + 0.1 mg/mL Sheared Salmon Sperm DNA with 5min intervals of resting time between each washing step. Then a drop of 200-300μL of secondary Abs [1:1000 of DNA-PAINT probes anti-mouse (D1), massive photonics] diluted in PBS-BSA2%+ 0.1 mg/mL Sheared Salmon Sperm DNA are deposited on cells for 3H at RT in the dark and washed 3 times with PBS. Lastly, a second fixation step is done, as previously described but with only 5min of PFA incubation, after the immunostaining step. The petri-dished is wrapped in aluminum foil and store at 4°C before imaging.

PD-1 transfection of Jurkat cells by electroporation: The plasmides came from Sanofi and consisted in the human PD1 sequence fused to Meos3.2 fluorophore sequence either in its Ct or Nt part. The transfection of PD-1 in Jurkat cells ((Clone E6-1 ATCC, TIB-152) is done via electroporation using the LONZA-AMAXA system or the Neon system.

- **Using LONZA-AMAXA system:** The electroporation is performed using the VCA-1003 Lonza Kit. Day-2 cultivated Jurkat cells (to be at the exponential growth phase) are centrifuged 10min at 800rpm, and washed with 10mL of PBS before centrifugation again at 800 rpm for 10min. After counting, 2 million cells are placed in a 1.5ml-Eppendorf tube and centrifuged. The supernatant is discarded and 2M of cells pellet is mixed with 4μg/mL of plasmids in 100μL of amaxa kit reagent. The cells-plasmid mixture is then deposited in the electroporation cuve and set into the Lonza system. The program X-001 high Viability is applied into the cuve. After the electroporation, cells are recovered from the cuve with 1mL of warm complete RPMI without penicillin/strepomycin and placed in wells of 12 multiwell plate for 24h/48h in the incubator 37°C 5%CO2 before being imaged.
- **Using NEON system:** After 10min at 800rpm of centrifugation, Jurkat cells are washed with 10mL of PBS. After counting, cells are centrifuged again 10min at 800rpm and then mixed with the Neon Buffer "E" at a final concentration of 500k cells /2μg plasmid / 10μL. Using the NEON 10μL pipet, the final mixture is electroporated using the characteristic shown in the table below; and deposited in a 12 well plate filled with 1mL/well of complete RPMI without penicillin/strepomycin for 24h/48h in the incubator 37°C 5%CO2 before being imaged.

DNA	Cell/10uL	Pulse voltage (V)	Pulse Width (ms)	PulseNumber
2μg (PD-1 Meos3.2-Ct)	500kC/10μL	1325	10	3

Calcium imaging using FLIPR HTS-system: 384-well culture treated plates (Greiner 781090) are coated with PLL at 5μg/mL or 100μ/mL for 45min at 37°C, or industrial pre-coated multi-well plate are used (Poly-D-Lysine Cell Coat greiner 781948). One vial of Ca5+ dye is previously mixed with 10mL of Ringer buffer for 30min at RT in the dark. Then the fluorescent solution is mixed with Jurkat cells in vol:vol ratio for 20min at 37° in the dark (4ml:4ml with a final cell concentration at 1.6M/ml). Cells are then seeded on coated 384-well plates for 40min at RT in the dark before being imaged. Reagent used for the experiments are prepared and deposited in non-binding 384 well plates (Greiner 781280). The FLIPR HTS-pipettor System take 5μL of the whole column from "Reagent" plates and distribute them into the associated cells destination wells (Reagents: anti-CD3 antibody OKT3, OKT3+anti-CD28 antibody, Phytohaemagglutinin PHA, Thapsigargin, Ionomycin, EGTA). The FLIPR-Tetra (Molecular Devices) system is handle by the software Screenworks, the wells of an entire 384-plate are screened simultaneously to perform live calcium imaging. The system uses lasers (Ex: 470-495, Intensity: 100, Em: 515-575) and detectors (Gain: 50, Exp Time: 0,40 s). For these experiments, one image has been acquired every 5 seconds for 15 min.

Calcium imaging using Video-imaging system: Coverslip are previously coated with PLL (Sigma PLL P4707) for 45min at 37°C and washed 3 times with PBS. Jurkat cells (200k cells/20μl) are mixed with 1μM of Fura2 calcium dye in complete RPMI and regularly agitated for 30min at RT in the dark. Then, the mix-Fura2-Cells is quickly centrifuged and cells are re-suspended in Ringer buffer. Depending of the type of experiment, cells are previously seeded on the PLL-coated-coverslip for 15min before imaging, or cells are dropped onto the coverslip directly during live acquisition. Using micro-tube and syringe, different reagents are injected directly in the coverslip live acquisitions. Different reagents are used to observe the calcium release of Jurkat cells (anti-CD3 antibody OKT3, OKT3+anti-CD28 antibody, Ionomycin, EGTA). Cells were exposed to UV light produced at alternating excitation wavelengths of 340 and 380 nm. The background from acquired images of both wavelength is measured and subtracted. Then the ratio of 340/380 images is collected online and measured. The calcium imaging is done via a standard inverted microscope equipped with a x40 Nikon objective, a Hamamatsu camera and 340/380nm LEDs. The control of devices, acquisition and analysis workflow are managed by MetaFluor software (Molecular Devices).

HCS-dSTORM setup. The HCS-SMLM setup is a conventional motorized inverted microscope Nikon TiE. It integrates a motorized stage (Tix, Tiy, Tiz) and the perfect focus system (PFS) fully controlled by the HCS-SMLM software. Single molecule acquisition data are collected through a high numerical aperture oil-immersion objective (100x, 1.49NA) in streaming mode using an EMCCD camera. A lower-magnification objective can be used for the pre-screening mode (40x), to pre-select position the coordinates before SR acquisition. The setup is also equipped with a temperature-controlled box and a humidified gas supply required to perform live imaging. A four-color laser bench (405/488/561/635nm) is connected through an optical fiber to the azimuthal TIRF illumination system of the microscope. Each lasers intensity and incidence angle of the excitation beam to the glass surface is software-controlled by the XYZebra plugin integrated in MetaMorph software. The incidence angle of the excitation beam can be precisely controlled and calibrated via galvanometer mirrors, enabling wide-field, Hilo or TIRF illumination through samples. Several laser intensities and TIRF angles can be defined and memorized into the software, information then used into the HCS-SMLM software to control the illumination during the automatic acquisition workflow.

Usually, in fluorescence microscopy field, excitation beams have Gaussian profiles, which can be very challenging for quantitative super-resolution imaging (Stehr et al[125], 2019).

Indeed, non-homogeneous illumination might lead to detection and fitting artefact. The common practice is to reduce FOV to the flat part of the Gaussian profile to record only the area which has the most homogeneous illumination (i.e. from 512*512 pxl to 256*256 pxl). However, a reduction of the field of view size leads to a decrease of the number of cells acquired simultaneously, resulting in an increase of the acquisition time to collect a given number of cells. However, buffer lifetime limits the total acquisition duration of HCS-dSTORM (estimated to 10h in Beghin et al.). To overcome this limit, we integrated an innovative beam shaper (Asphericon ©) to the optical path of the setup. Based on aspheric optics, this beam shaper generates a stable beam profile with a homogeneity superior to 95%. We confirmed its ability to provide homogeneous illumination on the entire FOV of SMLM acquisitions. We measured the average intensity of single molecules detected over 100 frames on resulting images as well as the vertical and horizontal line scans (Figure 66). This allowed us to acquire images with larger field of views, and as a consequence to increase by two-fold the number of cells for the same duration, improving our statistics while respecting dSTORM buffer limits.

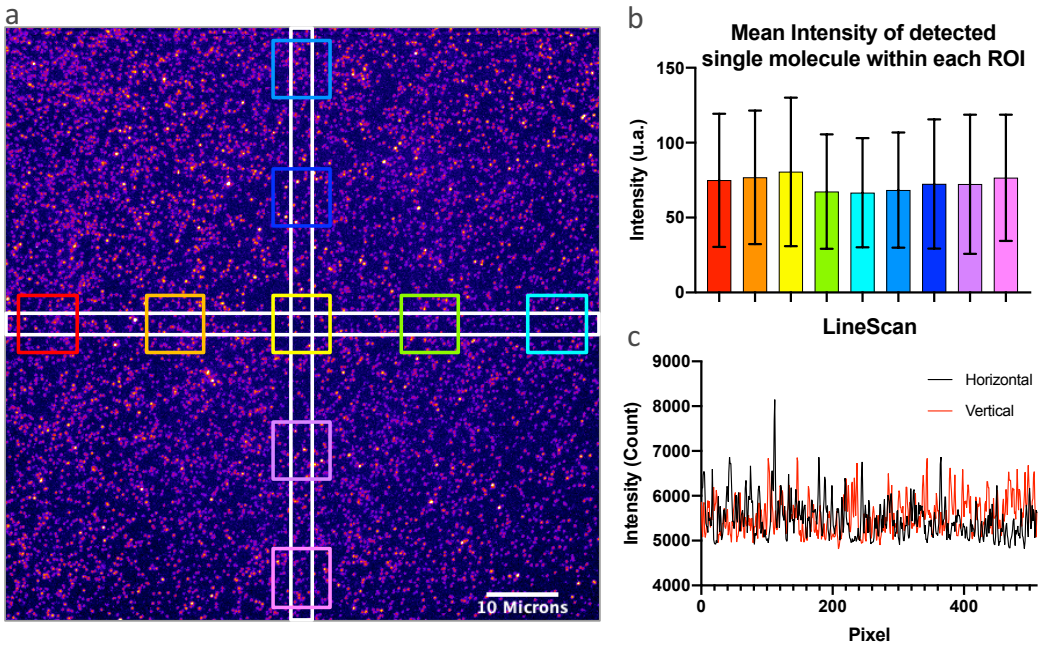

Figure 66. Top-shape illumination characterization by dSTORM*. AlexaFluor647 were evenly distributed onto a coverslip and acquired using dSTORM in order to characterize the homogeneity and the capabilities of the illumination provided by the top-shape beam. (a) Maximum intensity projection of 100 frames of dSTORM acquisitions. (b) Average Intensity of each colored square of (a). (c) Intensity profiles of horizontal and vertical line scans from the image.*

Protocols schema and antibodies used:

Primary Antibodies	Reference
Nivolumab anti-Human PD1 (Human)	Produced by Sanofi (4.82mg/mL)
IgG4 Isotype control (Human)	DDXCH04P-100, OriGene Technologies GmbH or Produced by Sanofi (13.31mg/ml)
Pembrozilumab anti-Human PD1 (Human)	Produced by Sanofi (10.16mg/ml)
PD-1 anti-Human (Mouse) clone 7A11B1	MA5-15780, Invitrogen
PD-1 anti-Human (Mouse) clone MIH4	14-99969-80, Invitrogen
PD-1 anti-Human (Rabbit) clone D67	MA5-29464, Invitrogen
CD3 anti-Human (Rabbit) clone SP162	ab135372, Abcam
CD3 anti-Human (Mouse) clone OKT3	16-0037-81, eBioscience
CD28 anti-Human (Mouse) clone CD28.2	16-0289-05, eBioscience
IgG2a Isotype control (Mouse)	14-4724-82, Life Technologies

Secondary Antibodies	Reference
A532 anti-Mouse (Goat)	A-11002, Invitrogen
A647 anti-Mouse (Goat)	A-21235, Invitrogen
A647 anti-Human (Goat)	A-21445, Invitrogen
A647 anti-Rabbit (Goat)	A-21244, Invitrogen
Unconjugated anti-Mouse (Goat)	115-005-071, Jackson ImmunoResearch
Unconjugated anti-Mouse (Goat)	A16080, Invitrogen

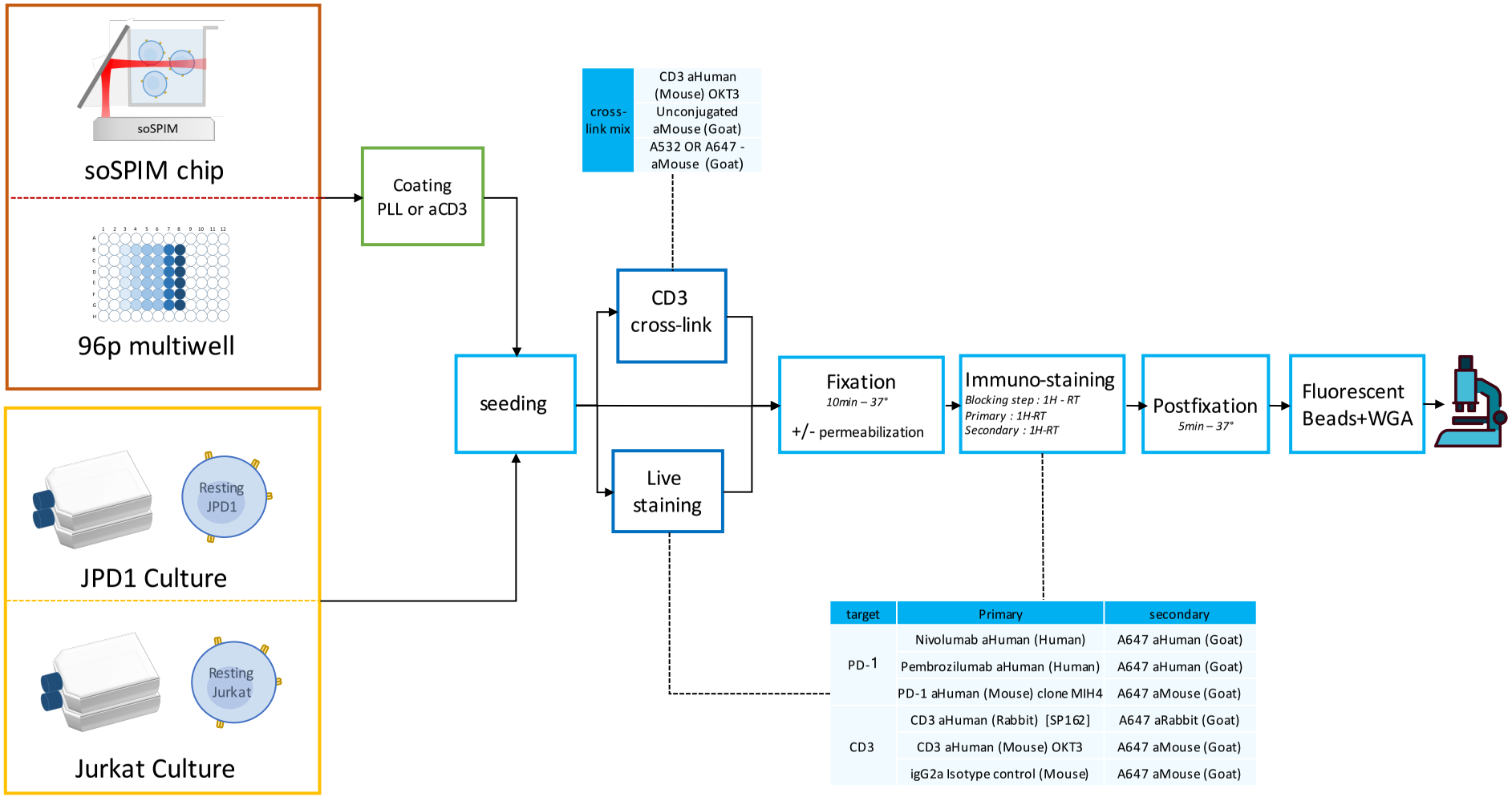

target	Primary	secondary
PD-1	Nivolumab aHuman (Human)	A647 aHuman (Goat)
	Pembrozilumab aHuman (Human)	A647 aHuman (Goat)
	PD-1 aHuman (Mouse) clone MIH4	A647 aMouse (Goat)
CD3	CD3 aHuman (Rabbit) [SP162]	A647 aRabbit (Goat)
	CD3 aHuman (Mouse) OKT3	A647 aMouse (Goat)
	igG2a Isotype control (Mouse)	A647 aMouse (Goat)

APPENDIX: *Software*

HCS-SMLM software settings.

LogFile	Load previous experiment settings	- Load LogFile
File saving	Head directory path	
Calibration	Calibrations of: Stage, image and Screening/Pre-screening objectives	- Pxl/µm, Pxl/Stage unit - Camera tilt - Plate Origin coordinates - Stage orientation - Stage Boundaries - Load/Save calibration
Imaging support format	Imaging support can be predefined or manually defined	- 96p, 8p, coverslip. - New format: number of wells, wells shape (round, square), wells size, inter-intra wells distances, etc.
Wells selection	Wells are selected in the GUI	- Click/Unclick
Positions selection	Automatic or manual selection of positions	- User-defined, random, centered, Grid (2x2,3x3,4x4)
Pre-screening mode	Positions selection via pre-screening images using a lower magnification objective and automatic coordinates calculation for the screening acquisition	- Positions selection via manual ROI selection on Pre-screening images
Perfect Focus mode	Tracking of PFS during the acquisition	- Focus window research (µm): Intra, extra wells
Acquisition mode	Screening acquisition flow: Order of acquisition (wells and positions)	- Manually defined, Random, vertical, horizontal, snake, serie-plate.
Wavelength settings	Number of wavelengths, Type of acquisition, Illumination settings	- Acquire/Snap, pumping phase/SMLM streaming acquisition - Delay - Exposure time - Number of frames - MM Illumination setting selection - Laser intensities.

Single Coverslip, 20 random positions

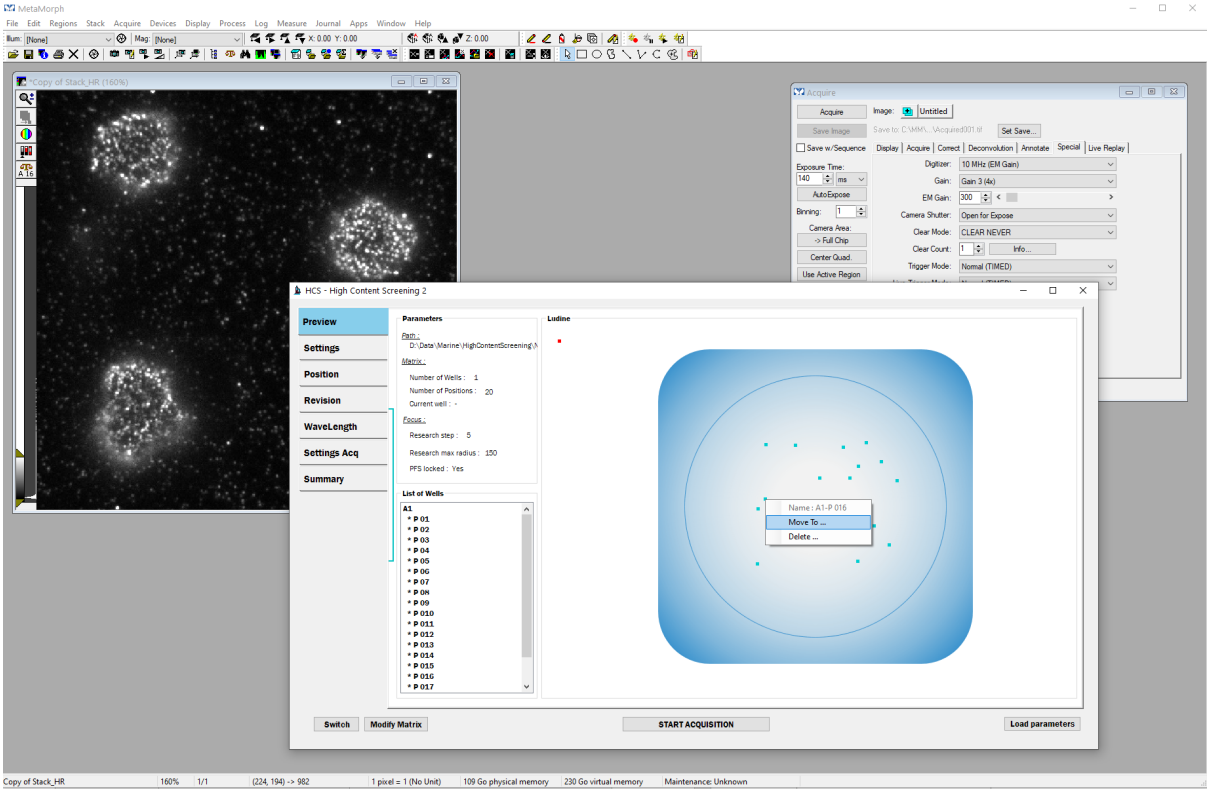

96-well plate, 2x2 Grid positions

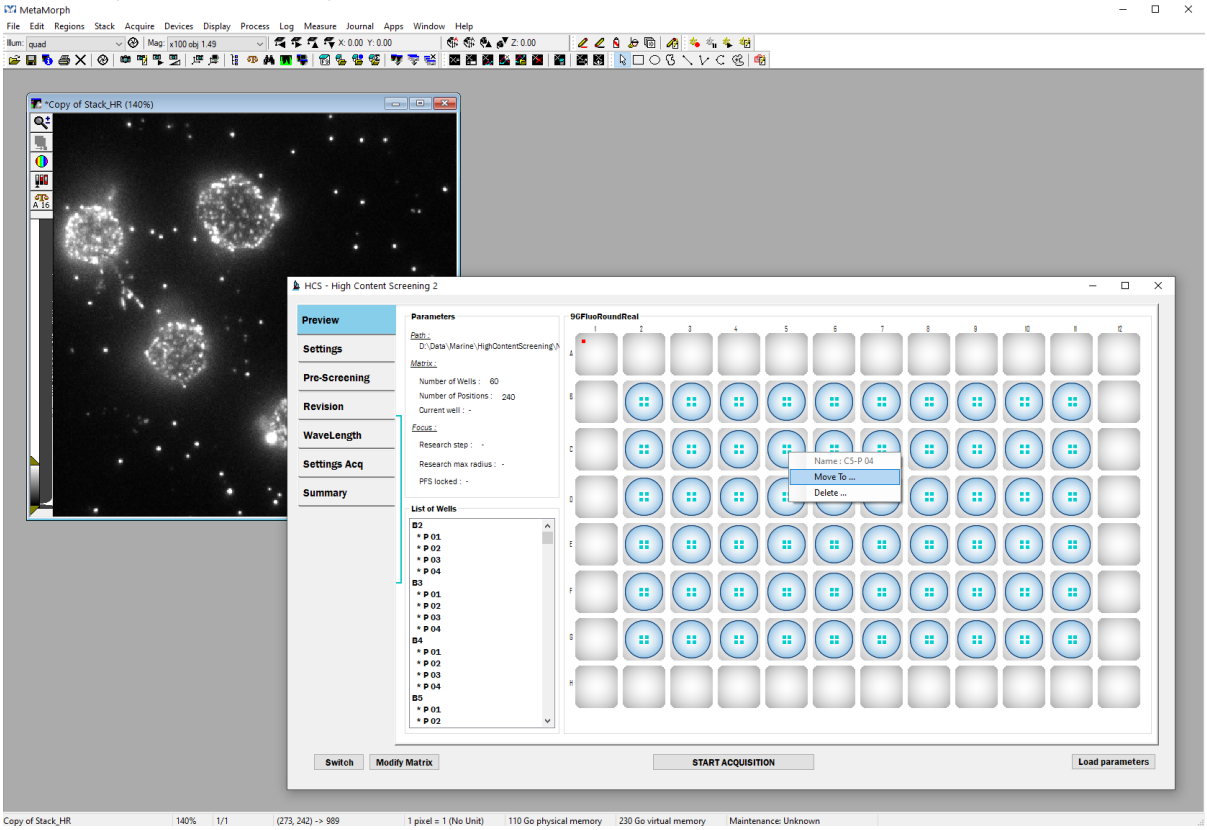

Z-Track software settings.

Files saving	- Head directory path
Calibration	- Pixel/µm - Camera tilt
Acquisition mode	- Single/Multiplane
Registration mode	- 2D/3D/No registration
Reference bead selection	- Manual/Automatic
Beads segmentation	- Wavelet threshold
Beads filtering	- SigmaXY, Chi^2
Acquisition settings	- Number of planes - Z-steps - Number of frames per plane (Batch mode)
Online Registration settings	- Binning/Continuous - Drift limits before registration (x_{max}, y_{max}, z_{max}) in nm - Initial coordinates averaging of the reference bead (frames) - Average sliding window for drift calculation

Z-Track multiplane acquisition, automatic bead extraction.

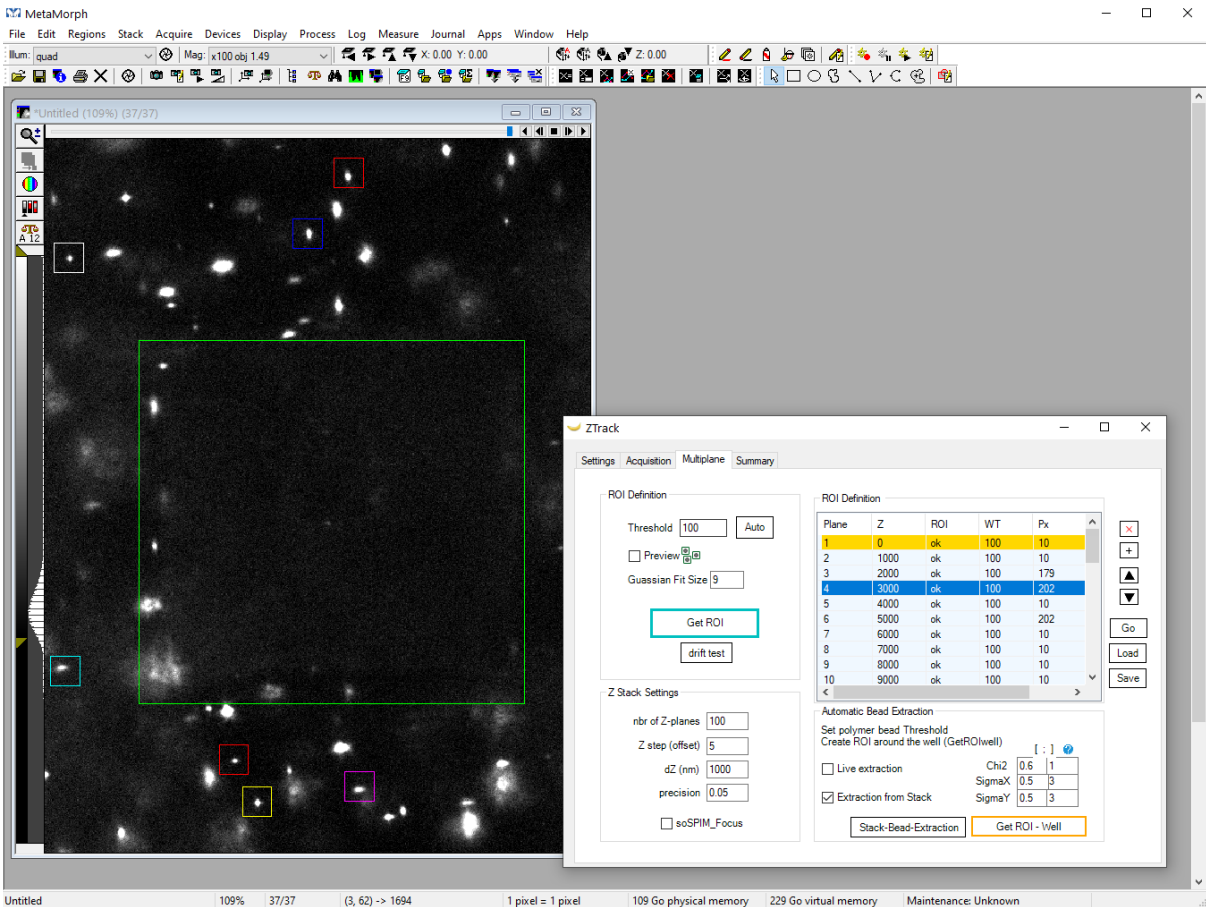

BIBLIOGRAPHY

1. Smith-Garvin, J. E., Koretzky, G. A. & Jordan, M. S. T Cell Activation. *Annu Rev Immunol* **27**, 591–619 (2009).
2. Gorentla, B. K. & Zhong, X.-P. T cell Receptor Signal Transduction in T lymphocytes. *J Clin Cell Immunol* **2012**, 005 (2012).
3. Kambayashi, T. & Laufer, T. M. Atypical MHC class II-expressing antigen-presenting cells: can anything replace a dendritic cell? *Nature Reviews Immunology* **14**, 719–730 (2014).
4. Chen, L. & Flies, D. B. Molecular mechanisms of T cell co-stimulation and co-inhibition. *Nat Rev Immunol* **13**, 227–242 (2013).
5. Pardoll, D. M. The blockade of immune checkpoints in cancer immunotherapy. *Nat Rev Cancer* **12**, 252–264 (2012).
6. Bremer, E. Targeting of the Tumor Necrosis Factor Receptor Superfamily for Cancer Immunotherapy. *ISRN Oncol* **2013**, (2013).
7. Bray, F. *et al*. Global cancer statistics 2018: GLOBOCAN estimates of incidence and mortality worldwide for 36 cancers in 185 countries. *CA: A Cancer Journal for Clinicians* **68**, 394–424 (2018).
8. Galluzzi, L. *et al*. Classification of current anticancer immunotherapies. *Oncotarget* **5**, (2014).
9. Kalos, M. & June, C. H. Adoptive T Cell Transfer for Cancer Immunotherapy in the Era of Synthetic Biology. *Immunity* **39**, 49–60 (2013).
10. Garfall, A. L. & June, C. H. Trispecific antibodies offer a third way forward for anticancer immunotherapy. *Nature* **575**, 450–451 (2019).
11. Suurs, F. V., Lub-de Hooge, M. N., de Vries, E. G. E. & de Groot, D. J. A. A review of bispecific antibodies and antibody constructs in oncology and clinical challenges. *Pharmacology & Therapeutics* **201**, 103–119 (2019).
12. Ishida, Y., Agata, Y., Shibahara, K. & Honjo, T. Induced expression of PD-1, a novel member of the immunoglobulin gene superfamily, upon programmed cell death. *The EMBO Journal* **11**, 3887–3895 (1992).
13. Leach, D. R., Krummel, M. F. & Allison, J. P. Enhancement of Antitumor Immunity by CTLA-4 Blockade. *Science* **271**, 1734–1736 (1996).
14. Sivanandam, V., LaRocca, C. J., Chen, N. G., Fong, Y. & Warner, S. G. Oncolytic Viruses and Immune Checkpoint Inhibition: The Best of Both Worlds. *Mol Ther Oncolytics* **13**, 93–106 (2019).
15. Chin, S. M. *et al*. Structure of the 4-1BB/4-1BBL complex and distinct binding and functional properties of utomilumab and urelumab. *Nature Communications* **9**, (2018).
16. Callahan, M. K., Postow, M. A. & Wolchok, J. D. Targeting T Cell Co-receptors for Cancer Therapy. *Immunity* **44**, 1069–1078 (2016).
17. Lu, R.-M. *et al*. Development of therapeutic antibodies for the treatment of diseases. *J Biomed Sci* **27**, 1 (2020).
18. Lin, D. Y. *et al*. The PD-1/PD-L1 complex resembles the antigen-binding Fv domains of antibodies and T cell receptors. *PNAS* **105**, 3011–3016 (2008).
19. Lazar-Molnar, E. *et al*. Crystal structure of the complex between programmed death-1 (PD-1) and its ligand PD-L2. *Proceedings of the National Academy of Sciences* **105**, 10483–10488 (2008).
20. Zak, K. M. *et al*. Structural Biology of the Immune Checkpoint Receptor PD-1 and Its Ligands PD-L1/PD-L2. *Structure* **25**, 1163–1174 (2017).
21. Francisco, L. M., Sage, P. T. & Sharpe, A. H. The PD-1 pathway in tolerance and autoimmunity: PD-1 pathway, Tregs, and autoimmune diseases. *Immunological Reviews* **236**, 219–242 (2010).
22. Riley, J. L. PD-1 signaling in primary T cells. *Immunological Reviews* **229**, 114–125 (2009).
23. Agata, Y. *et al*. Expression of the PD-1 antigen on the surface of stimulated mouse T and

B lymphocytes. *International Immunology* **8**, 765–772 (1996).
24. June, C. H., Ledbetter, J. A., Gillespie, M. M., Lindsten, T. & Thompson, C. B. T-cell proliferation involving the CD28 pathway is associated with cyclosporine-resistant interleukin 2 gene expression. *Molecular and Cellular Biology* **7**, 4472–4481 (1987).
25. Mullard, A. New checkpoint inhibitors ride the immunotherapy tsunami. *Nature Reviews Drug Discovery* **12**, 489–492 (2013).
26. Balagopalan, L., Sherman, E., Barr, V. A. & Samelson, L. E. Imaging techniques for assaying lymphocyte activation in action. *Nature Reviews Immunology* **11**, 21–33 (2011).
27. Pentcheva-Hoang, T., Chen, L., Pardoll, D. M. & Allison, J. P. Programmed death-1 concentration at the immunological synapse is determined by ligand affinity and availability. *Proceedings of the National Academy of Sciences* **104**, 17765–17770 (2007).
28. Yokosuka, T. *et al*. Programmed cell death 1 forms negative costimulatory microclusters that directly inhibit T cell receptor signaling by recruiting phosphatase SHP2. *The Journal of Experimental Medicine* **209**, 1201–1217 (2012).
29. Rossy, J., Williamson, D. J., Benzing, C. & Gaus, K. The integration of signaling and the spatial organization of the T cell synapse. *Front. Immun.* **3**, (2012).
30. Roh, K.-H., Lillemeier, B. F., Wang, F. & Davis, M. M. The coreceptor CD4 is expressed in distinct nanoclusters and does not colocalize with T-cell receptor and active protein tyrosine kinase p56lck. *Proceedings of the National Academy of Sciences* **112**, E1604–E1613 (2015).
31. Ma, Y., Lim, Y. J., Benda, A., Goyette, J. & Gaus, K. *Clustering of CD3ζ is sufficient to initiate T cell receptor signaling*. http://biorxiv.org/lookup/doi/10.1101/2020.02.17.953463 (2020) doi:10.1101/2020.02.17.953463.
32. Meddens, M. B. M. *et al*. Biophysical Characterization of CD6—TCR/CD3 Interplay in T Cells. *Frontiers in Immunology* **9**, (2018).
33. Jang, J. H. *et al*. Imaging of Cell–Cell Communication in a Vertical Orientation Reveals High-Resolution Structure of Immunological Synapse and Novel PD-1 Dynamics. *The Journal of Immunology* **195**, 1320–1330 (2015).
34. Ponjavic, A. *et al*. Single-Molecule Light-Sheet Imaging of Suspended T Cells. *Biophysical Journal* **114**, 2200–2211 (2018).
35. Wäldchen, F. *et al*. Whole-cell imaging of plasma membrane receptors by 3D lattice light-sheet dSTORM. *Nature Communications* **11**, (2020).
36. Feher, K., Halstead, J. M., Goyette, J. & Gaus, K. Can single molecule localization microscopy detect nanoclusters in T cells? *Current Opinion in Chemical Biology* **51**, 130–137 (2019).
37. F.R.S, L. R. XXXI. Investigations in optics, with special reference to the spectroscope. *The London, Edinburgh, and Dublin Philosophical Magazine and Journal of Science* **8**, 261–274 (1879).
38. Denk, W., Strickler, J. & Webb, W. Two-photon laser scanning fluorescence microscopy. *Science* **248**, 73–76 (1990).
39. Axelrod, D., Burghardt, T. P. & Thompson, N. L. Total Internal Reflection Fluorescence. *Annual Review of Biophysics and Bioengineering* **13**, 247–268 (1984).
40. Tokunaga, M., Imamoto, N. & Sakata-Sogawa, K. Highly inclined thin illumination enables clear single-molecule imaging in cells. *Nature Methods* **5**, 159–161 (2008).
41. Galland, R. *et al*. 3D high- and super-resolution imaging using single-objective SPIM. *Nature Methods* **12**, 641–644 (2015).
42. Schermelleh, L. *et al*. Super-resolution microscopy demystified. *Nature Cell Biology* **21**, 72–84 (2019).
43. Hell, S. W. & Wichmann, J. Breaking the diffraction resolution limit by stimulated emission: stimulated-emission-depletion fluorescence microscopy. *Opt Lett* **19**, 780–782 (1994).

44. Gustafsson, M. G. Surpassing the lateral resolution limit by a factor of two using structured illumination microscopy. *J Microsc* **198**, 82–87 (2000).
45. Betzig, E. *et al*. Imaging Intracellular Fluorescent Proteins at Nanometer Resolution. *Science* **313**, 1642–1645 (2006).
46. Hess, S. T., Girirajan, T. P. K. & Mason, M. D. Ultra-high resolution imaging by fluorescence photoactivation localization microscopy. *Biophys J* **91**, 4258–4272 (2006).
47. Rust, M. J., Bates, M. & Zhuang, X. Sub-diffraction-limit imaging by stochastic optical reconstruction microscopy (STORM). *Nat Methods* **3**, 793–796 (2006).
48. Heilemann, M. *et al*. Subdiffraction-Resolution Fluorescence Imaging with Conventional Fluorescent Probes. *Angewandte Chemie International Edition* **47**, 6172–6176 (2008).
49. Jungmann, R. *et al*. Multiplexed 3D cellular super-resolution imaging with DNA-PAINT and Exchange-PAINT. *Nat Methods* **11**, 313–318 (2014).
50. Betzig, E. *et al*. Imaging Intracellular Fluorescent Proteins at Nanometer Resolution. *Science* **313**, 1642–1645 (2006).
51. van de Linde, S. *et al*. Direct stochastic optical reconstruction microscopy with standard fluorescent probes. *Nat Protoc* **6**, 991–1009 (2011).
52. Jungmann, R. *et al*. Multiplexed 3D cellular super-resolution imaging with DNA-PAINT and Exchange-PAINT. *Nature Methods* **11**, 313–318 (2014).
53. Giannone, G., Hosy, E., Sibarita, J.-B., Choquet, D. & Cognet, L. High content Super-Resolution Imaging of Live Cell by uPAINT. *Methods in Molecular Biology* **950**, 95–110 (2013).
54. Sibarita, J.-B. High-density single-particle tracking: quantifying molecule organization and dynamics at the nanoscale. *Histochem Cell Biol* **141**, 587–595 (2014).
55. Möckl, L., Lamb, D. C. & Bräuchle, C. Super-resolved Fluorescence Microscopy: Nobel Prize in Chemistry 2014 for Eric Betzig, Stefan Hell, and William E. Moerner. *Angewandte Chemie International Edition* **53**, 13972–13977 (2014).
56. Deschout, H. *et al*. Precisely and accurately localizing single emitters in fluorescence microscopy. *Nature Methods* **11**, 253–266 (2014).
57. Thompson, R. E., Larson, D. R. & Webb, W. W. Precise Nanometer Localization Analysis for Individual Fluorescent Probes. *Biophysical Journal* **82**, 2775–2783 (2002).
58. Mortensen, K. I., Churchman, L. S., Spudich, J. A. & Flyvbjerg, H. Optimized localization analysis for single-molecule tracking and super-resolution microscopy. *Nat Methods* **7**, 377–381 (2010).
59. Sage, D. *et al*. Quantitative evaluation of software packages for single-molecule localization microscopy. *Nat Methods* **12**, 717–724 (2015).
60. Juette, M. F. *et al*. Three-dimensional sub-100 nm resolution fluorescence microscopy of thick samples. *Nat Methods* **5**, 527–529 (2008).
61. Abrahamsson, S. *et al*. Fast multicolor 3D imaging using aberration-corrected multifocus microscopy. *Nature Methods* **10**, 60–63 (2013).
62. Huang, B., Wang, W., Bates, M. & Zhuang, X. Three-dimensional super-resolution imaging by stochastic optical reconstruction microscopy. *Science* **319**, 810–813 (2008).
63. Pavani, S. R. P. & Piestun, R. Three dimensional tracking of fluorescent microparticles using a photon-limited double-helix response system. *Opt Express* **16**, 22048–22057 (2008).
64. Shtengel, G. *et al*. Interferometric fluorescent super-resolution microscopy resolves 3D cellular ultrastructure. *Proc Natl Acad Sci U S A* **106**, 3125–3130 (2009).
65. Bon, P. *et al*. Self-interference 3D super-resolution microscopy for deep tissue investigations. *Nature Methods* **15**, 449–454 (2018).
66. Bourg, N. *et al*. Direct optical nanoscopy with axially localized detection. *Nature Photonics* **9**, 587–593 (2015).
67. Kaplan, C. & Ewers, H. Optimized sample preparation for single-molecule localization-based superresolution microscopy in yeast. *Nature Protocols* **10**, 1007–1021 (2015).

68. Small, A. & Stahlheber, S. Fluorophore localization algorithms for super-resolution microscopy. *Nat Methods* **11**, 267–279 (2014).
69. Kechkar, A., Nair, D., Heilemann, M., Choquet, D. & Sibarita, J.-B. Real-Time Analysis and Visualization for Single-Molecule Based Super-Resolution Microscopy. *PLoS ONE* **8**, e62918 (2013).
70. Izeddin, I. *et al*. Wavelet analysis for single molecule localization microscopy. *Optics Express* **20**, 2081 (2012).
71. Balinovic, A., Albrecht, D. & Endesfelder, U. Spectrally red-shifted fluorescent fiducial markers for optimal drift correction in localization microscopy. *J. Phys. D: Appl. Phys.* **52**, 204002 (2019).
72. Hsiao, W. W.-W., Hui, Y. Y., Tsai, P.-C. & Chang, H.-C. Fluorescent Nanodiamond: A Versatile Tool for Long-Term Cell Tracking, Super-Resolution Imaging, and Nanoscale Temperature Sensing. *Accounts of Chemical Research* **49**, 400–407 (2016).
73. Diekmann, R. *et al*. Optimizing imaging speed and excitation intensity for single-molecule localization microscopy. *Nature Methods* **17**, 909–912 (2020).
74. Dempsey, G. T., Vaughan, J. C., Chen, K. H., Bates, M. & Zhuang, X. Evaluation of fluorophores for optimal performance in localization-based super-resolution imaging. *Nat Methods* **8**, 1027–1036 (2011).
75. Beghin, A. *et al*. Localization-based super-resolution imaging meets high-content screening. *Nature Methods* **14**, 1184–1190 (2017).
76. Olivier, N., Keller, D., Rajan, V. S., Gönczy, P. & Manley, S. Simple buffers for 3D STORM microscopy. *Biomedical Optics Express* **4**, 885 (2013).
77. Nahidiazar, L., Agronskaia, A. V., Broertjes, J., van den Broek, B. & Jalink, K. Optimizing Imaging Conditions for Demanding Multi-Color Super Resolution Localization Microscopy. *PLOS ONE* **11**, e0158884 (2016).
78. Hartwich, T. M. *et al*. A stable, high refractive index, switching buffer for super-resolution imaging. (2018) doi:10.1101/465492.
79. Bates, M., Huang, B., Dempsey, G. T. & Zhuang, X. Multicolor super-resolution imaging with photo-switchable fluorescent probes. *Science* **317**, 1749–1753 (2007).
80. Baddeley, D. *et al*. 4D Super-Resolution Microscopy with Conventional Fluorophores and Single Wavelength Excitation in Optically Thick Cells and Tissues. *PLoS ONE* **6**, e20645 (2011).
81. Lampe, A., Haucke, V., Sigrist, S. J., Heilemann, M. & Schmoranzer, J. Multi-colour direct STORM with red emitting carbocyanines. *Biology of the Cell* **104**, 229–237 (2012).
82. Bossi, M. *et al*. Multicolor Far-Field Fluorescence Nanoscopy through Isolated Detection of Distinct Molecular Species. *Nano Lett.* **8**, 2463–2468 (2008).
83. Schnitzbauer, J., Strauss, M. T., Schlichthaerle, T., Schueder, F. & Jungmann, R. Super-resolution microscopy with DNA-PAINT. *Nat Protoc* **12**, 1198–1228 (2017).
84. Zhang, M. *et al*. Rational design of true monomeric and bright photoactivatable fluorescent proteins. *Nature Methods* **9**, 727–729 (2012).
85. Manley, S. *et al*. High-density mapping of single-molecule trajectories with photoactivated localization microscopy. *Nature Methods* **5**, 155–157 (2008).
86. Rossier, O. *et al*. Integrins β 1 and β 3 exhibit distinct dynamic nanoscale organizations inside focal adhesions. *Nature Cell Biology* **14**, 1057–1067 (2012).
87. Nair, D. *et al*. Super-Resolution Imaging Reveals That AMPA Receptors Inside Synapses Are Dynamically Organized in Nanodomains Regulated by PSD95. *J. Neurosci.* **33**, 13204–13224 (2013).
88. Floderer, C. *et al*. Single molecule localisation microscopy reveals how HIV-1 Gag proteins sense membrane virus assembly sites in living host CD4 T cells. *Scientific Reports* **8**, (2018).
89. Williamson, D. J. *et al*. Pre-existing clusters of the adaptor Lat do not participate in early T cell signaling events. *Nature Immunology* **12**, 655–662 (2011).

90. Rossboth, B. *et al*. TCRs are randomly distributed on the plasma membrane of resting antigen-experienced T cells. *Nature Immunology* (2018) doi:10.1038/s41590-018-0162-7.
91. Hu, Y. S., Cang, H. & Lillemeier, B. F. Superresolution imaging reveals nanometer- and micrometer-scale spatial distributions of T-cell receptors in lymph nodes. *Proceedings of the National Academy of Sciences* **113**, 7201–7206 (2016).
92. Pageon, S. V. *et al*. Functional role of T-cell receptor nanoclusters in signal initiation and antigen discrimination. 11.
93. Rosenberg, J., Cao, G., Borja-Prieto, F. & Huang, J. Lattice Light-Sheet Microscopy Multi-dimensional Analyses (LaMDA) of T-Cell Receptor Dynamics Predict T-Cell Signaling States. *Cell Systems* **10**, 433-444.e5 (2020).
94. Razvag, Y., Neve-Oz, Y., Sajman, J., Reches, M. & Sherman, E. Nanoscale kinetic segregation of TCR and CD45 in engaged microvilli facilitates early T cell activation. *Nature Communications* **9**, 732 (2018).
95. Rossboth, B. *et al*. TCRs are randomly distributed on the plasma membrane of resting antigen-experienced T cells. *Nature Immunology* (2018) doi:10.1038/s41590-018-0162-7.
96. Jungmann, R. *et al*. Quantitative super-resolution imaging with qPAINT. *Nat Methods* **13**, 439–442 (2016).
97. Simoncelli, S. *et al*. *Multi-colour DNA-qPAINT reveals how Csk nano-clusters regulate T-cell receptor signalling*. http://biorxiv.org/lookup/doi/10.1101/857516 (2019) doi:10.1101/857516.
98. Racine, V. *et al*. Multiple-target tracking of 3D fluorescent objects based on simulated annealing. in *3rd IEEE International Symposium on Biomedical Imaging: Nano to Macro, 2006*. 1020–1023 (2006). doi:10.1109/ISBI.2006.1625094.
99. Levet, F. *et al*. SR-Tesseler: a method to segment and quantify localization-based super-resolution microscopy data. *Nature Methods* **12**, 1065–1071 (2015).
100. Bullen, A. Microscopic imaging techniques for drug discovery. *Nature Reviews Drug Discovery* **7**, 54–67 (2008).
101. Pereira, P. M., Almada, P. & Henriques, R. High-content 3D multicolor super-resolution localization microscopy. in *Methods in Cell Biology* vol. 125 95–117 (Elsevier, 2015).
102. Holden, S. J. *et al*. High throughput 3D super-resolution microscopy reveals Caulobacter crescentus in vivo Z-ring organization. *Proceedings of the National Academy of Sciences* **111**, 4566–4571 (2014).
103. Gunkel, M., Flottmann, B., Heilemann, M., Reymann, J. & Erfle, H. Integrated and correlative high-throughput and super-resolution microscopy. *Histochemistry and Cell Biology* **141**, 597–603 (2014).
104. Flottmann, B. *et al*. Correlative light microscopy for high-content screening. *BioTechniques* **55**, (2013).
105. Yasui, M., Hiroshima, M., Kozuka, J., Sako, Y. & Ueda, M. Automated single-molecule imaging in living cells. *Nature Communications* **9**, (2018).
106. Barentine, A. E. S. *et al*. 3D Multicolor Nanoscopy at 10,000 Cells a Day. *bioRxiv* (2019) doi:10.1101/606954.
107. Almada, P. *et al*. Automating multimodal microscopy with NanoJ-Fluidics. *Nature Communications* **10**, (2019).
108. Klevanski, M. *et al*. Automated highly multiplexed super-resolution imaging of protein nano-architecture in cells and tissues. *Nat Commun* **11**, 1552 (2020).
109. Jones, T. R. *et al*. CellProfiler Analyst: data exploration and analysis software for complex image-based screens. *BMC Bioinformatics* **9**, 482 (2008).
110. Dao, D. *et al*. CellProfiler Analyst: interactive data exploration, analysis and classification of large biological image sets. *Bioinformatics* **32**, 3210–3212 (2016).
111. Strauss, S. & Jungmann, R. Up to 100-fold speed-up and multiplexing in optimized DNA-

PAINT. *Nature Methods* **17**, 789–791 (2020).
112. Schueder, F. *et al*. An order of magnitude faster DNA-PAINT imaging by optimized sequence design and buffer conditions. *Nature Methods* **16**, 1101–1104 (2019).
113. Longo, D. M. *et al*. Inter-donor variation in cell subset specific immune signaling responses in healthy individuals. *Am J Clin Exp Immunol* **1**, 1–11 (2012).
114. Dempsey, L. A. Human T cell variations. *Nat Immunol* **15**, 1008–1008 (2014).
115. Petrovas, C. *et al*. Differential Association of Programmed Death-1 and CD57 with Ex Vivo Survival of CD8 + T Cells in HIV Infection. *J Immunol* **183**, 1120–1132 (2009).
116. Yang, W., Chen, P. W., Li, H., Alizadeh, H. & Niederkorn, J. Y. PD-L1: PD-1 Interaction Contributes to the Functional Suppression of T-Cell Responses to Human Uveal Melanoma Cells In Vitro. *Invest. Ophthalmol. Vis. Sci.* **49**, 2518 (2008).
117. Latchman, Y. *et al*. PD-L2 is a second ligand for PD-1 and inhibits T cell activation. *Nature Immunology* **2**, 261–268 (2001).
118. Ostergaard, H. & Clark, W. R. The role of Ca2+ in activation of mature cytotoxic T lymphocytes for lysis. *The Journal of Immunology* **139**, 3573–3579 (1987).
119. Valitutti, S., Dessing, M., Aktories, K., Gallati, H. & Lanzavecchia, A. Sustained signaling leading to T cell activation results from prolonged T cell receptor occupancy. Role of T cell actin cytoskeleton. *J Exp Med* **181**, 577–584 (1995).
120. Partiseti, M. *et al*. The calcium current activated by T cell receptor and store depletion in human lymphocytes is absent in a primary immunodeficiency. *J. Biol. Chem.* **269**, 32327–32335 (1994).
121. Santos, A. M. *et al*. Capturing resting T cells: the perils of PLL. *Nature Immunology* **19**, 203–205 (2018).
122. Fessas, P., Lee, H., Ikemizu, S. & Janowitz, T. A molecular and preclinical comparison of the PD-1–targeted T-cell checkpoint inhibitors nivolumab and pembrolizumab. *Seminars in Oncology* **44**, 136–140 (2017).
123. Zhong, L. *et al*. NSOM/QD-Based Direct Visualization of CD3-Induced and CD28-Enhanced Nanospatial Coclustering of TCR and Coreceptor in Nanodomains in T Cell Activation. *PLoS ONE* **4**, e5945 (2009).
124. Iwai, Y., Hamanishi, J., Chamoto, K. & Honjo, T. Cancer immunotherapies targeting the PD-1 signaling pathway. *J Biomed Sci* **24**, 26 (2017).
125. Stehr, F., Stein, J., Schueder, F., Schwille, P. & Jungmann, R. Flat-top TIRF illumination boosts DNA-PAINT imaging and quantification. *Nature Communications* **10**, (2019).
126. De Zitter, E. *et al*. Mechanistic investigation of mEos4b reveals a strategy to reduce track interruptions in sptPALM. *Nature Methods* **16**, 707–710 (2019).
127. Ovesný, M., Křížek, P., Borkovec, J., Švindrych, Z. & Hagen, G. M. ThunderSTORM: a comprehensive ImageJ plug-in for PALM and STORM data analysis and super-resolution imaging. *Bioinformatics* **30**, 2389–2390 (2014).
128. Wang, Y. *et al*. Localization events-based sample drift correction for localization microscopy with redundant cross-correlation algorithm. *Optics Express* **22**, 15982 (2014).

APPENDIX: Publication

Localization-based super-resolution imaging meets high-content screening

Anne Beghin[1,2,6], Adel Kechkar[3,6], Corey Butler[1,2,4], Florian Levet[1,2,5], Marine Cabillic[1,2], Olivier Rossier[1,2], Gregory Giannone[1,2], Rémi Galland[1,2], Daniel Choquet[1,2,5] & Jean-Baptiste Sibarita[1,2]

© 2017 Nature America, Inc., part of Springer Nature. All rights reserved.

Single-molecule localization microscopy techniques have proven to be essential tools for quantitatively monitoring biological processes at unprecedented spatial resolution. However, these techniques are very low throughput and are not yet compatible with fully automated, multiparametric cellular assays. This shortcoming is primarily due to the huge amount of data generated during imaging and the lack of software for automation and dedicated data mining. We describe an automated quantitative single-molecule-based super-resolution methodology that operates in standard multiwell plates and uses analysis based on high-content screening and data-mining software. The workflow is compatible with fixed- and live-cell imaging and allows extraction of quantitative data like fluorophore photophysics, protein clustering or dynamic behavior of biomolecules. We demonstrate that the method is compatible with high-content screening using 3D dSTORM and DNA-PAINT based super-resolution microscopy as well as single-particle tracking.

Innovations in high-content screening (HCS) or high-throughput (HT) analysis combined with advanced fluorescence microscopy techniques have enabled image-based screening assays, which have dramatically improved experimental throughput and content richness[1–3]. In parallel, super-resolution (SR) microscopy has revolutionized fluorescence microscopy and cell biology[4], as this technique allows researchers to monitor protein organization and dynamics at unprecedented resolution. Single-molecule localization microscopy (SMLM) approaches rely on the localization and temporal accumulation of a large number of sparsely distributed single emitters. Among these techniques, direct stochastic optical reconstruction microscopy (dSTORM)[5–7] and point accumulation for imaging in nanoscale topography (PAINT)[8–11] use conventional fluorescent probes such as labeled antibodies or chemical tags. Photoactivated light microscopy (PALM) is based on photoactivation of genetically encoded fluorescent proteins expressed in cells. When performed on live cells, it allows single-protein tracking coupled with PALM (sptPALM)[12–15]. It is also possible to combine all these SMLM techniques with 3D localization of single molecules[16–20]. However, the major limitations restricting the use of all these SMLM techniques in an HCS context are the low experimental throughput[21] as compared to traditional fluorescence microscopy and the need for manual interventions during acquisitions of multiple samples in different conditions. Only a few recent attempts to integrate super-resolution microscopy into an HCS-like pipeline have been achieved[22,23]; these attempts used a correlative approach in which a few cells of interest were manually identified at low resolution before switching to another microscope to perform the SR acquisition with corresponding coordinates. While these approaches are promising, the manual intervention makes the pipeline time consuming and incompatible with the constraints of large assays. Moreover, these studies compared cell phenotypes based on reconstructions of super-resolution images to draw conclusions, and this restricted the amount of information obtained by HCS-SMLM. Holden *et al.*[24] performed high-throughput PALM imaging in an elegant manner, using cell synchronization to study the temporal evolution of a protein of interest. However, while their approach allowed them to collect a large amount of SMLM data in a single workflow, their study considered a specific biological question with only a single biological condition. A recent review highlighted the importance and value of combining both SMLM and true high-content screening[25], but it did not collect data nor did it mention the key steps of data analysis.

We describe a platform for functional HCS-SMLM for use with both commercial and freely available equipment and software. This platform is composed of a fully automated microscope that integrates automatic online data analysis, metadata extraction and database creation Single Molecule Profiler (SMP) software, which allows organization of all the metadata in a functional database compatible with the Cell Profiler Analyst (CPA)[26] for data mining and statistical interpretation. We illustrate the versatility of our HCS-SMLM approach on different types of applications, covering

[1]Université de Bordeaux, Institut interdisciplinaire de Neurosciences, Bordeaux, France. [2]CNRS UMR 5297, Institut interdisciplinaire de Neurosciences, Bordeaux, France. [3]Ecole Nationale Supérieure de Biotechnologie, Constantine, Algeria. [4]Imagine Optic, Orsay, France. [5]Bordeaux Imaging Center, CNRS, Université de Bordeaux, UMS 3420, INSERM US4, Bordeaux, France. [6]These authors contributed equally to this work. Correspondence should be addressed to J.-B.S. (jean-baptiste.sibarita@u-bordeaux.fr).

RECEIVED 29 AUGUST; ACCEPTED 26 SEPTEMBER; PUBLISHED ONLINE 30 OCTOBER 2017; DOI:10.1038/NMETH.4486

proof-of-principle and quality-control experiments as well as fixed- and live-cell experiments with various levels of quantifications. We achieve SMLM with (to our knowledge) unprecedented throughput and content and thus open the door to new discoveries in chemistry, biology and drug applications.

RESULTS

High-content SMLM microscopy acquisition workflow

Our system is composed of a fully automated microscope that integrates automatic data analysis, metadata extraction and data mining (**Fig. 1**). The SMP software developed for this work allows researchers to organize all the metadata in a functional database compatible with the CPA software for data mining and statistical interpretation. Compatible with most standard supports, including multiwell plates, our platform uses an optimized workflow to facilitate SMLM acquisitions in an HCS fashion (**Supplementary Note 1**). The workflow is based on standard commercially available equipment and freely available software, and this makes it possible to upgrade traditional SMLM setups to HCS-SMLM.

Metadata computation and organization

Metadata are all quantitative single-molecule descriptors that can be used for the data-mining process. **Supplementary Table 1** describes the metadata used in this work, but more descriptors can be added. In order to optimize the workflow, single-molecule localization and tracking are computed online during the acquisition, and the raw images are directly saved to disk while they are acquired and do not need to be opened again for analysis (**Fig. 1b**). Clustering or photophysical parameters are computed offline after the acquisition, but directly from the localization metadata, which eliminates the need to reload the raw images. Metadata are automatically saved in a well-defined tree hierarchy, before they are compiled in a functional database using our SMP software for later data mining using CPA (**Fig. 1c**, **Supplementary Fig. 1** and **Supplementary Note 2**).

Database construction and data mining

Data mining allows for the extraction of relevant information from a very large pool of quantitative data computed from the HCS pipeline in order to represent the data in an intelligible manner.

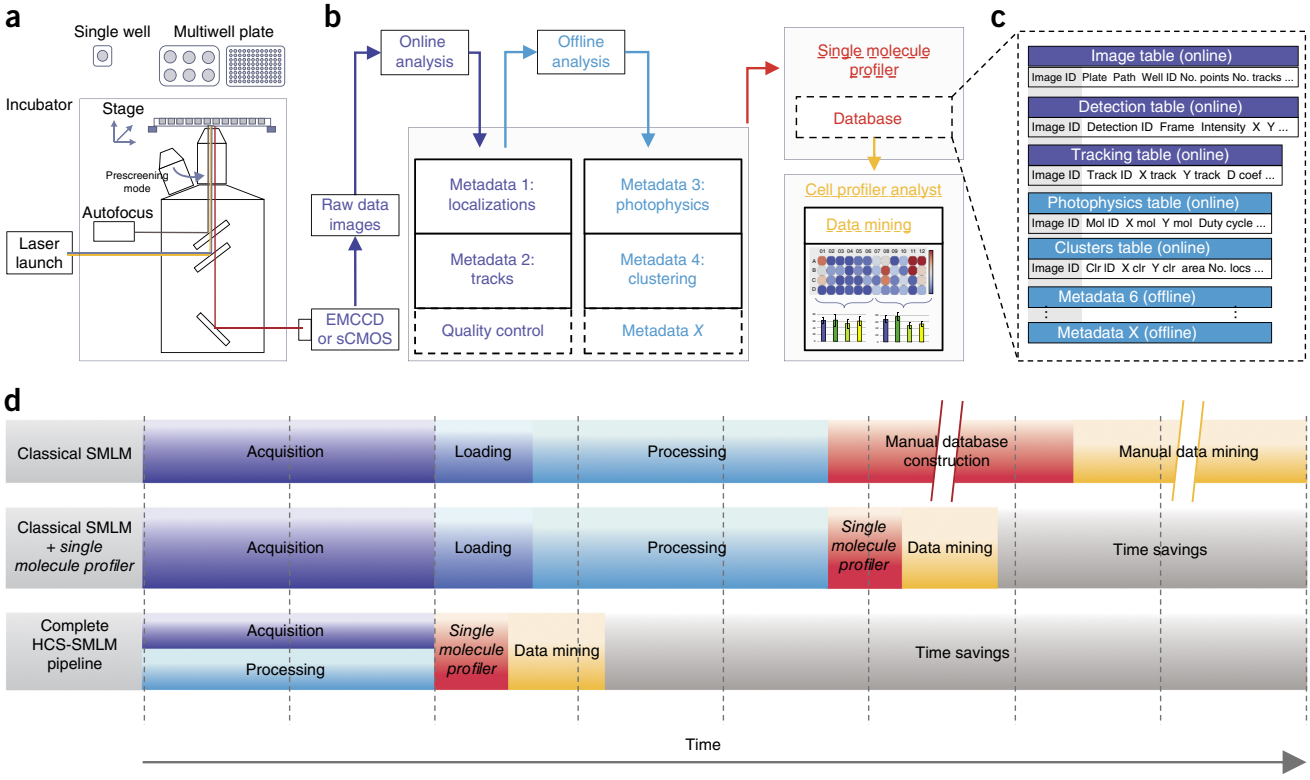

Figure 1 | HCS-SMLM acquisition setup and analysis workflow. (**a**) HCS-SMLM workflow. SMLM data are acquired on a conventional motorized inverted microscope equipped with a temperature-controlled box, a humidified gas supply, and a fully motorized stage (*X*, *Y*, *Z*) under HiLo or TIRF illumination for optimal single-molecule imaging. Different sample supports can be used, from single coverslips to 96-well plates. An autofocus device maintains the focus during the entire acquisition process. Prescreening acquisition with a low-magnification objective can be performed if needed. For each position, SMLM data are collected in streaming mode using an EM-CCD or sCMOS camera. (**b**) A massive amount of metadata—i.e., quantitative single-molecule data, are computed online during the acquisition (dark blue) and offline after the acquisition (cyan). Offline metadata are computed directly from the online metadata, which eliminates the need to load the raw images. The Single Molecule Profiler (SMP) software organizes all metadata into a unique database compatible with Cell Profiler Analyst (CPA) software. (**c**) HCS-SMLM metadata computed with SMP are composed of several tables linked together—"image table," which contains the image data information, and one or more SMLM metadata tables. Image and metadata tables are linked through a unique ID (ImageID). (**d**) Benchmarking between (top) classical SMLM without online processing or automatic database construction, (middle) classical SMLM coupled with SMP software to efficiently generate the database for data mining, and (bottom) complete HCS-SMLM workflow with online computation of the metadata coupled with SMP software. Breaks in the timelines indicate that the corresponding tasks are usually very long and fastidious, especially for large number of biological conditions.

© 2017 Nature America, Inc., part of Springer Nature. All rights reserved.

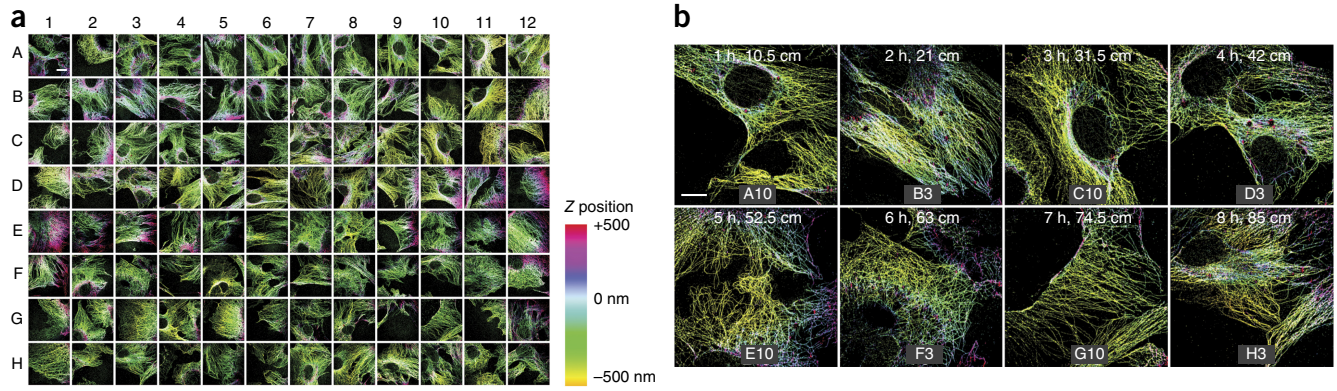

Figure 2 | HCS-SMLM allows fully automated 3D-dSTORM imaging of a complete 96-well plate. (**a**) 96 astigmatism-based 3D dSTORM images (20.5 × 20.5 µm FOV, 40 nm/px) of microtubules in Cos-7 cells automatically gathered using our HCS-SMLM approach. The total acquisition time was 8 h, including the localization and the reconstruction, and total traveling distance between the first and the last cell of the screen was 85 cm. The color codes indicate the *Z*-position. Scale bar, 5 µm. (**b**) Gallery of 3D dSTORM images with a regular time interval of 1 h between each image. Scale bar, 8 µm. Z-scale applies to (**a**) and (**b**).

For our data-mining purposes, we used CPA[26], a popular freely available software distributed under an open-source license (GNU General Public License, version 2), initially designed to explore and analyze cell-based screening data. Furthermore, we developed SMP software, which allows CPA to handle all the single-molecule metadata (**Fig. 1c** and **Supplementary Fig. 1** and **Supplementary Software**). This makes it possible to deal with millions of SMLM quantitative metadata in an intelligible and graphical manner using several representations, such as histograms, scatter plots and density plots. The SMP software can handle metadata computed with freely available super-resolution localization software such as ThunderSTORM[27] (see **Supplementary Note 3**).

All graphs are interactive and allow researchers to filter the metadata in a user-friendly manner. This filtering step, called gating in HCS, allows efficient comparison between various biological conditions. For example, it is possible to restrict the statistical analysis to a subpopulation of molecules displaying a given blinking behavior or a certain diffusive behavior or belonging to trajectories with a limited number of timepoints, etc. Finally, statistical analysis of SMLM metadata can be displayed using heatmap representations, which are graphical representations commonly used in HCS in order to visualize statistics in a multiwell plate format.

Benchmarking

A 96-well plate with ten positions per well screened with 4,000 512 × 512 × 16-bit images acquired at 50 frames per second (fps) represents 2 TB of raw images. Depending on localization density and molecular organization, the analysis of the raw data can lead to about 300 million single-molecule detections, 2 billion SMLM entries in the localization data table (i.e., *XY* coordinates, intensity, sigma, etc.) and 850 million dynamics metadata (i.e., trajectories, mean square displacement (MSD), diffusion coefficients, etc.). To illustrate our HCS-SMLM method's ability to efficiently screen a large number of biological conditions with optimal quality, we automatically acquired 3D dSTORM images of 96 cells located in 96 different wells. The entire screen, representing a total traveling distance of 85 cm, was achieved in 8 h and generated 500 GB of raw images, 200 million single-molecule detections, and an ASCII database of 70 GB. In comparison, a trained user can manually acquire 20 to 50 cells in a workday. All of the SMLM metadata were automatically organized with SMP software into a database, where they can be displayed for gating and statistical analysis—a long and tedious task in the case of manual screening (**Fig. 1d**).

Super-resolution imaging on a complete 96-well plate

We here demonstrate our HCS-SMLM method's ability to achieve astigmatism-based 3D SMLM[28] of biological samples consistently across a complete 96-well plate with state-of-the-art quality. We imaged microtubules labeled with the Alexa 647 fluorophore using dSTORM as a gold-standard biological control. The total HCS-SMLM acquisition took 8 h, including the 3D localization and image reconstruction, and this corresponded to about 5 min between each well. **Figure 2** displays a gallery of 96 3D super-resolution images automatically reconstructed from regular sampling of the 96-well plate. The high quality of the reconstructions qualitatively illustrates our system's ability to automatically screen an entire 96-well plate using 3D dSTORM without any user intervention.

We used several descriptors to control the quality of the reconstructions in a quantitative manner (**Supplementary Fig. 3**). We also analyzed both the number of localized molecules per frame and the frame at which 50% of the total localized molecules had been detected (frame_50% metadata) to quantify the effect of time on the dSTORM buffer efficiency (**Supplementary Fig. 4**). Despite the high quality of the reconstructions, we observed a continuous decrease of the frame_50% metadata over time, an observation that indicated the limits of the dSTORM buffer in achieving long acquisition times (more than 10 h). This observation is not surprising, since it is known that carbocyanine dyes are sensitive to the presence of oxygen, which induces a less efficient pumping phase and/or faster bleaching rate[7,29,30]. We used enzymatic oxygen scavengers (pyranose/catalase[31,32]) to reduce oxygen yield in solution. However, like any enzymatic system, these scavengers have a limited lifetime, and their efficiency is expected to decrease over time.

As an alternative SMLM approach to overcoming the buffer-lifetime limit of dSTORM, we performed HCS-SMLM using the DNA-PAINT technique[11,33]. As a result, during the same 8 h of acquisition needed to screen the 96 cells in dSTORM and using the same HCS-SMLM workflow, we acquired 3D images of 16 cells

© 2017 Nature America, Inc., part of Springer Nature. All rights reserved.

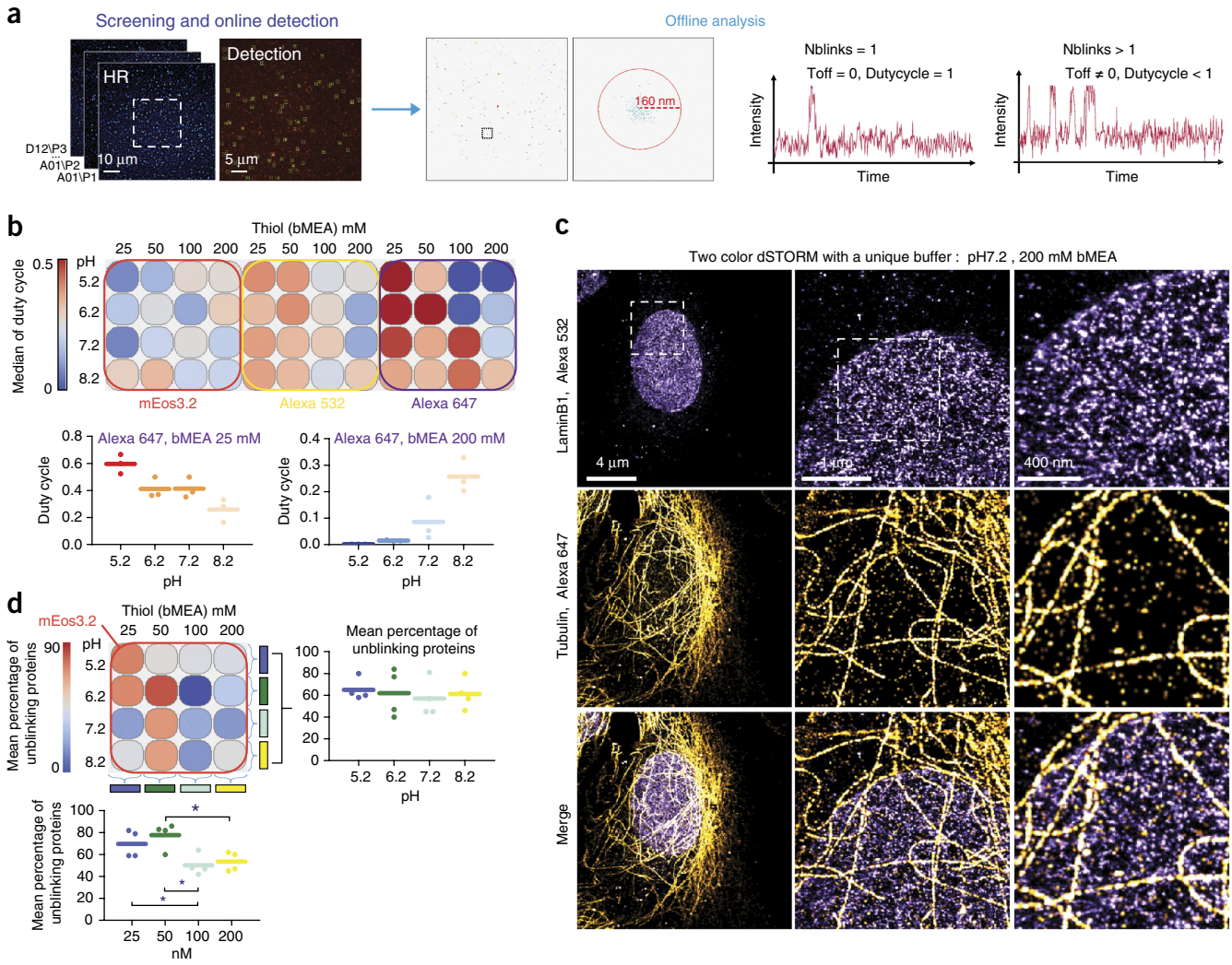

Figure 3 | Effect of dSTORM buffer on fluorophore photophysics. (**a**) Characterization of isolated fluorophores using sparsely distributed pure dyes adsorbed to the bottom coverglass of a 96-well plate. Single-molecule sequences are analyzed online (left). Clusters of localizations belonging to the same fluorophore are identified (center), and intensity fluctuations in each cluster are analyzed to extract the photophysical properties (right). (**b**) Data mining using the duty cycle metadata describing the blinking properties of the fluorophore. For Alexa 647, at low concentration of thiols (25 mM), an increase of the pH induced a decrease of the duty cycle (left box plot). The effect is reversed for high concentration of thiols (200 mM) (right box plot). Bar, mean of all positions. Dot, mean per position. (**c**) Two-color dSTORM acquisition of microtubules (labeled with Alexa 647) and laminB1 (Alexa 532) in Cos-7 cells using the same dSTORM buffer (200 mM bMEA at pH 7.2) selected from the previous screen. SMLM data were acquired at 5-µm axial distance from the coverslip, a distance corresponding to the top of the cell. (**d**) Data mining performed on mEos3.2 fluorescent protein photophysics. The bottom box plot shows the mean aggregation of all conditions grouped by thiol concentrations. It highlights a decrease of the fraction of nonblinking molecules induced by highest thiol concentration (±100 mM). Conversely, the pH does not seem to affect the fraction of blinking mEos3.2 proteins (top right box plot). Bar, mean of all positions. Dot, mean per position. *P* value < 0.05. *P* values were calculated using unpaired *t*-test.

with a constant single-molecule regime (**Supplementary Fig. 5**). The low frame rate requirement for DNA-PAINT acquisitions limits the overall acquisition speed. However, as DNA-PAINT does not require oxygen-scavenging enzymatic system, we did not detect any degradation of single-molecule descriptors during the acquisition, which makes DNA-PAINT a good alternative to dSTORM in the case of very long HCS-SMLM experiments.

The effect of dSTORM buffers on dye photophysics

We here illustrate how HCS-SMLM can be used to optimize conditions of super-resolution imaging by quantifying the photophysical properties of dyes commonly used for dSTORM. The final resolution of the super-resolution image relies on the number of collected photons per localization event above the background[34] as well as the density of localized molecules in the final reconstruction[35,36]. The resolution is therefore strongly dependent on the fluorophore photophysical properties, which are known to be affected by the chemical environment[6,7,30,37,38]. The composition of the imaging buffer is a crucial factor in achieving efficient dSTORM imaging. Two important factors of the buffer composition known to influence the fluorophore's photophysics are the pH[32] and the concentration of reductive species such as thiols[37]. Several studies have characterized buffer effects on fluorophore photophysics[6,7,30,37,38]. However, in the absence of a fully automated method, such an analysis is very complex and time consuming. Furthermore, it is of particular

© 2017 Nature America, Inc., part of Springer Nature. All rights reserved.

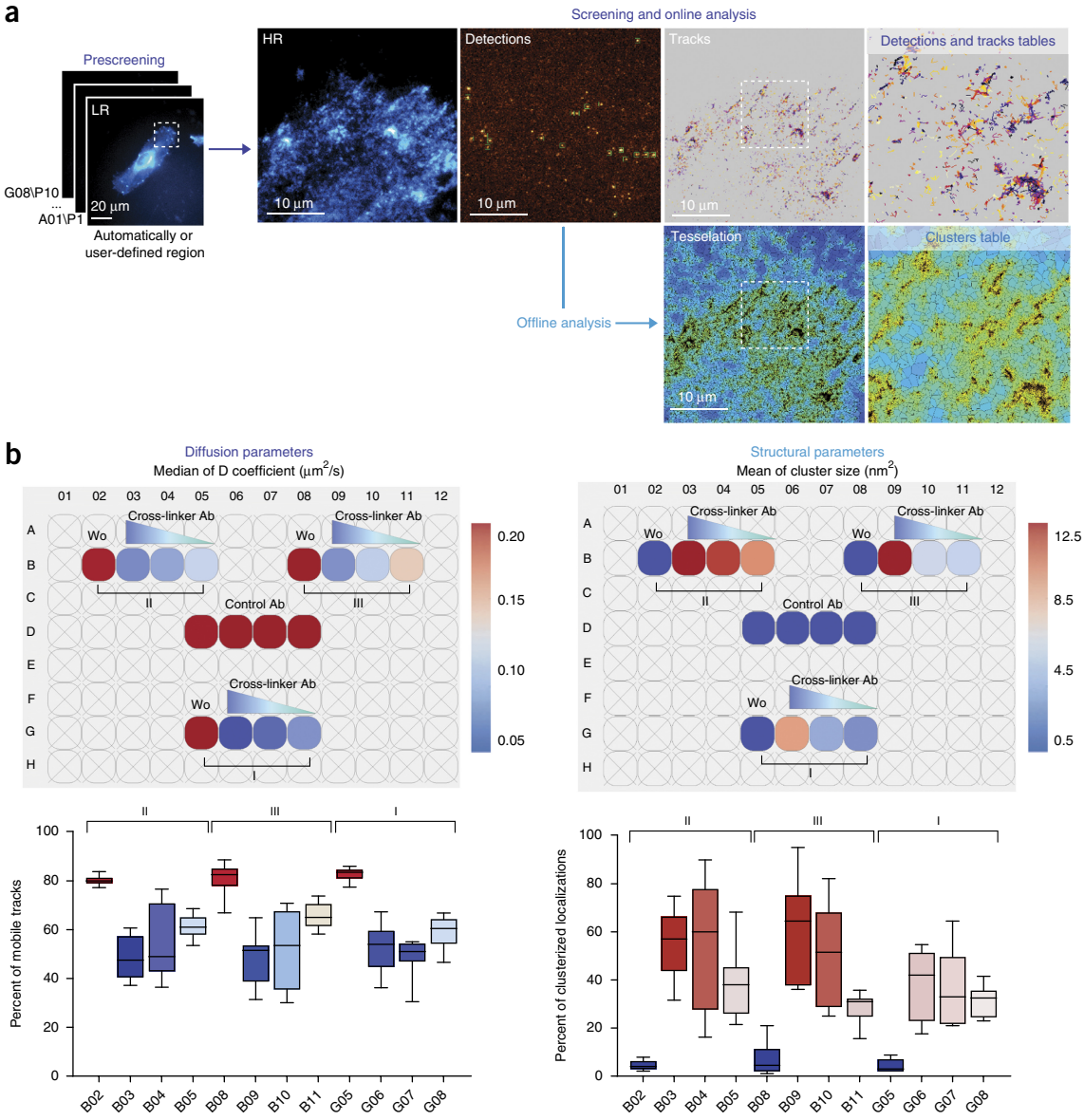

Figure 4 | Quantification of mobility and clustering of membrane proteins. (**a**) Example of HCS-SMLM workflow including a prescreening step using a low-magnification lens to select the regions of interest, followed by the SMLM screening. Metadata corresponding to localization coordinates (*x*, *y*, *t*) and dynamics (tracks, diffusion coefficients) are computed online. Clustering metadata are computed offline directly from online metadata. (**b**) Data mining showing heatmaps of median Dcoef (left) and mean cluster size (right) as a function of Ab cross-linker concentrations (Wo, without Ab cross-linkers). Box-plots of the fractions of mobile tracks (left) and clustered molecules (right) per well clearly display a correlation between the dose of Ab cross-linkers and receptor mobility and clustering. I, II, III represent the different modes of acquisition (see Online Methods and **Supplementary Fig. 11**). Box plots depict median values and IQR; whiskers represent min and max values. *P* value < 0.05. *P* values were calculated using unpaired *t*-test.

interest to study the influence of dSTORM buffers on the photoswitching properties of fluorescent proteins used for PALM, as combined PALM–dSTORM acquisition is commonly used to perform multicolor SMLM[39].

As a proof of concept, we screened several photophysical parameters of two organic dyes, Alexa 647 (carbocyanine) and Alexa 532 (rhodamine), and of one photoswitchable protein, mEos3.2 (ref. 40), in the presence of 16 different buffers (four concentrations of thiols β-MEA (β-Mercaptoethylamine) (25, 50, 100, 200 mM) combined with four different pH values (5.2, 6.2, 7.2, 8.2)), which resulted in a total of 48 conditions (**Fig. 3**; see **Supplementary Fig. 6** for control experiments). For Alexa 647 dyes, we observed that at low concentration of thiols (for 25 and 50 mM), increasing the pH induced a decrease of the duty cycle, which is in accordance with published results[32]. However, at higher thiol concentration (≥100 mM), we measured a stronger decrease of the duty cycle when the pH decreases. This dual effect of the pH dependence on thiol concentration is a novel aspect that has, to our knowledge, not been previously described. For Alexa 532 fluorophores, we found that it displayed the smallest duty cycle (0.2) for 200 mM of thiols at pH 6.2 and 7.2.

In order to confirm these results in a cellular context, we performed several two-color dSTORM experiments using the best and worst buffer combinations on microtubule, lamin and vimentin proteins

© 2017 Nature America, Inc., part of Springer Nature. All rights reserved.

immunostained with Alexa 647 and Alexa 532 fluorophores. While it was possible to reconstruct the labeled structures with good quality using 200 nM of thiols at pH 7.2 (**Fig. 3c** and **Supplementary Fig. 7**), the quality of the reconstructions strongly decreased with buffers at 25 mM of thiols or at pH 5.2 (**Supplementary Fig. 8**). The quality of all the super-resolution reconstructions support the quantifications made on the photophysical properties.

Finally, we measured a strong effect of thiol concentration on the fluorescent protein mEos3.2, with a two-fold higher percentage of blinking proteins induced by the highest thiol concentration (from 20–35% for 25–50 mM to 50–55% for ≥100 mM of thiols) (**Fig. 3d**). Conversely, the pH variation does not seem to affect the fraction of blinking mEos3.2 proteins (**Fig. 3d**).

Quantification of membrane-receptor dynamics

Activity and stimulus-dependent modulation of neurotransmitter-receptor trafficking and surface mobility are key steps in synapse development and plasticity[41,42]. Furthermore, it is likely that modulation of receptor trafficking is both a good reporter and a possible effector of a variety of pharmacological substances[43,44]. Hence, it is important to be able to measure and quantify receptor mobility and its modulation in a variety of experimental conditions. We here illustrate the capacity of our HCS-SMLM method to assess such parameters using sptPALM and demonstrate its ability to correlate fine modifications of protein mobility with structural organization in a single workflow.

We first checked cell viability over long-term acquisition and imaging medium autofluorescence (**Supplementary Fig. 9**) and controlled the homogeneity of the single-molecule signal across an entire plate (**Supplementary Fig. 10**). Then, as a proof-of-concept experiment, we incubated various antibody (Ab) concentrations with HeLa cells expressing the membrane receptor SEP::GluA1::mEos2 in order to quantify the dose effect of Ab cross-linkers on receptors' mobility. Induced modifications of membrane-receptor dynamics were obtained using four concentrations of a polyclonal anti-SEP antibody (0, 1/100, 1/300, 1/1,000) in optimized culture medium (**Supplementary Fig. 11**). We used the diffusion coefficient (Dcoef) metadata to characterize receptor dynamics and morphological metadata, such as the number of clusters and the number of localizations per cluster, to characterize the molecular organization (**Fig. 4a**). As a result, the HCS heatmap revealed a perfect correlation between Ab cross-linker concentration and receptor diffusion coefficient. Increasing the cross-linker concentration induced a decrease in receptor mobility, which was visible both in the median of Dcoef and in the percentage of immobile molecules (**Fig. 4b**, left, and **Supplementary Fig. 12**). We then quantified the correlation between the Ab cross-linker dose and receptor clustering using the SR-Tesseler polygon-based segmentation method[45] to automatically compute clusters from the localization metadata (**Fig. 4a**). We observed a positive correlation between Ab cross-linker concentration and both mean cluster area and fraction of clustered localizations (**Fig. 4b**, right).

DISCUSSION

The HCS-SMLM method presented here combines the advantages of two powerful approaches: SMLM and HCS. It provides an all-inclusive acquisition, data extraction and analysis workflow, and this allows quantification of SMLM data with improved throughput. In a single, automatic workflow, it allows researchers to screen the effect of drugs or chemical environments on the nanoscale organization and dynamics of target proteins or photophysical properties of fluorophores. Until now, single-molecule imaging techniques such as dSTORM, DNA-PAINT or (spt)PALM have principally been used to study biological processes at the single-cell level with only a limited number of cells and conditions. The automatic pipeline provided by our HCS-SMLM approach allows researchers to drastically multiply the statistics and the number of biological conditions that can be studied at nanoscale resolution. Compatible with conventional SMLM equipment and single-molecule-detection software, it can easily be implemented by research laboratories to improve throughput and biological content.

We here validate the HCS-SMLM method as a powerful investigation technique that enables the large-scale characterization of fluorescent dyes, nanoscale protein organization and dynamics of cells at the single-molecule level. At the biochemistry level, this method will facilitate the screening of new fluorescent dyes or mutated fluorescent proteins in order to improve or discover new photoswitchable probes and buffers with better photophysics for quantitative super-resolution applications (e.g., reduced blinking or photobleaching, better photoactivation control, improved duty cycle, etc.). The results obtained from the acquisition of a complete 96-well plate in dSTORM or DNA-PAINT suggest that, depending on the number of conditions, time may be an issue and a limiting factor. HCS-dSTORM allows very fast acquisitions but is limited to a maximum time of about 10 h, in which a total of about 100 cells can be screened. An alternative solution to this time limitation could be to use rhodamine dyes, such as Alexa 532, that are more stable and have been demonstrated to better tolerate oxygen[7,29] but are less bright than Alexa 647. Another solution could be automatic dispensing of buffer in each well using a pipetting robot or continuous flow of gas without oxygen synchronized with the well to image. HCS-DNA-PAINT is an interesting and powerful alternative approach, since it does not have this lifetime-limit issue and offers unique quantitative capabilities[46]. It is, however, 10 to 20 times slower than HCS-dSTORM, which would make large-scale screening experiments very time consuming. General solutions to increase the acquisition speed could be to increase the localization density and use 2D or 3D high-density localization algorithms[17,19,20,47], increase the acquisition field of view[48] or use faster PAINT-like labeling strategies. In cellular biology, HCS-SMLM will allow many extensive nanoscale investigations in a cellular context, such as investigations into the effects of drugs on protein targets, of new siRNA, of different mutants or protein deletions, of extracellular environments, etc. The workflow provided by HCS-SMLM is versatile and evolutionary, as it can be implemented or upgraded with new SMLM strategies. It is compatible with most SMLM equipment and recent quantitative single-molecule labeling techniques such as qPAINT[46]. It can be enriched with additional quantitative analysis methods or general classification methods commonly used in bioinformatics such as machine learning[3,49].

METHODS

Methods, including statements of data availability and any associated accession codes and references, are available in the online version of the paper.

Note: Any Supplementary Information and Source Data files are available in the online version of the paper.

© 2017 Nature America, Inc., part of Springer Nature. All rights reserved.

ACKNOWLEDGMENTS

This work was supported by the advanced ERC grant ADOS to D.C., the regional council of Aquitaine grant Dynascreen to D.C. and J.-B.S., the FranceBioImaging infrastructure ANR-10-INBS-04 to J.-B.S., the LabEx BRAIN and the IdEx Bordeaux to J.-B.S., and the Fondation pour la Recherche Médicale DEI20151234402 and ANR-Integractome to G.G.

AUTHOR CONTRIBUTIONS

A.B. performed all the experiments with the help of R.G., C.B. and M.C. A.K. developed the software for online processing and Single Molecule Profiler. F.L. and C.B. performed quantitative data analysis. M.C. developed the HCS-SMLM acquisition interface. O.R. and G.G. designed some biological control experiments. All the authors contributed to the manuscript. J.-B.S. and D.C. came up with the original idea. J.-B.S. supervised this work.

COMPETING FINANCIAL INTERESTS

The authors declare no competing financial interests.

Reprints and permissions information is available online at http://www.nature.com/reprints/index.html. Publisher's note: Springer Nature remains neutral with regard to jurisdictional claims in published maps and institutional affiliations.

1. Neumann, B. *et al.* High-throughput RNAi screening by time-lapse imaging of live human cells. *Nat. Methods* **3**, 385–390 (2006).
2. Wachsmuth, M. *et al.* High-throughput fluorescence correlation spectroscopy enables analysis of proteome dynamics in living cells. *Nat. Biotechnol.* **33**, 384–389 (2015).
3. Bray, M.A. *et al.* Cell Painting, a high-content image-based assay for morphological profiling using multiplexed fluorescent dyes. *Nat. Protoc.* **11**, 1757–1774 (2016).
4. Liu, Z., Lavis, L.D. & Betzig, E. Imaging live-cell dynamics and structure at the single-molecule level. *Mol. Cell* **58**, 644–659 (2015).
5. Rust, M.J., Bates, M. & Zhuang, X. Sub-diffraction-limit imaging by stochastic optical reconstruction microscopy (STORM). *Nat. Methods* **3**, 793–795 (2006).
6. van de Linde, S., Sauer, M. & Heilemann, M. Subdiffraction-resolution fluorescence imaging of proteins in the mitochondrial inner membrane with photoswitchable fluorophores. *J. Struct. Biol.* **164**, 250–254 (2008).
7. van de Linde, S. *et al.* Direct stochastic optical reconstruction microscopy with standard fluorescent probes. *Nat. Protoc.* **6**, 991–1009 (2011).
8. Duwé, S. *et al.* Expression-enhanced fluorescent proteins based on enhanced green fluorescent protein for super-resolution microscopy. *ACS Nano* **9**, 9528–9541 (2015).
9. Sharonov, A. & Hochstrasser, R.M. Wide-field subdiffraction imaging by accumulated binding of diffusing probes. *Proc. Natl. Acad. Sci. USA* **103**, 18911–18916 (2006).
10. Giannone, G. *et al.* Dynamic superresolution imaging of endogenous proteins on living cells at ultra-high density. *Biophys. J.* **99**, 1303–1310 (2010).
11. Jungmann, R. *et al.* Multiplexed 3D cellular super-resolution imaging with DNA-PAINT and Exchange-PAINT. *Nat. Methods* **11**, 313–318 (2014).
12. Hess, S.T., Girirajan, T.P. & Mason, M.D. Ultra-high resolution imaging by fluorescence photoactivation localization microscopy. *Biophys. J.* **91**, 4258–4272 (2006).
13. Betzig, E. *et al.* Imaging intracellular fluorescent proteins at nanometer resolution. *Science* **313**, 1642–1645 (2006).
14. Manley, S. *et al.* High-density mapping of single-molecule trajectories with photoactivated localization microscopy. *Nat. Methods* **5**, 155–157 (2008).
15. Sibarita, J.B. High-density single-particle tracking: quantifying molecule organization and dynamics at the nanoscale. *Histochem. Cell Biol.* **141**, 587–595 (2014).
16. Franke, C., Sauer, M. & van de Linde, S. Photometry unlocks 3D information from 2D localization microscopy data. *Nat. Methods* **14**, 41–44 (2016).
17. Min, J. *et al.* 3D high-density localization microscopy using hybrid astigmatic/ biplane imaging and sparse image reconstruction. *Biomed. Opt. Express* **5**, 3935–3948 (2014).
18. Winterflood, C.M., Platonova, E., Albrecht, D. & Ewers, H. Dual-color 3D superresolution microscopy by combined spectral-demixing and biplane imaging. *Biophys. J.* **109**, 3–6 (2015).
19. Ovesný, M., Pavel, K., Švindrych, Z. & Hagen, G. M. High density 3D localization microscopy using sparse support recovery. *Opt. Express* **22**, 31263–31276 (2014).
20. Babcock, H., Sigal, Y.M. & Zhuang, X. A high-density 3D localization algorithm for stochastic optical reconstruction microscopy. *Opt. Nanoscopy* **1**, 6 (2012).
21. Bullen, A. Microscopic imaging techniques for drug discovery. *Nat. Rev. Drug Discov.* **7**, 54–67 (2008).
22. Flottmann, B. *et al.* Correlative light microscopy for high-content screening. *Biotechniques* **55**, 243–252 (2013).
23. Gunkel, M., Flottmann, B., Heilemann, M., Reymann, J. & Erfle, H. Integrated and correlative high-throughput and super-resolution microscopy. *Histochem. Cell Biol.* **141**, 597–603 (2014).
24. Holden, S.J. *et al.* High throughput 3D super-resolution microscopy reveals Caulobacter crescentus *in vivo* Z-ring organization. *Proc. Natl. Acad. Sci. USA* **111**, 4566–4571 (2014).
25. Pereira, P.M., Almada, P. & Henriques, R. High-content 3D multicolor super-resolution localization microscopy. In *Methods in Cell Biology* Vol 125 (ed. Paluch, E.K.) Ch. 7 (Elsevier, 2015).
26. Jones, T.R. *et al.* CellProfiler Analyst: data exploration and analysis software for complex image-based screens. *BMC Bioinformatics* **9**, 482 (2008).
27. Ovesný, M., Křížek, P., Borkovec, J., Švindrych, Z. & Hagen, G.M. ThunderSTORM: a comprehensive ImageJ plug-in for PALM and STORM data analysis and super-resolution imaging. *Bioinformatics* **30**, 2389–2390 (2014).
28. Huang, B., Wang, W., Bates, M. & Zhuang, X. Three-dimensional super-resolution imaging by stochastic optical reconstruction microscopy. *Science* **319**, 810–813 (2008).
29. Heilemann, M., van de Linde, S., Mukherjee, A. & Sauer, M. Super-resolution imaging with small organic fluorophores. *Angew. Chem. Int. Edn Engl.* **48**, 6903–6908 (2009).
30. Endesfelder, U. *et al.* Chemically induced photoswitching of fluorescent probes—a general concept for super-resolution microscopy. *Molecules* **16**, 3106–3118 (2011).
31. Swoboda, M. *et al.* Enzymatic oxygen scavenging for photostability without pH drop in single-molecule experiments. *ACS Nano* **6**, 6364–6369 (2012).
32. Olivier, N., Keller, D., Gönczy, P. & Manley, S. Resolution doubling in 3D-STORM imaging through improved buffers. *PLoS One* **8**, e69004 (2013).
33. Jungmann, R. *et al.* Single-molecule kinetics and super-resolution microscopy by fluorescence imaging of transient binding on DNA origami. *Nano Lett.* **10**, 4756–4761 (2010).
34. Thompson, R.E., Larson, D.R. & Webb, W.W. Precise nanometer localization analysis for individual fluorescent probes. *Biophys. J.* **82**, 2775–2783 (2002).
35. Zhang, X. *et al.* Highly photostable, reversibly photoswitchable fluorescent protein with high contrast ratio for live-cell superresolution microscopy. *Proc. Natl. Acad. Sci. USA* **113**, 10364–10369 (2016).
36. Legant, W.R. *et al.* High-density three-dimensional localization microscopy across large volumes. *Nat. Methods* **13**, 359–365 (2016).
37. Dempsey, G.T., Vaughan, J.C., Chen, K.H., Bates, M. & Zhuang, X. Evaluation of fluorophores for optimal performance in localization-based super-resolution imaging. *Nat. Methods* **8**, 1027–1036 (2011).
38. Vogelsang, J. *et al.* Make them blink: probes for super-resolution microscopy. *Chemphyschem* **11**, 2475–2490 (2010).
39. Chazeau, A. *et al.* Nanoscale segregation of actin nucleation and elongation factors determines dendritic spine protrusion. *EMBO J.* **33**, 2745–2764 (2014).
40. Zhang, M. *et al.* Rational design of true monomeric and bright photoactivatable fluorescent proteins. *Nat. Methods* **9**, 727–729 (2012).
41. Triller, A. & Choquet, D. New concepts in synaptic biology derived from single-molecule imaging. *Neuron* **59**, 359–374 (2008).
42. Penn, A.C. *et al.* Hippocampal LTP and contextual learning require surface diffusion of AMPA receptors. *Nature* **549**, 384–388 (2017).
43. Heine, M. *et al.* Surface mobility of postsynaptic AMPARs tunes synaptic transmission. *Science* **320**, 201–205 (2008).
44. Zhang, H. *et al.* Regulation of AMPA receptor surface trafficking and synaptic plasticity by a cognitive enhancer and antidepressant molecule. *Mol. Psychiatry* **18**, 471–484 (2013).
45. Levet, F. *et al.* SR-Tesseler: a method to segment and quantify localization-based super-resolution microscopy data. *Nat. Methods* **12**, 1065–1071 (2015).
46. Jungmann, R. *et al.* Quantitative super-resolution imaging with qPAINT. *Nat. Methods* **13**, 439–442 (2016).
47. Min, J. *et al.* FALCON: fast and unbiased reconstruction of high-density super-resolution microscopy data. *Sci. Rep.* **4**, 4577 (2014).
48. Douglass, K.M., Sieben, C., Archetti, A., Lambert, A. & Manley, S. Super-resolution imaging of multiple cells by optimised flat-field epi-illumination. *Nat. Photonics* **10**, 705–708 (2016).
49. Jones, T.R. *et al.* Scoring diverse cellular morphologies in image-based screens with iterative feedback and machine learning. *Proc. Natl. Acad. Sci. USA* **106**, 1826–1831 (2009).

© 2017 Nature America, Inc., part of Springer Nature. All rights reserved.

ONLINE METHODS

Materials. For all experiments, the acquisitions were performed on an inverted motorized microscope (Nikon TiE, Japan) equipped with a 100 × 1.49 NA PL-APO objective (screening), a 40 × 1.4 NA PL-APO objective (prescreening, optional), a perfect focus system (Nikon, France), and a TIRF illumination arm (Nikon, France) allowing long acquisitions in oblique illumination mode. Illumination lasers (405 nm (Vortran, USA), 532 nm (Errol), 561 nm (Errol), 640 nm (Coherent, USA)) were collimated and collinearly combined via dichroic beam splitters and sent to the TIRF arm through a multimode optical fiber. An acousto-optic tunable filter (AOTF) was used to select one or several wavelengths, control intensities and provide on–off modulation. The fluorescence signal was collected by the objective and focused either onto a sensitive EMCCD camera (Evolve512, Photometrics) or an sCMOS camera (OrcaFash4.0, Hamamatsu) through the combination of dichroic and emission filters (D101-R561 and F39–617, respectively, Chroma). The entire setup was packaged in a temperature-controlled chamber with a humidified gas supply (Life Imaging Services, Switzerland). The resolution of the setup was measured to be 357 nm ± 20 nm using bidimensional Gaussian fitting on 100 nm isolated fluorescent microbeads (TetraSpeck, T7279, ThermoFisher).

The support used for all experiments was a 170 µm thick glass-bottom 96-well plate MatriplateTM (ref MGB096-1-2-LG-L (Brooks, USA)). For live-cell imaging, imaging was performed in FluorobriteTM DMEM (ref A1896702, ThermoFisher) supplemented with 1% Glutamax (ref 35050-061, Gibco) and 10% FBS (ref 16000-044, ThermoFisher).

The antibody used to stain microtubules was a mouse monoclonal antibody (DM1A clone) against alpha Tubulin (ref ab7291, Abcam). For Vimentin, the antibody was a rabbit polyclonal antibody (EPR3776 clone, ref ab92547, Abcam). The antibody used to induce a cross-link reaction was anti-GFP Tag Polyclonal Antibody (ref A-6455, ThermoFisher). The antibody used for immunolabeled lamin B1 and as a control in live-cell cross-link experiments was Anti-lamin B1 (ref ab16048, Abcam).

The secondary antibodies for dSTORM imaging were Anti Mouse Alexa 647 (ref A31571, ThermoFischer), Anti Mouse Alexa 532 (ref A11002, ThermoFischer), Anti Rabbit Alexa 647 (ref A21245, ThermoFischer), Anti Rabbit Alexa 532 (ref A11009, ThermoFischer).

Secondary antibodies, DNA probes and buffers for DNA-PAINT experiments were purchased from UltiVue Inc. (Cambridge, USA).

Fiducial markers used for dSTORM, DNA-PAINT acquisition and 3D calibration were fluorescent nanodiamonds (average size 100 nm, ref NDNV100nmMd10ml) from Adamas Nanotechnologies, Inc.

Final dSTORM imaging buffers were composed of 120 µg/ml Pyranose Oxidase (Sigma-Aldrich P4234) and catalase 57 µg/ml (Sigma-Aldrich C3515). β-Mercaptoethylamine (= cysteamine, β-MEA, ref 30070, from Sigma-Aldrich) was prepared as a 1 M stock solution in deionized water and stored at 4 °C. Tris–HCl (20 mM Tris, 50 mM NaCl) pH 7.2 was used as a base for the STORM buffer. Organic dyes Alexa 532 (ref A20001) and Alexa 647 (ref A37573) were purchased from Life Technologies, aliquoted at 1mg/ml in stock solution and stored at −20 °C.

Quality control. Quality control allows filtering out potential issues that arise during the screening process either because of optical problems (e.g., loss of focus) or nonoptimal photoactivation/photoswitching (e.g., too dense single-molecule events) (**Supplementary Fig. 10a**). In order to check the single-molecule regime, we use the full width at half maximum (FWHM) and the integrated intensity (I_0) metadata of each single-molecule localization event computed online by bidimensional Gaussian fitting as the main metric for quality control of our HCS-SMLM method along the entire screening process. We seeded 60 wells with electroporated Hela cells expressing the SEP::GluA1::mEos2 membrane protein. For each well, we acquired and analyzed automatically three cells by HCS-SMLM, leading to a total of 180 cells and 1 million localization events. The results show single peak distributions for both metadata, with FWHM = 367 nm (mean) ± 62 nm (SD) and I_0 = 84.1 photons (median) ± 41.2 (IQR) (n = 1,048,007). The FWHM is in good agreement with the resolution of the instrument measured on isolated beads, illustrating the stability of our HCS-SMLM system, both in keeping the focus and in its ability to maintain the single-molecule regime. Depending on the SMLM techniques and dimensions used in the HCS-SMLM pipeline (dSTORM, DNA-PAINT, (spt)PALM, 2D or 3D, etc.), additional metadata can be used to control the quality between wells, such as 3D calibration (**Supplementary Fig. 2**) or goodness to fit (**Supplementary Fig. 3**), and avoid, for example, potential border effects at the edge of a well plate (**Supplementary Fig. 10**).

mEOS 3.2 expression and purification. Briefly, *E. coli* BL21 RIPL-competent cells were transformed with the plasmid of interest (pbIG-mEOS3.2). Cells expressing the protein of interest were resuspended in a lysis buffer, sonicated at 4 °C following manufacturer's recommendations (Bioblock Scientific Vibra Cell Sonic VC505). After 1 h of centrifugation at 14,000*g* and 4 °C, the supernatant was collected and added to a HIS-Buster Nickel Affinity gel (Amocol). The protein was eluted at the manufacturer's recommendations and then dialized (SnakeSkin Dialysis Tubing) against PBS 1× (pH 7.4) overnight at 4 °C. Characterization of the protein was made by an SDS-PAGE gel and using an AKTAprime workstation. A Superdex 75 (HiLoad 16/600 Superdex 75 pg) column was used, and protein was recovered at the mass molecular weight expected. Finally, protein was concentrated and conserved at −80 °C before used.

Isolated fluorophore assay. Characterization of isolated fluorophores was performed using pure dyes directly adsorbed to a 96-well plate. 100 µl per well of a water solution of dyes Alexa 532 or Alexa 647 at 0.01 µg/ml or 2 nM of mEos3.2 protein containing multicolor fluorescent Tetraspecks microbeads (ref T07279, Life Technologies; for registration) were incubated at room temperature on the surface of a 96-well plate for 2 min and rinsed three times with PBS. Fluorophore isolation on the coated 96-well plate was verified by stepbleaching experiments using the PIF software[50] (**Supplementary Fig. 6a**). For stepbleaching analysis, fluorophores were imaged in five different positions per well in Tris–HCl p H7.5 buffer, (10 kW/cm^2, 20 ms per frame for 20 s).

Three random positions per well with 6,000 images per position were automatically acquired and analyzed providing at least 2,000 single-fluorophore intensity time traces per well (**Supplementary Fig. 6b**). We used seven metadata computed from isolated fluorophore acquisitions (**Supplementary Table 1** for definitions). By gating the number of blinks (#blinks) metadata, we defined two

© 2017 Nature America, Inc., part of Springer Nature. All rights reserved.

doi:10.1038/nmeth.4486

populations of fluorophores: blinking (#blinks > 1) and non-blinking (#blinks = 1) (**Fig. 3a**). This gate was used to filter out unblinking events and provide statistical results exclusively on blinking molecules.

Cell fixation and labeling for dSTORM and DNA-PAINT. Cells (Cos-7) used for dSTORM all prepared using an optimized protocol based on a fixation step with 4% Paraformaldehyde + 0.2% Glutaraldehyde + 0.3% Triton X-100 for 10 min at 37 °C, followed by the quenching of autofluorescence using 150 mM Glycine in PBS for 5 min at room temperature and an additional permeabilization step with 0.3% Triton X-100 in PBS for 20 min. Unspecific sites were blocked using 2% BSA in PBS, and primary antibodies were incubated overnight at 37 °C in the same blocking solution. Anti-tubulin antibodies were diluted at 1:1,000, anti-Vimentin at 1:400 and anti-Lamin B1 at 1:300. After three washes, secondary antibodies (anti-Mouse or anti-Rabbit coupled with either Alexa 647 or Alexa 532) were incubated for 1 h at 37 °C at 1:10,000 in blocking solution. For DNA-PAINT, anti-Mouse secondary antibodies were incubated using manufacturer buffer and recommendations (see "Materials").

dSTORM buffer preparation. Isolated fluorophores were imaged in Tris–HCl complemented with 25, 50, 100, or 200 mM β-MEA at pH 5.2, 6.2, 7.2 and 8.2. The pH of each solution was stable, measured just before and after the acquisition. Fixed cells were imaged in buffer at pH and β-MEA concentration specified in figures and complemented with an oxygen-scavenger system made of pyranose oxidase (120 µg/ml) and catalase (57 µg/ml) and 10% glucose.

2D dSTORM acquisition of isolated fluorophores and fixed cells. For organic dyes (Alexa 532 and Alexa 647) a 'pumping' phase was applied in order to transfer a maximum of molecules into dark states (640 nm: 40 kW/cm^2, 532 nm: 20 kW/cm^2 both for 10 s). Immediately after, the data-acquisition phase was automatically launched for 2 min at half laser power (6,000 frames at 50 frames per second (fps)) (**Fig. 2a**). For two-color fixed cell experiments, the same pumping and acquisition phases were performed but for 10 × 8,000 frames at 50 fps for lamin B1 staining and 2 × 8,000 frames at 50 fps for tubulin or vimentin staining. For isolated mEOS3.2 proteins, no 'pumping' phase was applied, and constant power of both 405 nm and 561 nm lasers was used for the acquisition phase (6,000 frames at 50 fps, 561 nm: 15 kW/cm^2, 405 nm: 200 mW/cm^2). As proved by the coherence of our results with previous work[32,37], this volume of data was sufficient to obtain interpretable results and a good compromise between the amount of data and the total acquisition duration.

3D dSTORM and DNA-PAINT acquisition. 3D localization was performed using the N-STORM astigmatic lens (Nikon, France). We performed anisotropic 2D Gaussian fitting of astigmatic single-molecule data followed by *Z*-coordinate retrieval as described in Kechkar *et al.*[51]. The astigmatism-based 3D point-spread function was calibrated using nanodiamonds located in 15 different wells acquired at successive depths by using *Z*-steps of 50 nm. The homogeneity of the 3D calibration over the entire wellplate allowed us to use the same calibration for all positions across the entire plate (**Supplementary Fig. 2**).

For 3D dSTORM acquisitions, a 'pumping' phase was applied at 640 nm (40 kW/cm^2) for 15 s (**Supplementary Fig. 6b**). Immediately after, the acquisition phase was launched at half laser power for 8,000 frames at 100 fps, 512 × 512 (20.5 µm × 20.5 µm FOV). Since Alexa 647 is sensitive to the presence of oxygen[30], and because of the long duration of the total acquisition, we designed a specific screening sequence. First, we seeded, fixed and labeled cells on the entire 96-well plate. Then, we distributed at the same time the dSTORM buffer using 200 mM of thiols at pH 7.2 combined with oxygen scavengers. Finally, we automatically acquired one cell per well in a serpentine mode, attempting to cover the entire wellplate before the loss of blinking efficiency due to oxygenation of the dSTORM buffer. Cells were prescreened manually before screening and acquired automatically using our HCS-SMLM pipeline as described earlier, covering a total traveling distance of 85 cm.

For 3D DNA-PAINT acquisitions, 561 nm DNA imager probes were incubated at the same time into every well following manufacturer recommendation (at final concentration of 0.3 nM) just before the acquisition phase. The acquisition was launched for 16,000 frames at 10 fps, 512 × 512 (20.5 µm × 20.5 µm FOV), following authors'[52] and manufacturer's recommendations for the exposure time and the number of frames. Similar to dSTORM, cells were prescreened manually before screening and acquired automatically in serpentine mode.

Single-fluorophore timeline data extraction, photophysical parameters and bead filtering. SR-Tesseler[45] was used to analyze fluorophore photophysics. A single fluorophore is represented as a group of several localizations occurring in a vicinity of time and space. Since the fluorophores are spatially isolated (see control with step bleaching), we ensured no blinking events were missed by defining a larger distance radius ω (160 nm, identical to the step-bleaching analysis) and a longer blinking time interval tolerance τ (100 s) than necessary. Multiple localizations occurring below ω and τ were tagged as being the same molecule, and seven photophysical parameters were individually computed (see **Supplementary Table 1** for definition). We automatically excluded fluorescent beads present in all frames from the analysis. First, for each localization, the number of localizations n in a radius r was calculated. We then identified the beads as having the number of localizations equal to the total number of frames acquired. Second, all the localizations inside r from the bead's barycenter were removed. For all data sets presented in this paper, we used r = 500 nm. To avoid any user input, the entire process was automated by the inclusion of a macro mode in SR-Tesseler.

Cluster analysis. We used the SR-Tesseler[45] software to quantify clusters from the localized molecule coordinates. Briefly, a Voronoï diagram subdivides a super-resolution image into polygons centered on localized molecules called seeds. For each seed, several parameters are computed, such as the distance to the closest molecules or local density at different ranks of neighborhood. Once the Voronoï diagram generated, the object segmentation process was computed in three steps: first, first-rank densities of the molecules were computed on the Voronoï diagram generated from the entire set of localizations. Second, histograms of the first-rank density were automatically thresholded using a bi-Gaussian fit. The intersection between these two Gaussians determined the

© 2017 Nature America, Inc., part of Springer Nature. All rights reserved.

automatic threshold for separating clustered molecules from isolated localizations. Third, clusters were computed by merging all selected adjoining polygons, and object outlines were defined by connecting all localizations belonging to the border of the objects. As for the photophysics data extraction, the whole process was automated using a macro mode.

Cell culture and electroporation. HeLa cells were electroporated with SEP::GluA1::mEOS2 according to the manufacturer's protocol (Lonza), using 2 µg of DNA for 2 million cells. Electroporated cells were immediately seeded on a glass-bottom 96-well plate at 60,000 cells per well or 6,000 cells per well for isolated cell experiments. Live acquisition was performed 48 h postelectroporation.

Optimization of cellular medium and cell viability. To study single fluorescent molecules in live cells with TIRF, we needed to find a medium that maintained cellular viability over several hours without any autofluorescence. The classical DMEM medium was thus replaced with Fluorobrite + Glutamax and optionally completed with 10% FBS. Cellular health in different wells was monitored using time-lapse microscopy over at least 8 h. The microscope was enclosed in a temperature-controlled box and a humidified gas supply, preventing the evaporation of culture medium and maintaining adequate pH. We observed that, after 4 h of acquisition, HeLa cells clearly required the presence of serum to stay alive and spread correctly on the support (**Supplementary Fig. 9b**). After 8 h of acquisition on the setup with the mix Fluorobrite + Glutamax + serum, a similar number of cells and identical shapes were obtained as with the classical medium (DMEM + SVF) (**Supplementary Fig. 9b**). Next, we examined the autofluorescence of the Fluorobrite medium supplemented with serum, and we found no significant difference in the single-molecule detection compared to PBS (**Supplementary Fig. 9c**). This medium was used for all live-cell experiments.

Drift-control assay. As for the isolated fluorophores assay, 2 nM of purified mEos3.2 protein was incubated for 2 min at room temperature in four wells of a 96-well plate (**Supplementary Fig. 10**). Wells were acquired and analyzed with strictly identical acquisition and processing parameters as for living cells. Ten random positions per well were automatically acquired in SMLM (TIRF, 405/561 nm excitation). No drift was detected for all wells (40 positions) over the 20 s of imaging. Furthermore, as expected, only a very weak fraction (10%) of tracks was considered as mobile (Dcoef up to 1.10^{-2} µm^2/s). These mobile tracks are due to the rare detaching of mEos3.2 proteins. No manual intervention was used to find or correct focus or to reload oil between positions and wells. We thus were able to detect the 'zero' of diffusion without drift or user intervention through a multiwell plate and validate all our automatic (spt)PALM process and tracking-reconnection parameters.

sptPALM acquisition. HeLa cells expressing the membrane receptor SEP::GluA1::mEos2 were photoactivated using a 405 nm laser (3 W/cm^2), and the resulting photoconverted molecule was excited with a 561 nm laser (0.8 kW/cm^2). HeLa cells were imaged at 37 °C with humidified air + 5% C02 gas in the bottom glass of a 96-well plate. Both lasers illuminated the sample simultaneously. Laser intensities were tuned to acquire fluorescence of a single molecule over multiple frames before bleaching. The acquisition was driven in streaming mode at 50 frames per second (20 ms exposure time) for 1,000 frames in order to find a compromise between total acquisition duration and statistical significance.

We first checked cell viability over long-term acquisition and imaging-medium autofluorescence (**Supplementary Fig. 9**) and controlled the homogeneity of the single-molecule signal across an entire plate (**Supplementary Fig. 10**). Induced modifications of membrane-receptor dynamics were obtained using four concentrations of a polyclonal anti-GFP (see "Materials") antibody (0, 1/100, 1/300, 1/1,000) in culture medium. We performed triplicate experiments and acquired ten positions per well, which led to a total of 12 wells and 120 stacks of 1,000 frames. In order to verify that the quantifications were independent of incubation time, three different acquisition sequences were performed (**Supplementary Fig. 11**): (i) Sequential acquisition: antibodies were incubated individually well by well, which required manual intervention between each well acquisition. (ii) Series acquisition: all antibody concentrations were loaded at the same time, at the beginning of the acquisition (no user intervention during acquisition), and the acquisition was performed sequentially, one Ab concentration after the other (0, 1/100, 1/300 and 1/1,000). (iii) Random acquisition: same as sequence ii, except that positions were randomly acquired across all concentrations. Positions were manually user defined during the prescreening step, which took less than 45 min for 120 positions. The overall experiment, composed of 12 wells and 120 stacks acquired at 50 frames per second, took less than 2 h, including online analysis.

For the quantification, we used the diffusion coefficient (Dcoef) metadata to characterize the receptor dynamics, and morphological metadata, such as the number of clusters and the number of localizations per cluster, to characterize the molecular organization (**Fig. 4a** and **Supplementary Table 1** for metadata definitions). Gating the Dcoef metadata, we defined two populations of trajectories: immobile (Dcoef < 10^{-2} µm^2/sec) and mobile (Dcoef > 10^{-2} µm^2/sec) (**Fig. 4b**), which we used to provide statistical analysis of the fraction of mobile and immobile receptors. The threshold value of 10^{-2} µm^2/sec was set in accordance with previously published work[53] and in agreement with our data from immobilized purified mEos protein by glass adsorption (**Supplementary Fig. 10**) and with the localization precision of the setup.

The dose response of Ab cross-linker led to similar results for the three acquisition modes, which illustrated the independence on Ab cross-linker incubation time (**Supplementary Fig. 12**). In order to check for Ab specificity, we added four control wells (ten positions per well) with Ab not directed against our protein of interest (Anti-laminB1). Similar to the wells without Ab, this control condition showed no modification of receptor mobility (**Fig. 4b** and **Supplementary Fig. 12**).

Motion analysis. Motion analysis is based on the mean square displacement (MSD) analysis. It measures the area r^2 explored by a molecule over time, and it is widely used to extract diffusion characteristics of molecules from their trajectories. For each MSD curve, the diffusion coefficient (Dcoef) can be computed by fitting the first four points of the MSD using $r^2 = 4 \times \text{Dcoef} \times t$ linear

© 2017 Nature America, Inc., part of Springer Nature. All rights reserved.

doi:10.1038/nmeth.4486

equation. This provides a global diffusion coefficient per trajectory. The instantaneous diffusion coefficient (instant Dcoef) was computed for each timepoint of the trajectory by linear fitting of the four following points of the MSD. It is important to note that the localization precision defines the minimum resolvable radius of confinement of the system. Below this limit, it is not possible to distinguish between immobilization and confinement.

Homogeneity of the diffusion coefficient. A validation was done to verify the homogeneity of protein diffusion in several wells of a 96-well plate under control conditions. We seeded the 60 wells in the middle of the plate with electroporated HeLa cells expressing the SEP::GluA1::mEos2 membrane protein (see Cell culture and electroporation). For each well, we acquired three different cells (total of 180 cells automatically acquired and analyzed). As showed in **Supplementary Figure 9c**, a very similar profile of protein diffusion was obtained across the different wells.

Data availability statement. The software and source code are freely available for academic use as **Supplementary Software**. Updated versions can be found at http://www.iins.u-bordeaux.fr/team-sibarita-CPA. Source data file for **Figure 4** is available online. A **Life Sciences Reporting Summary** is available.

50. McGuire, H., Aurousseau, M.R.P., Bowie, D. & Blunck, R. Automating single subunit counting of membrane proteins in mammalian cells. *J. Biol. Chem.* **287**, 35912–35921 (2012).
51. Kechkar, A., Nair, D., Heilemann, M., Choquet, D. & Sibarita, J.B. Real-time analysis and visualization for single-molecule based super-resolution microscopy. *PLoS One* **8**, e62918 (2013).
52. Schnitzbauer, J., Strauss, M.T., Schlichthaerle, T., Schueder, F. & Jungmann, R. Super-resolution microscopy with DNA-PAINT. *Nat. Protoc.* **12**, 1198–1228 (2017).
53. Nair, D. *et al.* Super-resolution imaging reveals that AMPA receptors inside synapses are dynamically organized in nanodomains regulated by PSD95. *J. Neurosci.* **33**, 13204–13224 (2013).

© 2017 Nature America, Inc., part of Springer Nature. All rights reserved.